Mesospheric studies with MIPAS and HIRDLS

Luis Federico Millán Valle

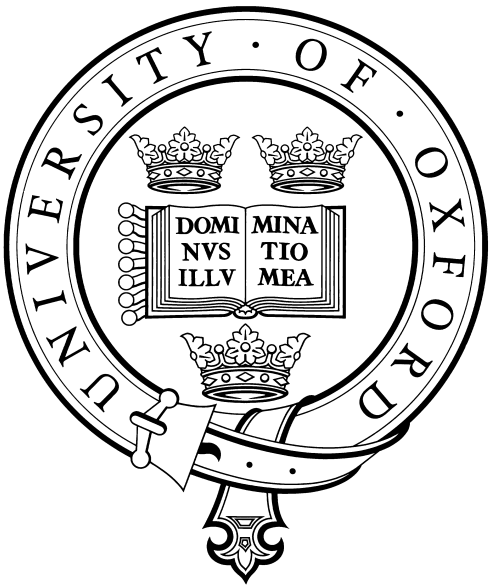

Thesis submitted for the degree of Doctor of Philosophy

Atmospheric, Oceanic and Planetary Physics
University of Oxford

Michaelmas Term 2009

Abstract

Luis Federico Millán Valle

Atmospheric, Oceanic and Planetary Physics

A thesis submitted for the degree of Doctor of Philosophy at the University of Oxford

Michaelmas Term 2009

This thesis discusses the mesospheric retrievals from high spectral resolution infrared limb measurements data as measured by the Michelson Interferometer for Passive Atmospheric Sounding (MIPAS). Altough MIPAS was designed for stratospheric studies, since April 2007, MIPAS measures the entire mesosphere at least every ten days using a special viewing mode. Retrieving geophysical properties at such high altitudes requires careful attention due to signal to noise limitations as well as the intrusion of non Local Thermodynamic Equilibrium (nonLTE) effects.

The three main parts of this thesis are:

(1) The evaluation of the Oxford MIPAS middle atmosphere dataset (profiles of pressure, temperature, H_2O, O_3, HNO_3, CH_4, N_2O, NO_2 and CO) as retrieved by the iterative algorithm MORSE. Comparisons of daily zonal means, daily zonal sections and comparisons of pairs of profiles against several mesospheric instruments are shown.

(2) The description and validation of a new linear (non-iterative) retrieval algorithm. This algorithm exploits the linearity of an optically thin path which allows to use all the available spectral points of the target parameter rather than just subset of the spectra.

(3) The validation of the modelled vibrational temperatures used either in the MORSE or in the linear retrieval to estimate the influence of the nonLTE effects upon the measured radiaces.

This thesis also briefly investigates the potential of the HIgh Resolution Dynamic Limb Sounder (HIRDLS) instrument to provide valuable mesospheric information, as well as the detection of polar mesospheric clouds using MIPAS radiances.

Acknowledgements

I would like to thank my supervisors, Anu Dudhia and John Barnett, for guiding me through the physics and mathematics of this DPhil and furthermore for coping without complaint with the vast number of grammatical mistakes corrected during the iterative process of writing up.

Thanks also to Manuel López Puertas for several informal chats about the intricacies of the nonLTE effects which helped to open my eyes to its complications.

Within AOPP, thanks to the various members of the Earth Observing Data Group for various useful discussions about physics and plotting problems. Thanks to Corwin and Ramin for their dramatical grammatical support and the conversations we have had over so many cups of tea.

Many thanks to my parents for their long distance love and the sponsored dinners. And finally, I turn to my two girls, Yatzil and Ángel. Thanks for joining me in this ride and putting up with me being late for dinner and a little bit (okay, more) grumpy than usual.

This research was funded by CONACYT (the National Council on Science and Technology of Mexico).

Contents

CHAPTER 1

Introduction

As shown in Figure 1.1, the atmosphere is usually divided into layers according to the sign of the temperature gradient: the troposphere, (the lowest layer) where the temperature decreases with height due to adiabatic expansion of convected air; the stratosphere, where the temperature increases due to ozone absorption of UV solar radiation; the mesosphere, where the temperature decreases again due to thermal radiation to space; and the thermosphere where the temperature increases mainly because of molecular oxygen absorption of UV solar radiation. The boundary regions between the layers are called the tropopause, stratopause, and mesopause, respectively.

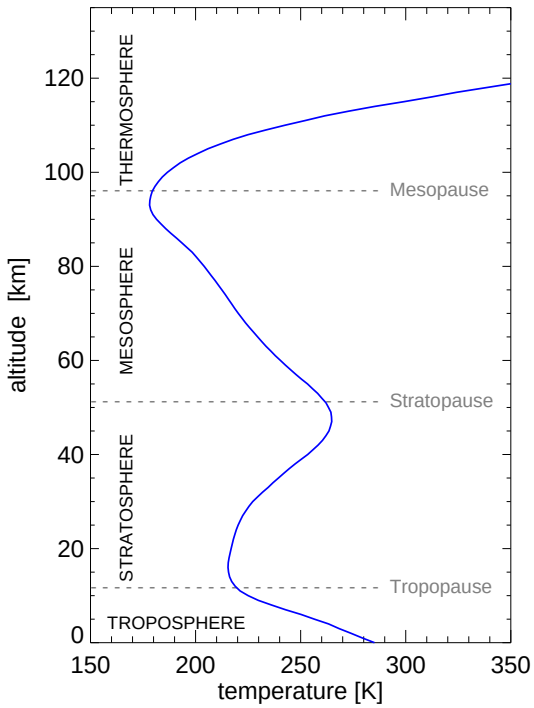

Figure 1.1: Thermal structure of the atmosphere.

The troposphere, also known as the lower atmosphere, is the atmospheric region where most of the clouds and weather systems occur. It has been extensively studied through meteorological soundings. The stratosphere, which contains the ozone layer, has been continuously monitored due to the importance of the absorption of harmful UV radiation by ozone. The mesosphere, despite its many fascinating phenomena (explained later) is to date one of the least explored parts of the atmosphere. The stratosphere and the mesosphere are together known as the middle atmosphere (MA). Above it, the thermosphere and the exosphere, where the atmosphere turns into space, are referred as the upper atmosphere.

The motivation of this thesis was to investigate the feasibility of using satellite infrared remote sensing to retrieve temperature, pressure and composition at mesospheric heights. In particular, to assess the quality of the atmospheric data retrieved with the Michelson Interferometer for Passive Atmospheric Sounding (MIPAS, detailed in section 3.1) and the HIgh Resolution Dynamics Limb Sounder (HIRDLS, detailed in section 3.2).

The mesosphere is the atmospheric region between about 50 km where stratospheric temperatures reach their maximum until about 85 km where mesospheric temperatures reach their minimum. Many interesting phenomena occur in this region. For instance, its temperature under polar sunlight conditions is the coldest natural temperature found on Earth, with mean temperatures of 130 K [Lubken and von Zahn, 1991]. Furthermore, despite the low H_2O concentrations at these altitudes, these low temperatures enable ice supersaturation to exist forming ice crystal clouds (named Polar Mesospheric Clouds). Many meteoroids burn up between about 75 km to 120 km depositing metal atoms which form global thin layers observable by spectroscopic techniques and LiDAR[1]. In addition, it hosts the secondary and tertiary ozone peaks and dynamical features such as tides and gravity waves play an important role on its winds, temperature and density fields.

1.1 Mesospheric thermal structure

Under radiative equilibrium the expected thermal structure of the mesosphere would be a cold area in the polar winter region due to the lack of direct solar radiation, warming up towards the summer region. However, as shown in Figure 1.2 the mesospheric temperature deviates considerably from radiative equilibrium showing warm temperatures over the winter pole and cold temperatures over the summer pole.

[1]LiDAR is the acronym for Light Detection And Ranging and basically it is an optical RADAR.

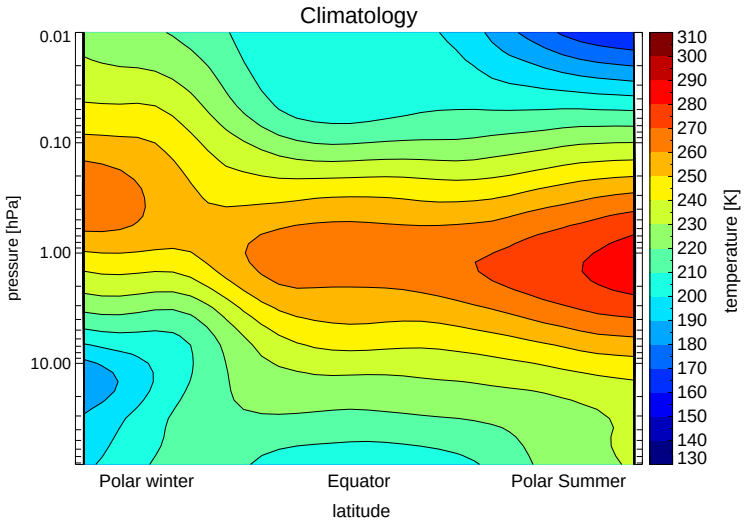

Figure 1.2: Schematic of zonal mean temperatures for June. The climatology used was CIRA [1988].

Murgatroyd and Singleton [1961] derived the mean meridional circulation required to explain such a temperature deviation so far from its radiative equilibrium. This circulation requires air ascent over the summer pole and air descent over the winter pole. These rising and descending motions lead to adiabatic cooling and heating respectively. Hence, the temperatures observed are a balance between the dynamical heating and the radiation among the atmospheric layers.

1.2 Mesospheric cooling

In addition to dynamical heating / cooling, an important source of heat in the mesosphere is the energy released when solar UV radiation breaks the chemical bonds of O_2 and O_3 while it is lost mainly by radiative cooling. Radiative cooling in the mesosphere is primarily driven by CO_2 emissions to space, followed by O_3 and H_2O [López-Puertas and Taylor, 2001]. Hence, an increase in greenhouse gases in the atmosphere should lead to a mesospheric cooling in addition to the tropospheric warming.

Roble and Dickinson [1989] predicted that doubling the CO_2 and CH_4 concentrations should cool the mesosphere up to 10 K due to the enhanced longwave radiation. Confirmation of this cooling effect was found by Aikin et al. [1991] by analyzing ten years of LiDAR data. Note that this is presumably the largest component of climate change. Furthermore, Roble and Dickinson [1989] also predicted a significant alteration of the compositional distributions of major and minor species. In particular, H_2O will increase with increasing CH_4, and CO will increase with increasing CO_2 concentrations.

1.3 Polar mesospheric clouds

Polar Mesospehric Clouds (PMCs) are the highest clouds on Earth located around 82 km [Jesse, 1887]. These clouds are composed of water ice particles [Hervig et al., 2001]. Hence, their existence is due to the polar summer mesospheric low temperatures that enables water ice saturation despite the low H_2O concentrations of the mesosphere. Thomas et al. [1989] suggested that, since PMCs can only form under special conditions, changes in their brightness and geographycal extension may be used as an indicator of climate change.

1.4 Mesospheric O_3

Ozone in the atmosphere acts as a shield by absorbing most of the biologically harmful ultraviolet sunlight. Its distribution in the middle atmosphere in general shows two distinct maxima, one located in the stratosphere (the so called ozone layer) and other located in the vicinity of the mesopause. Both maxima occur despite the continuing destruction of O_3 due to chemical reactions involving hydrogen. The stratospheric maximum occurs as the result of the large amounts of atomic oxygen being produced in this region due to photolysis of O_2 by solar radiation in the range 185 nm to 242 nm while the maximum in the mesopause region is due to atomic oxygen being produced by solar radiation in the 137 to 200 nm range.

In these regions, O_3 is produced faster by the 3-body reaction given by

$$\mathrm{O_2} + h\nu \rightarrow \mathrm{O} + \mathrm{O}$$

$$\mathrm{O} + \mathrm{O_2} + \mathrm{M} \rightarrow \mathrm{O_3} + \mathrm{M} \tag{1.1}$$

where M is a third body (i.e. molecular nitrogen); than it is destroyed. Bates and Nicolet [1950] proved that the depth of the minimum between these peaks depends on the amount of hydrogen radicals available.

In addition to this secondary maximum, Marsh et al. [2001] using satellite measurements showed the existence of a localized ozone maximum around 72 km restricted to high latitudes in the polar winter region. They showed that this local maximum is due to low concentrations of hydrogen radicals in this region. These hydrogen low concentrations are the consequence of low water vapour photolysis due to large optical depths.

1.5 Dynamical features

In section 1.1 it was said that the mesosphere requires a mean meridional circulation in order to deviate the temperature distribution from its radiative equilibrium. Nowadays, it is generally believed that the mechanism that provides most of the forcing required to drive this circulation is the 'breaking' of gravity waves [Andrews et al., 1987][2].

In simple terms, gravity waves are atmospheric waves where the restoring force is buoyancy. Most of these waves are generated in the lower atmosphere by topography or by convection but propagate upwards into the mesosphere where the density decreases and their amplitude rises. However, this growth eventually reaches a point where it becomes convectively unstable and the wave 'breaks' depositing momentum and producing turbulent mixing of chemical species.

In a addition to gravity waves 'breaking', other dynamic features that influence the winds, temperature and density in the mesosphere are planetary waves and atmospheric tides. Planetary waves are large scale oscillations under the influence of the Coriolis effect while atmospheric tides are global scale daily oscillations mainly forced by variations of solar absorption by ozone and water vapour (such as the well known equatorial tide).

1.6 Thesis outline

For the convenience of the reader, this section outlines the content of the following chapters:

- Chapter 2 provides a brief summary of the theoretical background needed (radiative transfer theory and retrieval theory).
- Chapter 3 describes the MIPAS and HIRDLS instruments as well as other satellite mesospheric instruments currently in operation.
- Chapter 4 describes work performed in order to evaluate the accuracy of the mesospheric MIPAS and HIRDLS measurements.
- Chapter 5 shows the feasibility of observing PMCs in the MIPAS spectra.
- Chapter 6 presents the validation of the MIPAS middle atmosphere geophysical products as retrieved by MORSE.

[2] As for the rest of this section

- Chapter 7 details a new linear scheme developed for middle atmosphere retrievals from MIPAS spectra.
- Chapter 8 covers an evaluation of the nonLTE vibrational temperatures used currently in the MIPAS retrieval scheme previously discussed.
- Chapter 9 summarizes the work presented in this thesis and outlines possible future work.

CHAPTER 2

Remote Sensing

Two years after the launch of the Sputnik, Kaplan [1959] suggested that the measurement of thermal infrared radiation reaching an earth-orbiting satellite could be used to deduce the temperature, pressure and moisture in the atmosphere. The viability of this technique rests on the fact that the infrared spectral radiation is determined by the vibration of individual atoms with respect to the others and also by the rotation of the molecule along any axis. The importance of these interactions is that they differ from molecule to molecule according to the geometrical alignment and the masses of their atoms which determine a set of discrete energy levels at which those interactions can occur.

The transition from one energy level to another implies the absorption or emission of a photon with energy equal to the difference of the energy levels given, ΔE, by:

$$\Delta E = hc\nu \tag{2.1}$$

where h is the Planck constant and ν is the wavenumber of the photon, and therefore a detector measuring such radiation will detect a decrease or an enhancement of the intensity at that particular wavenumber.

Furthermore, the combinations of the valid set of energy levels allow the molecule to emit or absorb photons usually in a clustered group of frequencies, forming, when dealing with in the infrared region of the spectra, a vibrational band; allowing the discrimination of radiation from different molecules by measuring different regions of the spectrum.

Once the observations are made in appropriate regions of the spectrum, the retrieval of atmospheric parameters requires the fitting of a theoretical model. The purpose of this model is to simulate the radiance received by the satellite instrument assuming a known atmospheric state along the

path. Such model is usually referred as the 'forward model' as opposed to the fitting process which is known as the 'inverse model'.

2.1 The Forward Model

Assuming a stratified atmosphere, the infrared atmospheric radiance leaving the atmosphere will be given by the absorption of the radiation from a given source plus the emission (and absorption by the following layers) of photons according to the characteristic temperature, pressure and composition of each layer. Assuming the geometry of Figure 2.1, at a particular wavenumber ν, the numerical integration of such radiative transfer equation can be formulated as,

$$L = L_0\tau_0 + \sum_i J_i \left[\tau_{i-1} - \tau_i\right] \tag{2.2}$$

where L_0 is the term associated to the cold space background at the end of the path, negligible for infrared wavelengths; τ_i corresponds to the transmittance from the satellite up to the stratified level i and J is the source function corresponding to each layer.

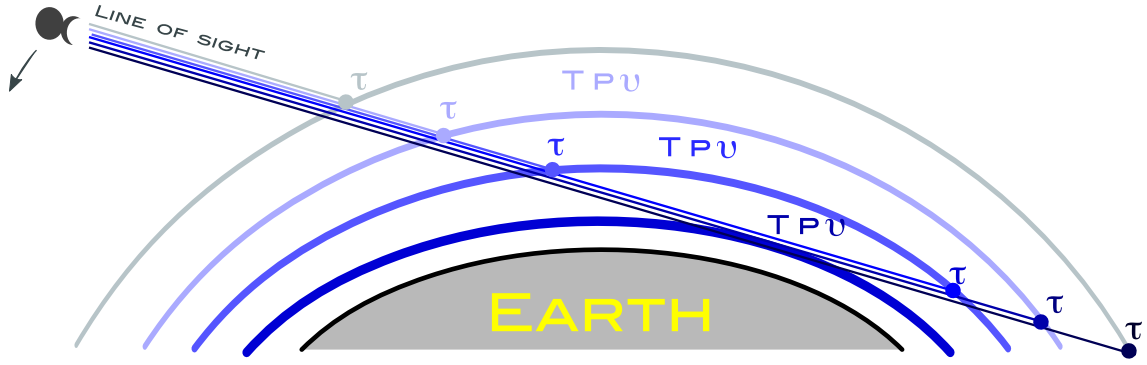

Figure 2.1: Schematic showing the type of geometry assumed in the forward model.

The source function specifies the number of photons that are emitted and absorbed in a light beam by certain material as the light passes through. Milne [1930] derived a general source function as,

$$J = \frac{2hc^2\nu^3}{(n_l g_u / n_u g_l) - 1} \tag{2.3}$$

where c is the speed of light, n is the population of molecules in the upper u and lower l energy levels with their corresponding degeneracies g. The significance of this equation is that the source function is different for each transition of each molecule varying accordingly to the population of the internal energies. Such populations are determined by a balance of excitation and deexcitation processes,

including emission and absorption of radiation, photochemical reactions and collision mechanisms [Wintersteiner et al., 1992]. Under local thermodynamic equilibrium (LTE), when these populations are coupled to local kinetic temperature of the surrounding gas, or more specifically, when the upper and lower levels in question are determined by the Boltzmann distribution given by,

$$\frac{n_u}{n_l} = \frac{g_u}{g_l} \exp\left(\frac{-hc\nu}{kT}\right) \tag{2.4}$$

where k and T are the Boltzmann constant and the kinetic temperature, respectively; the general source function reduces to the Planck function

$$B = \frac{2hc^2\nu^3}{\exp(hc\nu/kT) - 1} \tag{2.5}$$

which implies that it is merely a function of the wavenumber and the kinetic temperature of the gas, i.e. $B \equiv B(\nu, T)$

The transmittance, τ, is a complicated function which varies according to the wavenumber, the absorber volume mixing ratios v, the absorption coefficient σ and the air density ρ of the layer, and can be expressed as,

$$\tau_i = \exp\left(-\sum_{k=1}^{i} \chi_k\right) \tag{2.6}$$

$$\chi_k = \rho_k l_k \sum_j v_{kj}\sigma_{kj} \tag{2.7}$$

where χ_k is the optical thickness of the stratified atmosphere layer k , the suffix j represents different absorbers and l_k is the length along the path in layer k which varies depending on the instrument viewing geometry.

The absorption coefficient, σ, corresponds to those discrete sets of wavenumbers at which each molecule can absorb or emit radiation, known as absorption lines. In order to accurately retrieve concentrations, pressure and temperature from the observed spectra, their line position, line strength and line width must be properly modeled.

In simple terms, their line position corresponds to the discrete energy levels determined by the atomic structure of the molecule. The line strength S is given by,

$$S = \int_0^\infty \sigma d\nu \tag{2.8}$$

which is mainly determined by the population of the lower state of the correspondent transition.

In practice, the line width depends on two mechanisms: collisions between molecules or atoms (pressure broadening) which limits the lifetime of an excited state or Doppler shifts of the photon frequency (Doppler broadening) due to the movement of the molecules relative to the observer. As can be inferred, pressure broadening is the main broadening mechanism at low altitudes while Doppler broadening dominates at high altitudes where collisions are less frequent.

Although the modelling of the absorption coefficient is a fundamental part of the radiative transfer equation, a full discussion is beyond the scope of this thesis. A detailed discussion about line shapes can be found in Goody [1964].

Once the radiance leaving the atmosphere is known, the forward model needs to modify such radiances to simulate the effects of the instrument optics, in particular, the instrument line shape[1], ILS, and the instrument field of view, FOV. The simulated measurements S_m are then computed by the convolution of the modeled atmospheric radiance L with both of them:

$$S_{\mathrm{m}} = \int \int L * ILS d\nu FOV dz \tag{2.9}$$

As it may be inferred, the forward model is the more time consuming due to the numerous computer operations involved in solving equation 2.2 and equation 2.9.

In this thesis the model used is the Reference Forward Model (RFM) developed at Oxford University to provide, originally, MIPAS[2] spectral calculations but which has evolved into a general radiative transfer model [Dudhia, 2002*c*].

2.2 Inverse model

The inverse problem or the retrieval problem is the second step to infer atmospheric parameters from infrared radiation and it is the problem in science of fitting a mathematical model to a given set of observations.

Following Rodgers [2000], a common solution is to minimise the sum of the squares of the differences which is called the 'least squares fit'. Assuming a linear system:

$$\mathbf{y} = \mathbf{Kx} + \mathbf{e} \tag{2.10}$$

where **y** and **x** represent a given set of *m* measurements and a set of *n* adjustable model parameters

[1] The response of the instrument to a monochromatic radiance
[2] described in Chapter 3

(the state vector) respectively and where **K** is the Jacobian matrix ranked *m* $\times$ *n* (where m greater than n) with values $K_{ij} = \partial y_i / \partial x_j$. In addition, **e** represents a given set of *m* measurement errors.

It can be shown that the solution may be found by minimizing the cost function:

$$\chi^2 = (\mathbf{y} - \mathbf{K}\mathbf{x})^T \mathbf{S}_e^{-1} (\mathbf{y} - \mathbf{K}\mathbf{x}) \tag{2.11}$$

where $\mathbf{S}_e$ is the error covariance matrix, ranked *m* $\times$ *m*. The diagonal elements of this matrix are the measurement error variance while the off diagonal elements are the correlations (strictly, the covariances) between the different error elements. The error covariance matrix values are given by $S_{e_{ij}} = E(e_i e_j)$ where E is the expected value operator and e_i and e_j are the i^{th} and j^{th} elements of the measurements error.

The solution for the state vector, **x**, that minimises this cost function (equation 2.11) is given by

$$\mathbf{x} = \left(\mathbf{K}^T \mathbf{S}_e^{-1} \mathbf{K}\right)^{-1} \mathbf{K}^T \mathbf{S}_e^{-1} \mathbf{y} \tag{2.12}$$

with errors associated of

$$\mathbf{S}_x = \left(\mathbf{K}^T \mathbf{S}_e^{-1} \mathbf{K}\right)^{-1} \tag{2.13}$$

When the theoretical model is a highly non-linear system like the forward model explained in section 2.1, the fitting process needs to be solved iteratively. At each iteration the model is linearised around a certain set of conditions and therefore, even though the problem is not linear, the main calculations are similar. A linearization of the forward model, $\mathbf{F}(\mathbf{x}_0)$, around a given set of initial model parameters $\mathbf{x}_0$ can be written as,

$$\mathbf{y} - \mathbf{F}(\mathbf{x}_0) = \mathbf{K}_0(\mathbf{x} - \mathbf{x}_0) + \mathbf{e} \tag{2.14}$$

where $\mathbf{F}(\mathbf{x}_0)$ are the simulated measurements as a result of running the forward model with an initial state vector, $\mathbf{x}_0$. The solution for this problem can be found by rewriting the previous equation as $\Delta\mathbf{y} = \mathbf{K}_0 \Delta\mathbf{x} + \mathbf{e}$ and noticing that this resembles the linear system (equation 2.10) which solution, as explained before, will be given by,

$$\Delta\mathbf{x} = \left(\mathbf{K}_0^T \mathbf{S}_e^{-1} \mathbf{K}_0\right)^{-1} \mathbf{K}_0^T \mathbf{S}_e^{-1} \Delta\mathbf{y} \tag{2.15}$$

which can be rewritten as,

$$\mathbf{x} = \mathbf{x}_0 + \left(\mathbf{K}_0^T \mathbf{S}_e^{-1} \mathbf{K}_0\right)^{-1} \mathbf{K}_0^T \mathbf{S}_e^{-1} \left(\mathbf{y} - \mathbf{F}(\mathbf{x}_0)\right) \tag{2.16}$$

and which has an associated error given by equation 2.13

The state vector computed is not the final solution but rather just a better estimate of the initial guess, $\mathbf{x}_0$, and the process needs to be iterated with the state vector just computed as the new linearization point and equation 2.16 becomes,

$$\mathbf{x}_{i+1} = \mathbf{x}_i + \left(\mathbf{K}_i^T \mathbf{S}_e^{-1} \mathbf{K}_i\right)^{-1} \mathbf{K}_i^T \mathbf{S}_e^{-1} \left(\mathbf{y} - \mathbf{F}(\mathbf{x}_i)\right) \tag{2.17}$$

which implies that at each iteration the forward model needs to produce a new set of simulated measurements as well as new Jacobian values. Under this scenario, a convergence criterion needs to be defined for stopping the iteration process.

Although this method might reach convergence for cases when the non-linearities are weak, in general at any iteration it can estimate an state vector that increases the value of the cost function leading to divergence. A standard technique to cope with this problem is the Levenberg–Marquardt method [Press et al., 1986] which introduces the the Levenberg–Marquardt parameter λ into equation 2.17 that becomes,

$$\mathbf{x}_{i+1} = \mathbf{x}_i + \left(\mathbf{K}_i^T \mathbf{S}_e^{-1} \mathbf{K}_i + \lambda \mathbf{I}\right)^{-1} \mathbf{K}_i^T \mathbf{S}_e^{-1} \left(\mathbf{y} - \mathbf{F}(\mathbf{x}_i)\right) \tag{2.18}$$

where $\mathbf{I}$ is the identity matrix and where λ is increased or decreased during each iteration depending on the cost function changes. By doing this, each iteration is forced to get closer to the solution or discarded. It is important to note that the Levenberg–Marquardt method reaches the same solution[3] as the one found when using equation 2.17 because both are minimising the same cost function [Ridolfi et al., 2000].

So far, it has been assumed that the problem is well conditioned. Unfortunately, in general, inferring temperature, pressure and composition from infrared measurements is an ill-conditioned problem and in order to find a meaningful solution constraints need to be added to the retrieval problem. There are two main forms of constraining the retrieval: adding *a priori* information to the retrieval or incorporating a smoothing constraint.

[3] Assuming that at the last iteration λ was set to zero

When adding a *a priori* data, the additional information can come from a variety of sources such as other experiments, from previous retrievals of the same instruments or from climatological data sets such as the COSPAR International Reference Atmosphere (CIRA) [CIRA, 1988]. By doing this, the *a priori* atmospheric profile acts as an extra set of measurements and the cost function becomes

$$\chi^2 = (\mathbf{y} - \mathbf{K}\mathbf{x})^T \mathbf{S}_e^{-1} (\mathbf{y} - \mathbf{K}\mathbf{x}) + (\mathbf{x} - \mathbf{x}_a)^T \mathbf{S}_a^{-1} (\mathbf{x} - \mathbf{x}_a) \tag{2.19}$$

which linear solution and associated errors, following Rodgers [2000], will be given by,

$$\mathbf{x} = \mathbf{x}_a + \left(\mathbf{K}_a^T \mathbf{S}_e^{-1} \mathbf{K}_a + \mathbf{S}_a^{-1}\right)^{-1} \mathbf{K}_a^T \mathbf{S}_e^{-1} (\mathbf{y} - \mathbf{F}(\mathbf{x}_a)) \tag{2.20}$$

$$\mathbf{S}_x = \left(\mathbf{K}_a^T \mathbf{S}_e^{-1} \mathbf{K}_a + \mathbf{S}_a^{-1}\right)^{-1} \tag{2.21}$$

where $\mathbf{S}_a$ is the covariance matrix of the *a priori* information, $\mathbf{x}_a$. Providing that $\mathbf{S}_a$ is invertible, which is usually the case, the solution $\mathbf{x}$ can be found no matter how singular the matrix $\mathbf{K}_a^T \mathbf{S}_e^{-1} \mathbf{K}_a$ is. This regularisation method is known as Optimal Estimation and the solution can be thought as a compromise between the information from the measurements and the information of the *a priori* data[4]

The other type of constraint is the Twomey–Tikhonov regularisation that can be interpreted as a smoothing filter at the expense of vertical resolution. This regularisation can be obtained by minimising the cost function

$$\chi^2 = (\mathbf{y} - \mathbf{K}\mathbf{x})^T \mathbf{S}_e^{-1} (\mathbf{y} - \mathbf{K}\mathbf{x}) + \gamma (\mathbf{x} - \mathbf{x}_0)^T \mathbf{R} (\mathbf{x} - \mathbf{x}_o) \tag{2.22}$$

where γ is a factor that determines the strength of the regularisation and where $\mathbf{R}$ is a regularisation matrix which can be chosen to constrain the magnitude of a given order derivative of the retrieved profile $\mathbf{x}$.

The Twomey–Tikhonov regularised linear solution [Rodgers, 2000] is given by

$$\mathbf{x} = \mathbf{x}_0 + \left(\mathbf{K}_0^T \mathbf{S}_e^{-1} \mathbf{K}_0 + \gamma^{-1} \mathbf{R}\right)^{-1} \mathbf{K}_0^T \mathbf{S}_e^{-1} (\mathbf{y} - \mathbf{F}(\mathbf{x}_0)) \tag{2.23}$$

$$\mathbf{S}_x = \left(\mathbf{K}_0^T \mathbf{S}_e^{-1} \mathbf{K}_0 + \gamma^{-1} \mathbf{R}\right)^{-1} \tag{2.24}$$

[4] An alternative form of this approach is named sequential estimation. This form updates the state vector sequentially assuming uncorrelated measurements, thus minimizing the size of the matrices involved. Mathematically these two methods (optimal estimation and sequential estimation) should be equivalent.

The inverse theory explained so far is not an exhaustive summary of the possible approaches that can be used, it mainly explains the retrieval types that are going to be used in this thesis. A more detailed treatment of the inverse problem can be found in Rodgers [2000].

CHAPTER 3

Instruments

3.1 MIPAS

The Michelson Interferometer for Passive Atmospheric Sounding (MIPAS) is a Fourier Transform Spectrometer on board the ENVISAT satellite launched in March 2002 [Endemann, 1999; Fischer et al., 2000]. MIPAS observes the thermal radiation leaving the atmosphere in the limb sounding geometry, illustrated in Figure 3.1, with an instantaneous FOV of approximately 3 km in the vertical direction to achieve a good vertical resolution and 30 km in the horizontal direction to collect enough radiance [Endemann, 1999]. In this viewing geometry, MIPAS (actually any limb-sounding instrument) receives the radiation emitted by the atmosphere along a line of sight that is normally identified by the height closest to the surface, known as tangent height. Assuming a stratified atmosphere, it is easily visualized that most of the received radiation comes from the atmospheric layer related to the tangent height since it contains the longest horizontal segment of the path and the highest pressure (more molecules). This long ray path maximizes the amount of signal measured so that temperature and minor species can be detected even at high altitudes aided by the cold space as background.

.

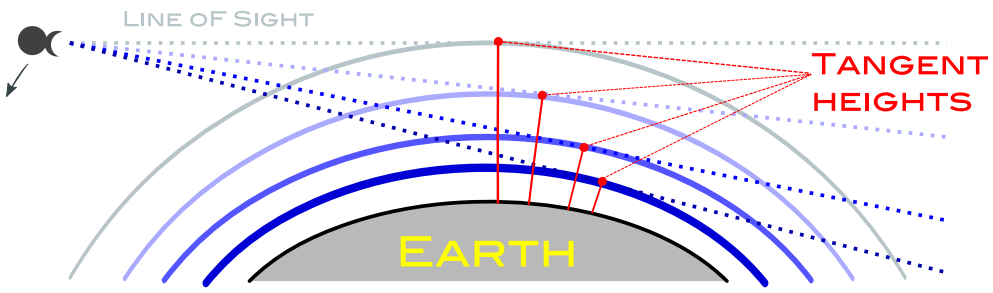

Figure 3.1: Schematic showing the limb viewing geometry.

MIPAS collects the atmospheric radiation by the input optics and directs it on to a two beam interferometer (a modified version of the Michelson Interferometer, Figure 3.2). Inside the interferometer,

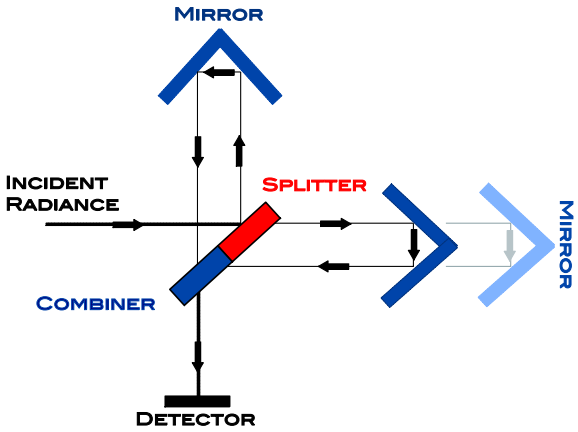

Figure 3.2: Michelson Interferometer basic optical configuration.

the radiance is focused on a beam splitter. The two beams (ideally of equal intensity) are reflected by moveable cube corners[1] into a beam combiner where the beams interfere. Constructive or destructive interference appears as function of the optical path difference, creating an interferogram.

The interferogram, $I(x)$, of a given spectrum, $L(\nu)$, measured by an ideal interferometer can be written as[2],

$$I(x) = \int_{-\infty}^{+\infty} L(\nu) \cos(2\pi\nu x)\, d\nu \tag{3.1}$$

where x is the optical path difference (cm). So by noting that the resulting interferogram is the Fourier transform of the incoming radiation, the original spectrum can be recovered using an inverse cosine Fourier transform,

$$L(\nu) = \int_{-\infty}^{+\infty} I(x) \cos(2\pi\nu x)\, dx \tag{3.2}$$

However, in practice the cube corners (or mirrors) of the interferometer can only travel a finite optical path difference (FOPD). In that case equation 3.2 becomes

$$L(\nu) = \int_{-L}^{+L} I(x) \cos(2\pi\nu x)\, dx \tag{3.3}$$

where L is the maximum FOPD. Figure 3.3 shows an example of the convolution of the original spectrum due to the FOPD of the interferometer. As can be noticed each emission line presents sidelobes which extend out to both sides. This can be understood by noting that the effect of the

[1]Unlike figure 3.2, MIPAS is configured in a slightly more complex optical layout where the two cube corners are moved, this leads to the advantage that two detectors can be installed to collect all the available photons [Beer, 1992] and it provides redundancy [Fischer et al., 2000]

[2]considering only the alternating component of the interferogram

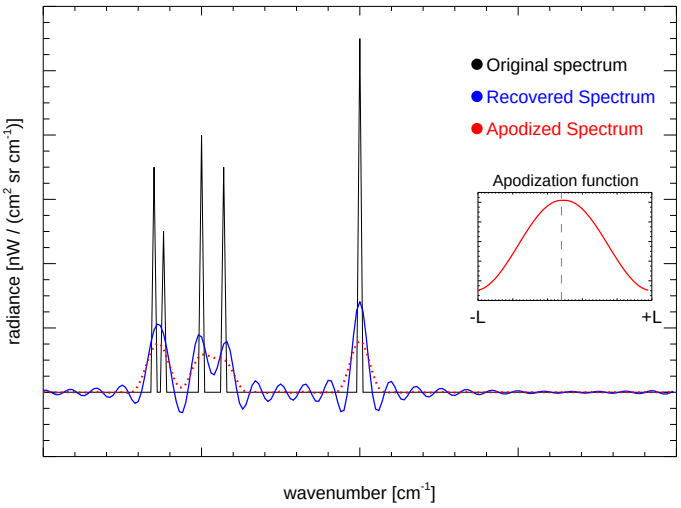

Figure 3.3: Convolution of an hypothetical spectrum due to the finite optical path difference (FOPD) of the interferometer before and after the apodization. The apodization function used is shown in the subplot.

FOPD is equivalent to multiplying the theoretical (infinite) interferogram (equation 3.2) by a boxcar function, that is to say, to convolve the original spectrum with a sinc function (the Fourier transform of the boxcar function). This sinc function determines the instrument line shape and the spectral resolution of the instrument (proportional to the FOPD).

In order to reduce these sidelobes in the spectrum, the measured interferogram can be multiplied by an apodizing function. As shown in Figure 3.3, the apodization of the spectra yields to reduced oscillations at the cost of spectral resolution. A commonly apodization used in the MIPAS algorithms is the Norton Beer strong apodization [Norton and Beer, 1976].

Between July 2002 and March 2004 MIPAS operated using a maximum optical path difference of 20 cm which corresponds to a spectral sampling every 0.025 cm^{-1}. These data are referred to as 'full resolution' data. Unfortunately, the instrument developed problems with the cube corner slide mechanism and the instrument was switched off in March 2004. In January 2005 operations were resumed restricting the mirror movement to 40% of is original maximum displacement corresponding to a reduced spectral sampling (referred to as 'reduced resolution' or sometimes 'optimised resolution' data) of 0.0625 cm^{-1}.

The wide spectral coverage of MIPAS (between 685 cm^{-1} and 2410 cm^{-1}) is divided into five bands listed in table 3.1. Its high spectral resolution, for the full or reduced resolution data, enables the discrimination of emissions from different species as well as from different isotopes and vibrational bands of the same species. Figure 3.4 shows the simulated radiance contributions at a 24 km tangent height for principal atmospheric emitters in the MIPAS spectral bands.

Table 3.1: MIPAS spectral bands

MIPAS band	Wavenumber range [cm^{-1}]	Wavelength [μm]	Principal atmospheric emitting species
A	685 – 970	10.30 – 14.59	CO_2, O_3, H_2O, HNO_3
AB	1020 – 1170	8.54 – 9.80	CO_2, O_3, H_2O, N_2O
B	1215 – 1500	6.67 – 8.23	H_2O, CH_4, N_2O
C	1570 – 1750	5.71 – 6.36	NO_2, H_2O
D	1820 – 2410	4.14 – 5.49	CO_2, O_3, H_2O, N_2O, NO, CO

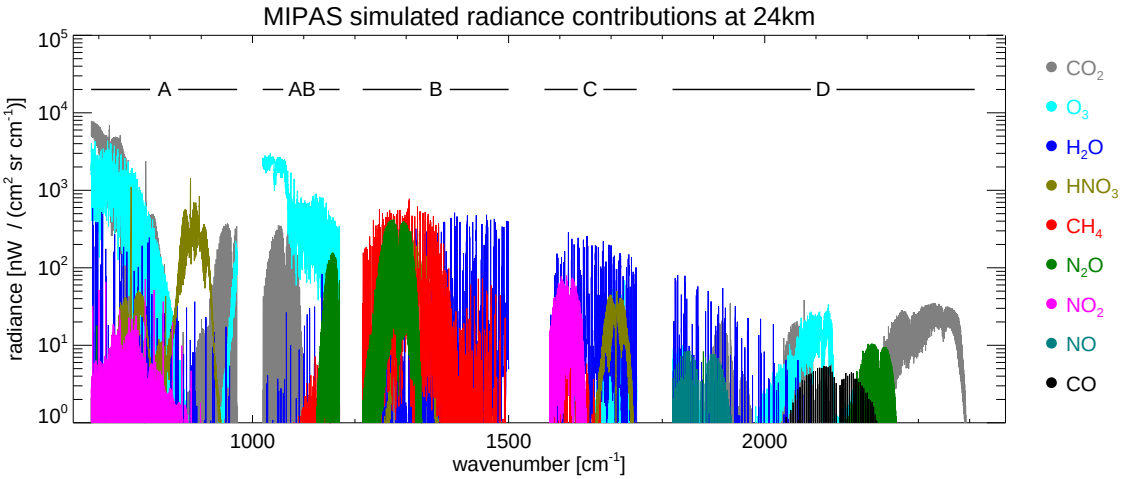

Figure 3.4: MIPAS radiance contributions at 24 km for major emitting species.

In the reduced resolution operation, the MIPAS nominal (NOM) measurement mode consists in measuring 27 tangent heights starting at 70 km and descending to 6 km (with overlapping of the FOV at some altitudes) but MIPAS altitude coverage can be extended well into the thermosphere using special measurements modes (Figure 3.5) such as the Middle Atmosphere (MA) mode with 29 tangent heights measuring from 102 km to 18 km and the Upper Atmosphere (UA) mode with 35 tangent heights between 172 km and 42 km. Since April 2007, one day in ten observations are made using the MA mode and another using the UA.

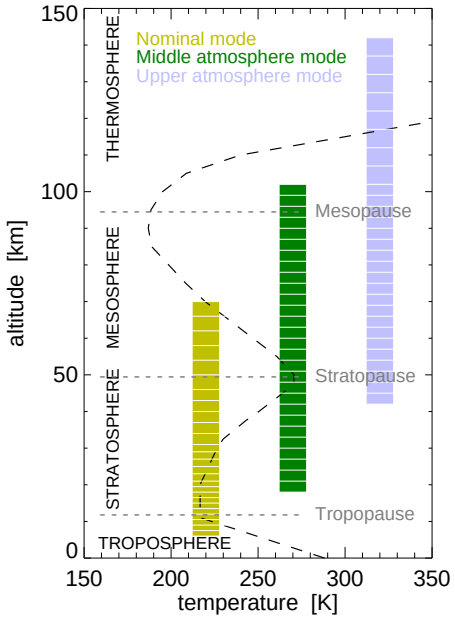

Figure 3.5: MIPAS reduced resolution operation measurement modes.

In addition, the ENVISAT sun-synchronous polar orbit (altitude 790 km, inclination 98°) allows

MIPAS to have a pole to pole coverage on each orbit and to measure both the day and night hemispheres. In general, MIPAS measures in the 'anti-flight' direction (rearwards) although it can also measure in the anti-sun direction (sideways)[3]. When looking in the rearward direction most measurements are made approximately around 10:00 or 22:00 local solar time (LST) which allows MIPAS to study the diurnal cycles of the molecules observed. The exceptions are the measurements near the poles where the satellite changes between the day time to night time conditions or vice versa. ENVISAT completes a single orbit in 100 minutes producing around 14 orbits per day giving MIPAS global coverage every 24 hours. Figure 3.6 displays the latitudinal - longitudinal coverage for MIPAS for a MA mode day. It also shows the good coverage around the polar regions given by the rearward direction.

3.1.1 MIPAS retrieval algorithms

Several algorithms have been developed to retrieve altitude profiles of temperature, pressure and composition from the MIPAS spectra [Ridolfi et al., 2000; von Clarmann et al., 2003; Hoffmann et al., 2005; Carlotti et al., 2006; Dudhia, 2002*a*]. All retrievals are based on techniques such as the ones described in section 2.2. These retrievals exploit the redundancy in MIPAS measurements which allows the selection of subsets of the spectra, known as microwindows. These microwindows maximize the information content as well as minimize the contribution of other parameters that influence the spectral lines selected, such as spectrally overlapping species, nonLTE emissions, etc.

The use of microwindows instead of broader spectral intervals helps to reduce the size of the matrices involved in the inverse problem as well as the computing cost of the forward model. These microwindows are usually less than $3\,\mathrm{cm}^{-1}$ wide and are preferred instead of using single spectral points because the atmospheric continuum can be also fitted reducing the effects of broadband features such as aerosols and thin clouds. The microwindow selection commonly used is described in detail in Dudhia et al. [2002]. This approach simulates a full retrieval profile modeling the propagation of the instrument errors as well as the errors associated with other unretrieved parameters such as the difference between the actual atmospheric concentration of molecules whose spectral signature overlap the spectral region of interest and the concentrations used in the forward model. Therefore, the microwindows selected with this method correspond to the best possible set of spectral regions for a single atmospheric profile. In order to have a set of microwindows that can be used at all latitudes and seasons the microwindows need to be chosen considering several atmospheric profiles which

[3]The sideways direction is only used for spectral campaigns such as detecting aircraft signatures in the MIPAS spectra and is not used in this thesis.

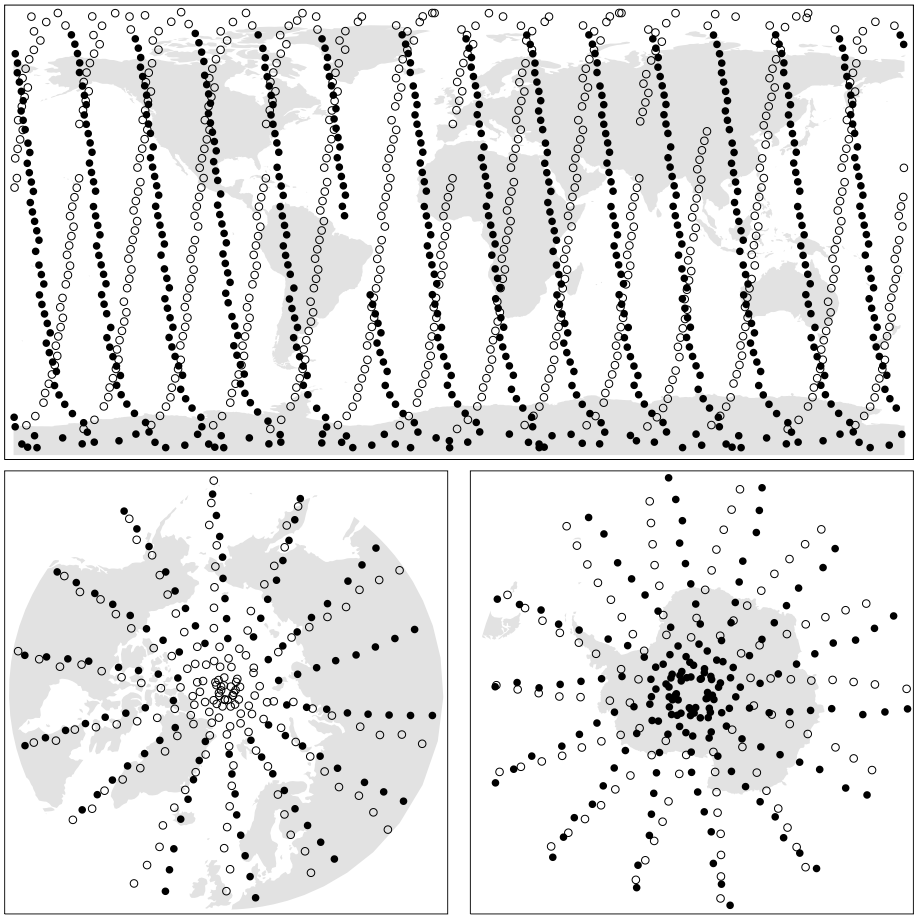

Figure 3.6: MIPAS coverage for the 3rd September 2007. The open and filled circles represent day and night measurements respectively. Note that every few profiles there are slight deviations along the orbit tracks. These deviations are due to some azimuth scanning as part of the rearward direction which allows the observations to be extended into the poles.

cover the atmospheric latitudinal variability.

In this thesis, the results of the MIPAS Orbital Retrieval using Sequential Estimation (MORSE) algorithm will be evaluated (Chapter 6) and a new linear retrieval will be discussed (Chapter 7).

MORSE

The MORSE inversion strategy is based in a optimal estimation technique. It was developed at Oxford University to replicate and if possible improve the results of the standard ESA processor but it has been upgraded to retrieve more constituents as well as to retrieve MIPAS data acquired using different viewing modes (MA mode and UA mode) [Dudhia, 2002*a*]. It uses the RFM as its forward

model and it retrieves sequentially (each microwindow from top to bottom) assuming that the noise errors are only correlated within each microwindow (due to the apodization) but not in altitude or across different microwindows. This is the same assumption used in the 'global fit' approach adopted by ESA, where all the measurements are incorporated simultaneously. Mathematically these two methods should be equivalent.

3.2 HIRDLS

HIgh Resolution Dynamics Limb Sounder (HIRDLS) [Dials et al., 1998] is a 21 channel infrared radiometer on board the EOS Aura satellite (altitude 705 km, inclination 98°), which was launched into a polar sun-synchronous orbit on July 2004. The instrument measures the limb atmospheric radiance with a FOV of 1 km in the vertical and 10 km in the horizontal scanning the atmosphere between 8 and 120 km. Its 1 km vertical resolution is the highest resolution achieved by an infrared limb satellite instrument.

The incoming radiance at the HIRDLS aperture is chopped against a space view, which provides a cold reference, and is directed through two sets of spectral filters[4]. The first set is used to define the spectral range of each channel (bandpass filters) and the second to suppress stray light going to the cooled detectors. The spectral bandpass filters (or channels) were selected to maximize the target molecule signal choosing carefully the spectral range to minimize the contribution from other gases and, furthermore, to quantify such contamination measuring the other gases in other channels. The detected radiance, R_{CH}, at each channel is given by,

$$R_{\mathrm{CH}} = \int_{\Delta\nu} L(\nu) f_{\mathrm{CH}} d\nu \tag{3.4}$$

where $L(\nu)$ is the radiance leaving the top of the atmosphere and f_{CH} is the filter response function over the spectral range $\Delta\nu$.

The channels and their spectral ranges are listed in Table 3.2 and illustrated in Figure 3.7. As can be seen, for important measurements such as temperature and O_3 several channels were designed to provide redundancy. Three channels were selected in spectral regions where there is a negligible radiance contribution from atmospheric gases to measure aerosol extinction. A detailed description of the selection of the HIRDLS channels can be found in Edwards et al. [1995].

[4]Spectral filters can be constructed by using the transmission and reflection properties of certain materials. A detailed description of the HIRDLS filters can be found in Hawkins et al. [1998].

Table 3.2: HIRDLS channel spectral ranges.

HIRDLS channel	Wavenumber [cm^{-1}]	Wavelength [μm]	Target species
1	563.06 – 587.89	17.00 – 17.76	N_2O
2	599.88 – 615.01	16.25 – 16.67	CO_2
3	610.13 – 639.80	15.63 – 16.39	CO_2
4	626.17 – 660.07	15.15 – 15.97	CO_2
5	654.88 – 679.81	14.71 – 15.26	CO_2
6	821.02 – 836.12	11.96 – 12.18	Aerosol
7	834.72 – 853.24	11.72 – 11.98	CFC_{11}
8	859.85 – 904.98	11.05 – 11.63	HNO_3
9	914.91 – 932.84	10.72 – 10.93	CFC_{12}
10	990.10 – 1010.1	9.99 – 10.10	O_3
11	1011.12 – 1048.22	9.54 – 9.89	O_3
12	1119.82 – 1140.25	8.77 – 8.93	O_3
13	1200.48 – 1219.51	8.20 – 8.33	Aerosol
14	1228.50 – 1259.45	7.94 – 8.14	N_2O_5
15	1256.28 – 1282.05	7.80 – 7.96	N_2O
16	1278.77 – 1298.70	7.70 – 7.82	$ClONO_2$
17	1324.50 – 1369.86	7.30 – 7.55	CH_4
18	1385.04 – 1434.72	6.97 – 7.22	H_2O
19	1402.52 – 1416.43	7.06 – 7.13	Aerosol
20	1422.48 – 1540.83	6.49 – 7.03	H_2O
21	1582.28 – 1633.99	6.12 – 6.32	NO_2

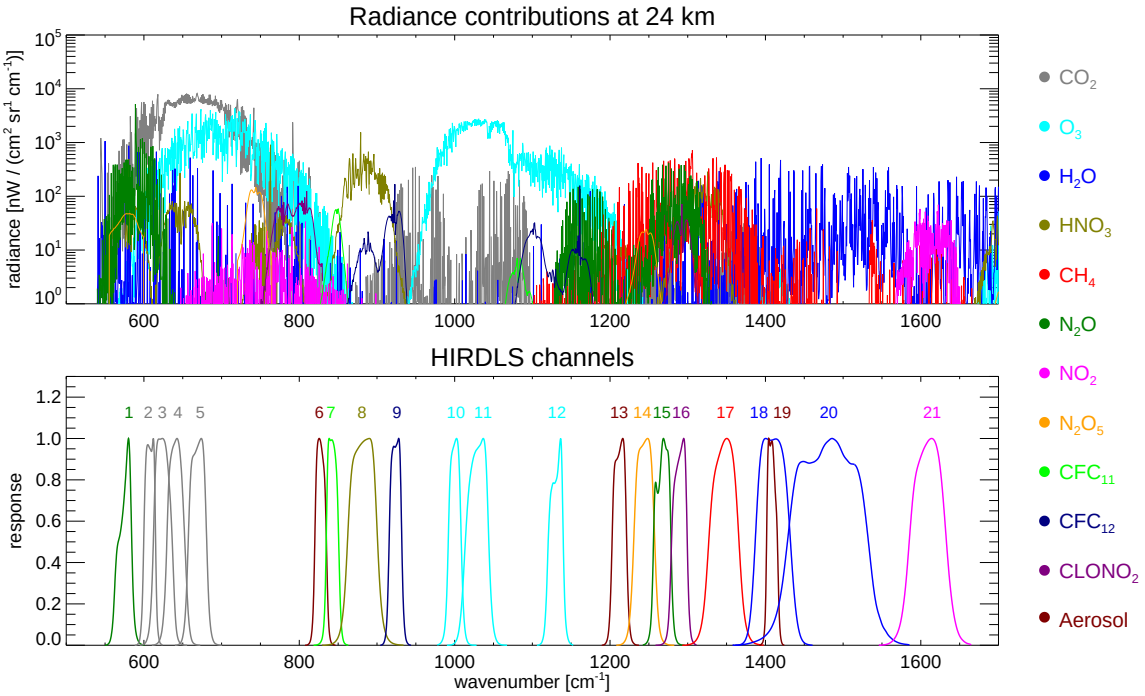

Figure 3.7: Radiance contributions at 24 km tangent height for HIRDLS target molecules and HIRDLS channel responses.

Soon after launch it was discovered that the measurements were not as expected. Several tests led to the conclusion that during launch, a plastic film (Kapton) used for insulation detached from one of the walls of the main aperture and it was blocking roughly 80% of the view [Barnett et al., 2005; Gille et al., 2008]. Figure 3.8 shows an schematic of the aperture blockage. As can be seen, most of HIRDLS horizontal coverage was lost, the only scans with external view being the ones made at the largest azimuthal angle away from the sun. Since the beam width is larger than the open width, the measurements at each detector are a combination of the infrared radiation of the blockage, the instrument radiation reflected by the blockage and the external (space or atmospheric) radiation. When scanning from top to bottom at this azimuthal angle, the measured signal increases because more blockage is seen and because the external radiation varies from cold space to a denser atmosphere. Unfortunately, the movement of the scanning mirror causes the plastic film to vibrate inducing oscillations in the measured signal.

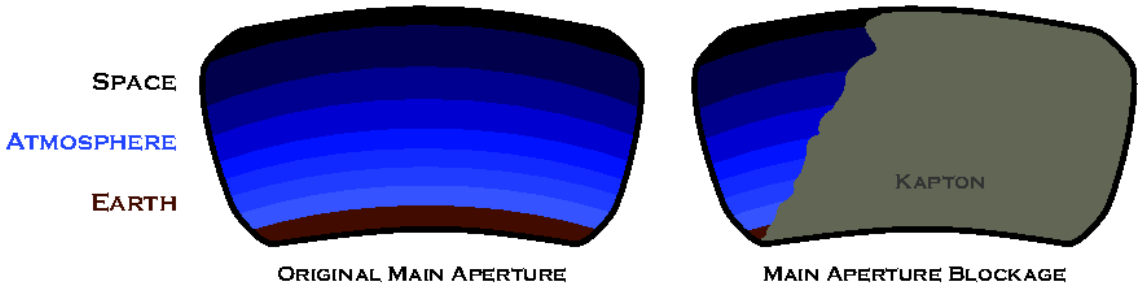

Figure 3.8: Schematic of the main aperture blockage.

A detailed description of the algorithms for the recovery of the data is given by Gille et al. [2008] and a summary follows here:

In order to extract the atmospheric signal from the composite signal data from a pitch up manoeuvre is used. In this orientation the external view is from space, so of zero radiance, and therefore the detectors only measure the signal from the blockage which is then analyzed using Singular Value Decomposition (SVD) at all elevation angles. The oscillations as well as the blockage emission are characterized using empirical orthogonal functions which then, assuming that the plastic film behaves similarly in the normal orientation, are used to remove the blockage signal. In the normal orientation, the measurements corresponding to elevation angles where only cold space and blockage are seen are used to infer the radiance blockage behaviour at elevation angles where the atmosphere is observed. Once the blockage signal is derived it can be subtracted from the composite signal leaving the atmospheric radiance reduced by a factor corresponding to the open area. So, to obtain the equivalent full beam radiance, the atmospheric radiance must be divided by the open area factor. These radiometric

corrections can be formulated as,

$$R_{\mathrm{FB}} = \frac{R_{\mathrm{M}} - R_{\mathrm{PF}}}{OAF} \tag{3.5}$$

where R_{FB}, R_{M} and R_{PF} correspond to the radiance of the full beam, the radiance measured and the radiance derived of the plastic film respectively, and where OAF is the open area fraction. The open area fraction is computed by modeling the blockage signal at an azimuthal angle viewing only the blockage, and at the angle with external view and subtracting them. Currently, uncertainties of +5 to -15% are estimated for this procedure.

Mostly due to these OAF uncertainties, these corrections are not completely accurate, nevertheless, a comparison between corrected and simulated radiances showed that the corrected radiances were in general too small but varied with height approximately as expected. A global average radiance adjustment factor was calculated using the Goddard Modeling and Assimilation Office (GMAO) Earth Observing System Version 5 (GEOS-5.01) meteorological analysis fields to correct for the OAF uncertainties. Ideally, as the blockage correction improves, this factor will tend to one. Currently it serves as a diagnostic of the correction algorithms. Work to refine the blockage emission subtraction continues.

Another consequence of the blockage is that HIRDLS coverage is restricted to between 65S and 82N as shown in Figure 3.9. Furthermore, since the measurements are taken viewing practically sideways, the local solar time between each geographical location varies.

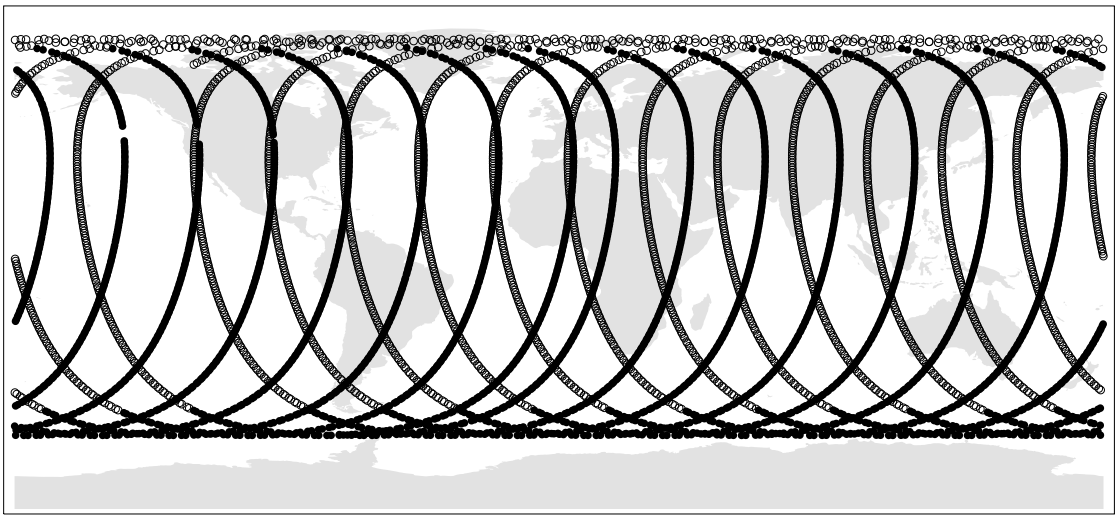

Figure 3.9: HIRDLS coverage for the 3rd of September 2007. The open and filled circles represent day and night measurements respectively.

Despite the unfortunate accident during the HIRDLS launch, the effectiveness of the blockage

removal algorithms and the quality of HIRDLS data has been demonstrated in validation papers for temperature, ozone, nitric acid, and aerosols [Gille et al., 2008; Kinnison et al., 2008; Massie et al., 2007; Nardi et al., 2008]. The HIRDLS retrieval algorithm is based in an optimal estimation technique and it is described by Lambert et al. [1999]. It uses a forward model developed exclusively for HIRDLS described by Francis et al. [2006].

3.3 Other mesospheric instruments

The purpose of this section is to give a brief description of the satellite instruments currently measuring the mesosphere. These can be divided into limb viewing and occultation viewing instruments.

3.3.1 Limb viewing instruments

MLS

The Microwave Limb Sounder (MLS) is an instrument that measures thermal microwave limb emission in five spectral regions from 115 GHz to 2.5 Thz. It was launched (as was HIRDLS) in July 2004 on board the Aura spacecraft. MLS scans the limb from the ground to about 95 km 3500 times per day. It covers between 82°S and 82°N providing near global coverage. The vertical resolution of this data is about 3 km [Waters et al., 1999, 2006]. In the current version (2.2) the following parameters are retrieved: temperature, BrO, CH_3CN, ClO, CO, geopotential height, H_2O, HCl, HCN, HNO_3, HO_2, HOCl, cloud ice water content, ice water path, N_2O, O_3, OH, relative humidity with respect to ice and SO_2. These data have been extensively validated [Santee et al., 2007; Pumphrey et al., 2007; Barnes et al., 2008; Froidevaux et al., 2008; Schwartz et al., 2008].

OSIRIS

The Optical Spectrograph and Infrared Imaging System (OSIRIS) measures spectra across the visible range from 274 nm to 810 nm every 0.3 nm using diffraction gratings. It is onboard the Odin satellite which is in a sun synchronous orbit (altitude 600 km, inclination 97°) with ascending and descending nodes near sunset and sunrise. Due to the nature of its measurements, this implies that OSIRIS can only scan the summer hemisphere. In addition, the Odin satellite is a multipurpose mission which alternates between astronomical and atmospheric measurements in one day bins [Llewellyn et al., 2004]. OSIRIS scans the atmosphere from around 7 to 65 or 90 km depending in the observing mode with an irregular vertical resolution. There are several inversion algorithms [Haley et al., 2003;

von Savigny et al., 2003; Kaiser et al., 2004] which retrieve the following parameters: O_3, NO_2, aerosols, BrO and OH. Note that since April 2007 Odin is a full-time atmospheric instrument since the astronomy mission was stopped [ONSALA-webpage, 2010].

SMR

The Sub-Millimetre Radiometer (SMR) measure in the frequencies 486.1–503.9 and 541.0–580.4 GHz with a variable spectral resolution from 150 kHz to 1 MHz [Frisk et al., 2003]. It is mounted (as OSIRIS) on the Odin satellite. It can measure O_3, ClO, N_2O, HNO_3, H_2O and CO between 7 to 110 km with a varying vertical resolution from 1.5 km in the stratosphere to 5 km in the mesosphere [Ricaud et al., 2007].

SABER

The Sounding of the Atmosphere using Broadband Emission Radiometry (SABER) is an infrared radiometer launched on the Thermosphere Ionosphere Mesosphere Energetics and Dynamics (TIMED) satellite in December, 2001. TIMED has a circular orbit (altitude 625 km) which precesses relative to the local solar time, so has to be rotated 180° in the yaw direction every 60 days. SABER observes thermal infrared limb emission in 10 channels between 650 and 5880 cm^{-1} from the ground up to 400 km [Mlynczak, 1997]. It obtains profiles from 52°S to 83°N for about 60 days and then from 83°S to 52°N for another 60 days before returning to the first latitudinal coverage. The SABER vertical resolution is about 2 km [Remsberg et al., 2003]. SABER observations are retrieved with an algorithm which includes nonLTE processes [Mertens et al., 2001]. The data used here correspond to version 1.7. Validation of this version for temperature and ozone has been submitted for publication according to SABER-webpage [2008] but the papers are still not published. Only temperature and ozone are available from the SABER experiment.

3.3.2 Occultation viewing instruments

In the occultation geometry (illustrated in Figure 3.10) a given source (Sun or Stars) is measured first above the atmosphere and then through the atmosphere at descending altitudes (or in the opposite direction, starting through the atmosphere and then upwards). As the radiance from the source passes through the atmosphere, absorption features can be distinguished. A series of occultations at different tangent heights are then used to derived atmospheric vertical profiles.

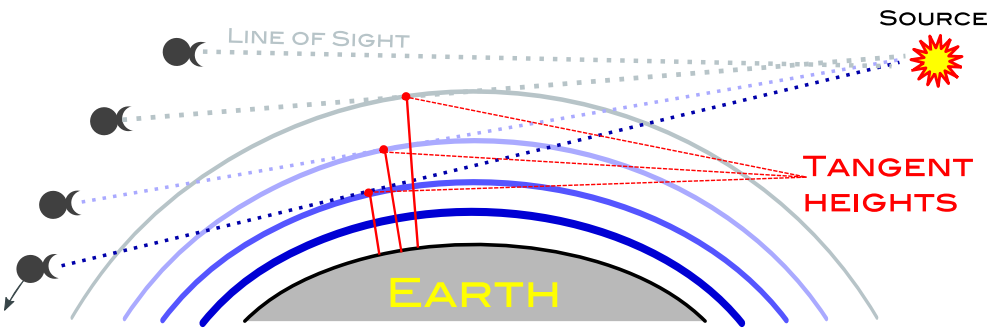

Figure 3.10: Schematic showing the solar occultation geometry.

One of the main advantages of the occultation measurements is that by dividing the occultations I_{OCC} (typically below 100 km) by the radiances measured above the atmosphere I_{REF} (around 150 km) a self calibrated transmission spectrum,

$$T = \frac{I_{\mathrm{OCC}}}{I_{\mathrm{REF}}} \tag{3.6}$$

is obtained.

The main limitations of this technique is that the measurements need to be taken during sunrise or sunset (or the star equivalent) limiting the number of measurements to two per orbit for a given source.

SOFIE

The Solar Occulation For Ice (SOFIE) experiment was launched on board the Aeronomy of Ice in the Mesosphere (AIM) satellite in April 2007. SOFIE measures atmospheric absorption spectra in 16 spectral channels between 1879 to 34,480 cm^{-1} at tangent heights from around 100 km down to the tropopause. Due to the AIM circular orbit (altitude 600 km), SOFIE measures 15 sunrises and 15 sunsets per day, each of them at the same latitude but spaced by 24° in longitude. In about 4 months, SOFIE sunrise coverage will vary from 65 N to 85 N while the sunset measurements varies from 65 S to 85 S. The SOFIE vertical resolution is about 1.5 km. The current version (1.01) includes the retrieval profiles of temperature, O_3, H_2O, CH_4 and Ice extinction [Russell et al., 2009; Gordley et al., 2009].

ACE – FTS

The Atmospheric Composition Experiment (ACE) satellite was launched in August 2003 into a low earth circular orbit (altitude 650 km, inclination 74°). Its main instrument is a Fourier Transform

Spectrometer (ACE – FTS) with a spectral coverage from 750 to 4400 cm^{-1} with a spectral sampling of 0.02 cm^{-1}. It measures atmospheric absorption spectra at tangent heights from 150 km down to 4 km with a vertical resolution between 3 to 4 km during sunrise or sunset. Although, the ACE-FTS covers only two latitudes per day, by assembling several days, global coverage can be achieved. Version 2.2 (the current version) includes the following molecules: pT, H_2O, O_3, N_2O, CO, CH_4, NO, NO_2, HNO_3, HF, HCL, N_2O_5, $CLONO_2$, CCl_2F_2, CCl_3F, COF_2, CH_2Cl, HDO, SF_6, HCN, CH_3Cl, CF_4, C_2H_2, C_2H_6,ClO and N_2 [Bernath, 2006].

GOMOS

The Global Ozone Monitoring by Occultation of Stars (GOMOS) is a spectrometer onboard the ENVISAT satellite (as the MIPAS instrument). It measures atmospheric absorption spectra in the ultraviolet region between 248 to 690 nm with a spectral sampling of 0.31 nm at tangent heights from 100 km down to 4 km. In addition, it also measures in the near infrared between 750–776 and 916–956 nm with a sampling of 0.06 nm. GOMOS vertical resolution is 1.7 km. GOMOS provides near global coverage daily due to the several suitable star targets, however strict quality controls must be used when dealing with faint stars. It also provides both day and night measurements. The atmospheric parameters retrieved by GOMOS are O_3, NO_2, NO_3, neutral density, aerosols, H_2O, O_2 and in favourable conditions OClO and BrO.

SCIAMACHY

The Scanning Imaging Absorption spectrometer for Atmospheric Cartography (SCIAMACHY) instrument is also on board the ENVISAT satellite (as well as MIPAS). It is a spectrometer that measures solar radiation in the ultraviolet, the visible and the near infrared spectral regions (240 nm – 2380 nm) at a moderate spectral resolution (0.2 nm – 1.5 nm) either in nadir[5], solar/lunar occultation or limb viewing observations. These viewing modes are used during each orbit to retrieve tropospheric, stratospheric and mesospheric compositions. For mesospheric observations limb / occultation measurements are used. Operationally, only the O_2 and NO products covers the entire mesosphere. In these modes, the atmosphere is scanned from the ground up to 150 km in 3 km steps [Bovensmann et al., 1999]. Furthermore, the limb / occultation radiances can be used to detect polar mesospheric clouds as described in von Savigny et al. [2004].

[5]In this type of geometry the atmosphere is seen near the local vertical. This allows to have good horizontal coverage but limits the vertical resolution.

CHAPTER 4

Mesospheric Radiances

4.1 MIPAS calibration

An accurate calibration of any instrument is needed to ensure that the datasets generated are reliable for quantitative applications. In general, MIPAS calibration can be divided in three steps: radiometric, spectral and geolocation calibration. The radiometric and spectral calibrations convert the raw scene into a limb radiance spectrum assigning absolute values to the y-axis in nW / (cm^2 sr cm^{-1}) and to the x-axis in wavenumbers (cm^{-1}). The geolocation is the process of determining the tangent altitude of a particular measurement as well as its lat/lon position on Earth. A detailed description of the processing steps is given by Kleinert [2007] and a summary follows here:

The radiometric calibration is performed using deep space as a cold source and an internal calibration blackbody as a hot source. The deep space measurements are performed every four scans in order to derive the instrument self emission (the major source of offset in the spectra) which is affected by thermal variations. This offset calibration is performed separately for the forward and reverse movement of the cube corner reflectors to cope with asymmetries in the response of the interferometer. A combination of deep space and calibration blackbody measurements are used to derived the gain, G, as,

$$G = \frac{S_{\mathrm{BB}}}{L_{\mathrm{BB}} - L_{\mathrm{DS}}} \tag{4.1}$$

where S_{BB} is the expected radiance due to the emission of the internal blackbody, L_{BB} and L_{DS} are the observed radiance of the blackbody target and the deep space scenes. The gain calibration is performed once per week.

An important aspect of the radiometric calibration is its sensitivity, normally expressed as the noise equivalent spectral radiance (NESR). The NESR is the standard deviation of a set of measure-

ments for a well defined target (i.e. internal blackbody or deep space) in order to be able to identify the noise generated by the instrument itself. In simple terms, it represents the measurement random error in units of radiance and it is assumed to be uncorrelated between spectral points.

In addition to the NESR derived looking at deep space or the internal blackbody, the NESR is derived as well at each tangent height from the imaginary part of the calibrated spectrum by taking the standard deviation of the spectral points in $10\,\mathrm{cm}^{-1}$ bins.

The original NESR requirements for MIPAS operating at full resolution are listed in table 4.1. These requirements were designed to enable the retrieval of several species with high accuracy. Note that these requirements were designed for unapodized spectra, for apodized spectra their values fall for approximately a factor of 2.

Table 4.1: MIPAS NESR requirements [Fischer et al., 2000]

MIPAS band	NESR requirement [nW / (cm^2 sr cm^{-1})]
A	50
AB	40
B	20
C	6
D	4.2

[Dudhia, 2007] investigated the equivalent NESR values for MIPAS operating at the reduced resolution. The effects of the shorter FOPD is that the NESR is degraded by a factor of $\sqrt{0.4}$.

The spectral calibration is carried out using standard measurements from the atmosphere between 29 to 35 km. From these scenes the wavenumber scale is determined using isolated spectral lines with well known spectral postions. This calibration also corrects for any Doppler shift induced due to the relative movement of the spacecraft and the atmosphere.

The geolocation refers to the process of assigning an altitude and a lat-lon position to a given tangent height spectrum derived from the line of sight pointing angles and the spacecraft position.

4.1.1 Radiometric offset

The accuracy of the radiometric offset subtraction can be estimated by analyzing if there is still an offset in the calibrated spectra. Considering that at mesospheric heights the emission lines from most gases are sparse and weak, after masking them, the remaining spectra can be treated as the residual emission from the instrument itself.

The derivation of the offset starts by averaging apodized spectra at each tangent height for a

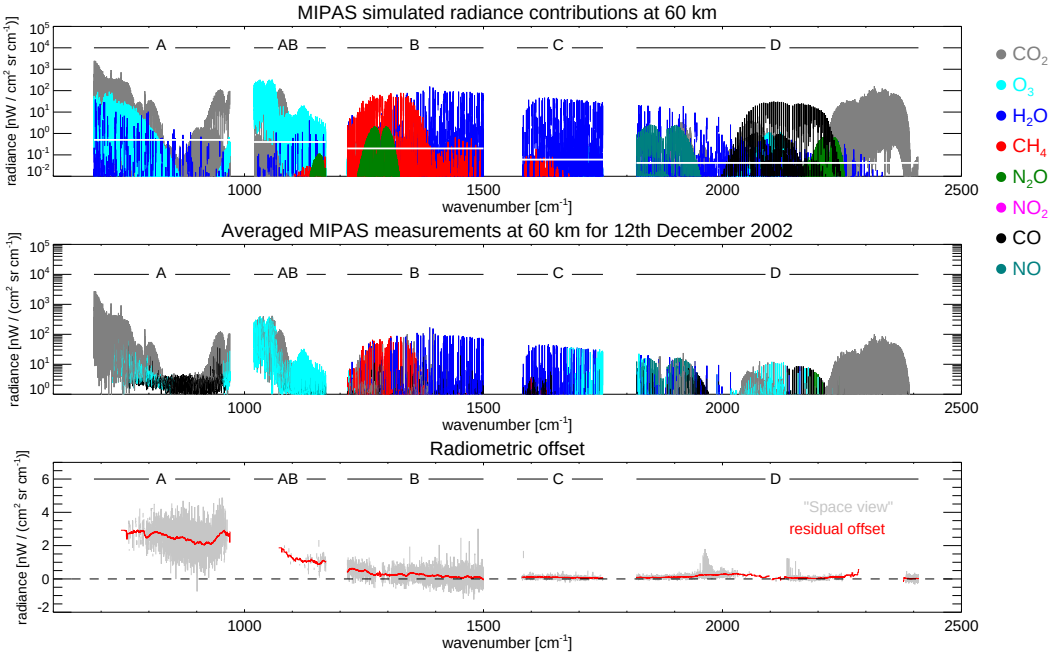

Figure 4.1: Simulated and averaged spectra for the 12th December 2002. The white line in the top panel represents the threshold level for identifying an emission line. Bottom panel shows the mesospheric "space view" and the residual offset (see text).

whole day in order to improve the S/N ratio. Afterwards, simulations of the most abundant gases in the mesosphere are used to identify the emission lines and remove them leaving, theoretically, a "space view". These simulations were performed using the RFM and assuming nonLTE midlatitude conditions for the molecules listed in Figure 4.1. If a simulated emission line was greater than 1% of NESR for the corresponding MIPAS band that measurement was masked out.

Figure 4.1 displays the spectra simulated for each molecule, the averaged spectra for the 12th December 2002 at 60 km tangent height as well as the "space view" derived after the application of the spectral masks. The residual offset is a smoothed version of the "space view". Although these residual offsets are nonzero, they are below the MIPAS noise levels. An unexpected emission feature remains in band D around 1980 cm^{-1}, although the conclusions at the end of this section are not affected by it because it will only affect a small section of the offset of band D.

Since the instrument offset is particularly sensitive to changes in the instrument temperature, despite the fact that it is determined around 20 times per orbit, small deviations will be found along the orbit. Figure 4.2 shows the mean derived offset orbital variation for the band A at the tangent height of 60 km for the 12th December 2002. Analysis of the deviations of the derived offset may be used to detect unidentified molecular emission (e.g. the one found around 1980 cm^{-1}) or atmospheric phenomena such as the emission of polar mesospheric clouds (PMC) (chapter 5).

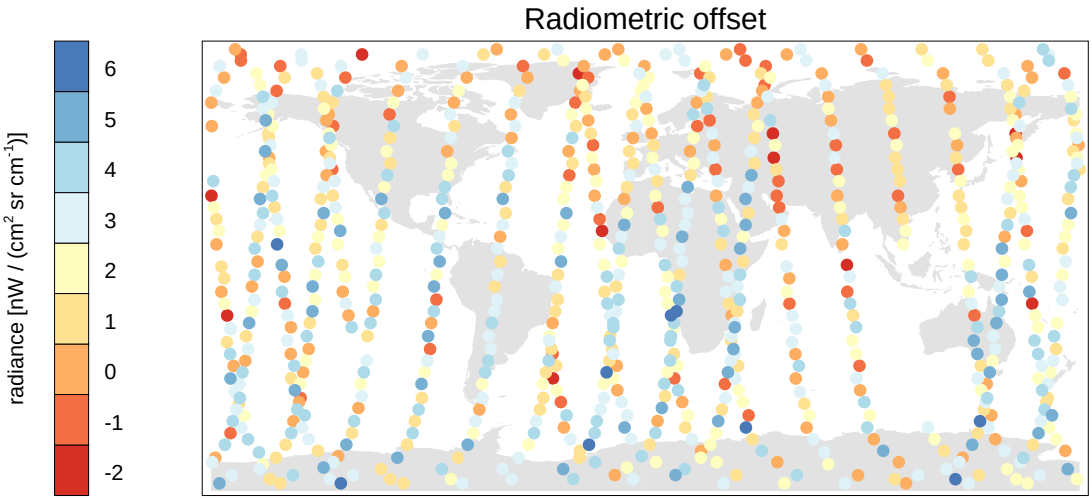

Figure 4.2: Radiometric offset derived from the mesospheric "space view" for MIPAS band A along the 12th December 2002.

As described previously, the offset calibration is performed separately for the forward and reverse movement of the cube corners. The same analysis can be applied to an average spectra of only forward or reverse sweeps to investigate if there are any anomalies in the different calibrations. Figure 4.3 compares the radiometric offset derived for forward and reverse sweeps averaged over one day, for full and reduced resolution operation.

As can be seen, there is a large systematic difference between the forward and reverse offset for the full resolution operation. This behaviour was found in several days analyzed and is reported in Kleinert [2007]. Theoretically, a systematic difference between the forward and reverse sweeps can induce systematic oscillations in the atmospheric retrievals because adjacent tangent heights are measured with opposite sweep directions.

In the case of the reduced resolution operation there is no large difference between the two offsets derived. Although the offsets are smaller than 10% of the NESR at each MIPAS band, they are still non zero. Furthermore, at mesospheric heights where the radiance amplitude is significantly reduced in magnitude this offset might induce an overestimation of the atmospheric parameters unless the retrieval fits the offset as well. Note that the ESA level 2 retrievals and MORSE fit a radiometric offset in each of the microwindows.

4.1.2 NESR

As has been said the NESR quantifies the noise levels in the data. In practice, the NESR is important because it determines the measurement error covariance matrix (the weighting for each spectral

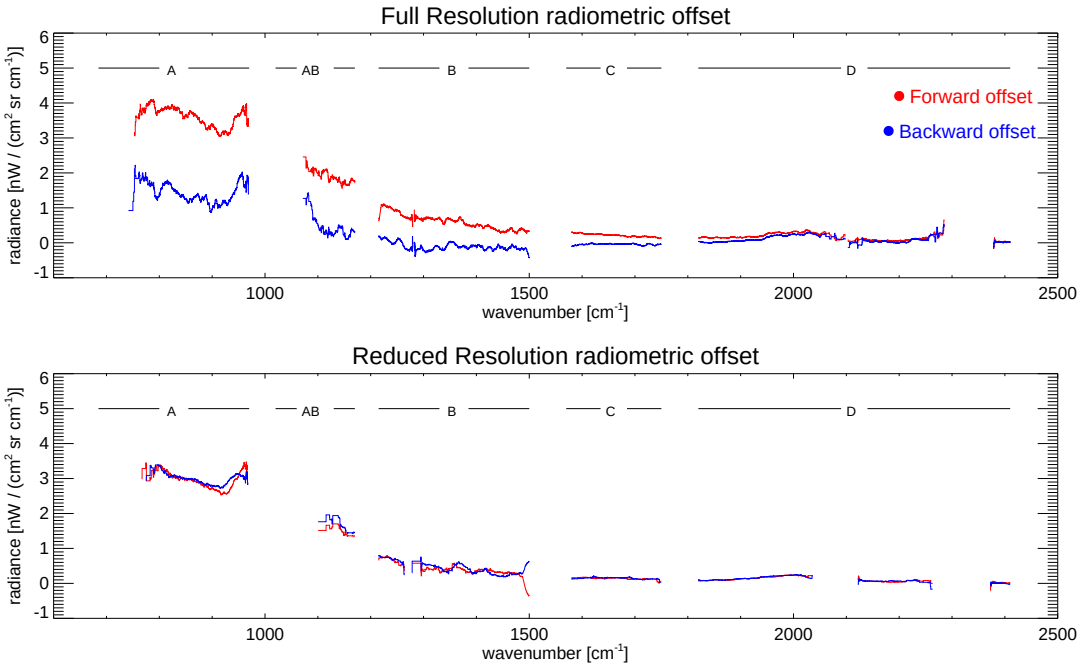

Figure 4.3: Forward and reverse offsets for full and reduced resolution. The 12th December 2002 was analyzed for the full resolution while the 7th June 2007 for the reduced resolution operation.

point) used in any of the retrieval schemes explained in section 2.2. Using a simple standard deviation approach, the mesospheric "space view" measurements can also be used to validate the NESR estimate. Figure 4.4 shows the NESR reported in the L1B data and the derived for a full and a reduced resolution scan at 60 km for an apodized spectrum. In this case only one scene (not averaging over one whole day) is used to directly compare it against the values of NESR in the L1B file.

Generally, these NESR estimates are in good agreement. The sudden "spikes" in the mesospheric "space" derived values (for instance around 2250 cm^{-1}) is due to the smoothing over regions containing masked values. In those regions atmospheric emission lines were identified and therefore, masked out. The NESR meets the requirements of the full resolution operation and the equivalent requirements for the reduced resolution operation. According to Kleinert [2007] the most important effect on the NESR is ice accumulation on the detector which may worsen by a factor of 20% between decontaminations.

4.2 Middle atmosphere calibration

In theory, the different MIPAS viewing modes only differ in the tangent heights measured, that is to say, all of them should be equally well calibrated. In practice, as will be shown, the radiometric calibration of the middle atmosphere data differs considerably from the nominal mode.

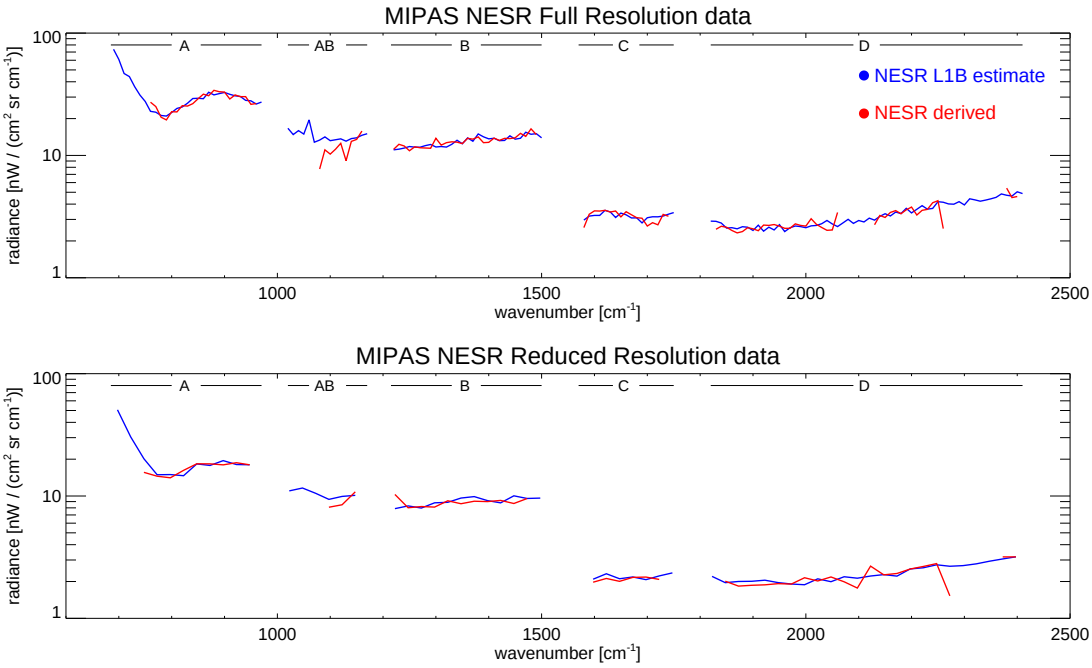

Figure 4.4: NESR estimated by the L1B processor and derived from the mesospheric "space view". The scan analyzed for the full resolution is the first scan of orbit 04154 and for the reduced resolution operation is the first scan of orbit 27540. Both orbits correspond to the first orbit of the days used in Figure 4.3 respectively.

The test is based in comparing averaged radiances (between 20 S and 20 N) of adjacent tracks of consecutive days. Three adjacent tracks as displayed in Figure 4.5 are used. Two of them correspond to NOM viewing modes and the other one to MA mode (either immediately after or before the nominal mode tracks).

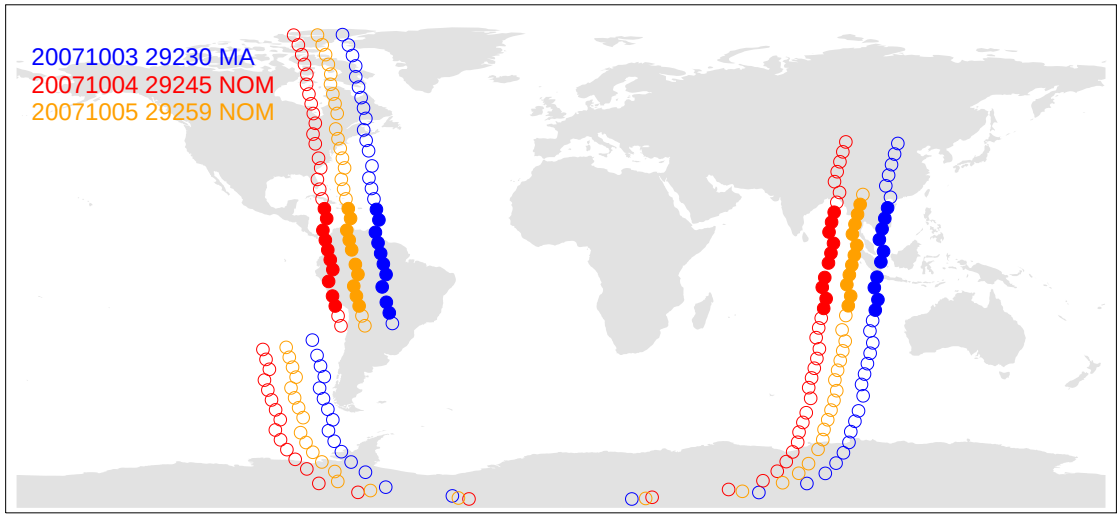

Figure 4.5: Three MIPAS orbit tracks in consecutive days used to compare the MA calibration. The solid circles show the scans between 20 S and 20 N. The orbit tracks are color coded according to the date, orbit number and viewing mode.

The difference between the NOM–NOM and the difference between the MA–NOM averaged radiances should be comparable assuming that no significant atmospheric change occurred during those days. Figure 4.6 shows the MA–NOM and the NOM–NOM differences at 18.87 km. Since the spectra are at different engineering altitudes, the NOM spectra was interpolated to the lowest engineering altitude of the MA data to avoid extrapolation, in this case 18.87 km . As can be seen, the difference found in the MA–NOM case is bigger than that found in the NOM–NOM case and furthermore it displays some structure rather than being close to zero and flat.

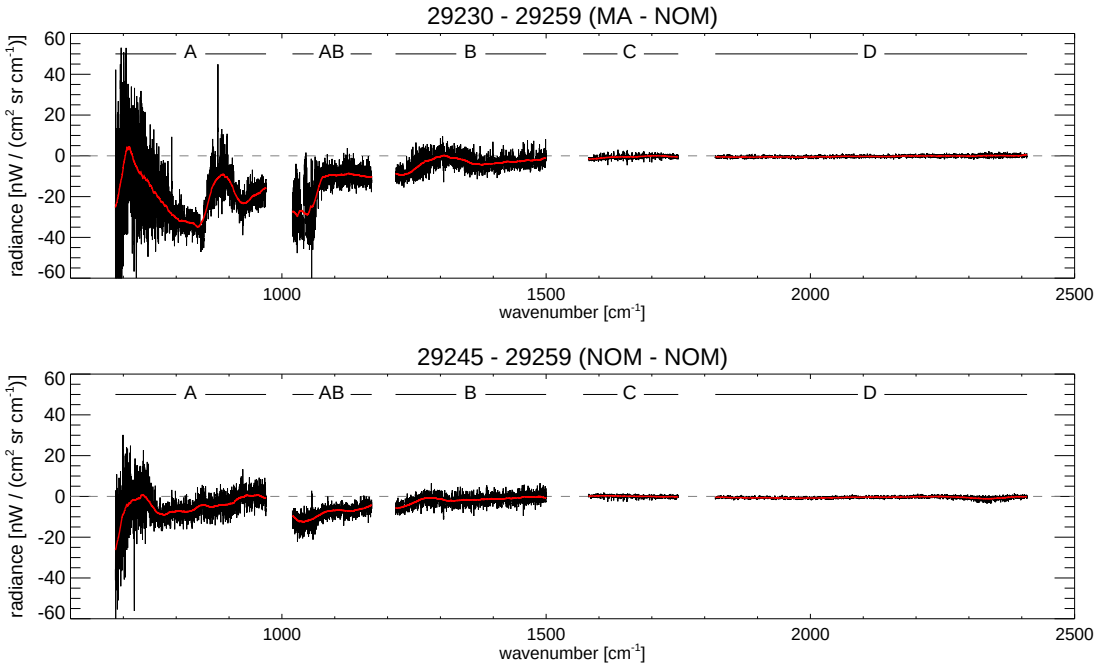

Figure 4.6: Averaged spectral difference between 20 S and 20 N for MA–NOM orbits (top) and NOM–NOM orbits (bottom) at the lowest MA tangent height. The red line displayed is the smoothed version of these differences.

To investigate this further, Figure 4.7 shows the smoothed differences at several tangent heights for the MA–NOM and the NOM–NOM cases. For these comparisons (as well as for Figure 4.6) the nominal mode average radiances were interpolated to the averaged MA tangent heights between 18 to 70 km to avoid extrapolation. As portrayed in the Figure, the MA–NOM smoothed differences are always larger than the NOM–NOM ones and, in addition, the smoothed difference corresponding to the tangent height at 18.87 km (lowest MA tangent height red line) seems to have an anomalous behaviour.

Several consecutive orbit tracks, as listed in table 4.2, were analyzed to investigate if the MA calibration discrepancies were consistent with time. Figure 4.8 shows the smoothed differences for the MA–NOM and the NOM–NOM cases at the lowest tangent height corresponding to the MA averaged

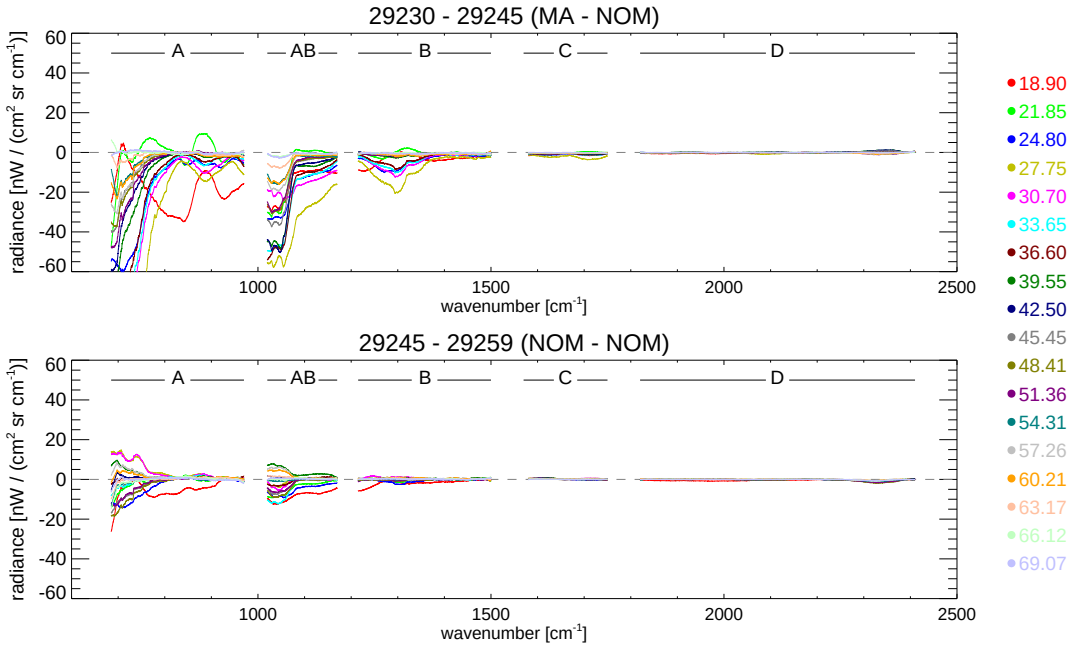

Figure 4.7: Smoothed averaged spectral difference between 20 S and 20 N at several tangent heights.

tangent height. As can be seen, when comparing the NOM–NOM cases with the MA–NOM cases, it seems that there is always an anomalous behaviour at this tangent height. The smoothed differences for the rest of tangent heights (not shown here) also show the same behaviour as in Figure 4.7 (i.e. always show a greater spread and not an almost flat difference).

Figure 4.9 shows the MA–NOM difference for the 29230–29245 consecutive tracks as well as the pressure Jacobian treated with the same smoothing. As can be seen, the similarity of the two curves is remarkably good, suggesting that these anomalies are associated with a pointing problem.

It is important to note that although the previous MA calibration analysis has been presented only for scans between 20 S and 20 N, similar results are obtained at all latitudes. As has been said, the standard MIPAS algorithms fit a radiometric offset in each microwindow and hence, presumably, these MA calibration anomalies will not affect the retrievals.

Table 4.2: Consecutive orbit tracks used to compare the MA calibration.

MA	NOM	NOM
2007/06/07 27541	2007/06/08 27555	2007/06/09 27569
2007/10/03 29230	2007/10/04 29245	2007/10/05 29259
2008/10/23 34756	2008/10/22 34741	2008/10/21 34727
2009/02/25 36545	2009/02/24 36531	2009/02/23 36517

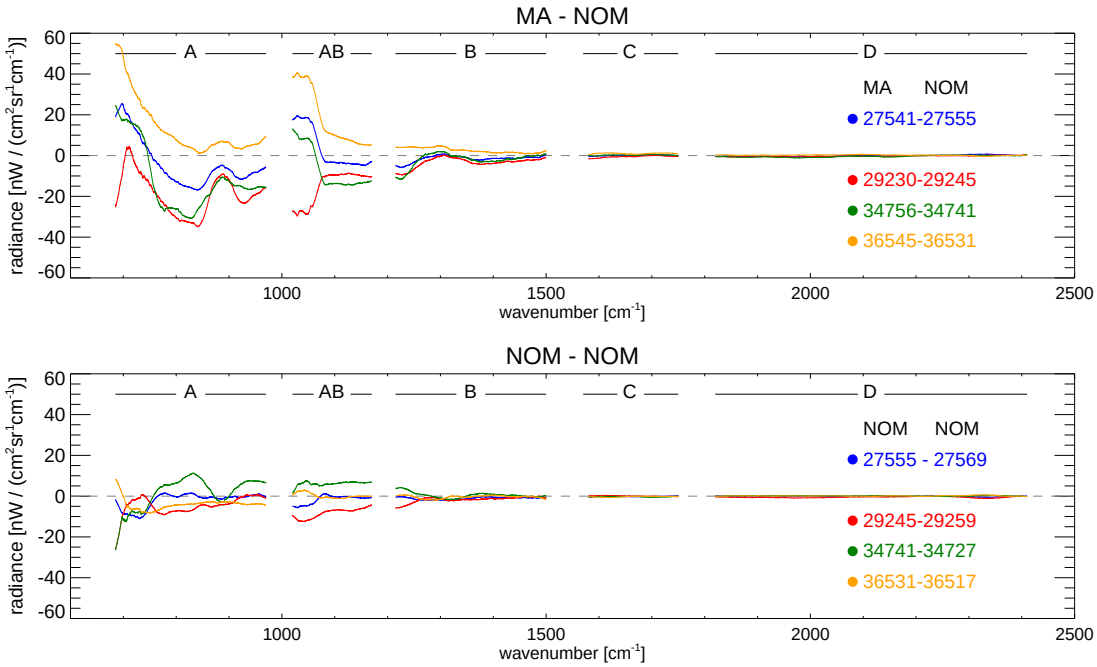

Figure 4.8: Smoothed averaged spectral difference between 20 S and 20 N at the lowest MA tangent heights for several consecutive orbit tracks.

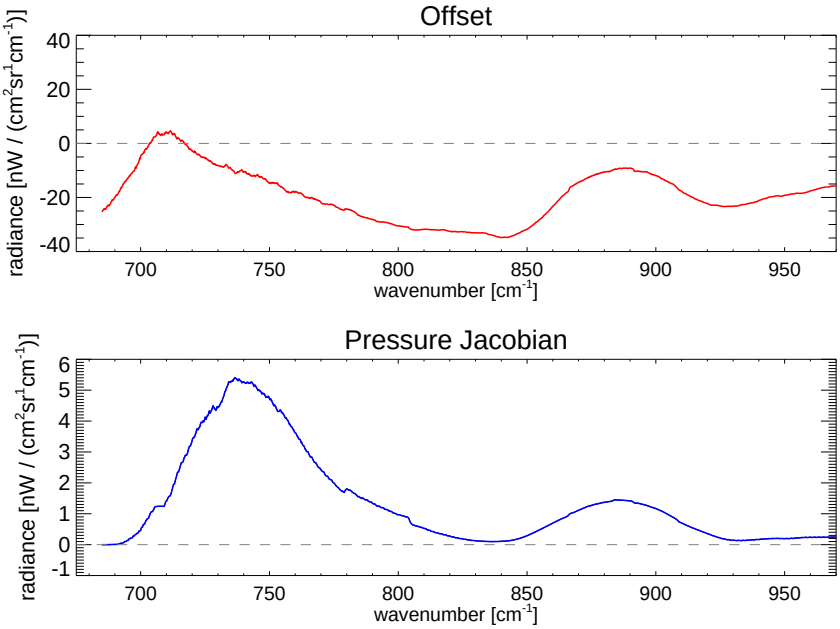

Figure 4.9: (top) MA–NOM discrepancy and (bottom) pressure Jacobian spectrum treated with the same smoothing.

4.3 HIRDLS mesospheric radiances

Due to the main aperture blockage[1], HIRDLS radiances are subject to several corrections. In theory, these corrections subtract the Kapton emission from the measured radiance leaving only the atmospheric emission. So far, the HIRDLS scientific team has managed to correct the radiances around the upper troposphere and the stratosphere, however not so much attention has been given to the mesospheric radiances. In the following, an analysis of the HIRDLS mesospheric radiance behaviour is presented.

Much insight can be gained by simply looking at averaged radiances. Figure 4.10 displays the result of this averaging for each channel for the 15th January 2006. The version used was 4.00 (also known as 2.04.19) which is the latest released version. As can be seen, the mean radiance of

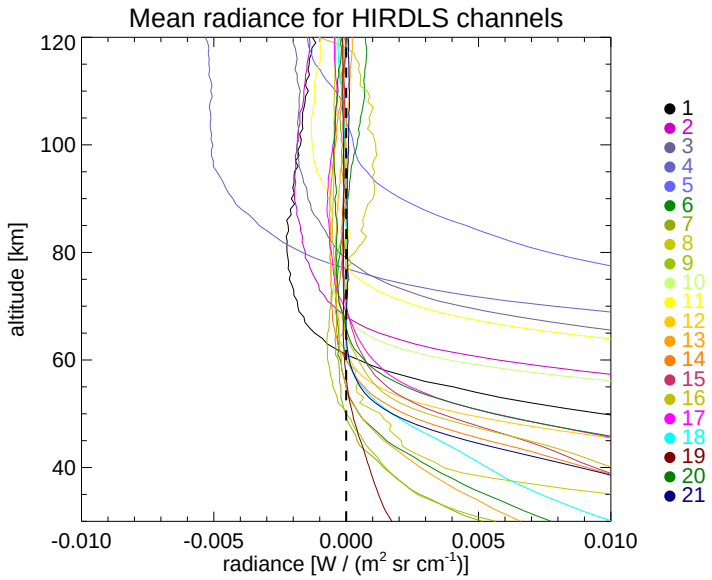

Figure 4.10: Averaged radiance for HIRDLS channels (for reference see Figure 3.7) for the 15th January 2006. Each channel is represented by a different colour.

all channels becomes negative towards upper levels. This occurs because during one of the multiple correction processes the radiances are forced to be zero at certain height. Presumably, above this level, the radiances are considered "space view" and therefore used in the correction blockage algorithm as explained in section 3.2.

The altitude of this forced zero height is fairly consistent in time for all the channels except for number 8 (the HNO_3 channel). Figure 4.11 shows the mean radiance for channel 8 for several days in 2006. It seems that the radiances become negative in a range of 20 km depending on the day, below the forced zero height. Since channel 8 is the only one that presents an anomalous behaviour regarding

[1] explained in section 3.2.

the forced zero crossing when comparing it with the rest of the channels, it was recommended to the HIRDLS scientific team that the correction of this channel was verified. Figure 4.11 also shows the mean radiance for channel 11 to illustrate the behaviour found in the rest of the channels. It can be noted that the radiances become negative practically at the same height every day analyzed. The

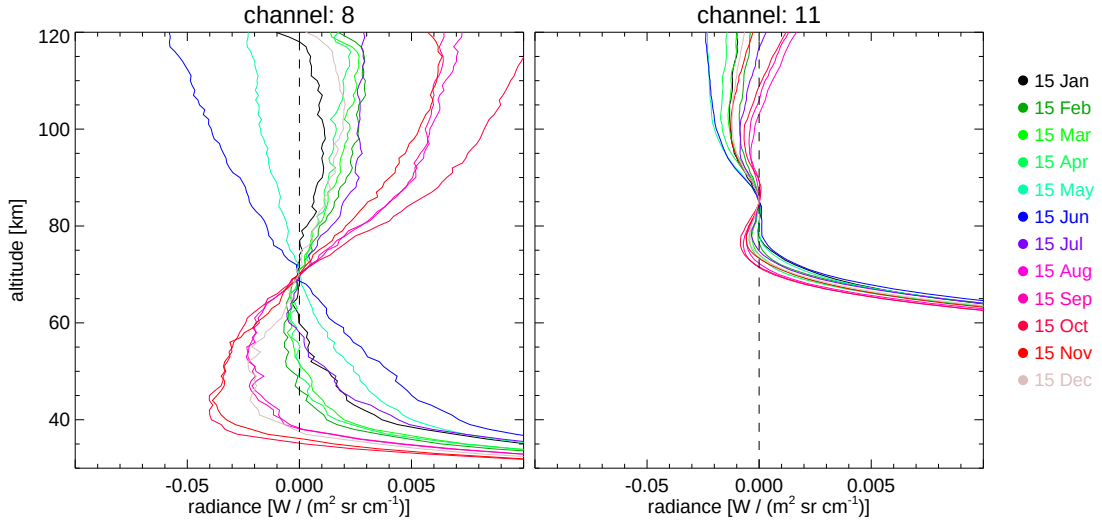

Figure 4.11: Averaged radiance for HIRDLS channels 8 and 11 for several days in 2006. Each day is represented by a different colour.

mean radiances of channel 11 (an O_3 channel originally designed to sound well into the mesosphere) are shown because, in addition to the forced zero height, they display a hump where the second O_3 maximum lies (section 1.4).

To see if the peak around 90 km in channel 11 coincides with the second O_3 maximum, simulations of the HIRDLS radiances were performed using MIPAS measurements.

4.4 HIRDLS simulations

To simulate the HIRDLS radiances with the MIPAS data, the filter function of the HIRDLS channel 11 was interpolated onto the MIPAS spectral grid. The filter response and the MIPAS spectral range are shown in Figure 4.12.

Unfortunately, the MIPAS measurements only partially overlap with the filter width because the HIRDLS channel 11 spectral range coincides with the gap between the MIPAS A and AB bands, therefore, a correction factor for the broader HIRDLS spectral coverage was developed.

This correction factor, φ, was defined as the ratio between the channel 11 response to the MIPAS

measured part, S_{M}, and the response to the whole spectral coverage, S_{H}, for a given tangent height.

$$\varphi = \frac{S_{\mathrm{M}}}{S_{\mathrm{H}}} \tag{4.2}$$

Simulations of both responses were generated using the RFM. These simulations were performed using midlatitude conditions and assuming that only O_3 emits in that spectral range. This correction factor tends toward one as the height increases because the part of the HIRDLS channel not measured by MIPAS corresponds to the tail of the filter and furthermore the O_3 emission lines are weak in that region (as illustrated in Figure 4.12).

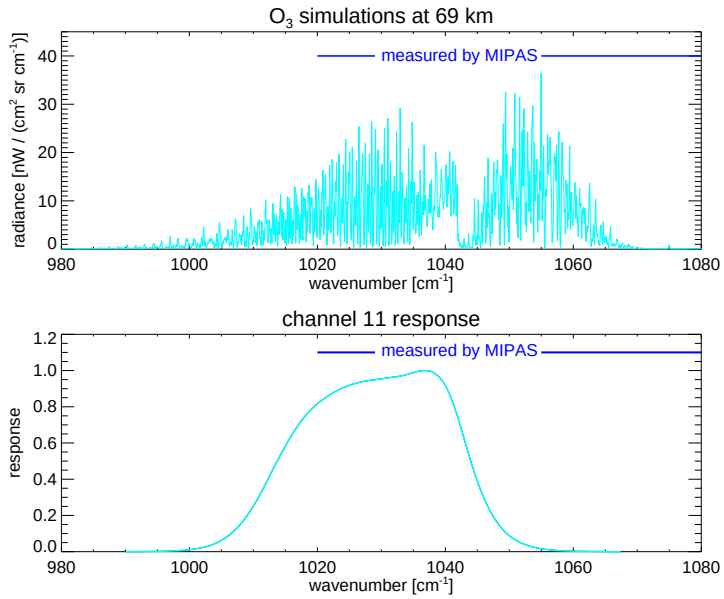

Figure 4.12: (Top) O_3 simulated spectra at 69 km. (Bottom) HIRDLS channel 11 filter response.

Once the filter is interpolated, the integrated HIRDLS–MIPAS radiance can be found using,

$$L_{\mathrm{H}} = \varphi \sum_i L_{\mathrm{M}}(\nu_i) F(\nu_i) \Delta\nu \tag{4.3}$$

where L_{H} is the simulated HIRDLS radiance, L_{M} is the MIPAS measured radiance for the wavenumber ν_i, $F(\nu_i)$ is the HIRDLS filter function at the corresponding wavenumber and $\Delta\nu$ is the MIPAS spectral interval (0.0625 cm^{-1}). Also, φ will vary depending on the tangent height integrated.

A unit scaling was also applied to convert from the MIPAS units [nW / (cm^2sr cm^{-1})] to the HIRDLS units [W / (m^2sr cm^{-1})]. The different latitude coverage of the instruments was also taken into account: MIPAS data north of 80N and south of 65S were discarded.

Figure 4.13 (left) shows the result for this simulation for the 22nd of April 2007 when MIPAS

and HIRDLS mesospheric measurements were available. Despite the obvious offset[2], the HIRDLS radiance profile resembles well the vertical structure of the radiances derived with MIPAS and also the radiance peaks coincide at 85 km. Furthermore, the HIRDLS and MIPAS data can be divided into day and night measurements to show the ozone decrease during day time. These results are also shown in Figure 4.13 (right) and they strongly suggest that the HIRDLS mesospheric radiances may contain useful atmospheric information despite the main aperture blockage.

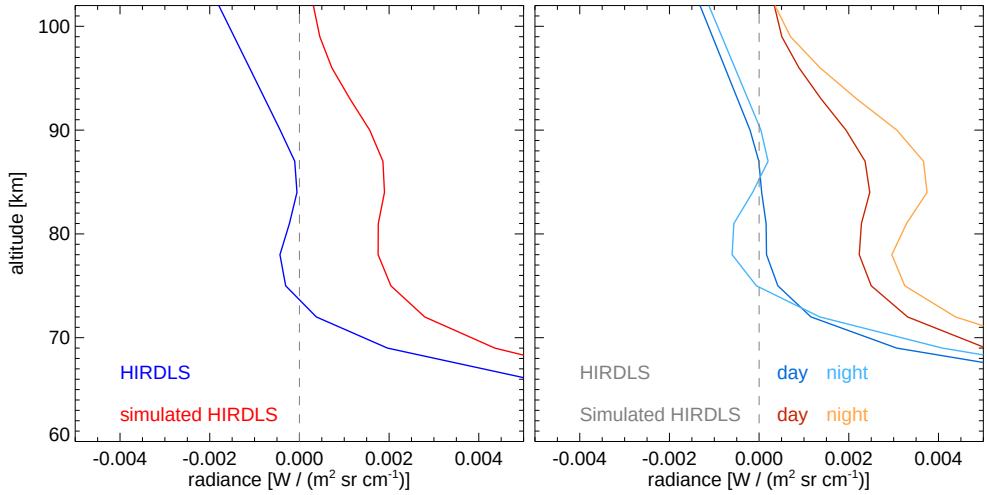

Figure 4.13: (left) HIRDLS channel 11 mean radiance and HIRDLS simulated measurements using MIPAS data for the 22nd of April 2007. (right) Same analysis as previously but dividing the data into day and night measurements.

Although this analysis has been presented for channel 11, it can be used on any other channel providing that there is a considerable overlap with the MIPAS measurements. Another technique to validate HIRDLS measurements using MIPAS was developed by Waymark [2009]. It consists in feeding a radiative transfer model with MIPAS retrieval results to simulate the full HIRDLS spectral range. These simulations are then integrated into the corresponding HIRDLS filters functions.

4.5 Conclusions

In this chapter a technique to use the MIPAS mesospheric radiance to derive the radiometric offset and to validate the noise estimates was introduced. For the full resolution data, a discrepancy between the forward and reverse sweep was found, this discrepancy has also been noted by Kleinert [2007].

Moreover, a technique was introduced to evaluate the calibration between adjacent tracks of consecutive days. This technique was used to compare the calibration of the MIPAS middle atmosphere

[2]This offset is presumably induced by the main aperture blockage or by the correction algorithm.

viewing mode in comparison to the nominal viewing mode. It was discovered that the MIPAS middle atmosphere radiances seem to suffer from a pointing problem.

Also, HIRDLS radiances were studied to investigate their behaviour at mesospheric heights. Unfortunately, as part of the Kapton correction algorithm, the HIRDLS radiances are forced to cross zero at a given height (around the lower mesosphere) and they are not calibrated above this level. Nevertheless using MIPAS measurements to simulate the HIRDLS radiances it was found that the HIRDLS radiances show clear signatures of the second O_3 peak suggesting that if the forced zero level height can be risen up above the mesosphere the HIRDLS radiances can be used for mesospheric studies.

CHAPTER 5

Polar Mesospheric Clouds

Noctilucent clouds (NLCs) are cloud-like phenomena so faint that they can only be observed visually during twilight hours (i.e., when the sun is below the horizon illuminating the cloud against a dark background). The first public records of these phenomena were in 1885 by Leslie [1885] and Backhouse [1885] and two years later their height was determined to be around 82 km using photographic triangulation [Jesse, 1887]. By the beginning of the 20th century it was established that they occur mainly during the summertime in both hemispheres at latitudes greater than 50° and that they are geometrically confined to a 1 km to 3 km layer [Thomas, 1991].

These clouds are composed of water ice particles [Hervig et al., 2001]. Hence, their spatio-temporal restrictions are due to the requirement of extremely low temperatures to produce water ice saturation. These temperatures are only observed in the summer polar mesopause region as explained in section 1.1.

Thomas et al. [1989] suggested that their appearance in 1885 may have been due to the increase of CH_4 following the start of the industrial revolution considering that in the middle atmosphere CH_4 oxidizes to H_2O, hence, enhancing the water vapour available for the clouds growth. That is to say: NLCs are one of the first atmospheric manifestations of human activities.

When viewed from space these clouds are termed Polar Mesospheric Clouds (PMCs) and have been detected mostly measuring scattered solar radiation either in the visible or in the UV part of the spectrum [Thomas and Olivero, 1989; Hervig et al., 2001; von Savigny et al., 2004; Bailey et al., 2005; Petelina et al., 2006]. Thomas and Olivero [1989], after analyzing nine summer seasons of satellite data, concluded that the PMC season starts at high latitudes about 20 to 40 days before the summer solstice (mid-March), that the maximum occurrence was found 3 weeks after the solstice (around mid-July) and that no PMCs where detected about 60 days after the solstice (mid-August).

5.1 PMC detection by MIPAS

The PMC detection in the thermal infrared is challenging due to the low signal associated to the extreme low polar summer temperatures. Nevertheless, Grossmann et al. [2006] detected PMC spectral signature around 833 cm^{-1} by averaging limb emission spectra recorded by the CRyogenic Infrared Spectrometers and Telescopes for the atmosphere (CRISTA-2) experiment which flew in August 1997 on the Space Shuttle mission STS-85. Hence, the MIPAS radiometric offset derived (as discussed in section 4.1.1) around 833 cm^{-1} should be affected by the PMC infrared emission.

Figure 5.1 (left) shows the averaged offset derived between 800 and 860 cm^{-1} at three different latitude bins (90S–60 S, 20S–20 N and 60N–90 N) for two height levels (one where PMCs are suppose to exist, ∼82 km and one where no PMCs are expected ∼96 km). As can be seen, both offsets (∼82 km and ∼96 km) display a seasonal behaviour in the polar bins, with a maximum around their corresponding summer season while neither offset in the equatorial bin displays any seasonality. This suggest that the main seasonality in the polar offset is associated with the constant illumination around the polar summer areas rather than PMCs.

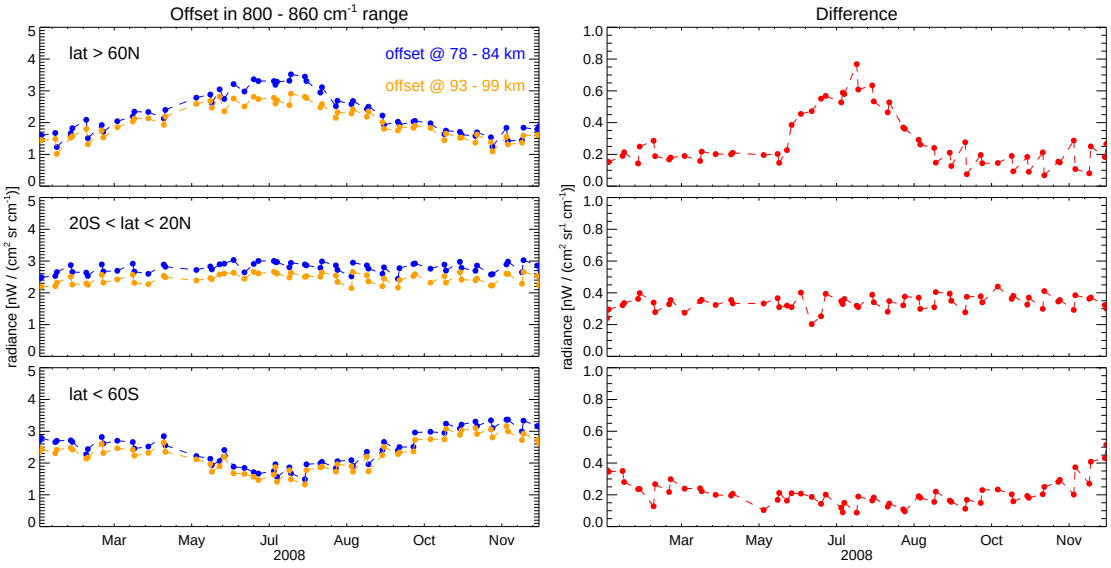

Figure 5.1: MIPAS radiometric offset in the MA mode averaged over 800–860 cm^{-1}.

Figure 5.1 (right) also displays the difference between the 82 km offset and the 96 km (i.e., at and above the PMCs altitude) for each latitude bin. As portrayed, there is a clear enhancement around the PMC season in the 60 N–90 N bin, while there is no enhancement in the 20S–20 N bin and a hint of it in the 90 S–60 S bin suggesting that it is possible to determine a PMC signature in the data.

To corroborate that the enhancement found corresponds to the PMC season, it was overplotted (Figure 5.2) with the SCIAMACHY cloud frequency and the MLS saturation over ice frequency

for the 2007 and 2008 north polar summers. In this Figure, the offset corresponds to the latitude bin between 60 N and 80 N to match the other datasets. The cloud frequency is simply the ratio of the SCIAMACHY scans flagged as cloudy and the total scans (between 60 N and 80 N). The SCIAMACHY PMC detection algorithm specifics can be found in von Savigny et al. [2004]. The supersaturation with respect to ice frequency was derived using MLS temperatures and water vapour concentrations[1]. The supersaturation with respect to ice frequency is the ratio of the scans where supersaturation exist against the total amount of scans (between 60 N and 80 N also). The saturation vapour pressures were derived using the Marti and Mauersberger [1993] results for temperatures between 170 K and 250 K and using Mauersberger and Krankowsky [2003] results for temperatures below 170 K.

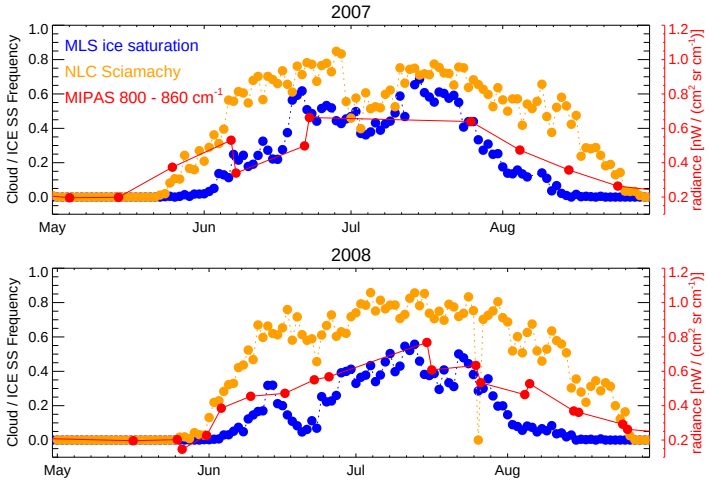

Figure 5.2: PMC frequency (SCIAMACHY), ICE super saturation frequency (MLS) and MIPAS radiometric offset difference averaged over 800–860 cm^{-1} between 60 N and 80 N.

As shown in Figure 5.2, the SCIAMACHY cloud frequency, the MLS ice saturation frequency and the offset enhancement rise, peak and fall in the same manner, suggesting that this offset enhancement really is due to the PMC emission[2].

In order to investigate further the possibility of detecting PMCs not just on a day by day basis but scan by scan, Figure 5.3 shows polar stereographic plots of the horizontal distribution of the MIPAS averaged radiance between 800 and 860 cm^{-1} (the difference between the 78–84 km minus the 93–99 km as before) which is assumed to be an indicator of absence or presence of PMCs. It also displays the supersaturation derived from MLS temperature and water vapour dataset.

[1] The MLS dataset was used instead of the MIPAS MA dataset because the MIPAS H_2O values retrieved seem anomalous as will be shown in Chapter 6.

[2] A similar scheme to detect PMCs using MIPAS data was derived by López-Puertas et al. [2007] at the same time that this method was being developed.

As can be seen, there is some correlation between the relatively high values in the MIPAS radiometric offset and the supersaturation plots considering that the two instruments measure the atmosphere at two different local times. Hence, this again suggests that PMCs emission can be detected in the MIPAS radiances, however, it should be emphasized the PMCs signature is smaller that the instrument noise and several false positives using this technique are presumably expected.

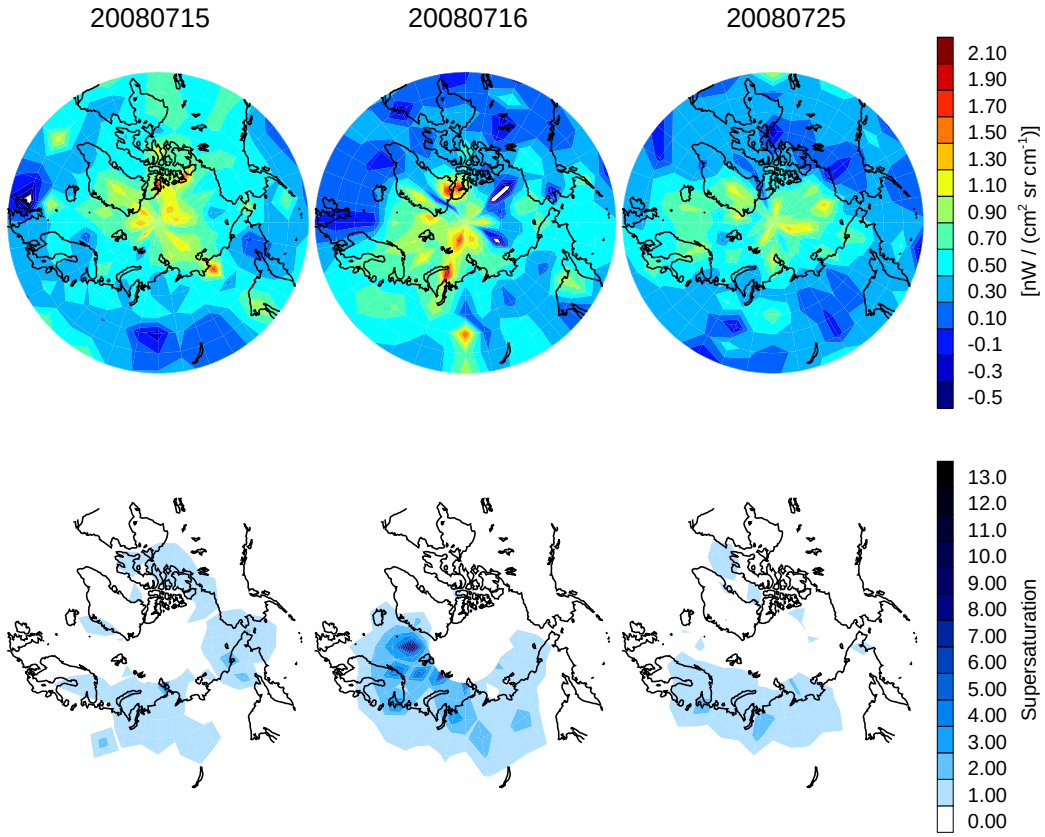

Figure 5.3: Stereographic plots of MIPAS radiometric offset difference and MLS ice supersaturation.

5.2 NLC viewing mode

In addition to the MIPAS viewing modes introduced in section 3.1, MIPAS can measure using viewing modes specifically designed to search for a given atmospheric signature such as the influence in the stratosphere of volcanic eruptions or PMCs (as previously mentioned, also called NLCs). As with the MA mode, the so called NLC viewing mode measures the limb from 39 to 102 km with 3 km spacing

but with three extra tangent heights at 79.5, 82.5 and 85.5 km, oversampling the heights where PMCs are expected to occur.

Table 5.2 lists the days when MIPAS used the NLC viewing mode.

Table 5.1: NLC viewing mode days

Date	Date
2005/07/19	2008/07/06
2005/07/20	2008/07/07
2005/07/21	2009/01/05
2007/07/04	2009/01/06
2007/07/05	2009/01/07
2007/07/14	2009/07/05
2007/07/15	2009/07/06
2008/07/05	2009/07/07

To investigate the usefulness of this special viewing mode, Figure 5.4 displays mean profiles of the averaged radiance between 800 and 860 cm^{-1} for cases with PMCs present or absent. It was assumed that a PMCs was present when the averaged radiance between 800 and 860 cm^{-1} between 81 and 84 km was greater than the averaged radiance between 93 and 99 km by 30%. These mean profiles were created using three NLC viewing mode days (20090605 – 20090607) and using three MA viewing modes for comparison (20090715, 20090716 and 20090725).

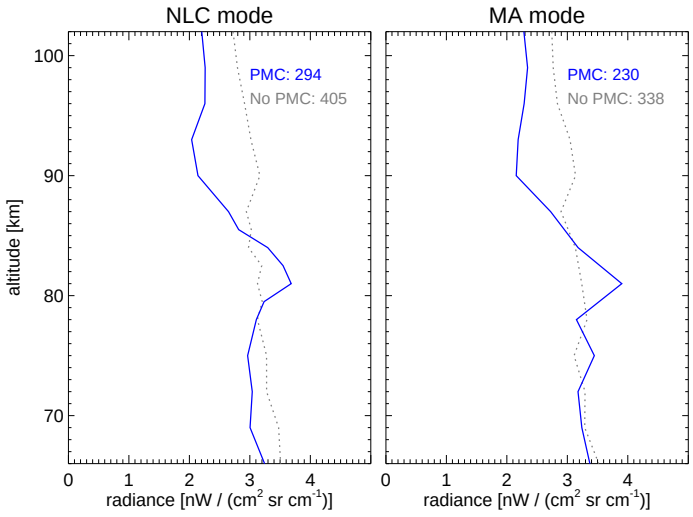

Figure 5.4: Mean MIPAS radiance profile averaged over 800 and 860 cm^{-1} for conditions where PMCs were either detected or absent for three days either in the NLC viewing mode or the MA viewing mode. The number of profiles averaged for each line is shown at the top corner of the subplots.

As can be seen in Figure 5.4 the two profiles (one for the NLC and one for the MA mode) where PMCs were present show an enhancement around 82 km (the height where most of the PMCs are

supposed to occur), while no obvious signature can be found in the two profiles where PMCs were absent. Furthermore, comparing the two profiles where PMCs were detected, it can be seen that the one derived with the NLC viewing mode shows more structure than the one derived using the MA viewing mode due to the extra heights added to the NLCs viewing mode. Hence, it is suggested that at least during the northern hemisphere summer the NLC mode is used instead of the MA viewing mode to sample more the PMCs expected heights.

5.3 Conclusions

This chapter proves that the PMCs emission can be detected in MIPAS radiances between 800–860 cm^{-1} despite their low emission due to the extremely cold temperature of the mesopause. Good agreement was found between an enhancement of the radiometric offset and PMCs detection by the SCIAMACHY instrument as well as the ICE supersaturation frequency derived from MLS data. However, it is expected that the technique introduced here will result in several false positives when using to detect PMCs scan by scan.

PMCs need to be studied further and therefore it is suggested that the NLC viewing mode is used instead of the MA viewing mode during the summer of (at least) the northern hemisphere.

CHAPTER 6

Middle Atmosphere data intercomparison

Several satellite instruments have been measuring the entire mesosphere to produce global maps of temperature and trace constituents of this region for a variety of reasons such as radiative balance estimates, meteorological and climatological requirements, dynamical studies, etc [Beig, 2002].

Furthermore, mesospheric datasets are becoming important to the climate change debate because its predicted impact [Roble and Dickinson, 1989] will be of a greater magnitude and detectable sooner that at tropospheric altitudes. However, before applying these data to any further analysis, it is important to have an idea of their quality. The purpose of this chapter is to compare the different datasets of the current instruments measuring at least part of the mesosphere against the MIPAS middle atmosphere (MA) mode retrievals using MORSE.

In general three approaches are used when comparing different satellite datasets: (1) Comparisons of zonal means over daily or seasonal timescales, (2) Comparisons of almost coincident profiles from two datasets which implies the definition of a window in time and space and (3) Comparisons of profiles with a broader time – space window using a model to map one profile (time and location) into the other (known as the data assimilation technique).

The comparisons presented here use the first approach (daily zonal means and zonal sections) to easily gain an idea of the state of the data and the second to corroborate the conclusions drawn from the first.

6.1 Considerations

Comparisons for all the MIPAS MA products were made against most of the mesospheric instruments (MLS, OSIRIS, SMR, SABER, HIRDLS, SOFIE, ACE and GOMOS) detailed in chapter 3 to verify the quality of the datasets. The parameters compared for each instrument are listed in table 6.1.

Table 6.1: Parameters compared for each instrument. The question mark symbols are used for products that are either under development, or not yet public.

	Tem	H_2O	O_3	HNO_3	CH_4	N_2O	NO_2	CO
MIPAS	Y	Y	Y	Y	Y	Y	Y	Y
MLS	Y	Y	Y	Y		Y		Y
OSIRIS			Y				Y	
SMR	Y	?	Y					?
SABER	Y		Y					
HIRDLS	Y	?	Y	Y	?	?	?	
SOFIE	Y	Y	Y		Y			
ACE	Y	Y	Y	Y	Y	Y	Y	Y
GOMOS	?	?	Y					

Figure 6.1 displays a timeline of these satellite observations. Note that this timeline was built on the basis that only one day of data was needed through the corresponding month to consider that there was data available on that particular month. Also, note that although the MIPAS measurements are available since 2002, in this thesis the data used is the middle atmosphere observations only available since 2005 and regularly (around 3 days per month) since April 2007. The days used in these comparisons are listed in Table 6.2.

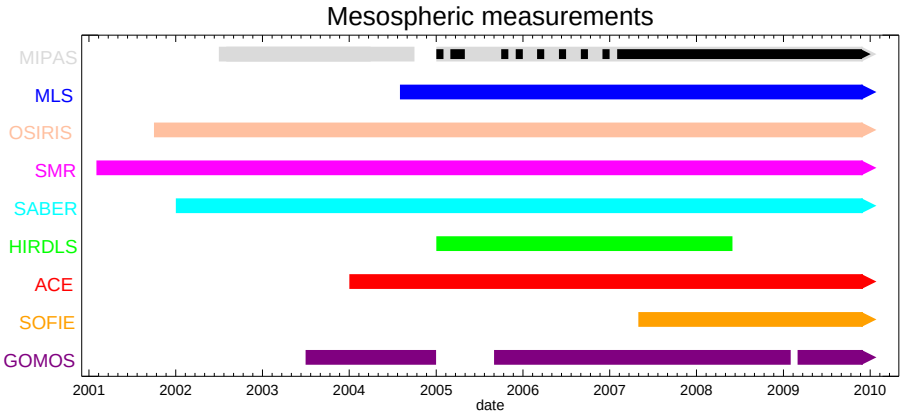

Figure 6.1: Timeline of satellite mesospheric measurements. The arrows indicate that the instruments are currently (December 2009) collecting data. The gray timeline displays the availability of the MIPAS nominal viewing mode which extends up to the lower mesosphere. The black timeline displays the availability of the MIPAS MA viewing mode data here discussed.

Each of the comparisons is structured in three parts:

Table 6.2: MIPAS MA viewing mode days used in the comparisons.

20070412	20070824	20080225	20080814	20081202
20070422	20070903	20080306	20080824	20081212
20070504	20070913	20080316	20080903	20081222
20070514	20071003	20080326	20080923	20090101
20070525	20071104	20080603	20081003	20090111
20070607	20071209	20080616	20081013	20090205
20070622	20071229	20080625	20081023	20090215
20070725	20080108	20080715	20081102	20090225
20070804	20080126	20080725	20081112	20090307
20070814	20080215	20080804	20081122	

(1) For each limb viewing satellite, the zonal mean of the corresponding parameter for the 7th June 2007 will be shown. This date was selected because all the instruments offered almost complete global coverage. Their relative difference or their percentage difference will also be shown depending on whether the comparisons are for temperature or for gas concentration respectively. As a reference, the zonal mean derived from climatology will be displayed.

Figure 6.2 shows the geographical coverage for the 7th June 2007 of each of the limb viewing instruments used in these comparisons.

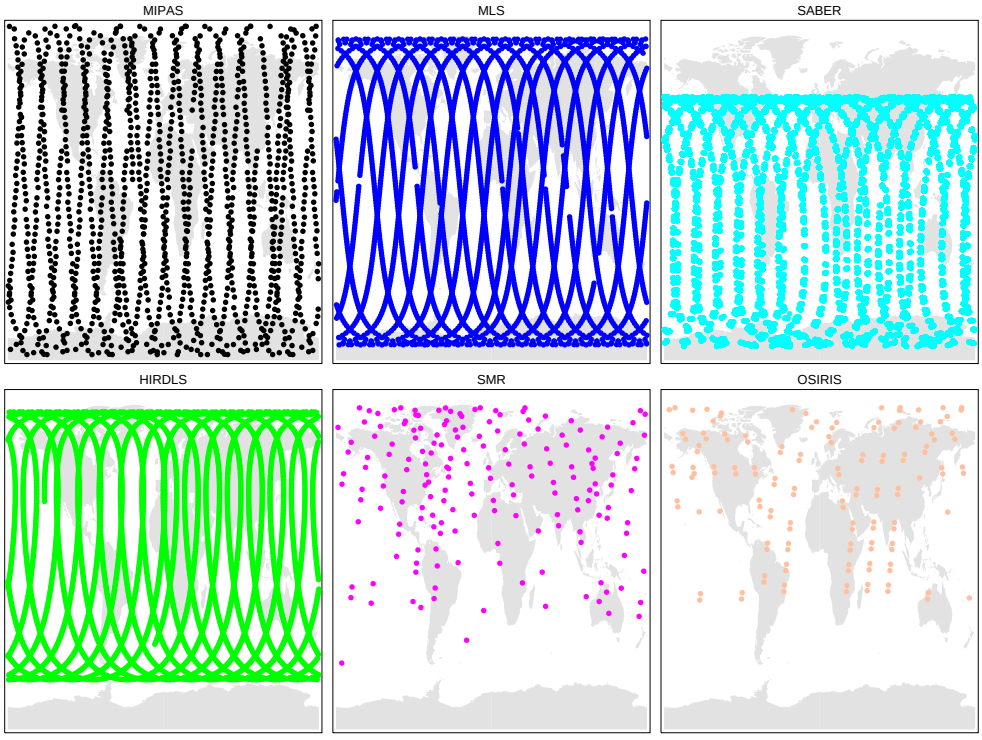

Figure 6.2: Geographical coverage of the limb viewing instruments for the 7th June 2007.

(2) For each solar occultation satellite (ACE and SOFIE), a zonal section of the corresponding

parameter for the 15th of July 2008[1] will be shown for the winter hemisphere rather than for the summer hemisphere since there is more zonal structure due to planetary waves. On this date data from all sunrise/sunset occultations were available which ensures that these measurements spread over the whole longitude circle in order to provide a complete zonal section. As for the zonal mean plots, their relative difference or their percentage difference depending on whether the comparisons are for temperature or for gas concentration are displayed. Figure 6.3 shows the geographical coverage for the 15th of July 2008.

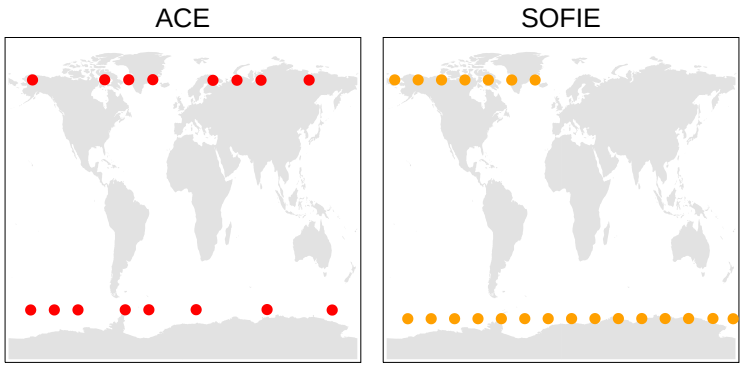

Figure 6.3: Geographical coverage of the solar occultation instruments for the 15th July 2008.

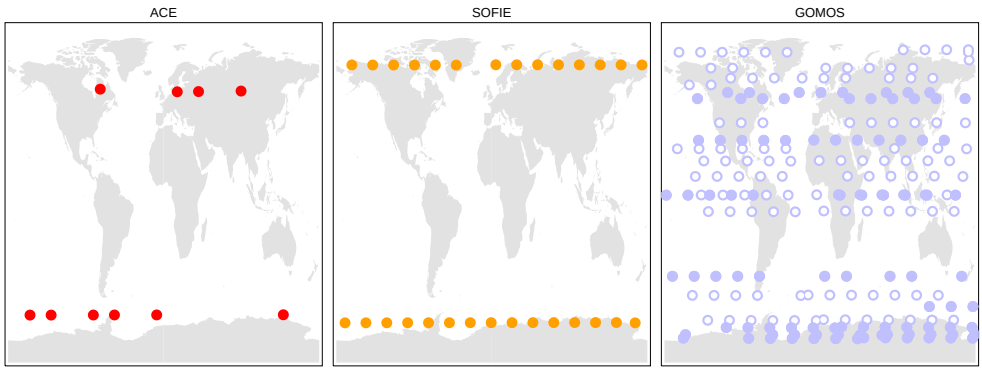

Figure 6.4: Geographical coverage of the solar/star occultation instruments for the 25th July 2007. In the GOMOS subplot open circles corresponds to measurements of faint stars (magnitudes greater than 2) while closed circles corresponds to bright stars (magnitudes lower than 2).

For the O_3 comparison a zonal section for the 25th of July 2007 will be shown because these were no GOMOS measurements on the 15th of July 2008. This date offers GOMOS measurements of bright stars in a suitable latitude range. Figure 6.4 shows the geographical coverage for the 25th of July 2007. Note that this date is only used for the O_3 comparison due to the ACE lack of complete longitudinal coverage. For the rest of the comparisons (temperature, H_2O, ...) the 15th of July 2008 is used instead.

[1]This date is not used for the limb sounder zonal mean comparison because HIRDLS data is not available for that day.

In addition to the occultation instruments, a zonal section of MIPAS and MLS will be shown for comparison. MLS was chosen among the other instruments because, as can be seen in Table 6.1, it offers more overlapping among the species compared considering only officially released products and because it is generally considered to be of reliable quality.

(3) The last graph shown for each parameter is a seasonal comparison of coincident profiles between the MIPAS dataset and all the other instruments. For these comparisons, two profiles are considered to be coincident if they are within a 500 km radius and 6 hours. The seasonal bins compared correspond to latitude bins between 90 S–50 S, 20 S–20 N and 50 N–90 N and sorted into winter, equatorial and summer according to the date of the profile. These bins were selected to try to cover the full range of atmospheric variability.

In addition to the seasonal biases, these comparisons also show the standard deviation of the profiles compared to gain an idea of the variability in the data. Furthermore, the MIPAS expected systematic and random errors are shown. These expected systematic and random errors are those computed as part of the microwindows selection as described and processed by Dudhia et al. [2002]. Under this scheme, the random errors refer to the locally correlated (due to the apodization of the spectra) component of the measurement error, while the systematic errors refer to other sources of errors such as: climatological variability, uncertainties in the retrieved temperature and pressure, uncertainties in the radiometric gain, spectral calibration, spectroscopics uncertainties and deficiencies in the forward model (horizontal temperature gradients, nonLTE emissions and CO_2 line mixing).

To asses the magnitude of the bias as well as the magnitude of the observed scatter, the expected climatological variability of the atmospheric parameter compared is shown. These variabilities are those given in the IG2 climatology [Remedios et al., 2007] (more information in section 6.2.10).

Before averaging, all the retrieved profiles were interpolated to the pressure grid, p, given by,

$$p = \frac{10^{i/12}}{100}[hPa] \tag{6.1}$$

where $i = 0, \ldots 48$ in one step increments.

Note that for each instrument, all the data were used except where user guidelines were provided.

6.2 Data Sources

6.2.1 MORSE

The MORSE retrievals used here are those processed by Dudhia [2002*b*] which correspond to MORSE version 1.0. These data can be downloaded from:

`ftp://ftp.atm.ox.ac.uk/pub/user/dudhia/mipl2/`

These data are stored as IDL sav files (one file per day) and can be ingested into IDL by simply using the "restore" function.

Note that the MIPAS MA scenes where the measurements have not significantly improved the *a priori* uncertainty were masked out. This implies that, even though the MIPAS MA retrievals extend to about 0.01 hPa, for some molecules there is not enough information in the radiances to achieve retrievals without significant *a priori* contribution at these high altitudes.

6.2.2 HIRDLS

The HIRDLS products used here correspond to version 4 (also called version 2.09.14). Temperature, O_3 and HNO_3 have been validated [Gille et al., 2008; Kinnison et al., 2008; Nardi et al., 2008] and are the only official products of this version, the rest of the species are work in progress. These data are publicly available and can be downloaded from:

`http://mirador.gsfc.nasa.gov/index.shtml`

It is in the Hierarchical Data Format Release 5 (HDF5) and there are routines available for ingesting and analyzing the data. Routines to ingest AURA data (HIRDLS, MLS, TES and OMI) into IDL or Fortran are available from:

`http://www.eos.ucar.edu/hirdls/data/access.shtml`

6.2.3 MLS

The MLS geophysical products used here correspond to version 2.2 [Livesey et al., 2006] following the usage guidelines described in the data quality document [Livesey, 2007]. HNO_3, CO, H_2O, O_3 and temperature have been subject to an extensive validation [Santee et al., 2007; Pumphrey et al., 2007; Barnes et al., 2008; Froidevaux et al., 2008; Schwartz et al., 2008].

These data are publicly available and can be download from the same webpage as the HIRDLS data. It is also in the HDF5 file format. Note that the HIRDLS ingest routines also read MLS data.

6.2.4 SABER

Although version 1.6 has been validated [Remsberg et al., 2003], Version 1.7 includes nonLTE processes in the retrieval algorithm leading to, presumably, more accurate results and hence the SABER products used here correspond to the new version.

These data are publicly available and can be downloaded from:

`http://saber.gats-inc.com/`

It is in the Network Common Data Form (NetCDF) and there are built-in routines in IDL and MATLAB to ingest it.

6.2.5 SMR

The SMR products used here correspond to version 2.1. Note that only products of the summer mesosphere viewing mode are used because these viewing mode was designed to extend into most of the mesosphere and pressure is retrieved which made the comparisons straightforward.

These data can by downloaded after registration from:

`http://odin.rss.chalmers.se/`

It is formatted in the Hierarchical Data Format - Earth Observing System (HDF-EOS) format and routines for ingesting this data into IDL and MATLAB are also provided in the same webpage.

6.2.6 OSIRIS

The OSIRIS products used here are those processed by the Saskatoon algorithm [Bourassa et al., 2008]. This algorithm does not report pressure but rather altitude. For the comparisons these altitudes are converted into pressure by converting them first into geopotential height using the relation given by Houghton [1986] and interpolating them to pressure using the CIRA-86 geopotential height climatology.

These data can be downloaded with previous registration at:

`http://eopi.esa.int/esa/esa`

It is saved in the HDF5 format and it can be ingested by the routines to ingest AURA data.

6.2.7 SOFIE

The SOFIE products used here correspond to version 1.022 [Gordley et al., 2009]. These data are publicly available and can be downloaded from:

http://sofie.gats-inc.com/sofie/index.php

It is saved in the NetCDF format and an IDL ingestion routine is provided on the same webpage.

6.2.8 ACE

The ACE products used here correspond to version 2.2 (and for Ozone version 2.2 updated) following the usage guidelines described in the file format level 2 description document [Walker et al., 2006].

These data are only available to the ACE science team and authorized users. The ACE data (version 1.0) is available from:

http://www.ace.uwaterloo.ca/data.html

6.2.9 GOMOS

The GOMOS products used here correspond to the software version 5.00. As explained in section 3.3 the quality of these data varies according to the star observed. In this comparison, in order to ensure good quality data, only bright stars (magnitude lower than 2.0) were used.

These data can be downloaded with previous registration at:

http://eopi.esa.int/esa/esa

These data can be ingested with the Basic Envisat Atmospheric Toolbox (BEAT) available for downloading at:

http://www.stcorp.nl/beat/

Unfortunately for the days here compared only O_3 data was available.

6.2.10 Climatology

Two climatologies are used in these comparisons. The first, used only for the temperature comparison, is the COSPAR International Reference Atmosphere (CIRA-86) which provides empirical models of atmospheric temperature as recommended by the Committee on Space Research (COSPAR) [CIRA, 1988]. The second, used for the trace gas concentrations comparisons, is the IG2 seasonal climatology for MIPAS produced by Remedios et al. [2007]. This climatology is used as initial guess (IG) in the ESA operational and the MORSE retrieval schemes.

CIRA-86 climatology is used for temperature because it is a more detailed climatology (monthly 5° latitude resolution rather than 4 seasons and 6 latitude bands). As can be appreciated in Figure 6.5, it also resembles more the expected thermal structure of the atmosphere. For a direct comparison against observations see Figure 6.6

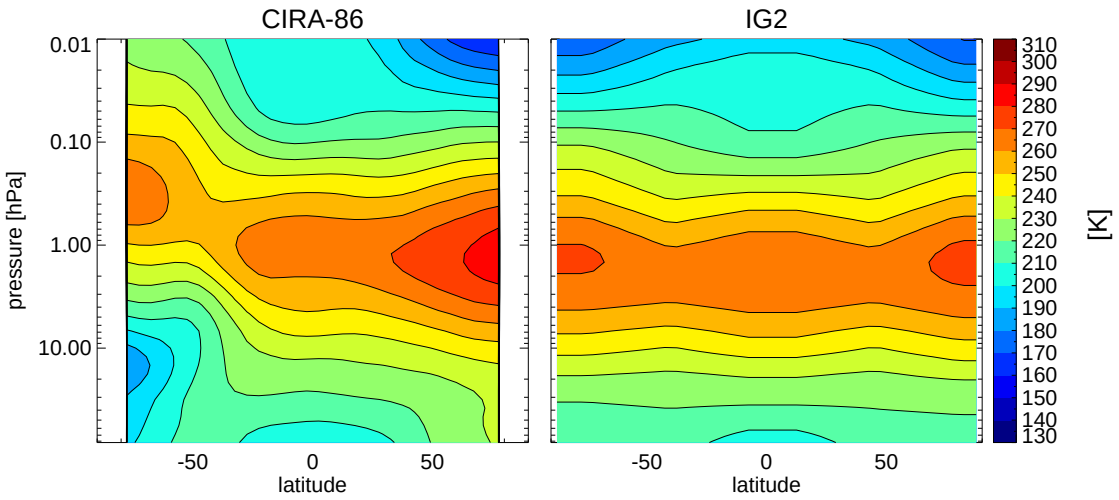

Figure 6.5: Temperature values for June for the CIRA-86 and the IG2 climatologies showing inconsistencies particularly in the winter pole (< 50S).

6.3 Temperature comparison

Figure 6.6 displays temperature zonal mean profiles of MIPAS, MLS, SABER, HIRDLS, SMR and climatology data. As can be seen, the absolute values of the observations resemble the structure found in the CIRA-86 climatology with a higher stratopause over the winter pole ($< 50°$S for this particular day) and extremely cold temperatures in the upper mesosphere around the summer pole ($> 50°$N).

The difference subplots show that, for pressure levels greater than 5 hPa, the difference between the datasets is relatively small. For smaller pressures, the MIPAS$-$MLS shows a series of maxima and minima (also hinted in the HIRDLS differences), the MIPAS$-$SMR difference presumably shows an overestimation of the temperature by the SMR dataset. The other recurrent difference in most of the comparisons is the MIPAS overestimation of the summer polar mesopause temperatures.

Figure 6.7 displays a temperature zonal section for the winter hemisphere for the ACE, SOFIE, MLS and MIPAS data. As can be seen in the absolute plots, the ACE, MLS and MIPAS observations agree in the temperature structure of the zonal section with a maximum around 50E and 0.2hPa. As shown in the difference subplots, there is more variability in these differences than in the zonal mean differences. These large differences are probably induced by planetary waves.

Figure 6.8 shows temperature seasonal comparisons of coincident profiles between MIPAS and the other satellites, as well as the standard deviation (the 1-σ scatter) of such comparisons. The first thing to note is that all the biases are between the expected temperature variability implying that all are carrying new information about the state of the atmosphere.

Most of the biases encountered in the winter bin are between a 3 K difference at all pressure levels,

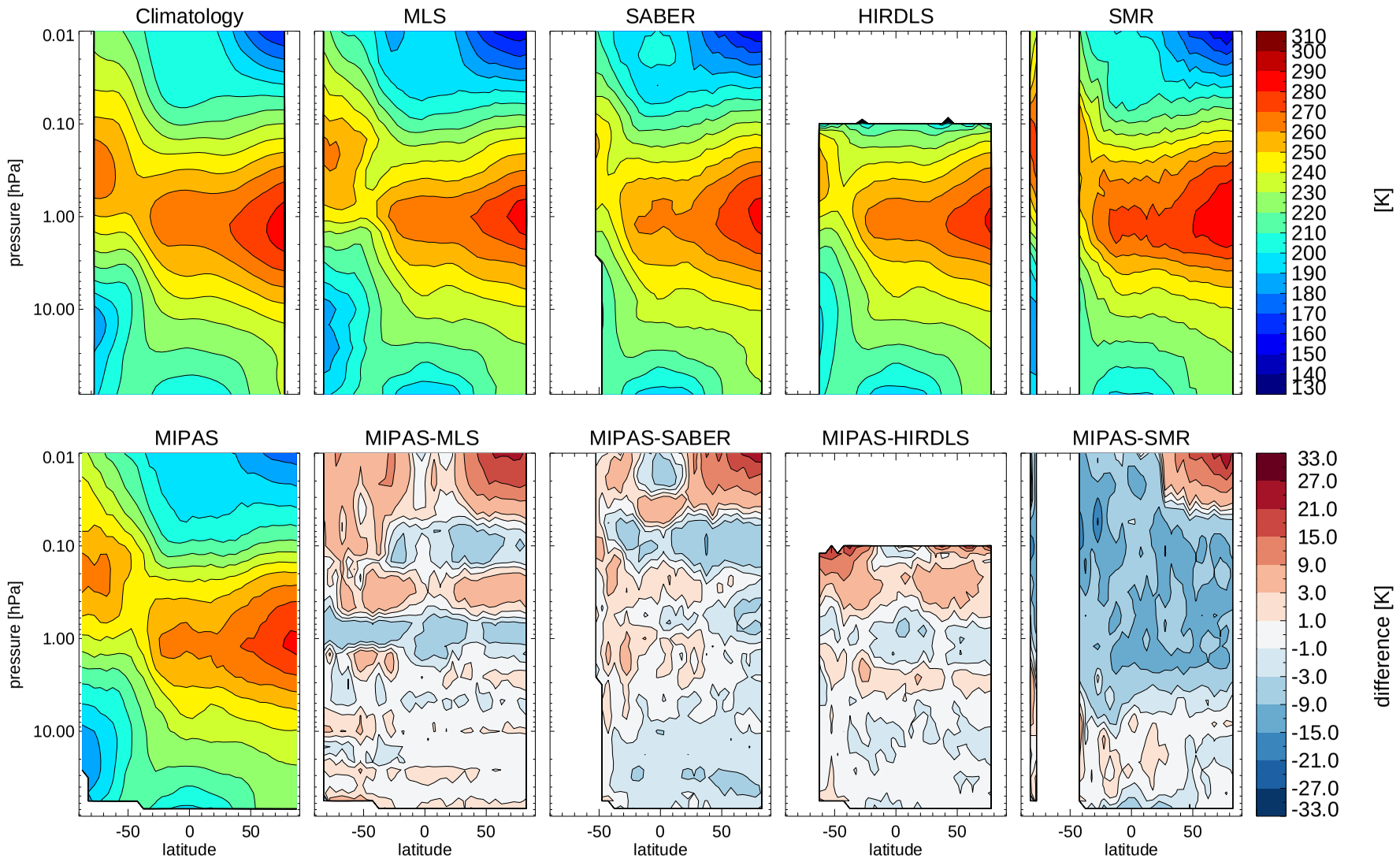

Figure 6.6: Temperature zonal mean for the 7th June 2007 from different satellites. The top row displays all the data sources (except MIPAS) while the bottom row displays the MIPAS results as well as the absolute difference between the observations (MIPAS − satellite). Note that the contours in the difference subplots are not equally spaced.

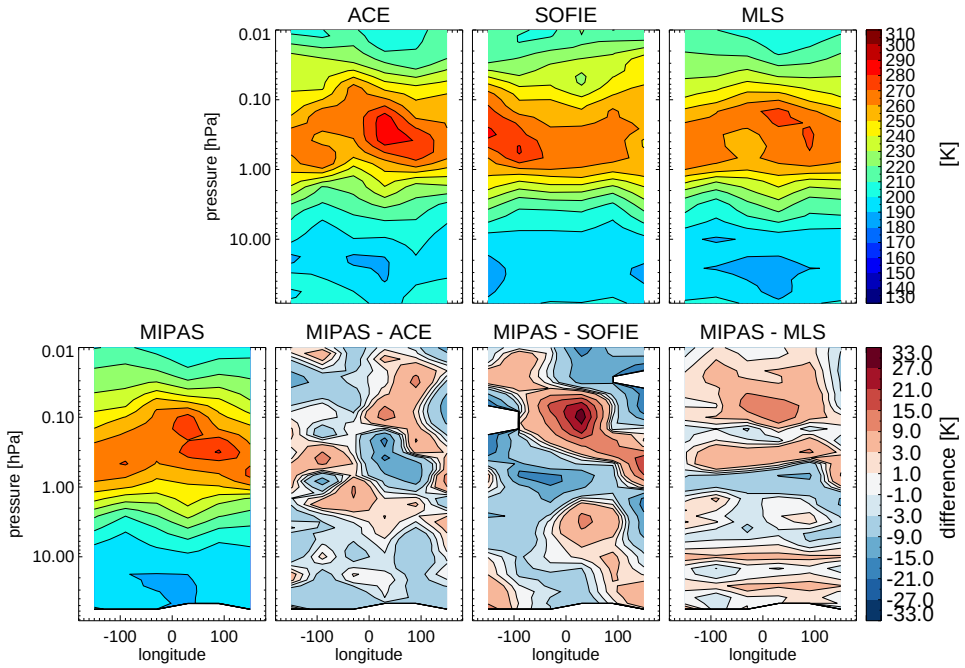

Figure 6.7: Temperature zonal section (southern,i.e. winter hemisphere) for the 15th of July 2008. The top row displays the ACE (62 S), SOFIE (67 S) and MLS (65 S) results while the bottom row displays the MIPAS (65 S) results as well as the absolute difference between the observations. Note that the contours in the difference subplots are not equally spaced.

the MIPAS−SABER comparison being the exception which shows clear anomalies (also shown in the high standard deviation of this comparison). Note that the sharp feature in the MIPAS−HIRDLS is presumably an artifact induced by the Kapton correction algorithm (section 3.2) rather than a real feature (this feature appears in the following HIRDLS comparisons and it will not be commented further) .

The differences encountered in the equator bin are also within 3 K for the three instruments compared in this region. The reason for small number of coincident profiles for each instrument in this bin is because by the nature of the observations it is easier to find temporal matches near the poles where the local solar time changes than near the tropics. Note that although the MIPAS−SABER comparison seems to be normal in this seasonal bin, the standard deviation of this comparison is greater that the one found either in the MIPAS−MLS or MIPAS−HIRDLS comparisons.

As can be seen, the comparisons for the summer bin are not as good as the other two seasonal bins. All these comparisons show differences smaller than 3 K at pressure levels greater than 5 hPa but for lower pressure levels show differences up to 10 K with a clear maximum near 0.1 hPa. Furthermore, the standard deviation at upper mesospheric pressures of these comparisons is the greatest found in the three seasonal bins.

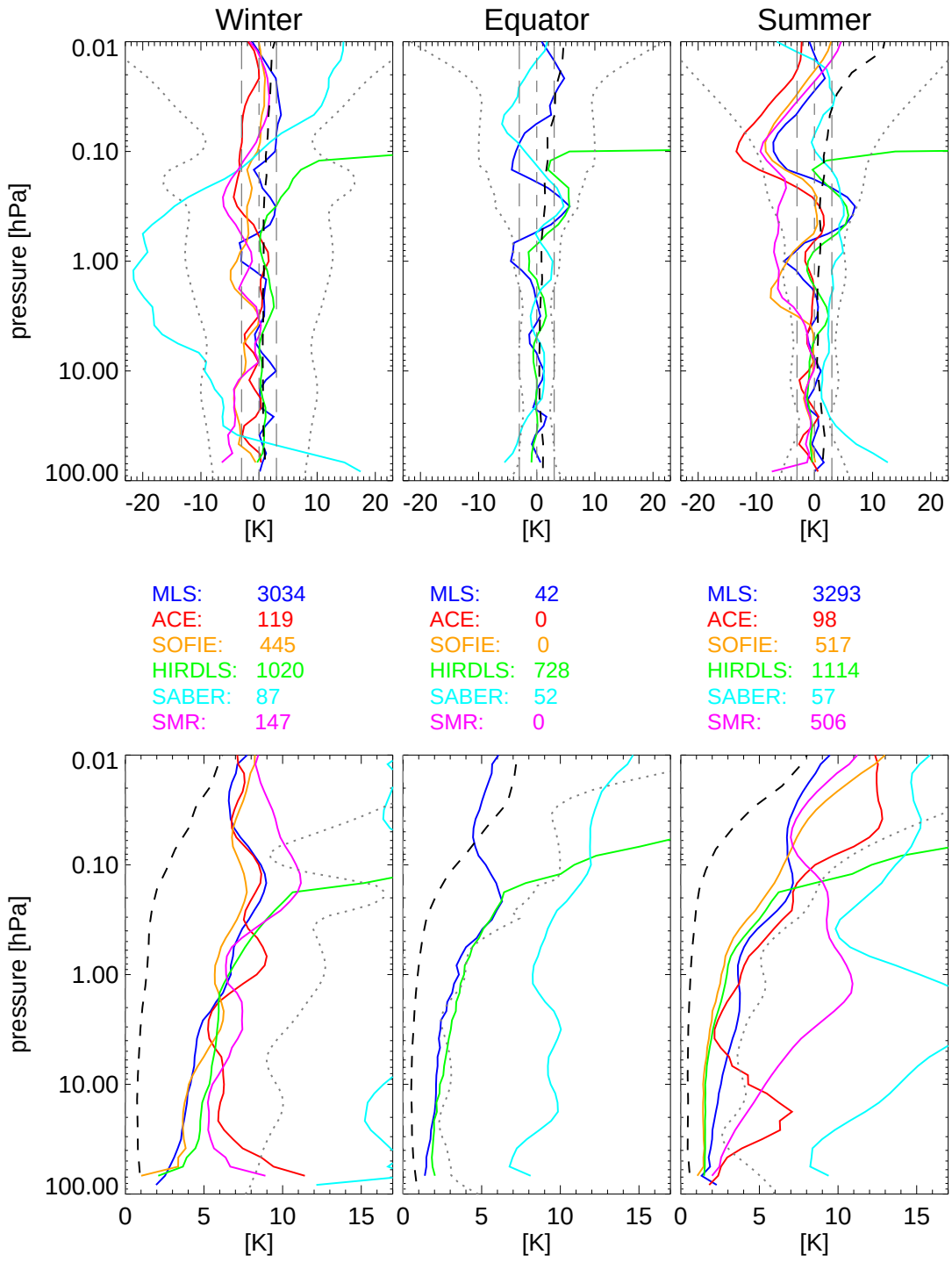

Figure 6.8: Seasonal temperature biases (top) and scatter (bottom) between MIPAS and six datasets (MIPAS−satellite). The gray dotted lines show the expected temperature variability over the corresponding season while the gray dashed line shows a 3 K difference. The dashed black lines display the systematic (top) and the random (bottom) errors expected for the MIPAS measurements. The number of profiles averaged is shown in the middle row. The Winter, Equator and Summer bins correspond to latitudes 90 S−50 S, 20 S−20 N and 50 N−90 N sorted according to the day analyzed.

Temperature conclusions

Comparisons with coincident profiles suggest that MIPAS temperatures are retrieved within a 3 K range difference for pressure levels between 100 and 0.01 hPa under polar winter and equatorial and polar summer conditions, being the only exception an underestimation by up to 15 K around 0.1 hPa for polar summer conditions.

During these comparisons it was also revealed that SABER temperatures present anomalous behaviours under polar winter conditions and that SMR overestimates the temperature between 3 hPa and 0.1 hPa under polar summer conditions by around 7 K.

6.4 H_2O comparison

The H_2O zonal mean comparisons are shown in Figure 6.9. As can be seen, MLS and MIPAS display roughly the same structure for pressures greater than 0.1 hPa, with a gradual increase in stratospheric H_2O peaking between 0.5 hPa and 0.1 hPa over the equator. This behaviour is also shown, although greatly smoothed, in the IG2 climatology. This is consistent with the theory that the principal stratospheric source of water vapour is the oxidation of methane [Brasseur and Solomon, 1986]. Since practically all the the tropospheric water vapour freezes around the cold tropopause and nearly all CH_4 is oxidized for pressures greater than 0.5 hPa (see for instance Figure 6.15) the H_2O peak should appear around this pressure level.

Even though this localized maximum is present in MLS and MIPAS, the MIPAS ($\sim$ 9 pmmv) and MLS ($\sim$ 8 ppmv) retrievals show higher values than climatology ($\sim$ 6 ppmv). Another discrepancy between these two datasets is the MIPAS underestimation of the water vapour concentration around the polar summer mesopause ($> 50°$N). The increase of water vapour around this area is a consequence of the upward transport around the polar summer regions (that also causes the temperature to drop) and therefore the MLS observations may be more valid. This appears in the MIPAS$-$MLS percentage difference as an underestimation of the water vapour for pressures lower than 0.1 hPa for latitude poleward 50°S. This relatively high H_2O concentration over the summer polar region is absent in the IG2 climatology. The HIRDLS and SMR H_2O concentrations seem unrealistic at practically all pressure levels.

The H_2O zonal section (winter hemisphere) for the ACE, SOFIE, MLS and MIPAS datasets is shown in Figure 6.10. The ACE, SOFIE and MLS agree roughly in structure and in magnitudes (as seen in the percentage difference subplots). Note that SOFIE presents some clear anomalies for pres-

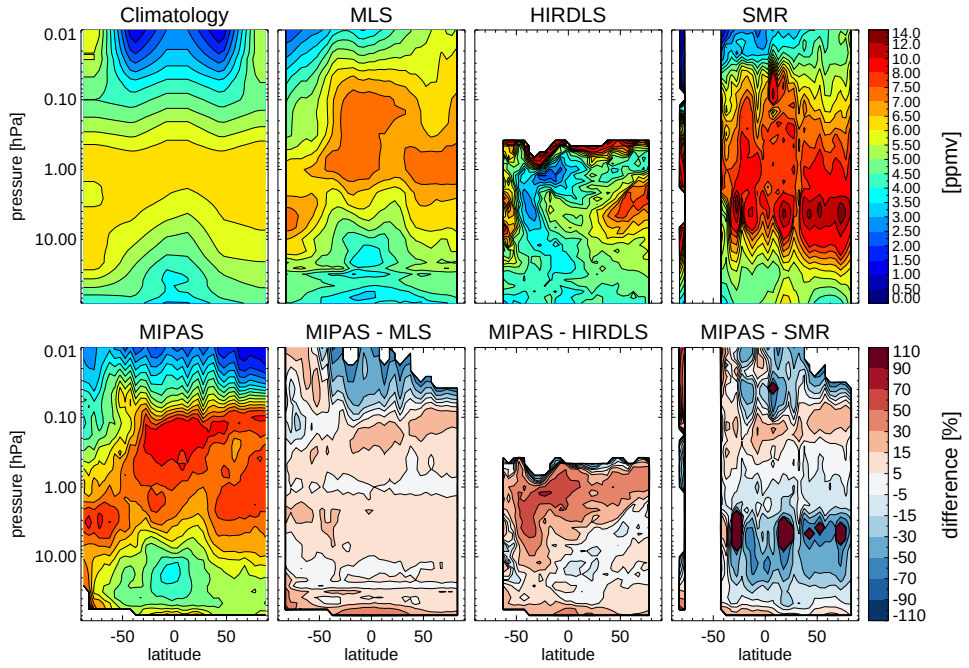

Figure 6.9: H_2O zonal mean for the 7th June 2007 for different instruments. The top row displays all the data sources (except MIPAS) while the bottom row displays the MIPAS results as well as the percentage difference between the observations (MIPAS−satellite). Note that the contours are not equally spaced.

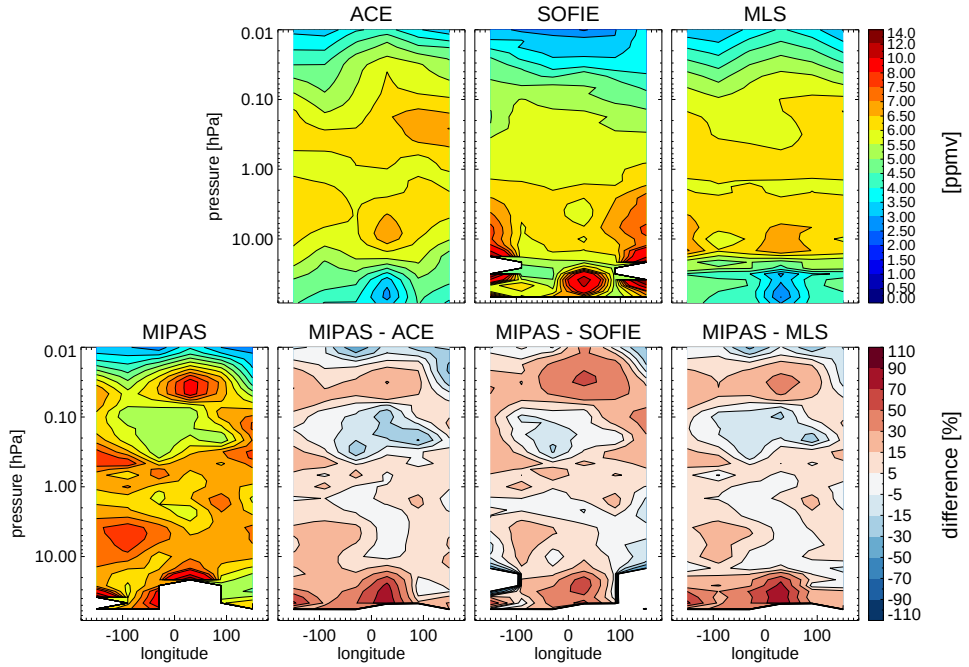

Figure 6.10: H_2O zonal section (southern,i.e. winter hemisphere) for the 15th of July 2008. The top row displays the ACE (62 S), SOFIE (67 S) and MLS (65 S) results while the bottom row displays the MIPAS (65 S) results as well as the percentage difference between the observations. Note that the contours are not equally spaced.

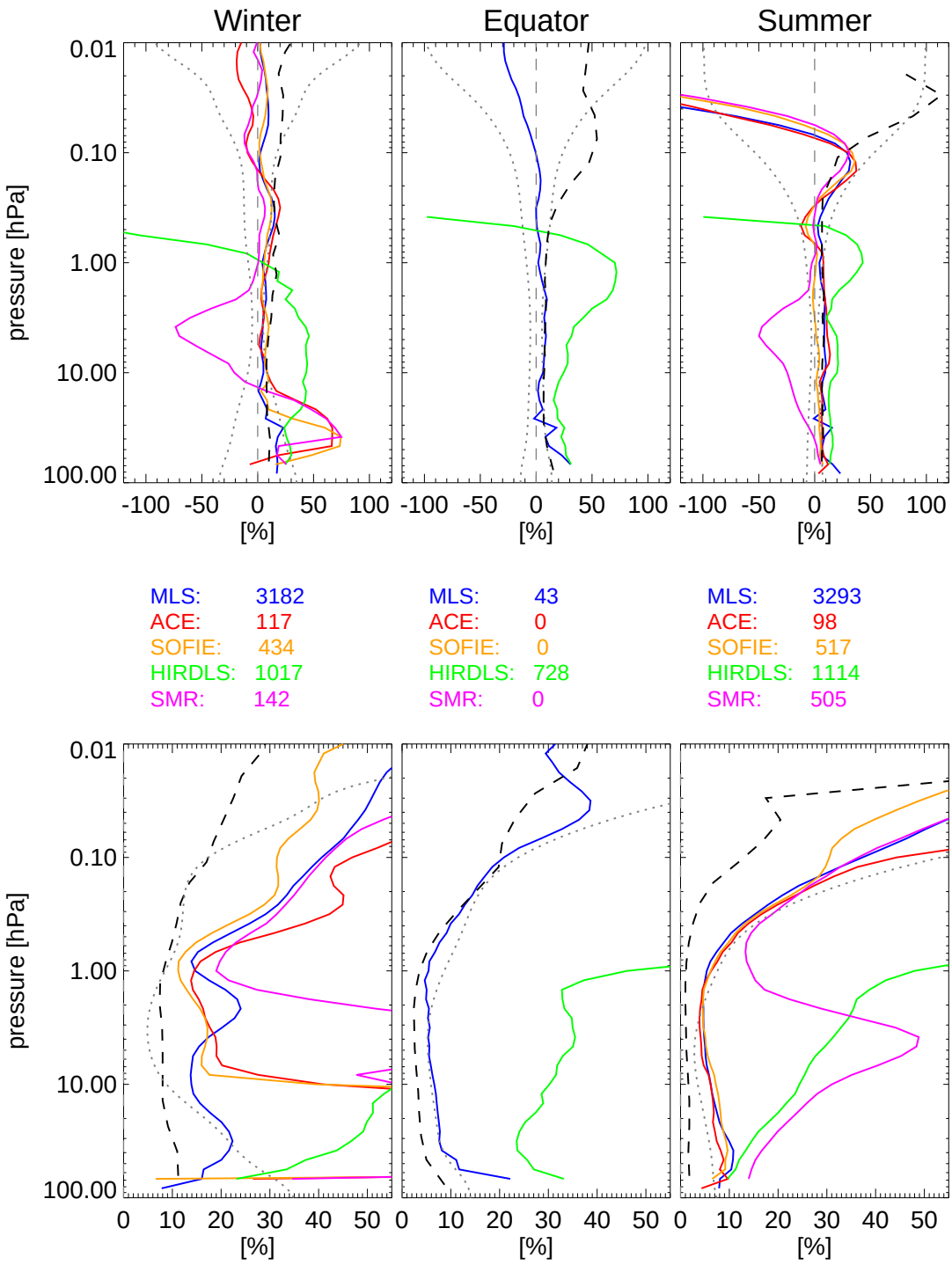

Figure 6.11: Seasonal H_2O biases (top) and scatter (bottom) between MIPAS and five datasets (MIPAS−satellite). The gray dotted lines show the expected H_2O variability over the corresponding season. The dashed black lines display the systematic (top) and the random (bottom) errors expected for the MIPAS measurements. The number of profiles averaged is shown in the middle row. The Winter, Equator and Summer bins correspond to latitudes 90 S−50 S, 20 S−20 N and 50 N−90 N sorted according to the day analyzed.

sure greater than 10hPa. The MIPAS values do not resemble any of the other datasets, the percentage differences show that for most pressure levels, MIPAS is overestimating the H_2O concentrations up to 60%.

Figure 6.11 shows H_2O seasonal comparisons of coincident profiles between MIPAS and the other instruments as well as the standard deviation of such comparisons. Most of the biases displayed in the winter seasonal bin are within the expected variability at most pressure levels, the exceptions being the HIRDLS comparison at all pressure level, the ACE, SOFIE and SMR comparisons for pressures greater than 10 hPa which display an overestimation up to 50% (not shown in the MLS comparison) and the SMR comparison which shows an underestimation up to 75% between 10 and 1 hPa. Outside these ranges the biases shown are within a 20% range even at upper mesospheric pressures.

In the equatorial seasonal bin only coincident profiles for HIRDLS and MLS were found. From among these comparisons only the MLS one is within the expected variability, being the biases less than 10% for pressures greater than 0.1 hPa and up to 30% for smaller pressures.

The MLS, ACE and SOFIE comparisons in the summer seasonal bin show biases within a 10% range difference for pressures greater than 0.2 hPa and for smaller pressures show a clear underestimation by MIPAS of the H_2O concentrations (also shown in the SMR comparison.) This underestimation of the water vapour is probably due to the lack of relatively high values of H_2O in the polar summer climatology (as shown in Figure 6.9) in addition to the constant illumination of the region which may be triggering nonLTE effects not taken into account in the current MIPAS algorithm.

Note that at the three seasonal bins, the MIPAS$-$HIRDLS standard deviation is greater than the other standard deviations implying more variability in the HIRDLS results than in the other datasets.

H_2O conclusions

Comparisons with coincident profiles suggest that MIPAS is retrieving within less than 20% difference range under polar winter equatorial and polar summer conditions for practically all the pressure levels, being the exception the polar summer bin for pressure levels smaller than 0.1hPa where MIPAS is clearly underestimating the H_2O concentration by more than 100%. This underestimation of the water vapour under polar summer conditions is probably due to the lack of a proper *apriori* or due to nonLTE effects.

During these comparisons it was noted that the H_2O IG2 climatology need a revision to more accurately represent the real atmosphere, that the HIRDLS comparisons seem unrealistic, and that SMR is overestimating the H_2O concentration (at least under polar winter and polar summer conditions) by

more than 50% around 4 hPa.

6.5 O_3 comparison

As shown in Figure 6.12, all the O_3 datasets resemble the IG2 climatology with the maximum ozone concentration at the equatorial stratosphere and the decrease toward the poles. In addition, the three datasets show the O_3 ascent in the winter polar region ($<50°$S) not evident in the IG2 climatology.

The difference subplots show that, in general, there is good agreement between MIPAS, MLS, SABER and HIRDLS datasets for pressures greater than 1 hPa. The SMR and OSIRIS comparisons reveal that presumably SMR is underestimating the O_3 concentration at around 10 hPa while OSIRIS is overestimating at pressures greater than 10hPa and underestimating for smaller pressures. For pressures greater than 1hPa there is no agreement between the percentage difference subplots.

When comparing against HIRDLS, SABER and SMR for pressures between 1 hPa and 0.1 hPa there seems to be a clear underestimation of O_3 by MIPAS while for smaller pressures (comparing only against SMR and SABER) it seems to be an overestimation. This overestimation is also present in the MLS comparisons.

The O_3 zonal section (winter hemisphere) for ACE, SOFIE, GOMOS, MLS and MIPAS is shown in Figure 6.13. As can be seen in the percentage difference subplots, the MIPAS results seems to be overestimating the O_3 concentration for pressure levels smaller than 0.1 hPa when comparing to ACE and SOFIE. However, it seems to be underestimating the O_3 concentration when comparing it to GOMOS. For greater pressures, ACE, GOMOS, MLS and MIPAS O_3 concentrations agree roughly in structure as well as in magnitude.

Figure 6.14 shows O_3 seasonal comparisons of coincident profiles between MIPAS and the other instruments as well as the standard deviation of such comparisons. Most of the biases in the winter seasonal bin are within the expected variability being the exceptions the OSIRIS comparisons at all pressure levels, the SABER comparison between 20 and 2 hPa and the GOMOS comparison around 20 hPa. Without considering these exceptions, the biases shown for pressure levels greater than 0.3hPa are within a 20% range difference. For smaller pressures, although all the comparisons indicate an overestimation of the O_3 concentration by MIPAS they do not agree in the magnitude varying from 30 to 70%.

In the equatorial seasonal bin only coincident profiles for MLS, HIRDLS, SABER, OSIRIS and GOMOS were found. From among these comparisons only the MLS, HIRDLS and SABER are

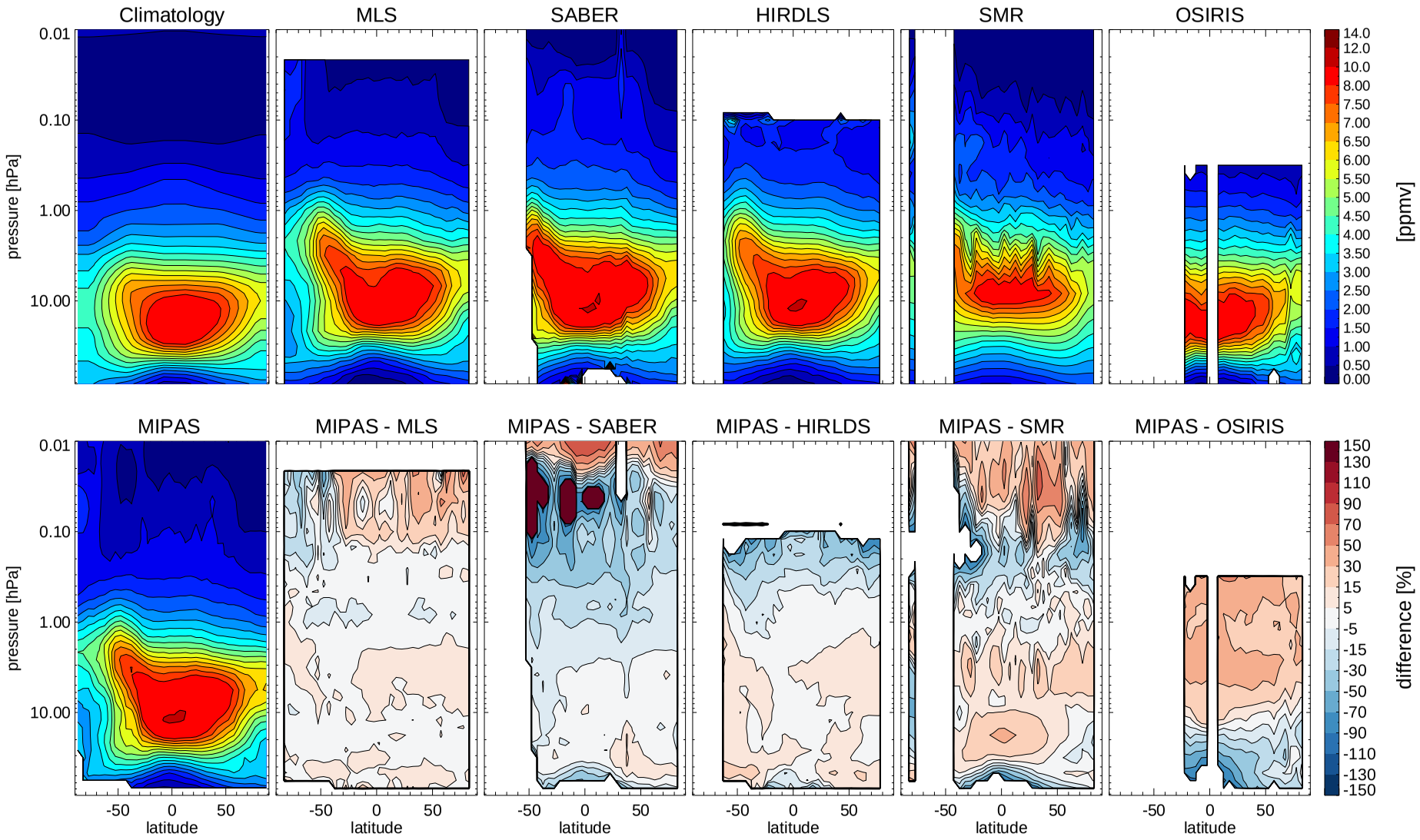

Figure 6.12: O_3 zonal mean for the 7th June 2007 for different instruments. The top row displays all the data sources (except MIPAS) while the bottom row displays the MIPAS results as well as the percentage difference between the observations (MIPAS−satellite). Note that the contours are not equally spaced.

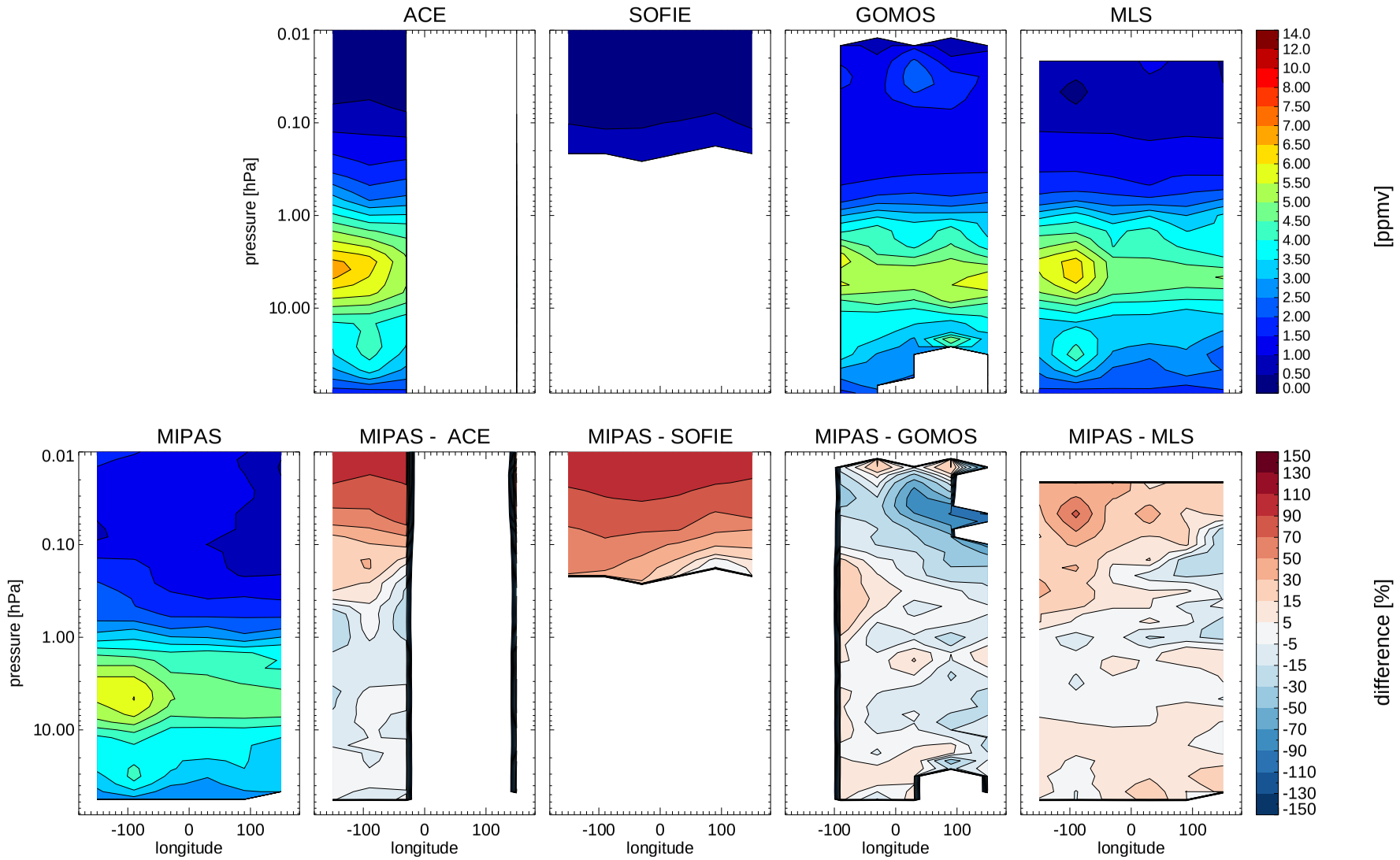

Figure 6.13: O_3 zonal section (southern,i.e. winter hemisphere) for the 25th of July 2007. The top row displays the ACE (64 S), SOFIE (68 S), GOMOS (70 S) and MLS (65 S) results while the bottom row displays the MIPAS (65 S) results as well as the percentage difference between the observations. Note that the contours are not equally spaced.

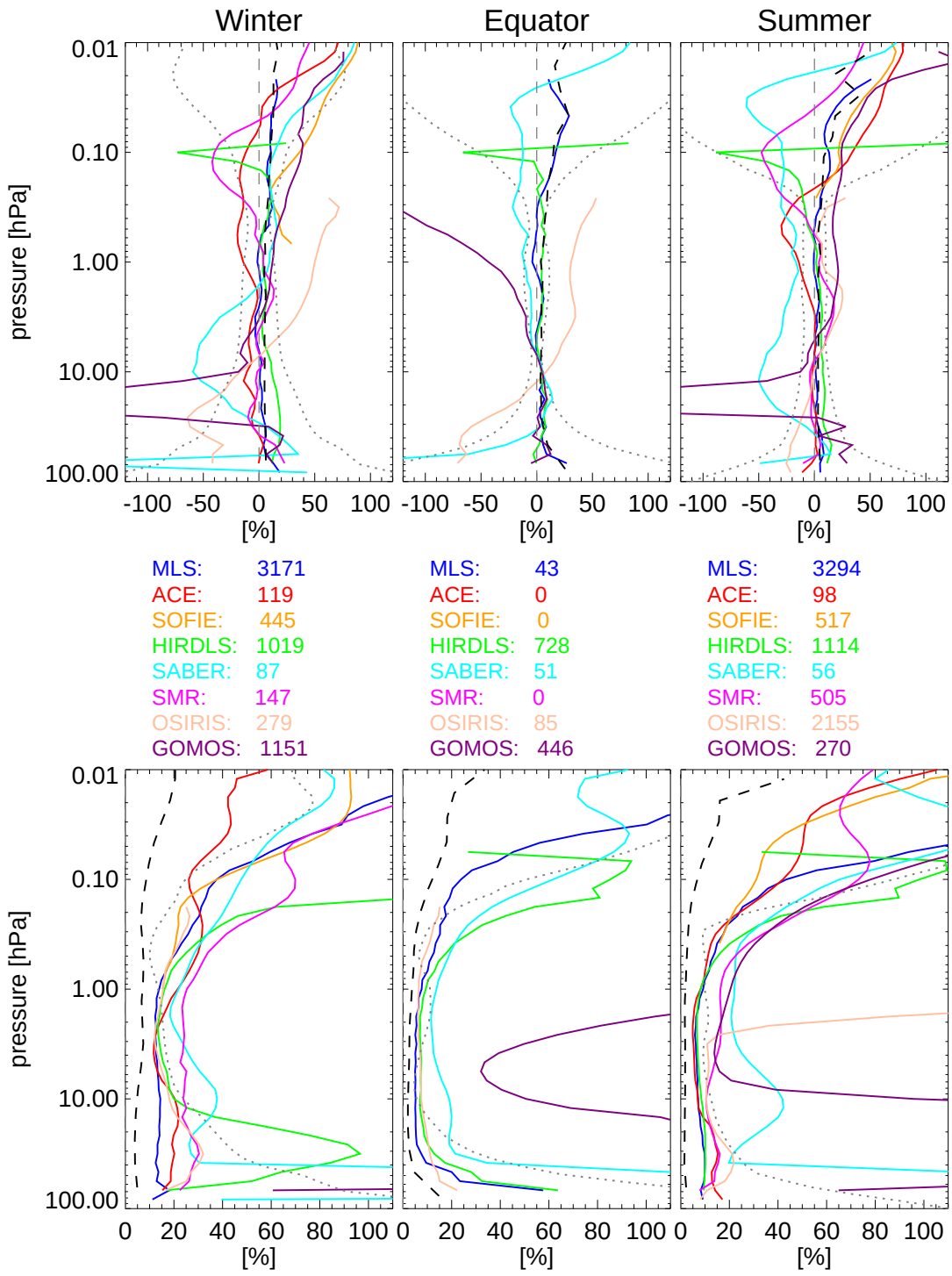

Figure 6.14: Seasonal O_3 biases (top) and scatter (bottom) between MIPAS and eight datasets (MIPAS−satellite). The gray dotted lines show the expected O_3 variability over the corresponding season. The dashed black lines display the systematic (top) and the random (bottom) errors expected for the MIPAS measurements. The number of profiles averaged is shown in the middle row. The Winter, Equator and Summer bins correspond to latitudes 90 S−50 S, 20 S−20 N and 50N−90N sorted according to the day analyzed.

within the expected variability and, furthermore, within a 20% range difference for pressure levels greater than 0.02hPa. For smaller pressures only SABER comparisons were available and therefore no conclusions were drawn.

Most of the biases displayed in the summer seasonal bin are within expected variability being the exceptions the SABER comparison for pressures greater than 0.2 hPa and the GOMOS comparison around 20 hPa. Disregarding these exceptions, the rest of the biases are within a 20% difference for pressures greater than 0.1 hPa. For smaller pressures, as in the winter seasonal bin, it seems that MIPAS is overestimating the O_3 concentration varying the magnitude of this bias from 30% to 70%.

O_3 conclusions

Comparisons with coincident profiles suggest that MIPAS is retrieving within a 20% range for pressures between 100 and 0.1 hPa under polar winter, equatorial and polar summer conditions. For pressure smaller than 0.1 hPa MIPAS seems to overestimate the O_3 concentration varying the magnitude of this bias from 30% to 70% depending on the dataset compared.

During these comparisons it was noted that the OSIRIS comparisons are non-physical, that the GOMOS data present an anomaly around 20 hPa for polar conditions and that it overestimates the O_3 concentration under equatorial conditions by more than 100%.

6.6 CH_4 comparison

Figure 6.15 displays the CH_4 zonal mean comparisons (for this molecule only MIPAS, HIRDLS and climatology). As can be seen, both datasets resemble roughly the same structure found in the IG2 climatology with high values around the equator reflecting the rapid vertical motion of the Hadley cell [Brasseur and Solomon, 1986] and a concentration decrease toward the poles. However, the HIRDLS dataset seems to have extremely high values compared with typical tropospheric concentrations ($\sim$2 ppmv).

The CH_4 zonal section (southern,i.e. winter hemisphere) for ACE, SOFIE and MIPAS is shown in Figure 6.16. As shown in the absolute plots the three datasets displayed seem to agree in structure with decreasing values with height. The percentage difference subplots indicate an underestimation by MIPAS at all pressure levels when comparing against ACE also hinted in the SOFIE comparison.

Figure 6.17 shows CH_4 seasonal comparisons of coincident profiles between MIPAS and HIRDLS, ACE and SOFIE as well as the standard deviation of such comparisons. In the winter seasonal bin,

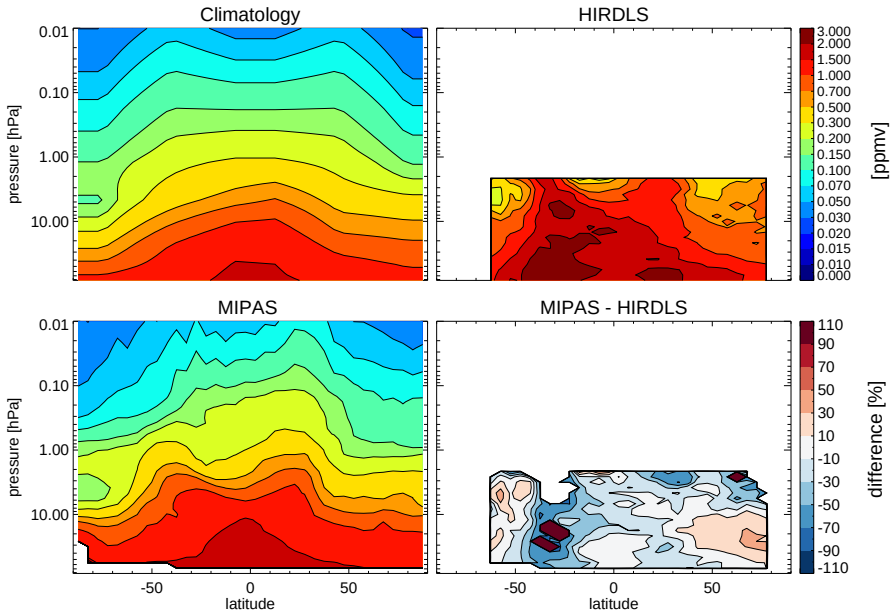

Figure 6.15: CH_4 zonal mean for the 7th June 2007 for two instruments. The top row displays the Climatology and HIRLDS data while the bottom row displays the MIPAS results as well as the percentage difference between the observations (MIPAS−satellite). Note that the absolute subplots are in a semilogarithmic scale to make better use of the colour range.

the three comparisons are within the expected variability at all pressure levels, except for the SOFIE comparison between 20 and 80 hPa. Furthermore, outside this range, the three comparisons are within a 20% difference range for pressure greater than 0.2 hPa. For smaller pressures only comparisons against SOFIE were available and they display either an underestimation by MIPAS or the equivalent overestimation by SOFIE.

Unfortunately in the equatorial seasonal bin, only comparisons against HIRDLS were possible. The bias shown is inside the expected variability which for most of the pressure levels compared (for this comparison only for pressures greater than 2 hPa) is smaller than 20%.

In the summer seasonal bin, the comparisons shown are within the expected variability at all pressure levels and within a 20% difference range for pressure greater than 0.06 hPa. For smaller pressures only comparisons against SOFIE were possible. This comparison indicates, as in the winter bin, an underestimation of the CH_4 concentration by MIPAS (or the equivalent overestimation by SOFIE). However, in this case, the ACE comparison follows closely the SOFIE comparison up to that level suggesting that this bias is due to an underestimation of the CH_4 concentration by MIPAS rather than an overestimation by SOFIE.

Note that at the three seasonal bins, the MIPAS−HIRDLS standard deviation is greater than the other standard deviations implying more variability in the HIRDLS results than in the other datasets.

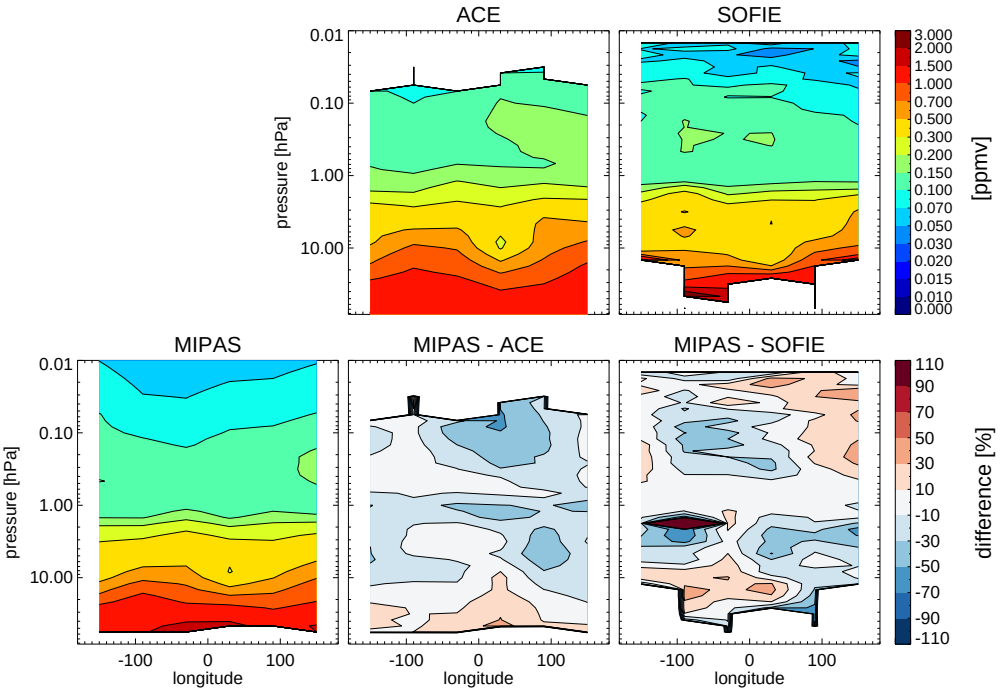

Figure 6.16: CH_4 zonal section (southern, i.e. winter hemisphere) for the 15th of July 2008. The top row displays the ACE (62 S) and SOFIE (67 S) results while the bottom row displays the MIPAS (65 S) results as well as the percentage difference between the observations. Note that the absolute subplots are in a semilogarithmic scale to make better use of the colour range.

CH_4 conclusions

Comparisons with coincident profiles show that MIPAS is retrieving CH_4 concentration within a 20% range difference for pressures between 100 and 0.1 hPa (although it seems that MIPAS CH_4 concentration is at all pressure levels around 20% low). For smaller pressures the comparisons suggest that MIPAS is underestimating the CH_4 concentration particularly under polar summer conditions by more than 100%.

6.7 HNO_3 comparison

The HNO_3 zonal mean comparisons for MIPAS, MLS and HIRDLS are shown in Figure 6.18. The three satellite datasets follow the structure found in the IG2 climatology with low concentrations around the equator and high concentrations around the poles with a maximum over the winter pole. In addition, they also show the denitrification in the winter polar vortex [Santee et al., 2004].

As depicted in the difference subplots, the MIPAS retrievals seem to consistently underestimate the HNO_3 concentrations at all latitudes and pressure levels. This underestimation is more pro-

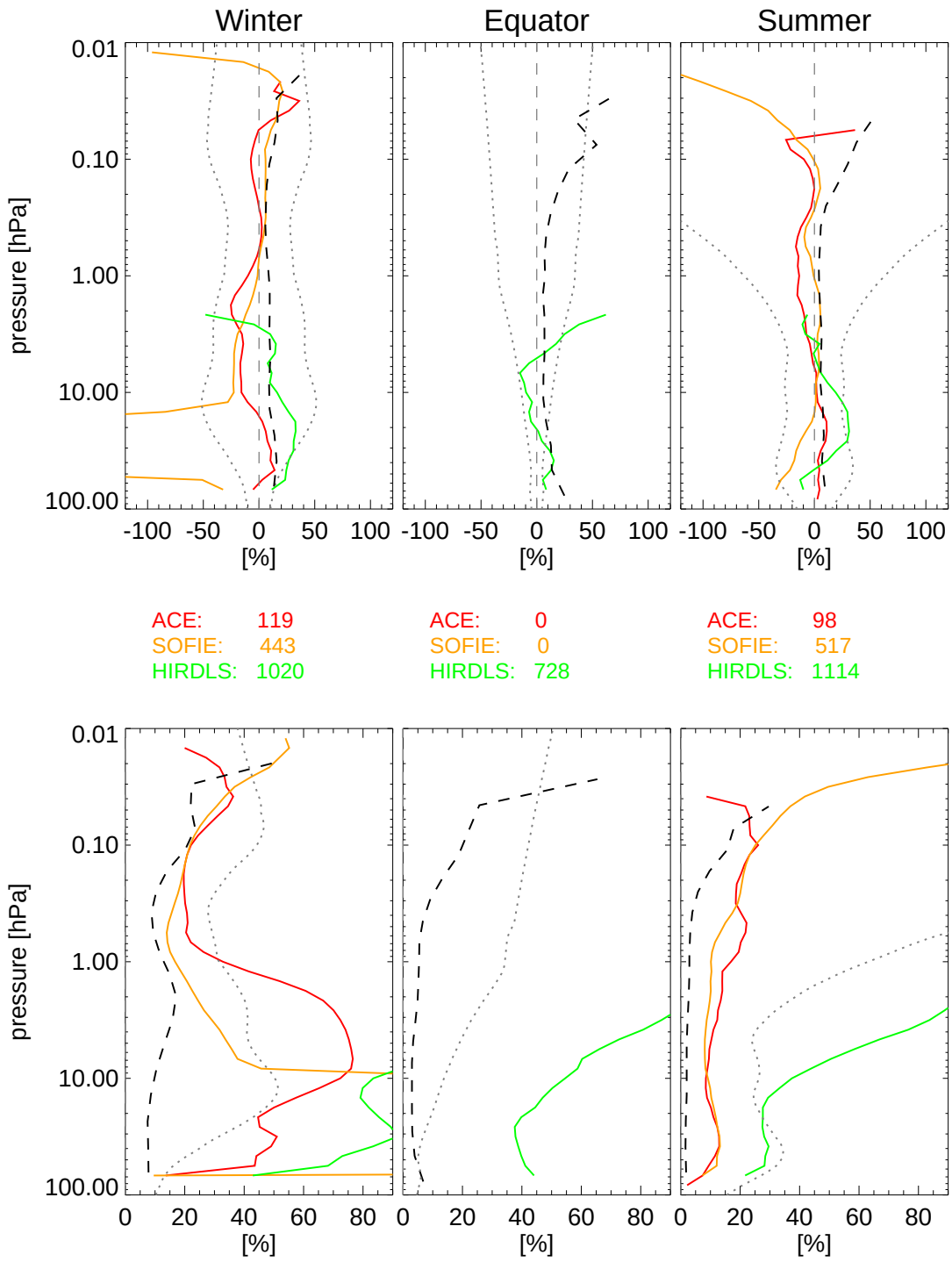

Figure 6.17: Seasonal CH_4 biases (top) and scatter (bottom) between MIPAS and three datasets (MIPAS−satellite). The gray dotted lines show the expected CH_4 variability over the corresponding season. The dashed black lines display the systematic (top) and the random (bottom) errors expected for the MIPAS measurements. The number of profiles averaged is shown in the middle row. The Winter, Equator and Summer bins correspond to latitudes 90 S−50 S, 20 S−20 N and 50 N−90 N sorted according to the day analyzed.

nounced around 10hPa over the equator.

The HNO_3 zonal section (winter hemisphere) for the ACE, MLS and MIPAS datasets is shown in Figure 6.19. As can be seen in the absolute value subplots both satellite instruments present a similar structure and magnitudes for HNO_3 concentrations. As can be seen, while the ACE comparison indicates an underestimation at most pressure levels, the SOFIE comparison indicates an overestimation.

Figure 6.20 shows HNO_3 seasonal comparisons of coincident profiles between MIPAS and MLS, ACE and HIRDLS as well as the standard deviation of such comparisons. Unfortunately, although the MIPAS HNO_3 retrievals extend up to around 0.2 hPa only comparisons up to 3 hPa were possible.

The three biases shown in the winter bin are within the expected variability and furthermore within a 20% difference range. However, inside this margin, the biases does not seem to agree, showing at the smallest pressure level a negative value for the ACE comparison and a positive value for the MLS comparison. In the equatorial seasonal bin, only comparisons against MLS and HIRDLS were possible. Both biases are within the expected variability and within a 20% difference range. In the summer seasonal bin, the three biases shown are within the expected variability and within a 20% difference range. As in the winter seasonal bin, the ACE and MLS bias show opposite trends at the smallest pressure level.

Note that at the three seasonal bins, the MIPAS−HIRDLS standard deviation is greater than the other standard deviations implying more variability in the HIRDLS results than in the other datasets.

HNO_3 conclusions

Although the MIPAS retrievals extend up to 0.2 hPa, comparisons with coincident profiles were only possible between 100 hPa and 3 hPa. Within this pressure range, all of the comparisons are within a 20% range difference. However, inside this margin the biases do not agree and hence no conclusion can be drawn.

6.8 N_2O comparison

The N_2O zonal mean comparisons are shown in Figure 6.21. As shown, in general, the three satellite observations follow the N_2O latitudinal structure found in the IG2 climatology with the maximum concentration in the equatorial stratosphere as with CH_4 (due to the upward transport in this area) and the decrease toward the poles. As shown in the percentage difference subplots, the MLS comparison is practically at all pressure levels within a 20% range difference while the HIRDLS difference shows

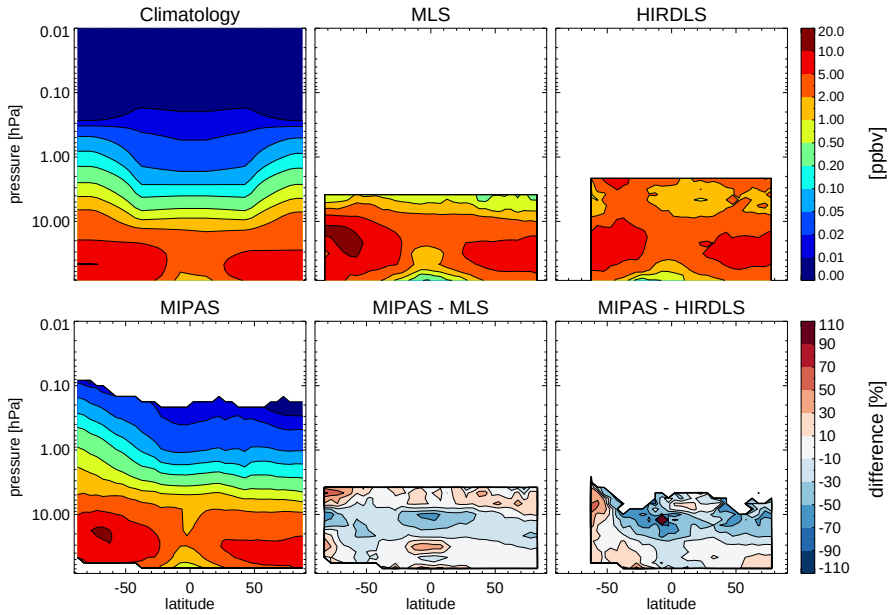

Figure 6.18: HNO_3 zonal mean for the 7th June 2007 for different instruments. The top row displays all the data sources (except MIPAS) while the bottom row displays the MIPAS results as well as the percentage difference between the observations (MIPAS−satellite). Note that the absolute subplots are in a semilogarithmic scale to make better use of the colour range.

values up to 120%.

The N_2O zonal section (winter hemisphere) for the ACE, MLS and MIPAS datasets is shown

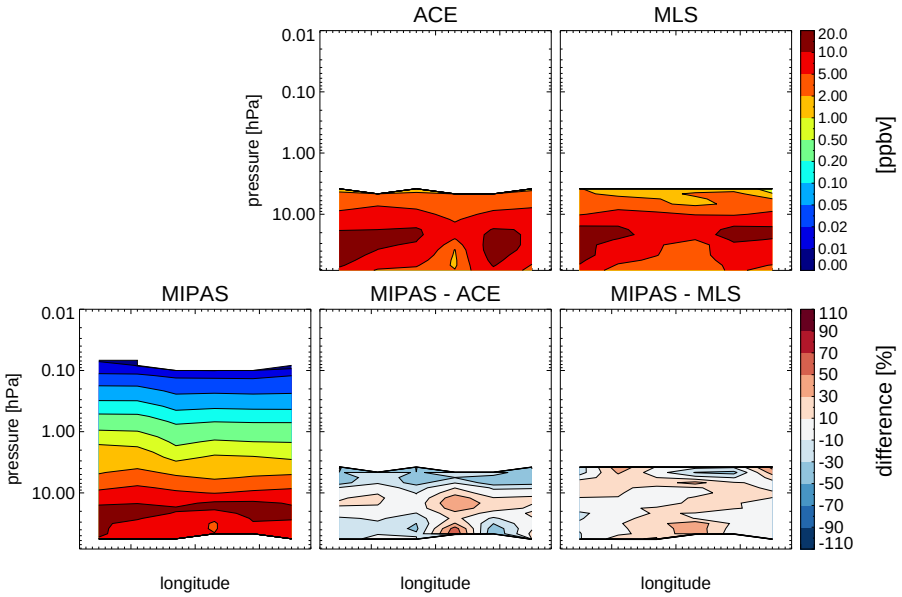

Figure 6.19: HNO_3 zonal section (southern,i.e. winter hemisphere) for the 15th of July 2008. The top row displays the ACE (62 S) and MLS (62 S) results while the bottom row displays the MIPAS (62 S) results as well as the percentage difference between the observations. Note that the absolute subplots are in a semilogarithmic scale to make better use of the colour range.

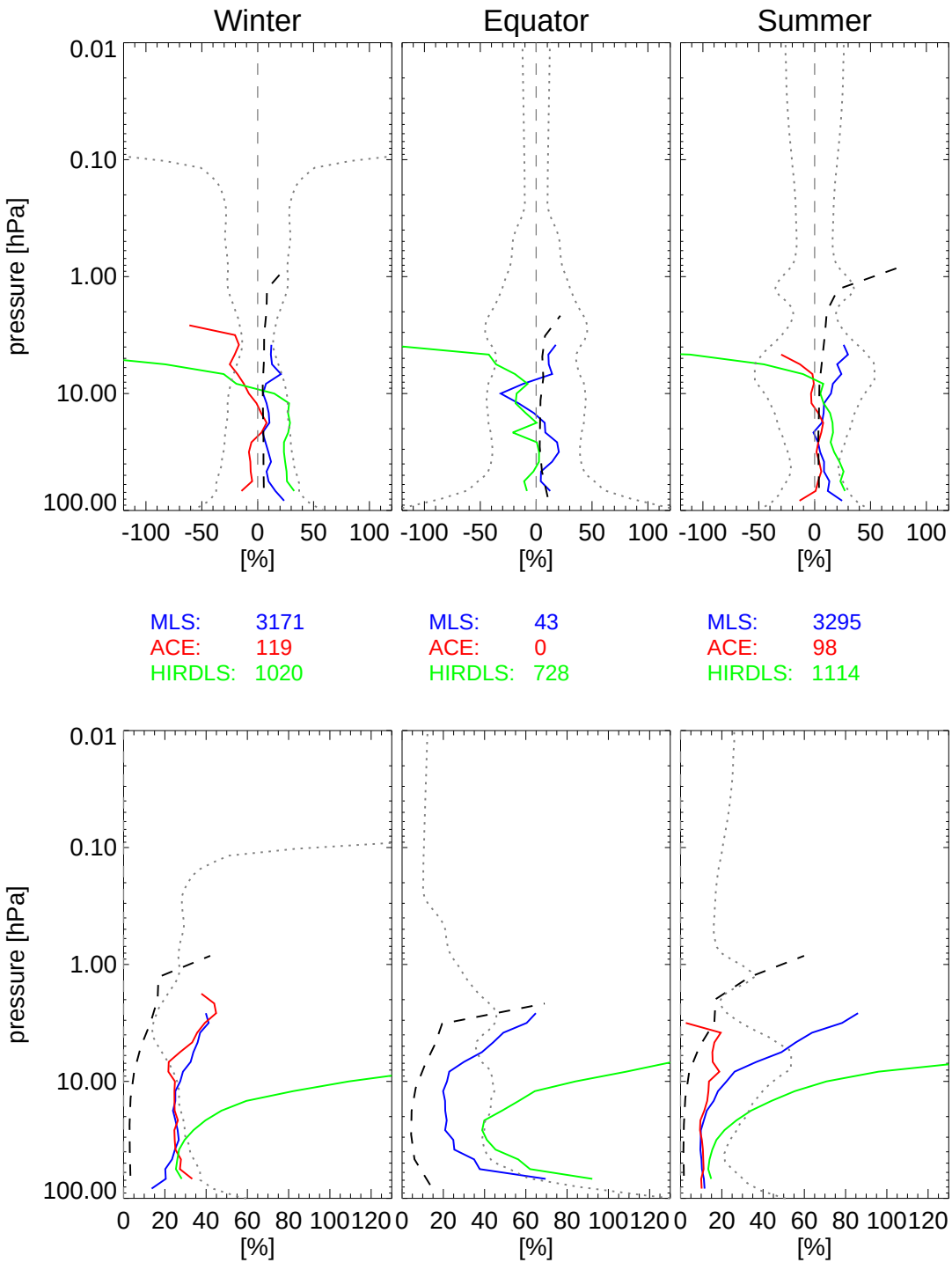

Figure 6.20: Seasonal HNO_3 biases (top) and scatter (bottom) between MIPAS and three datasets (MIPAS−satellite). The gray dotted lines show the expected HNO_3 variability over the corresponding season. The dashed black line (bottom) displays the systematic errors expected for the MIPAS measurements. The number of profiles averaged is shown in the middle row. The Winter, Equator and Summer bins correspond to latitudes 90 S−50 S, 20 S−20 N and 50 N−90 N sorted according to the day analyzed.

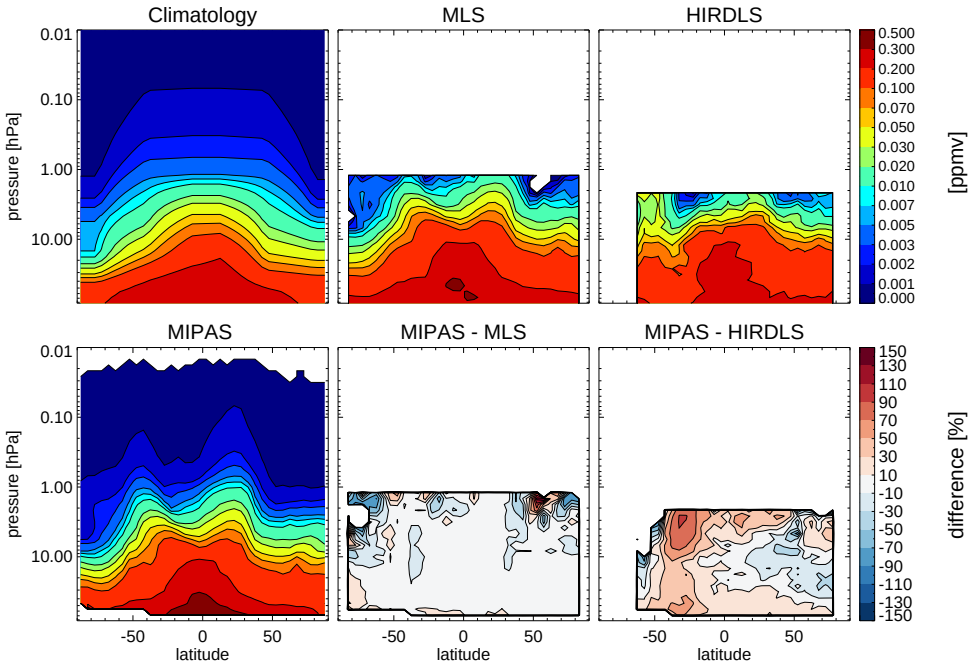

Figure 6.21: N_2O zonal mean for the 7th June 2007 for different instruments. The top row displays all the data sources (except MIPAS) while the bottom row displays the MIPAS results as well as the percentage difference between the observations (MIPAS−satellite). Note that the absolute subplots are in a semilogarithmic scale to make better use of the colour range.

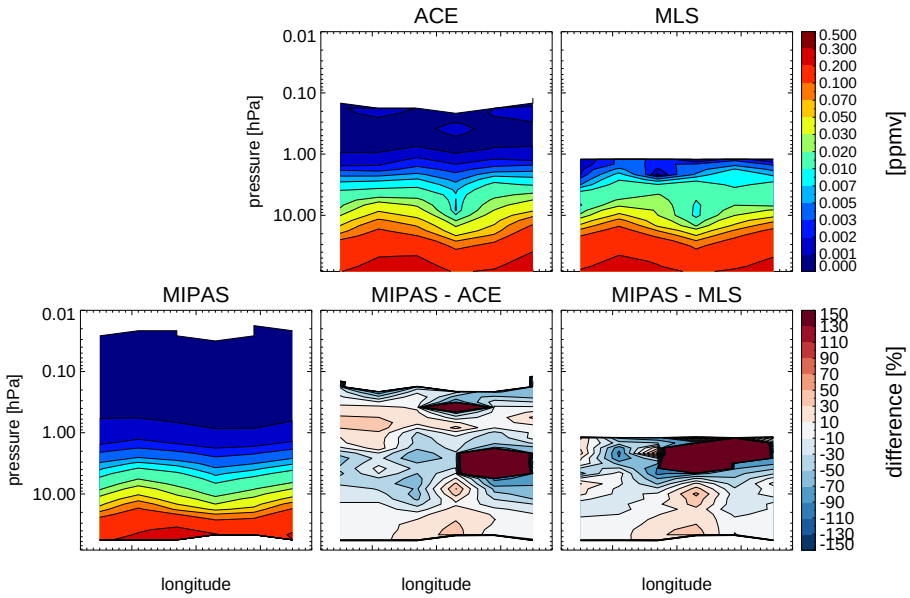

Figure 6.22: N_2O zonal section (southern,i.e. winter hemisphere) for the 15th of July 2008. The top row displays the ACE (62 S) and MLS (62 S) results while the bottom row displays the MIPAS (62 S) results as well as the percentage difference between the observations. Note that the absolute subplots are in a semilogarithmic scale to make better use of the colour range.

in Figure 6.22. As can be seen in the absolute value subplots all the satellite instruments present a similar structure. However, the percentage difference subplot, indicates an underestimation by MIPAS of N_2O concentration by up to 40%.

Figure 6.23 shows N_2O seasonal comparisons of coincident profiles between MIPAS and MLS, ACE and HIRDLS as well as the standard deviation of such comparisons. In the winter seasonal bin, the three biases shown lie within the expected variability but outside the 20% difference range. From among these comparisons, the ACE and the MLS biases present the same structure with a minimum around 10 hPa but do not agree in magnitude.

In the equatorial seasonal bin, only comparisons between MIPAS and MLS and HIRDLS were available. The MLS comparison is within the expected variability at all pressure levels and within a 10% difference range up to 2 hPa. Between 2 and 1 hPa the MLS comparison suggests either an overestimation by MIPAS or an underestimation by MLS. The HIRDLS bias is outside the expected variability for pressures greater than 10 hPa and within for smaller pressures.

In the summer seasonal bin, the three comparisons displayed are within the expected variability. Between 100 and 2 hPa the ACE and MLS comparisons agree with each other suggesting and underestimation of the N_2O concentration by MIPAS. For pressures smaller than 2 hPa these two biases disagree, while the ACE bias still shows negative values, MLS bias displays positive ones.

Note that these comparisons display in general large standard deviations showing the signification variation among the observations.

N_2O conclusions

Comparisons with coincident profiles indicate that for pressures greater than 10 hPa MIPAS is retrieving N_2O concentrations within a 20% difference range. Between 10 and 1 hPa the ACE and MLS comparisons suggest an underestimation by MIPAS between 50% up to 100%. For smaller pressures the comparisons disagree and hence no conclusions can be drawn.

6.9 NO_2 comparison

Figure 6.24 shows the NO_2 zonal mean comparisons for MIPAS and HIRDLS. OSIRIS is not used in this comparison because it can only measure during daytime and due to the NO_2 strong diurnal variation comparisons of day and nightime data against only daytime data are not useful. The MIPAS and HIRDLS data in general follows the structure shown in the climatology, with a NO_2 stratospheric

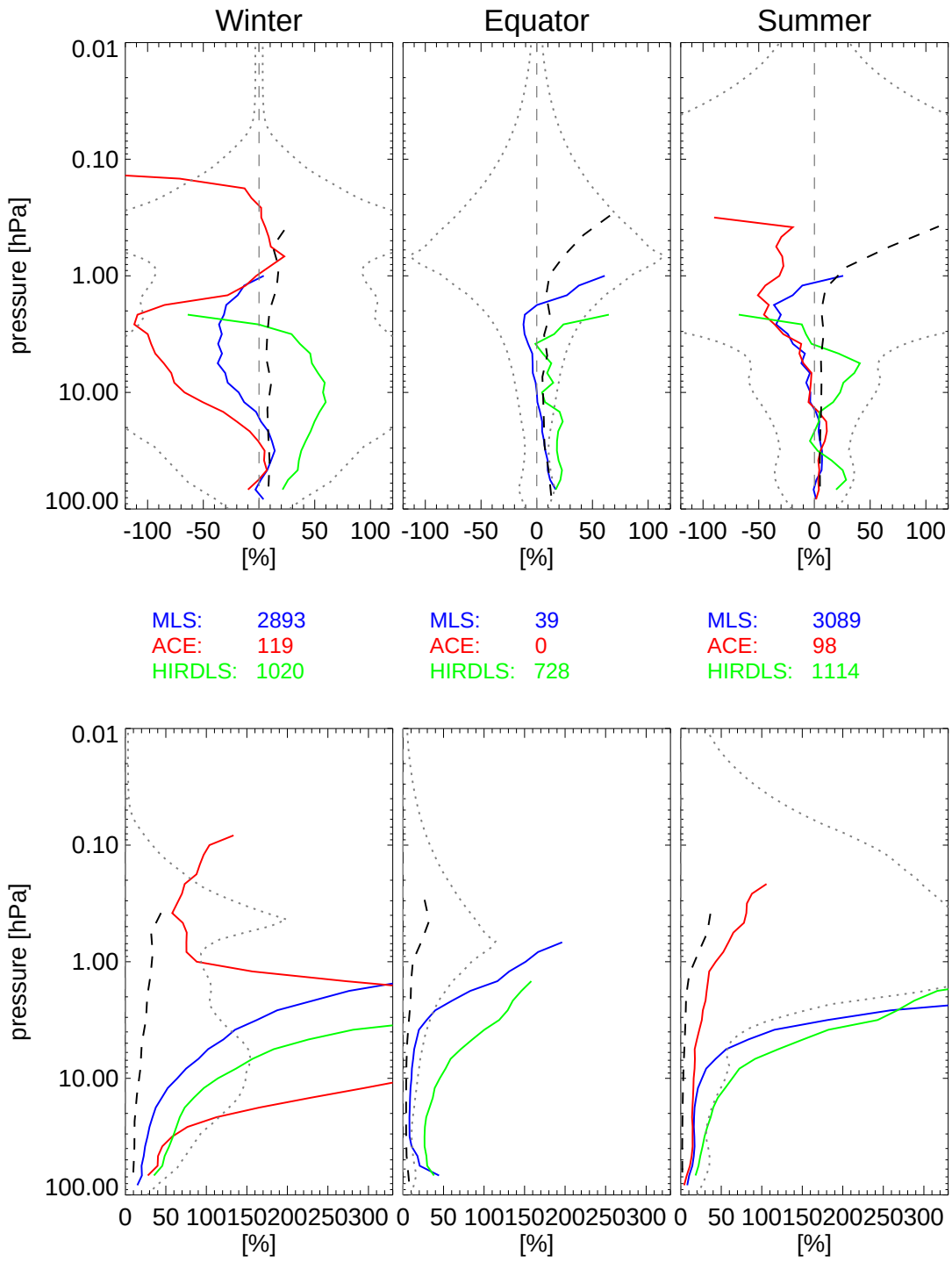

Figure 6.23: Seasonal N_2O biases (top) and scatter (bottom) between MIPAS and three datasets (MIPAS−satellite). The gray dotted lines show the expected N_2O variability over the corresponding season. The dashed black lines display the systematic (top) and the random (bottom) errors expected for the MIPAS measurements. The number of profiles averaged is shown in the middle row. The Winter, Equator and Summer bins correspond to latitudes 90 S−50 S, 20 S−20 N and 50 N−90 N sorted according to the day analyzed.

maximum (due to N_2O photodissociation), and an another maximum over the polar winter mesopause (due to NO_2 descent from the thermosphere). Note that the local maximum over the polar summer mesopause as shown in the climatology is also present in the MIPAS dataset with a significantly reduced magnitude.

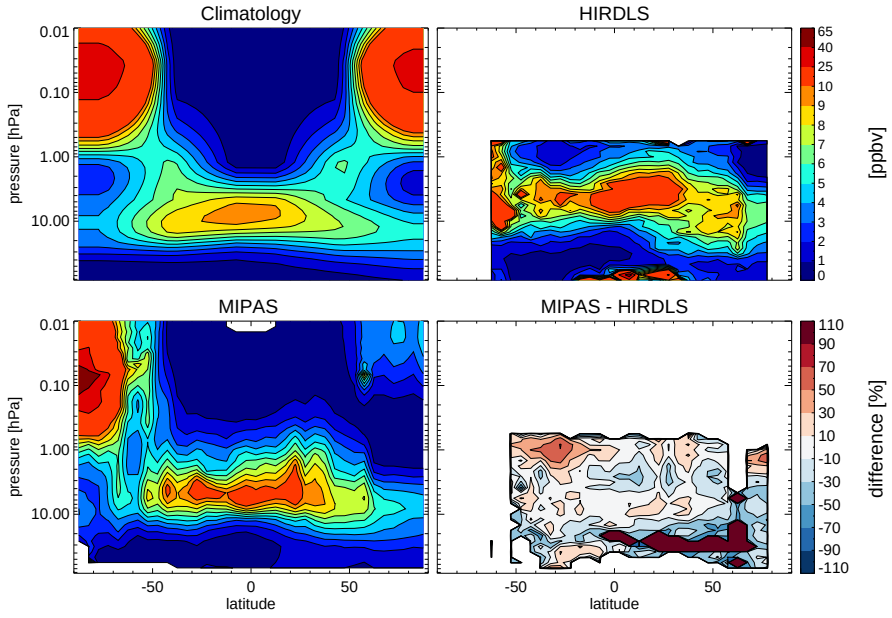

Figure 6.24: NO_2 zonal mean for the 7th June 2007 for several instruments. The top row displays Climatology and HIRDLS data while the bottom row displays the MIPAS results as well as the percentage difference between the observations (MIPAS−satellite). Note that the countours of the absolute subplots are not equally spaced.

Figure 6.25 shows the NO_2 zonal mean comparisons for MIPAS, HIRDLS and OSIRIS daytime observations. As can be seen, the HIRDLS comparison reveals either and underestimation of the NO_2 concentration by about 20% or the equivalent overestimation by HIRDLS. The OSIRIS data do not resemble either the MIPAS or the HIRDLS data.

The NO_2 zonal section (southern, i.e. winter hemisphere) for the ACE and MIPAS datasets is shown in Figure 6.26. As in Figure 6.25 only daytime data is used to compare directly the two datasets. As can be seen in the absolute value subplots the observations do not agree either in magnitude or in structure.

Figure 6.27 shows NO_2 seasonal comparisons of coincident profiles between MIPAS and ACE, OSIRIS and HIRDLS as well as the standard deviation of such comparisons.The three biases shown in the winter seasonal bin are within the expected variability but are outside a 20% difference range. As shown they do not agree neither in structure nor magnitude.

In the equatorial seasonal bin, only comparisons against HIRDLS and OSIRIS were possible.

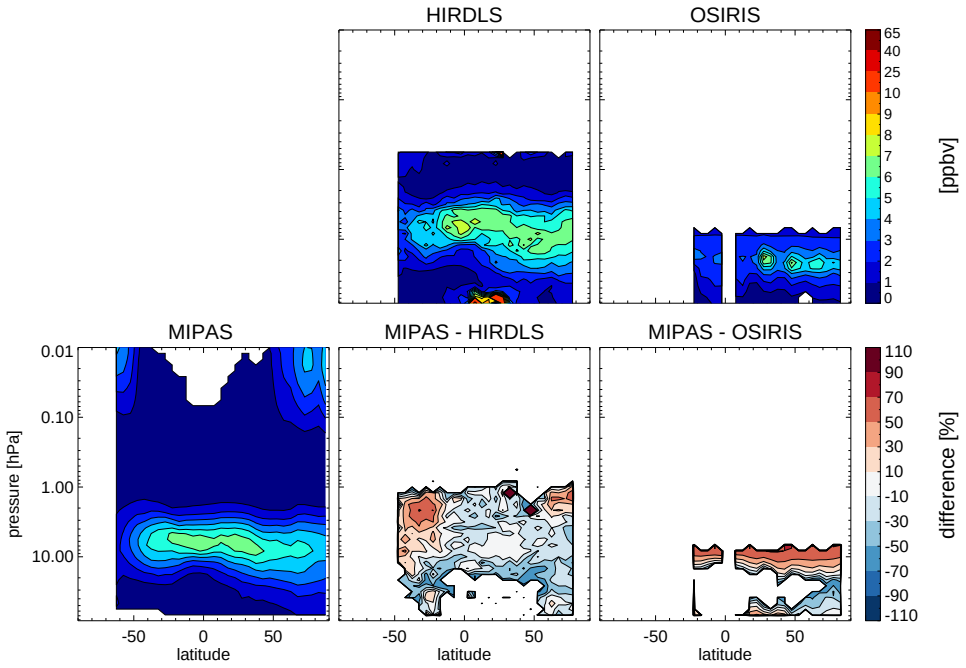

Figure 6.25: NO_2 zonal daytime mean for the 7th June 2007 for several instruments. The top row displays Climatology, HIRDLS and OSIRIS data while the bottom row displays the MIPAS results as well as the percentage difference between the observations (MIPAS−satellite). Note that the countours of the absolute subplots are not equally spaced.

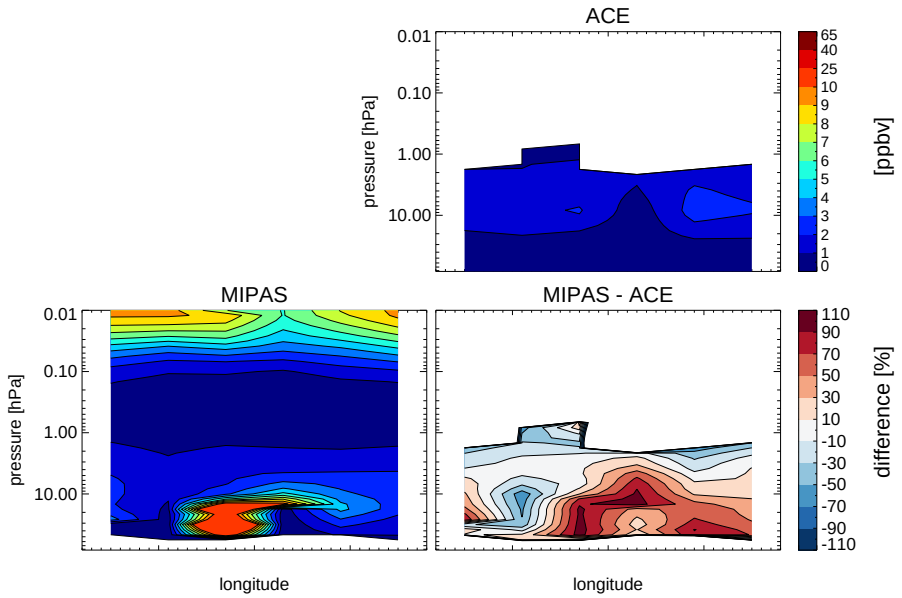

Figure 6.26: NO_2 zonal daytime section (southern, i.e. winter hemisphere) for the 15th of July 2008. The top row displays the ACE (62 S) results while the bottom row displays the MIPAS (6 2S) results as well as the percentage difference between the observations. Note that the countours of the absolute subplots are not equally spaced.

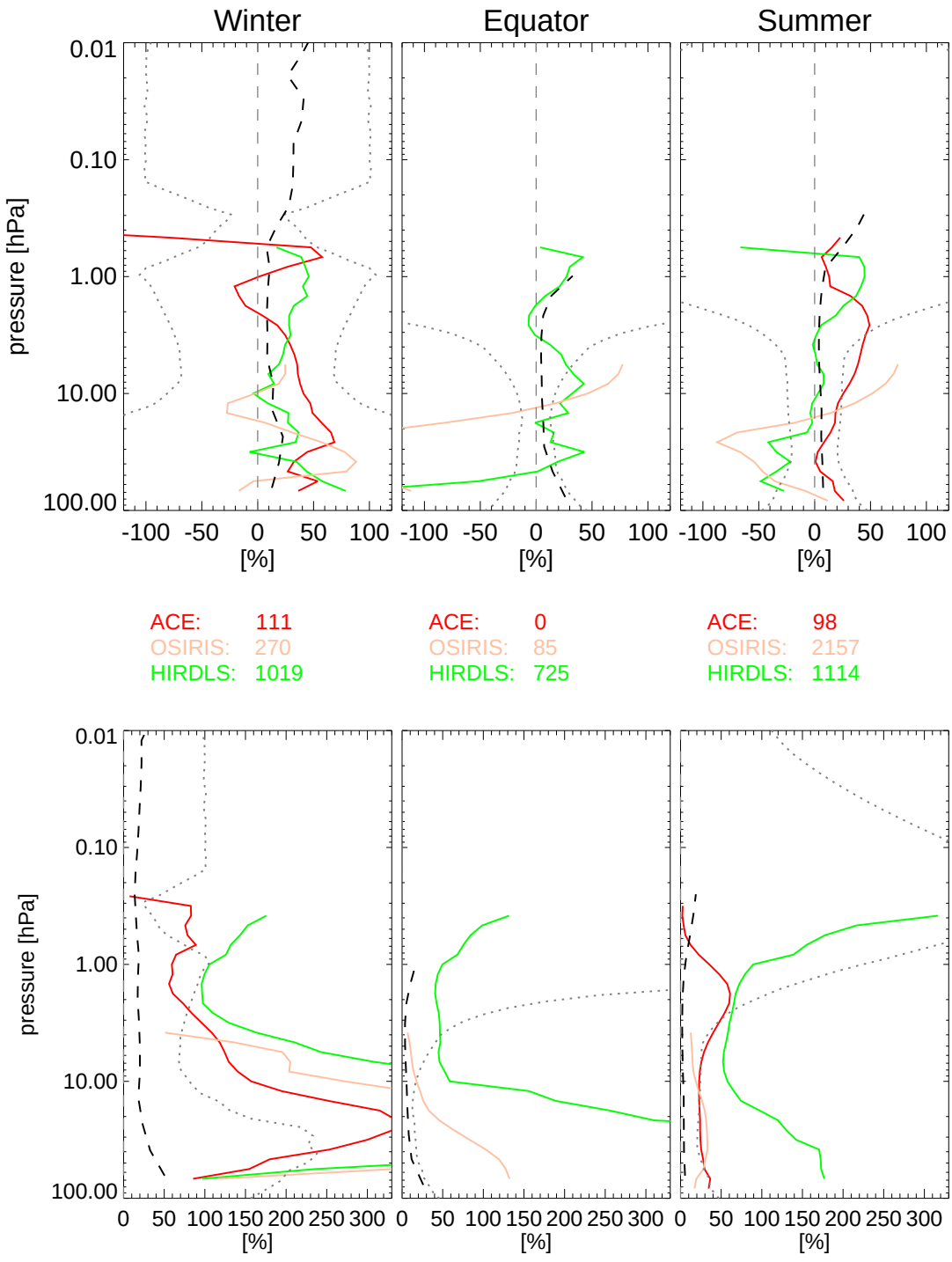

Figure 6.27: Seasonal NO_2 biases (top) and scatter (bottom) between MIPAS and two datasets (MIPAS−satellite). The gray dotted lines show the expected NO_2 variability over the corresponding season. The dashed black lines display the systematic (top) and the random (bottom) errors expected for the MIPAS measurements. The number of profiles averaged is shown in the middle row.The Winter, Equator and Summer bins correspond to latitudes 90 S−50 S, 20 S−20 N and 50 N−90 N sorted according to the day analyzed.

For pressures greater than 3 hPa the HIRDLS comparison is within the expected variability mainly because it is huge. This comparison indicates either an overestimation of the NO_2 concentration by MIPAS up to 50% for certain pressure levels or the equivalent underestimation by HIRDLS. The OSIRIS comparison is unrealistic at all pressure levels.

In the summer seasonal bin the three comparisons shown are within the expected variability for most of the pressure levels, however they do not agree either in structure nor in magnitude.

NO_2 conclusions

Although most of NO_2 agree within the expected variability (but not within a 20% difference range), practically no agreement was found between the biases and hence no conclusions can be drawn.

During these comparisons it was noted that the NO_2 IG2 climatology needs a revision to more accurately represent the real atmosphere and that the OSIRIS results seems non-physical.

6.10 CO comparison

The CO zonal mean comparisons are shown in Figure 6.28. As can be seen, the MLS and MIPAS datasets show, in broad terms, the structure shown in the climatology with an increase in CO concentrations with altitude around the upper mesosphere due to photolysis of CO_2. However, it should be noted that while the climatology shows an increase of the CO concentration around the upper mesosphere at all latitudes, MLS and MIPAS display it only around the polar winter region. These high values around the polar winter mesosphere are related to air descent inside the polar vortex. The MIPAS−MLS percentage difference shows either an overestimation of the CO concentration by the MIPAS data or the equivalent underestimation by MLS.

The CO zonal section (southern, i.e. winter hemisphere) for the ACE, MLS and MIPAS datasets is shown in Figure 6.29. As can be seen in the absolute value subplots the ACE and MLS observations agree in the structure and roughly in magnitude while MIPAS retrievals are up to 80% higher at upper mesospheric pressures and extremely lower (outside the range plotted) between 10 and 1 hPa (as shown in the percentage difference subplot).

Figure 6.30 shows CO seasonal comparisons of coincident profiles between MIPAS and ACE and MLS as well as the standard deviation of such comparisons. In the winter seasonal bin, the two comparisons indicate an overestimation of around 100% of the CO concentration by MIPAS.

Unfortunately, in the equatorial seasonal bin only comparison against MLS were possible. The

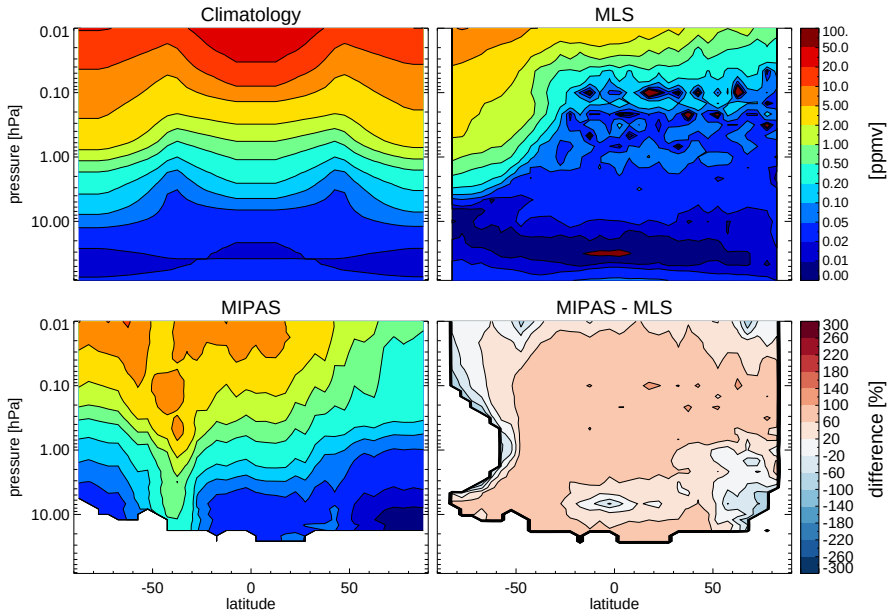

Figure 6.28: CO zonal mean for the 7th June 2007 for two instruments. The top row displays the Climatology and HIRDLS data while the bottom row displays the MIPAS results as well as the percentage difference between the observations (MIPAS−satellite). Note that the absolute subplots are in a semilogarithmic scale to better use of the colour range. Note that the absolute subplots are in a semilogarithmic scale to make better use of the colour range.

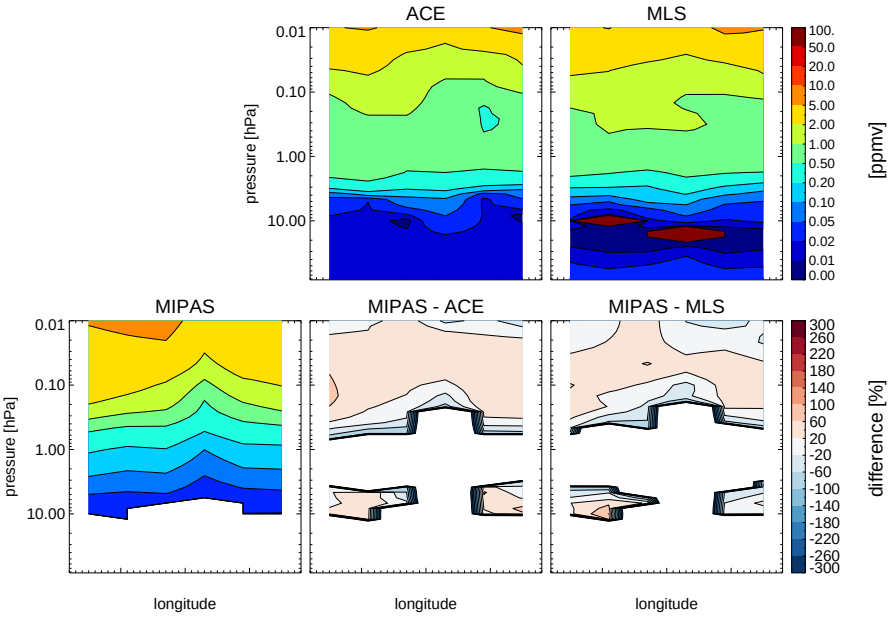

Figure 6.29: CO zonal section (southern, i.e. winter hemisphere) for the 15th of July 2008. The top row displays the ACE (62 S) and MLS (62 S) results while the bottom row displays the MIPAS (62 S) results as well as the percentage difference between the observations. Note that the absolute subplots are in a semilogarithmic scale to make better use of the colour range.

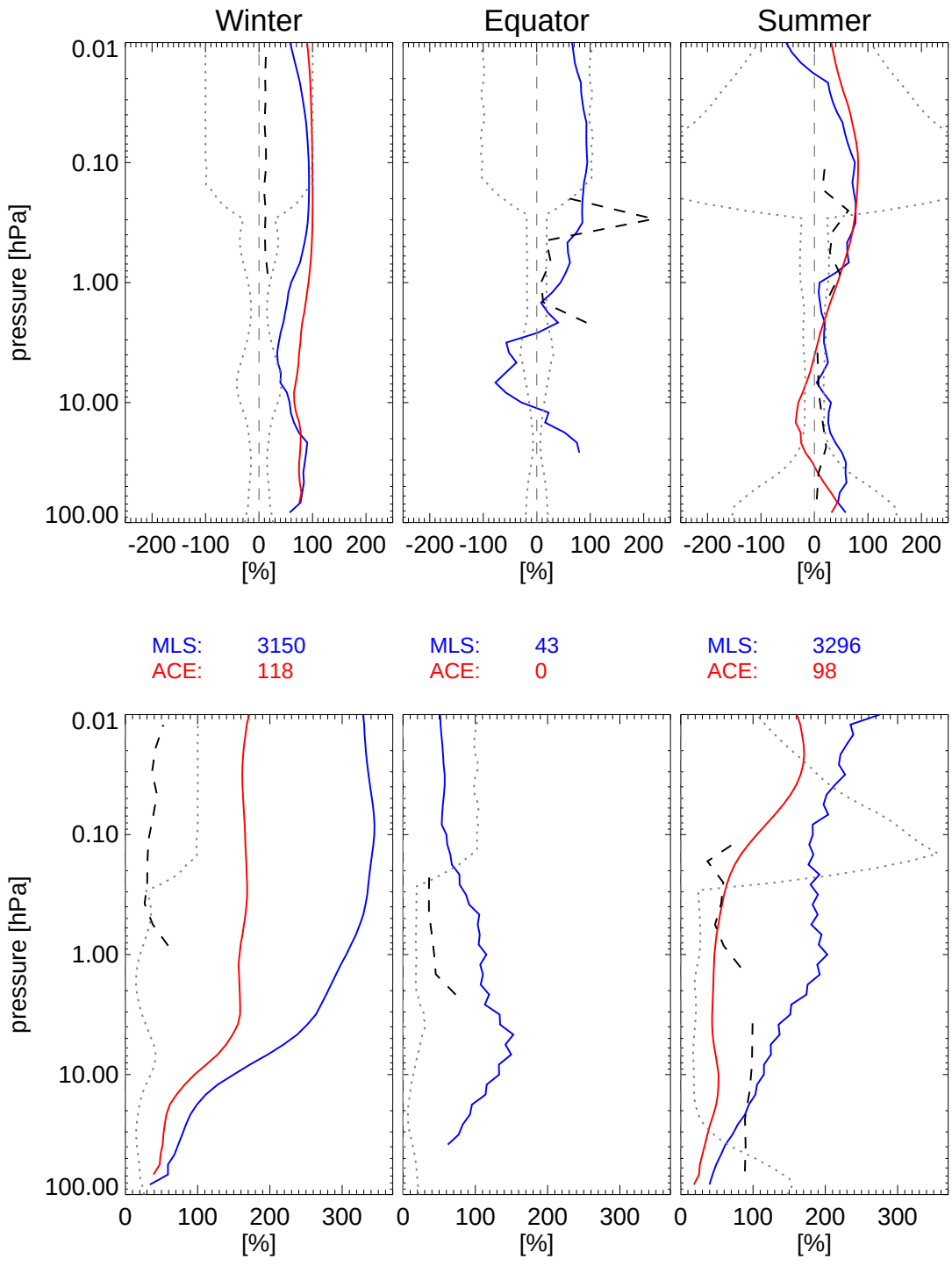

Figure 6.30: Seasonal CO biases (top) and scatter (bottom) between MIPAS and three datasets (MIPAS−satellite). The gray dotted lines show the expected CO variability over the corresponding season. The dashed black lines display the systematic (top) and the random (bottom) errors expected for the MIPAS measurements. The number of profiles averaged is shown in the middle row. The Winter, Equator and Summer bins correspond to latitudes 90 S−50 S, 20 S−20 N and 50 N−90 N sorted according to the day analyzed.

bias shown displays an underestimation between 9 and 2 hPa and an overestimation of around 100% for lower pressure of the CO concentrations by MIPAS (or the equivalent for MLS).

In the summer seasonal bin the two comparisons shown agree in structure between 2 and 0.05 hPa indicating an overestimation up to 75% of the CO concentration by MIPAS. Outside this range the two comparisons disagree.

The significant overestimation of CO by MIPAS is probably due to the strong influence of nonLTE processes in CO observations above the stratosphere as discussed by Walker [2008].

CO conclusions

Comparisons of coincident profiles show that in general, MIPAS overestimates the CO concentrations at all pressure levels by around 100%. This significant overestimation is presumably due to nonLTE processes.

During these comparisons it was noted that the CO IG2 climatology needs a revision to more accurately represent the real atmosphere.

6.11 Conclusions

An estimation of the quality of the MIPAS MA MORSE retrievals and other instruments has been performed. In order to do this, comparisons in the zonal mean for the limb viewing instruments were presented as well as the relative (for the temperature comparison) or percentage (for the composition comparisons) differences. In these comparisons, the climatological values were also displayed as a reference. It was noted that the IG2 climatology for temperature, H_2O, NO_2 and CO need a revision to more accurately represent the atmosphere.

For the solar/star occultation instruments a zonal section of the winter hemisphere was shown to compare the zonal structure induced by planetary waves. The zonal section of MIPAS and MLS was also shown for comparison.

The last comparison shown was a seasonal comparison of coincident profiles between MIPAS and all the other instruments. Two profiles were considered coincident within a 500 km radious and 6 hours. The seasonal bin compared correspond to latitude bins between 90 S−50 S, 20 S−20 N and 50 N−90 N and sorted into winter, equatorial and summer according to the date of the profile. Table 6.3 summarizes the general results while Table 6.4 summarizes the MIPAS MA results of these comparisons.

Table 6.3: Summary of the comparisons. 'Y' indicates that the data may be used for scientific studies (i.e. a 3 K or 20% difference), '±' indicates that at certain pressure levels or under certain seasonal conditions the data should be used with caution, '?' indicates that the data is available but no agreement was found between the datasets and 'N' indicates that the data is still not suitable for scientific studies.

	Tem	H_2O	O_3	HNO_3	CH_4	N_2O	NO_2	CO
MIPAS	Y	±	±	Y	±	±	?	N
MLS	Y	Y	Y	Y		Y		Y
OSIRIS			N				N	
SMR	Y	±	Y					
SABER	±		±					
HIRDLS	Y	N	Y	Y		±	?	
SOFIE	Y	Y	Y		±			
ACE	Y	Y	Y	Y	Y	Y	?	Y
GOMOS			±					
IG2 clim.	±	N	Y	Y	Y	Y	±	±

Table 6.4: Summary of the MIPAS comparisons. 'Y' indicates that the given parameter is within a 3 K or a 20% range difference, '+' or '-' indicates an overestimation or an underestimation respectively, 'W','S' indicates that a given overestimation or underestimation occur only under polar winter or polar summer conditions respectively and '?' indicates that no agreement was found in the comparisons.

hPa	Tem	H_2O	O_3	HNO_3	CH_4	N_2O	NO_2	CO
0.01	Y	+	+		-			+
0.03	Y	+	+S		-S			+
0.1	-S	+	+S		-S	?		+
0.3	+S	Y	Y		Y	-WS	?	+
1.0	Y	Y	Y		Y	-W	?	+
3.0	Y	Y	Y	Y	Y	-W	?	+
10.0	Y	Y	Y	Y	Y	Y	?	+
30.0	Y	Y	Y	Y	Y	Y	?	+

CHAPTER 7

A ‘non-iterative’ linear retrieval

As explained in section 2.2, the inversion of atmospheric radiances into atmospheric parameters is the basic problem in science of fitting a model to observations subject to errors. In this case, the model is usually nonlinear and the inversion requires an iterative approach to be solved. At each iteration the forward model is run using the atmospheric estimates from the previous iteration until given convergence criteria are fulfilled. As an example, the least squares solution to this type of problem is given by:

$$\mathbf{x}_{i+1} = \mathbf{x}_i + \left(\mathbf{K}_i^T \mathbf{S}_e^{-1} \mathbf{K}_i\right)^{-1} \mathbf{K}_i^T \mathbf{S}_e^{-1} \left(\mathbf{y} - \mathbf{F}(\mathbf{x}_i)\right) \tag{7.1}$$

where $\mathbf{x}_{i+i}$ and $\mathbf{x}_i$ are the current and previous atmospheric estimates, $\mathbf{y}$ are the measurements, $\mathbf{K}$ is the Jacobian matrix and where $\mathbf{S}_e$ is the measurement error covariance matrix.

However, assuming that the forward model really is linear:

$$\mathbf{F}^*(\mathbf{x}) = \mathbf{F}(\mathbf{x}_0) + \mathbf{K}_0(\mathbf{x} - \mathbf{x}_0) \tag{7.2}$$

the inversion can be solved without iterations, that is to say, just solving:

$$\mathbf{x} = \mathbf{x}_0 + \left(\mathbf{K}_0^T \mathbf{S}_e^{-1} \mathbf{K}_0\right)^{-1} \mathbf{K}_0^T \mathbf{S}_e^{-1} \left(\mathbf{y} - \mathbf{F}(\mathbf{x}_0)\right) \tag{7.3}$$

or a constrained version of it. This implies that the simulated spectra ($\mathbf{F}(\mathbf{x}_0)$) and the Jacobians ($\mathbf{K}_0$) only need to be calculated once. Hence, an inversion under these conditions should be able to incorporate all the spectral points corresponding to the target parameters without worrying about the computing speed limitations associated with re-running the forward model. This should theoretically lead to better precision than the iterative schemes that are forced to use only subsets (i.e. microwin-

dows) of the spectra.

This chapter describes a (non iterative) linear retrieval scheme for the inversion of MIPAS limb radiances but the results should be equally applicable to other limb viewing spectrometer instruments.

7.1 Linearized forward model

As detailed in section 2.1, the atmospheric limb monochromatic radiance leaving the atmosphere at a given tangent height (see Figure 2.1) is given by equation 2.2 here rewritten as ,

$$L = \sum_i B(T_i) \left[\exp\left(- \sum_{k=1}^{k=i-1} \chi_k \right) - \exp\left(- \sum_{k=1}^{k=i} \chi_k \right) \right] \tag{7.4}$$

where the stratified atmosphere is assumed to be in LTE, $B(T_i)$ is the Planck function at temperature T_i of a given stratified layer i and where the transmittance, τ, has been expressed in terms of the optical thickness, χ from the satellite to the stratified layer k.

Assuming that the path is optically thin ($\chi \ll 1$), equation 7.4 can be approximated by,

$$\begin{aligned} L &\simeq \sum_i B(T_i) \left[1 - \sum_{k=1}^{k=i-1} \chi_k - \left(1 - \sum_{k=1}^{k=i} \chi_k \right) \right] && (7.5) \\ &\simeq \sum_i B(T_i) \left[\sum_{k=1}^{k=i} \chi_k - \sum_{k=1}^{k=i-1} \chi_k \right] && (7.6) \\ &\simeq \sum_i B(T_i) \chi_i && (7.7) \end{aligned}$$

which implies that in the optically thin case the contribution of each atmospheric layer to the total radiance is independent of the others layers or, rephrasing, that the rest of the atmosphere becomes transparent.

Furthermore, substituting equation 2.7 here reprinted

$$\chi_i = \frac{p_i}{RT_i} l_i \sum_j v_{ij} \sigma_{ij} \tag{7.8}$$

where p is pressure, R is the universal gas constant, l is the length along the path and v_j and σ_j are the absorber volume mixing ratio and the absorption coefficient of the absorber j respectively; into equation 7.7, the radiance received at the satellite when the absorption is weak becomes,

$$L \simeq \sum_i B(T_i) \frac{p_i}{RT_i} l_i \sum_j v_{ij} \sigma_{ij} \tag{7.9}$$

This equation implies that when the path is optically thin, the forward model is linear with respect to the gas concentration. For instance, assuming that the temperature and the pressure are known and observing an spectral region where the radiation is mainly from one gas, the only remaining unknown in equation 7.9 will be the gas concentration, allowing this equation to be expressed as,

$$L \simeq \sum_i \alpha_i v_i \tag{7.10}$$

where α is a constant determined by the rest of the terms in equation 7.9.

7.1.1 VMR forward model linearity

To test the validity of the linearity of the forward model due to VMR changes, simulated CH_4 spectra were used. These spectra were simulated for CH_4 spectral points for midlatitude conditions for the MIPAS band B ($1200-1500\,\mathrm{cm}^{-}1$) with MIPAS reduced resolution ($0.0625\,\mathrm{cm}^{-}1$), ILS and FOV. As an example, Figure 7.1 shows the modelled spectra at 30, 60 and 90 km.

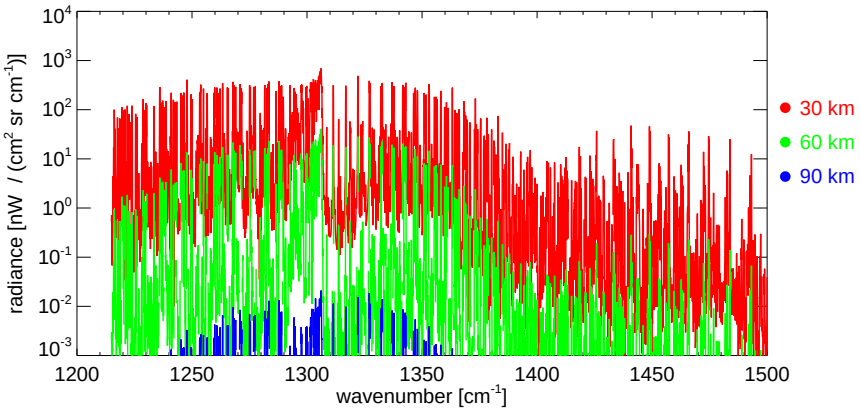

Figure 7.1: CH_4 spectra for midlatitudes conditions.

Figure 7.2 (left) shows the mean value of $\mathbf{F}(\mathbf{x})-\mathbf{F}(\mathbf{x}_0)$ (the actual difference) where $\mathbf{x}$ corresponds to an increase of 1, 5, 10, 20 or 50% of $\mathbf{x}_0$ (midlatitudes conditions). In addition, it also shows a scaling (the estimated difference) of the 1% actual difference to show how well both differences agree. The vertical structure displayed (for instance the maximum around 54 km) is due probably due to the varying absorption coefficient dependence of pressure and temperature values for the spectral points averaged. As expected, Figure 7.2 (right) shows that the deviation between the actual and the estimated difference grows as $\mathbf{x}$ departs from $\mathbf{x}_0$.

To continue on testing the linearity of the forward model an inversion of the previously computed spectra was performed. This retrieved values were obtained using a linear least squares fit constrained

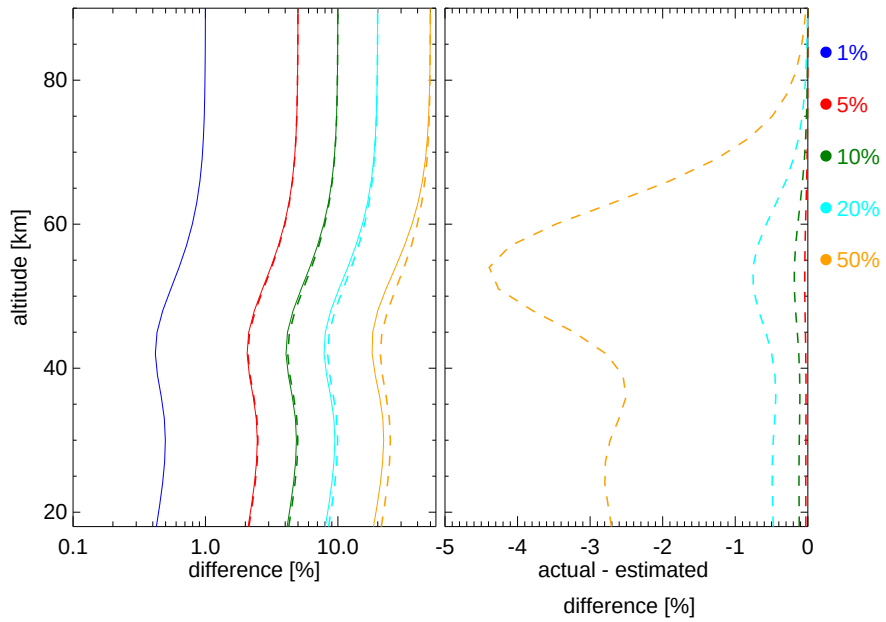

Figure 7.2: (left) Actual (solid) and estimated (dashed) mean spectral percentage difference for CH_4 emission lines. (Right) Actual − estimated difference

by a Twomey–Tikhonov regularisation. That is to say, solving equation,

$$\mathbf{x} = \mathbf{x}_0 + \left(\mathbf{K}_0^T \mathbf{S}_e^{-1} \mathbf{K}_0 + \gamma^{-1} \mathbf{R}\right)^{-1} \mathbf{K}_0^T \mathbf{S}_e^{-1} \left(\mathbf{y} - \mathbf{F}(\mathbf{x}_0)\right) \tag{7.11}$$

rather than equation 7.3. This regularisation was added to avoid artifacts at high altitudes induced by numerical noise inside the radiative transfer calculations. This numerical noise appears as consequence of the small numbers involved in the calculation of the Jacobians when looking at low altitudes but perturbing at high altitudes. Hence, in addition to the Twomey–Tikhonov regularisation, only Jacobians near the tangent heights were used.

For these simulated retrievals $\mathbf{F}(\mathbf{x})$ was used as measurements and the measurement error covariance matrix was set to the identity matrix ($\mathbf{S}_e = \mathbf{I}$). Figure 7.3 (left) shows the CH_4 retrieved values for different increases of the initial guess CH_4 VMR concentration. It also shows (right) the difference between the actual and the retrieved values. Note that although in theory radiances become more linear with altitude, the retrievals worsen. This deterioration is probably due to numerical noise due to the small numbers involved in these calculations.

As can be seen in the difference subplot of Figure 7.3 the linearity assumption holds up to a 20% difference between the initial guess and the actual value with a 2% margin of error. However, in any practical implementation, this accuracy will be reduced by the presence of noise.

Note that although there is no attempt here to discriminate between optically thin and optically

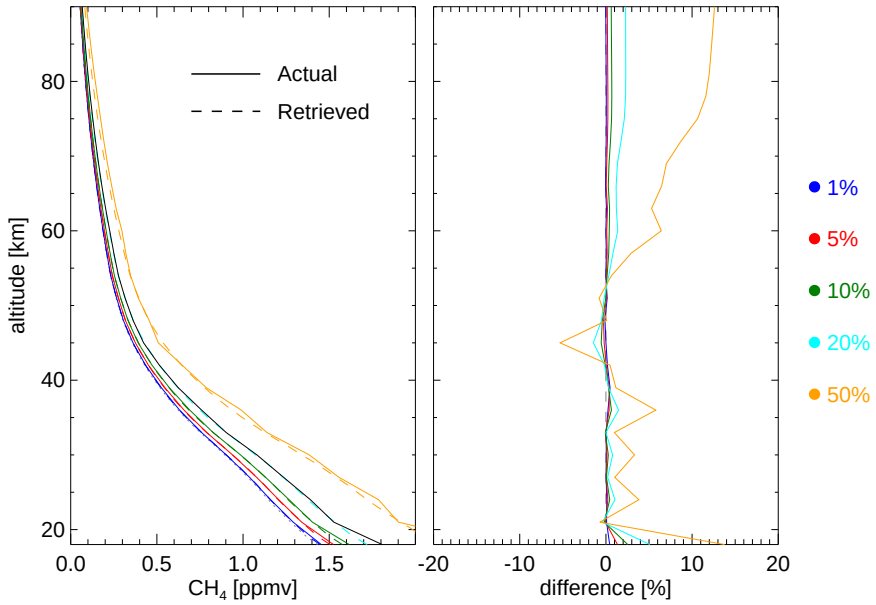

Figure 7.3: (left) CH_4 concentration retrieved linearly for several VMR concentration increments of the initial guess. (right) Percentage difference between the actual and retrieved value

thick lines, the Jacobians will weight the optically thick lines lower. That is to say, effectively masking them out.

7.1.2 Pressure forward model linearity

The forward model (equation 7.9) is not as linear with respect to pressure as for the VMR changes due to the pressure dependence of the absorption coefficient. A linear relationship between the radiance and pressure or temperature can be obtained by applying a Taylor expansion around a given profile $\mathbf{x}_0$ (the linearization point) assuming that is close to the true profile $\mathbf{x}$. When this is the case, the higher order terms in the expansion can be truncated leaving only the linear term (effectively equation 7.3).

In this case, the simulations performed to test the linearity of the forward model were of CO_2 spectral points in MIPAS band A ($685-970\,\mathrm{cm}^{-1}$) with the MIPAS resolution, ILS and FOV as in the previous section. As an example, Figure 7.4 shows the modelled spectra at 30, 60 and 90 km.

Figure 7.5 (left) portrays the linearity of the forward model to changes in pressure in the same manner as Figure 7.2. In addition, Figure 7.5 (right) also shows the linearly retrieved and actual values for the same pressure increments.

As can be seen from the forward model linearity subplots, the estimated spectra agrees within a 1% error margin up to a 20% increase in pressure, for the 50% increase the actual$-$ estimated difference is less than 5%. These values translate in terms of accuracy in the retrieved values to better

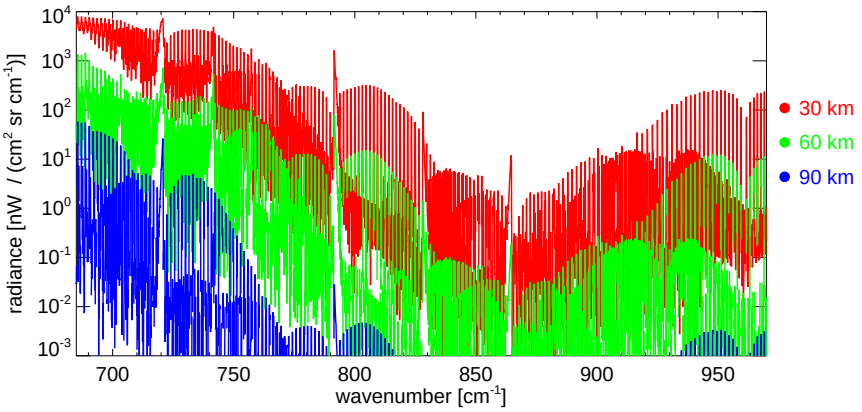

Figure 7.4: CO_2 spectra for midlatitudes conditions.

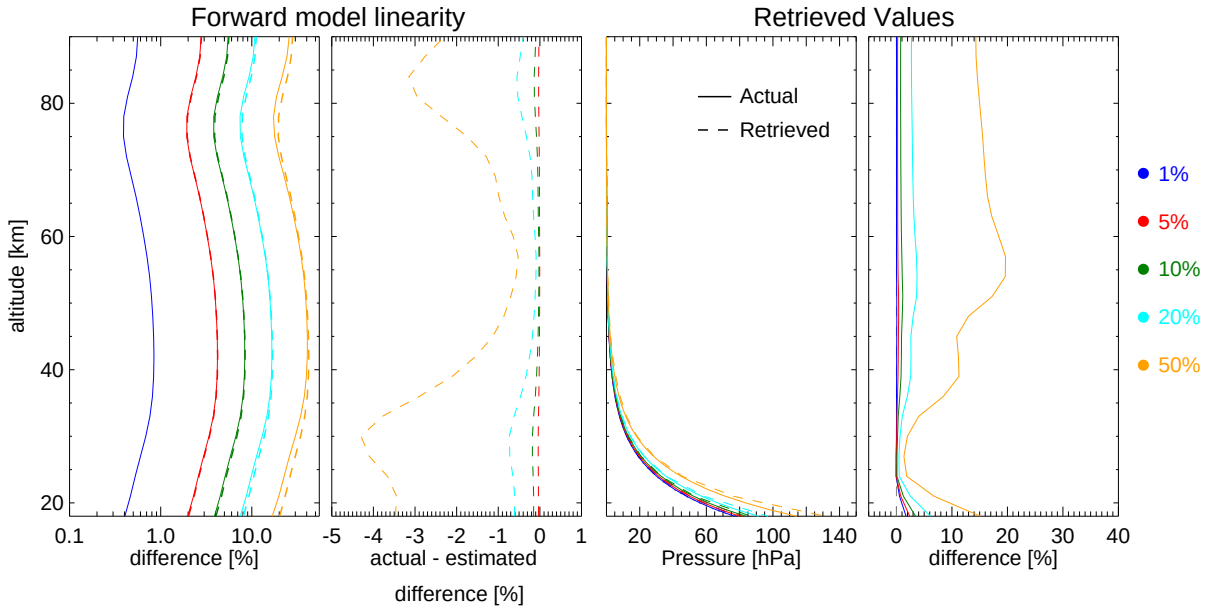

Figure 7.5: (left) forward model linearity with respect to changes in pressure (equivalent to Figure 7.2) (right) Pressure linearly retrieved values for several pressure increments (equivalent to Figure 7.3)

than 3% up to a pressure increment of 20% of the linearization point.

7.1.3 Temperature forward model linearity

Analyzing briefly equation 7.9 will show that temperature is the least linear parameter due to the temperature dependence of the Planck function and the absorption coefficient. Figure 7.6 (left) shows the difference linearity of the forward model with respect to changes in temperature. In this case, the CO_2 spectra averaged correspond to temperature increases of 1, 5, 10, 20 and 50 K.

As expected, temperature is the more non-linear parameter of the forward model. For instance, for changes up to 10K of the initial temperature, the actual – estimated spectral difference is up to 5%. This spectral difference translates to an difference between the actual and retrieved temperature

of up to 3K (Figure 7.6 right). However, it should be noted that this difference is localized only near the stratopause (i.e. where the temperature gradient changes sign) and outside this region the actual–retrieved difference is practically zero.

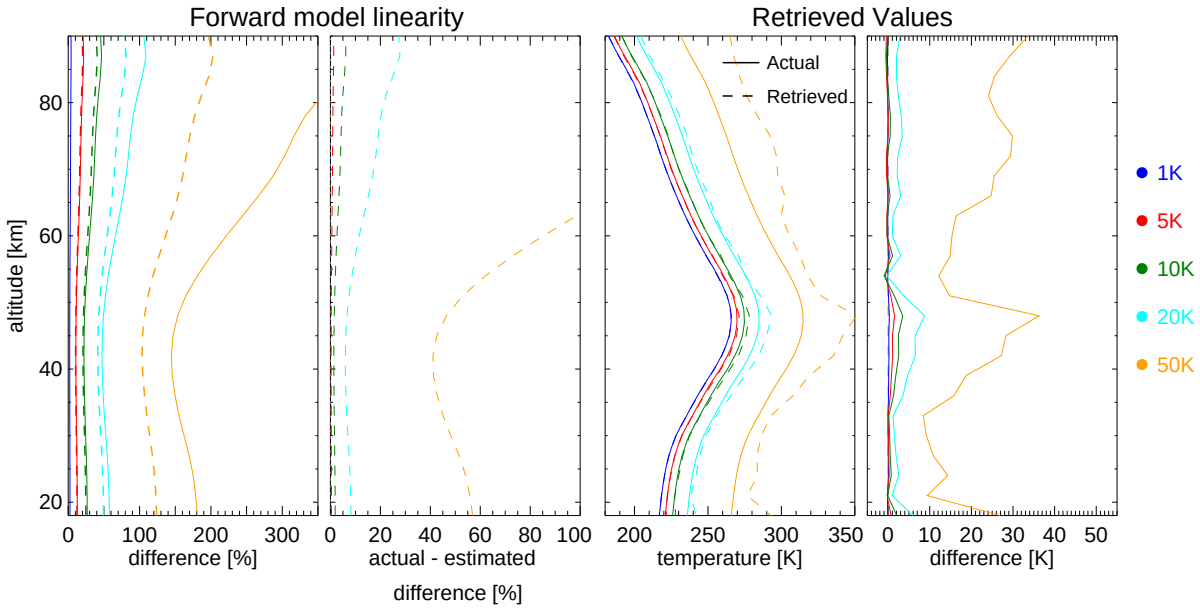

Figure 7.6: (left) forward model linearity with respect to changes in temperature (equivalent to Figure 7.2) (right) Temperature linearly retrieved values for several temperature increments (equivalent to Figure 7.3)

Planck function simulations

To try to improve the linearity of the forward model due to changes in temperature, rather than retrieving temperature directly, Planck function can be retrieved instead.

To convert the temperature Jacobian generated by the radiative transfer model into a Planck function Jacobian, the following formula is applied

$$\frac{\partial L}{\partial B(T)} = \frac{\partial L}{\partial T}\frac{dT}{dB(T)} \tag{7.12}$$

where dT corresponds to a temperature change of 1K and $dB(T)$ is the corresponding change in Planck function at a fixed wavenumber chosen to be in the middle of the spectral region of interest. Once the retrieval is complete, the retrieved Planck function can be converted back to temperature.

Figure 7.7 displays the retrieved and actual values for the same temperature increments of the initial guess as in Figure 7.6. As can be seen the linearity of the problem improves considerably when retrieving temperature via the Planck function. Note that the forward linearity graph will be the same as in Figure 7.6 (left) because the same temperature increments are used.

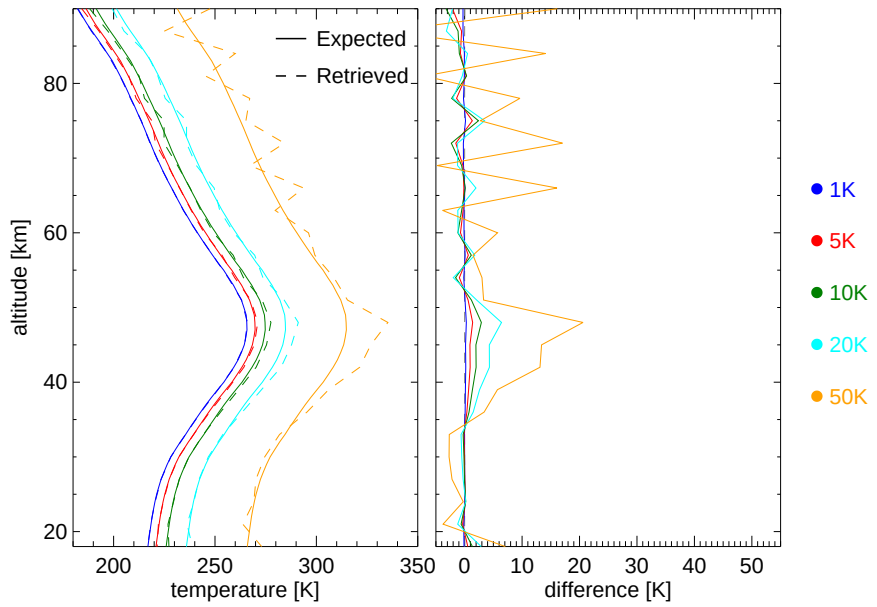

Figure 7.7: (left) Temperature concentration retrieved linearly via Planck Function for several temperature increments of the initial guess. (right) Difference between the actual and retrieved value

The results shown so far suggest that the retrievals of gas concentration, pressure and temperature can be treated linearly up to a difference between the initial guess and the actual profile of 20% in CH_4 concentration for a 2% error margin, up to a 20% pressure difference for a 3% error margin and up to a 10K difference for a 3 K error margin near the stratopause and less than 1 K elsewhere. However, so far, signal to noise limitations, overlapping emission by other molecules and nonLTE effect have been avoided. Also, the perturbations have been made over the whole profile rather than level by level. Before the linear algorithm can produce useful results in a practical application, the influence of these factors needs to be properly taken into account.

7.2 pT Practical considerations

The techniques to retrieve temperature and pressure from infrared emission measurements are based on the observations of radiation from a well mixed gas or a gas with a known distribution. By doing this, the only remaining unknowns are the temperature and pressure which can be inverted by measuring at least two different spectral points. In the infrared region the spectral region used is usually the CO_2 band around 700 cm^{-1}.

7.2.1 Emission from other gases

As a first step to simulate more realistic data, a pT profile was simulated using all gases listed in table 3.1 for MIPAS band A and not only CO_2 lines. This is needed to include the signal contributions of these interfering gases in this spectral region. For this test, the pT profile corresponds to the same profile used to compute the forward model simulations and the Jacobians in order to isolate the effects of increasing the concentration of the interfering species.

Figure 7.8 displays the temperature difference between the actual value and the retrieved values for three different cases. First, for comparison, the retrieved profile when the forward model simulations are also used as measurements is shown (blue line). In this retrieved profile, since the concentration of interfering species matches the concentration of the initial guess no temperature discrepancies are induced to the pT values (effectively is as if all concentrations were known). Then, to show the effect of the overlapping emissions, the same pT profile with a 50% increased VMR concentration for the overlapping species was simulated and retrieved (red line). As can be seen if the overlapping emissions are not taken into account the retrieved values are greatly influenced.

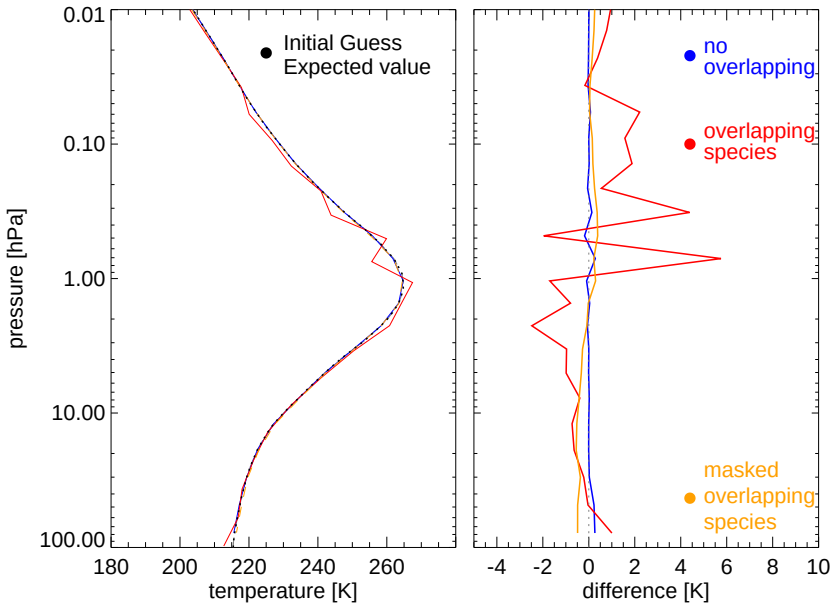

Figure 7.8: Simulated retrievals showing the influences of the emission of other gases in the pT retrievals when not taken into account

The last retrieved profile shown (orange line) corresponds to the simulations as the previous profile but when the overlapping emissions were masked out. The spectral points assumed to be due to

"pure" CO_2 emissions were selected using,

$$0.9 \leq \frac{L_{\mathrm{CO_2}}}{L_{(\mathrm{CO_2,H_2O,O_3,HNO_3})}} \leq 1.1 \tag{7.13}$$

where $L_{\mathrm{CO_2}}$ is a CO_2–only simulated spectrum and $L_{(\mathrm{CO_2,H_2O,O_3,HNO_3})}$ is a general simulated spectrum.

As depicted in the Figure, the difference between this retrieved values and the actual values is again practically negligible showing that the influence of the other species has been almost completely removed.

7.2.2 nonLTE emissions

Although most gases depart from Local Thermodynamic Equilibrium (LTE) at low pressures, so far the emissions considered in the retrievals have been simulated assuming LTE at all heights. Hence, in a practical implementation the upper mesospheric retrievals will be affected from departures from LTE conditions.

Figure 7.9 shows the difference between the actual and retrieved pTprofiles for three different cases. As previously, the actual pT profiles is the same as the initial guess to isolate the effects of the nonLTE emissions. First, as reference, the difference when the simulated measurements (**y**) and the forward model simulations (**F**(**x**)) are in LTE is shown. As expected there is no difference at any height. Then, the difference when the simulated measurements are affected by nonLTE processes. As potrayed in the figure, the upper mesospheric retrieved values are significantly influenced. Note that this difference is the expected error due to assuming LTE at midlatitudes. The same type of simulations can be used to estimate the error due to assuming LTE under for other latitudes.

At last, the difference when spectral masks has been applied to select spectral points for vibrational band less influenced by nonLTE effects. This spectral masks were constructed using,

$$0.9 \leq \frac{L_{\mathrm{CO_2(nonLTE)}}}{L_{(\mathrm{CO_2(LTE)}}} \leq 1.1 \tag{7.14}$$

where $L_{\mathrm{CO_2(nonLTE)}}$ and $L_{(\mathrm{CO_2(LTE)}}$ are CO_2-only simulated spectra either in nonLTE or in LTE respectively.

As shown, the differences between the actual and the retrieved profile have improved, however, some nonLTE influence is still present. In order to properly reduce the influence of nonLTE emissions in the retrievals, either the vibrational temperatures need to be retrieved as part of the retrieval scheme

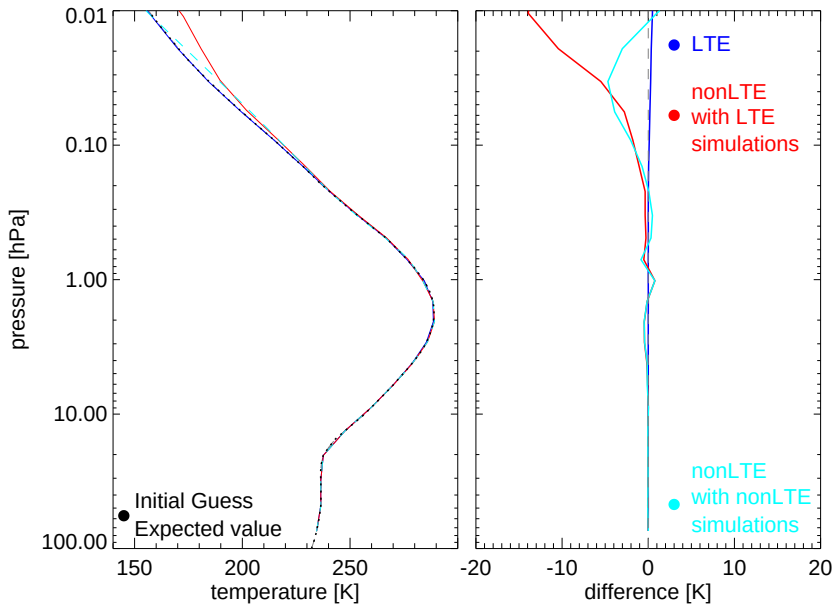

Figure 7.9: Simulated retrievals showing the effects of nonLTE emissions at high altitudes

(currently too computationally expensive) or a nonLTE climatology needs to be developed.

7.2.3 Hydrostatic constraint

The pT retrievals can be constrained using the engineering data defining the line of sight (the pointing information at each tangent height) as an indirect measurement of the state vector. Assuming hydrostatic balance, these engineering altitudes can be used to constrain the temperature and pressure via the hydrostatic equation,

$$z_{i+1} - z_i = \left(\frac{R}{g}\right) \frac{T_i + T_{i+i}}{2} \log\left(\frac{p_i}{p_{i+1}}\right) \tag{7.15}$$

where z correspond to two tangent point altitudes (i and $i+1$) with associated temperatures T and pressures p, R is the specific gas constant for dry air and g is gravity (as a function of height and latitude).

This constraint is implemented by incorporating the engineering altitudes as part of the measurement vector (with their corresponding uncertainties) and by constructing pT Jacobians by differentiating Equation 7.15 with respect to either pressure or temperature. These scheme is also used by the operational ESA level 2 retrieval described by Ridolfi et al. [2000].

7.2.4 Measurement noise

In this case, the measurement noise will account for most of the errors in the retrieved parameters. In the linear retrieval scheme these errors are computed by equation 2.24 here rewritten,

$$\mathbf{S}_x = \left(\mathbf{K}^T\mathbf{S}_e^{-1}\mathbf{K} + \gamma^{-1}\mathbf{R}\right)^{-1} \tag{7.16}$$

where $\mathbf{K}$ is the Jacobian matrix, $\mathbf{S}_e$ is the measurement error covariance matrix, γ is a factor that determines the strength of the regularisation matrix $\mathbf{R}$.

Since the linear retrieval uses entire emission bands rather than just microwindows, the analysis of a single tangent height involves several thousand spectral points. Thus, inverting the apodization-induced correlated error covariance matrix becomes a time consuming process (computationally expensive as running the radiative transfer model in the iterative schemes).

This processing time can be reduced by noting that the apodization only correlates adjacent spectral points and therefore the error covariance matrix is a band matrix[1]. Hence, the matrix can be inverted storing only the non-zero values saving a lot of CPU usage. However, this inversion is still too computationally expensive to process the MIPAS data operationally.

Although an easy solution will be to neglect the apodization-induced correlations (i.e. the covariance matrix will be just a diagonal matrix), it has been shown that neglecting the effects of the apodization could induce systematic discrepancies [Boone et al., 2002]. As an alternative, the almost negligible MIPAS NESR variation through the day can be exploited. That is to say, the error covariance matrix can be inverted just once each day allowing for the minor changes in each scan by

$$\mathbf{S}_\epsilon^{-1} = \mathbf{S}_{\epsilon_0}^{-1}\left(\frac{\epsilon}{\epsilon_0}\right)^{-1} \tag{7.17}$$

where $\mathbf{S}_\epsilon$ is the updated error covariance matrix, $\mathbf{S}_{\boldsymbol{\epsilon_0}}$ is the error covariance matrix constructed with the error of the first scan (ϵ_0), and ϵ is error associated with the current scan.

Figure 7.10 displays the error estimate of the linear pT retrieved values corresponding to the characteristic noise present in MIPAS radiances for different approximations of the measurement error covariance matrix. As can be expected, the error (either for pressure or temperature) increases with height due to the signal lost attributed to the exponential decrease of the pressure and the cold temperatures of the upper mesosphere.

[1] A sparse matrix whose non-zero values are around the main diagonal

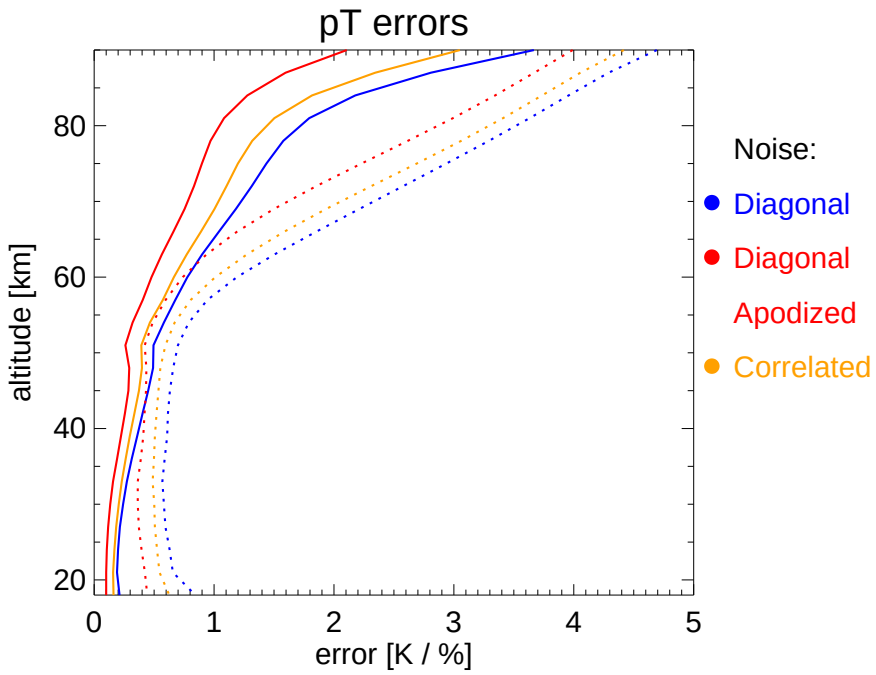

Figure 7.10: Error estimates for pressure (dotted line) and temperature (solid line) values retrieved linearly for different approximations to the error measurement covariance matrix. Midlatitude conditions were used for the Jacobian calculations

As shown, the error computed when taking into account the correlations among adjacent points is a compromise between the estimated error for a unapodized diagonal noise vector and the estimated error for a apodized diagonal noise vector. It should be noted that in this error estimate it is assumed that there is no influence of nonLTE emissions, hence, when dealing with real data the pT error estimates for upper mesospheric altitudes will be optimistic.

7.3 pT retrievals

As an example, the scan 14 (around 38 N during daytime) of orbit 28800 (an orbit on the 3rd of September 2007) will be linearly retrieved and compared against the MORSE pT results. In this case the lower limit is given by the lowest level (18 km) of the MIPAS MA mode and the upper limit was set to 90 km where the temperature and pressure errors are around 3 K or 5% respectively (matching also the MORSE MA altitude range). For the initial guess simulations midlatitude conditions were used. Spectral masks were used to isolate CO_2 emission lines.

To illustrate some of the practical considerations discussed in section 7.2, Figure 7.11 shows the retrieved values for three different constraining conditions on top of the corresponding MORSE pT retrievals and the initial guess profile (midlatitude conditions). It also shows the difference between

MORSE, the IGs and the linearly retrieved values. Note that the difference between MORSE and the IG is less than 10 K up to around 1 hPa and up to around 20 K for lower pressures, which implies that, according to the estimates performed in section 7.1.3, the linearity should hold within an error margin of 3 K.

The first retrieved profile shown (Linear) corresponds to a retrieval performed assuming a constant and uncorrelated noise across the measurements without any hydrostatic constraint. This profile follows closely the MORSE result up to 0.03 hPa where the temperature suddenly drops. At this level, the pressure retrieved was also nonphysical.

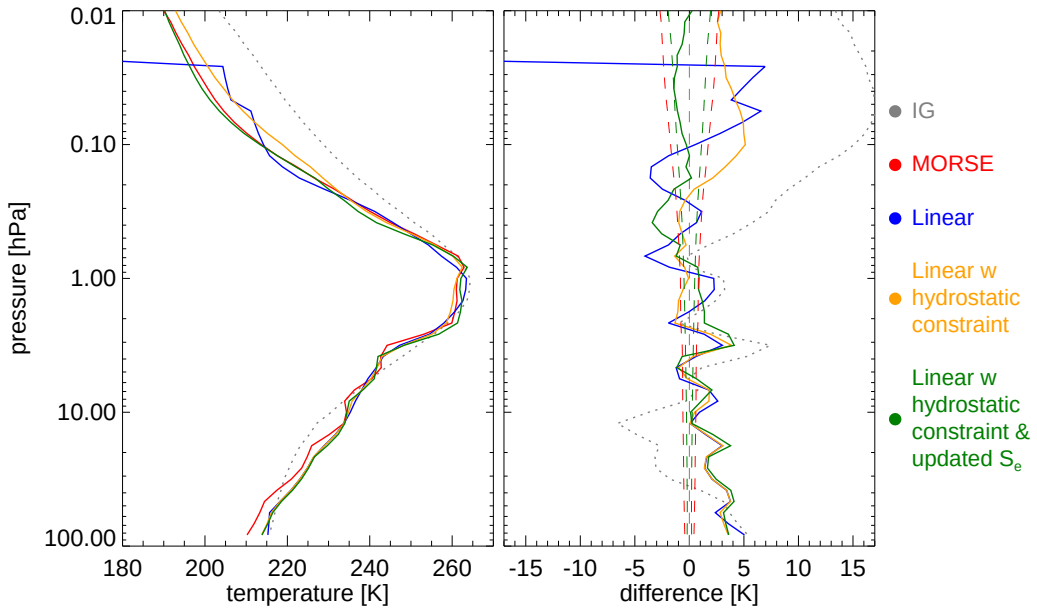

Figure 7.11: pT retrieval at different stages to see the improvements of the hydrostatic constraint and using the full measurement error covariance matrix. The MORSE and 'Linear w hydrostatic constraint & updated $\mathbf{S}_\epsilon$' errors are also shown. The gray dotted line shows either the IG profile (left) or the difference between the IG and MORSE (right)

The following profile shown corresponds to a retrieval performed assuming the same noise but using the pointing information to hydrostatically constrain the pT retrieval (Linear w hydrostatic constraint). As can be seen, the retrieval improves considerably not only avoiding the temperature drop out above 0.03 hPa but also reproducing better the features found in MORSE temperature (such as the stratopause at around 1hPa).

In order to improve the linear retrieval, an appropriate error covariance matrix needs to be used to properly weight the least square fit. The last profile shown displays the result of using the appropriate error covariance matrix and the hydrostatic constraint (Linear w hydrostatic constraint and updated $\mathbf{S}_\epsilon$). As can be noted, the linear retrieval improves considerably at high altitudes.

Note that theoretically the linear retrieval is more precise.

7.3.1 pT linearization points

So far, it has been shown that the pT linear retrieval agrees with a given pT MORSE results when the hydrostatic constraint and a proper covariance matrix are used. However, the scan retrieved was chosen to be close to the initial guess (midlatitude conditions) and, obviously, the linearity depends on the proximity of the solution to the linearization point. So the next question to answer is whether the linear retrieval can use climatological profiles as linearization points to retrieve true profiles.

Figure 7.12 shows the temperature variation against a global mean profile for the MIPAS MA viewing mode days available in June, July and August for 2007, 2008 and 2009. These months are expected to exhibit the largest atmospheric variation (i.e. the polar winter and the polar summer temperatures). It also shows the variation encountered about a mean profile for 60° and for 30° latitude bins.

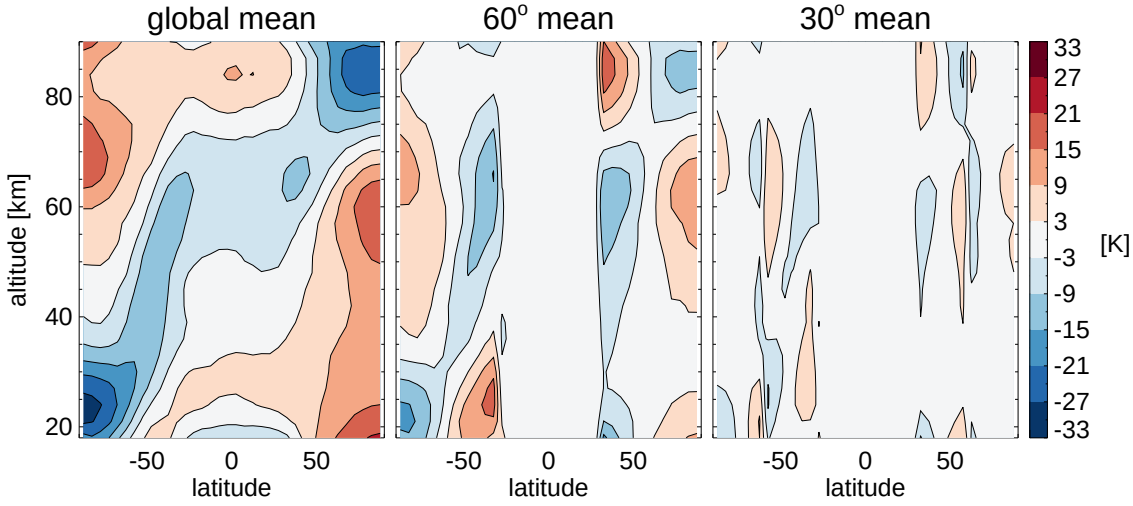

Figure 7.12: Temperature variation about a Global (left), 60° (middle) and 30° (right) latitude bin profiles for June, July and August for 2007, 2008 and 2009

As can be seen an IG for every 30° is needed in order to have a variation in each bin of equal or less than the 10K proximity that seems to be required for a successful linear retrieval (section 7.1.3).

Figure 7.13 shows the pressure variation. This also suggests that the pressure retrieval needs an initial guess for every 30° to ensure that the difference between the IG and the atmospheric state is less than the required 20% proximity. Unfortunately this IG climatology has not been yet created, instead, an IG ensemble has been used to study further this algorithm.

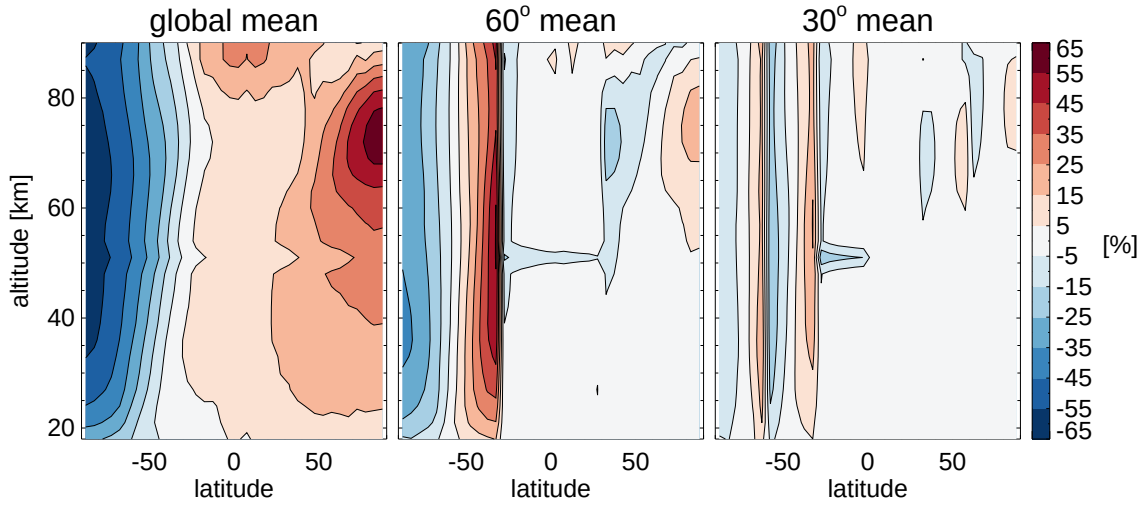

Figure 7.13: Pressure variation about a Global (left), 60° (middle) and 30° (right) latitude bin profiles for June, July and August for 2007, 2008 and 2009

7.3.2 Multiple linearization points

It should be noted that there is no intrinsic limit to the number of different initial guesses that can be used. Within an initial guess ensemble, the initial guess that minimizes a χ^2 function (i.e., the square of the residuals between the measurements and the expected spectrum for the linearly adjusted profile) can be used. The χ^2 function suggested for this purpose is,

$$\chi^2 = \frac{[\mathbf{y} - [\mathbf{F}(\mathbf{x}_0) + \mathbf{K}(\mathbf{x} - \mathbf{x}_0)]]^T \, \mathbf{S}_e^{-1} \, [\mathbf{y} - [\mathbf{F}(\mathbf{x}_0) + \mathbf{K}(\mathbf{x} - \mathbf{x}_0)]]}{\mathbf{y}^T \mathbf{y}} \tag{7.18}$$

where the $\mathbf{y}^T\mathbf{y}$ term is needed to weight the residuals according to each tangent height radiance strength and where the error covariance matrix is approximated as $\mathbf{S}_e = \sigma\mathbf{I}$ (only for the selection process).

The current implementation of the linear retrieval uses five IGs corresponding to equator, midlatitude day, midlatitude night, polar summer and polar winter conditions. Figure 7.14 shows the IGs selected for the 7th June 2007 using equation 7.18.

As shown, this criterion is selecting for the south pole mostly the polar winter IG while for the north pole mostly the polar summer IG which are the expected choices. For equatorial and midlatitude conditions this criterion is selecting a mixture of the day, night midlatitude and the equatorial IG. It seems that this criterion needs to be improved (for instance, using the Solar Zenith angle information to weight the criterion towards the corresponding IG profile).

In order to add more linearization points, simulated spectra would need to be created first. This

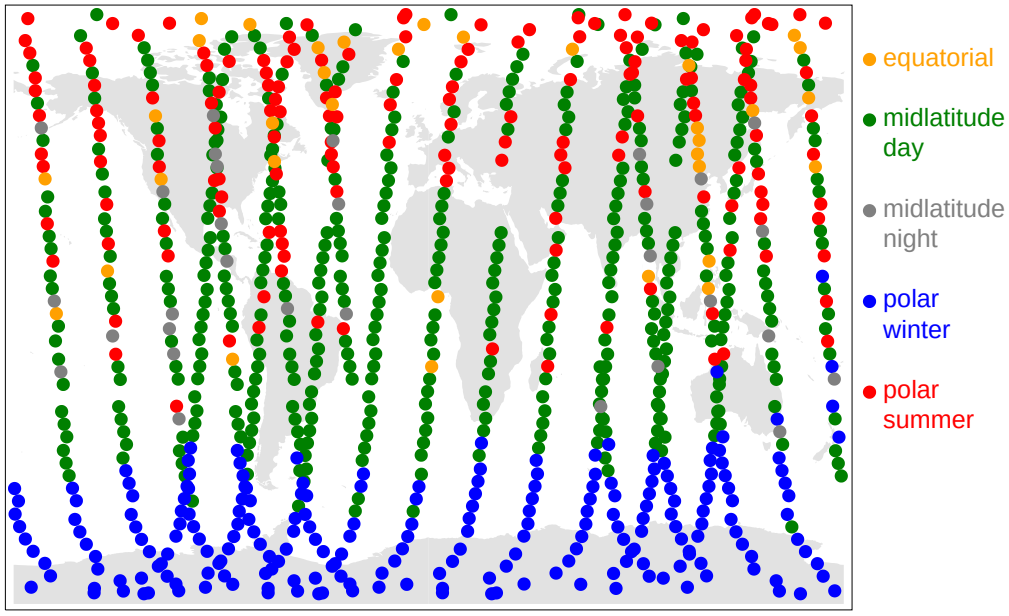

Figure 7.14: IGs selected within an IG ensemble (equatorial, midlatitude day, midlatitude night, polar summer and polar winter profiles) using equation 7.18 for the retrieval of 7th June 2007.

implies simulating LTE general spectra (including most of the infrared emitting gas), and spectra for the molecule of interest in LTE and nonLTE (for the masking process) as well as the Jacobians.

7.4 pT evaluation

To gain an idea of the performance of the linear retrieval Figure 7.15 shows a zonal mean comparison for the 7th June 2007 between the linear retrieval and MORSE. It also displays the CIRA climatology for that period.

The linear retrieval results display the structure shown in the climatology data and in MORSE with cold temperatures in the polar summer mesopause ($>$50 N for this day) and a higher stratopause in the polar winter ($<$50 S). However, as seen in the absolute difference subplot, compared to MORSE the linear retrieval seems to overestimate the temperatures for pressure between 0.1 hPa and 0.03 hPa at all latitudes and underestimat the temperature for smaller pressures. For pressures greather than 0.1hPa there seems to be in general no significant difference between the linear and the MORSE results.

Figure 7.16 shows a comparison of of coincident profiles between the linear retrieval and MLS, HIRDLS, SABER, SMR, ACE and SOFIE datasets following the methodology established in chap-

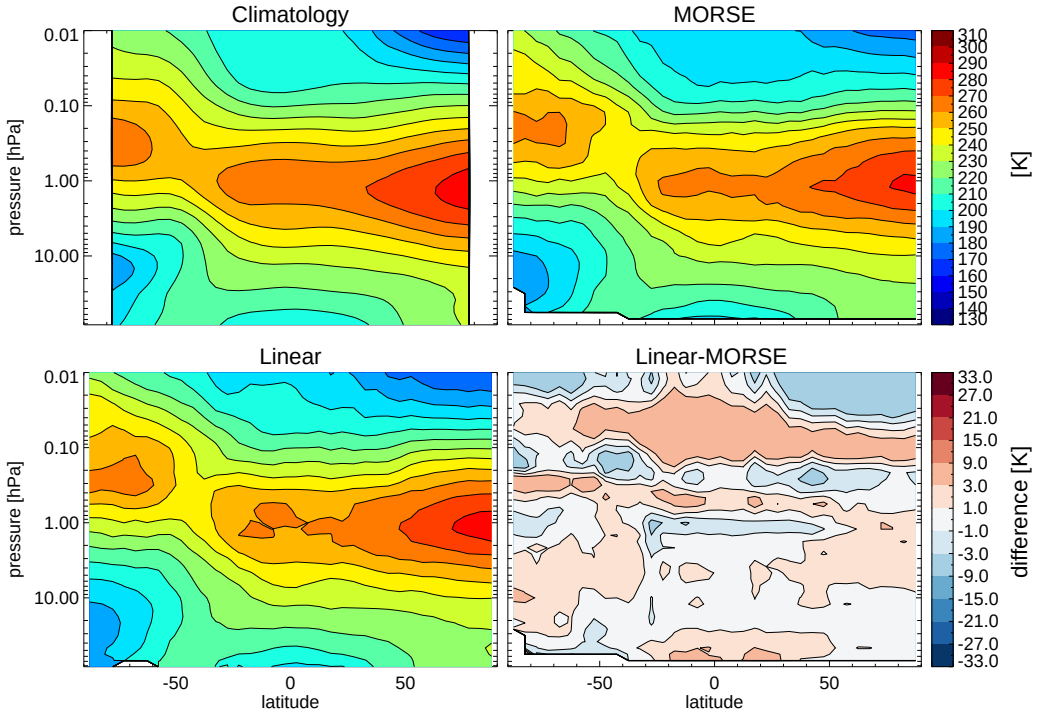

Figure 7.15: Temperature zonal mean for the 7th June 2007 for climatology, MORSE and the linear retrieval. The top row displays climatology and MORSE while the bottom row displays the linear retrieval results as well as the absolute difference between the two retrievals (linear−MORSE).

ter 6.

Most of these biases are within the expected climatological variability (following Remedios et al. [2007]) for the three seasonal bins, the linear−SABER comparison being the exception which show clear anomalies in the winter and summer bins and which also shows a high variability in the standard deviation subplots.

In the winter seasonal bin, most of the biases (disregarding the SABER bias) are within a 3 K difference at all pressure levels. One exception is the bias found when comparing against MLS which shows positive values up to around 10 K around 0.03 hPa. In the equatorial seasonal bin, the three seasonal bias shown are within 3 K at practically all the pressure levels, the exception again being the MLS bias again at 0.03 hPa.

For the summer seasonal bin, most of the biases displayed agree within 3 K up to 0.3 hPa. The SMR bias is the exception displaying an underestimation between 0.2 hPa and 0.1 hPa. For pressures lower than 0.3 hPa, most of the ACE, SOFIE, SMR and MLS biases indicate that the linear retrieval is overestimating the temperature by 5 K when comparing against ACE and by 10 K when comparing against SOFIE, SMR and MLS.

A comparison of Figure 7.16 and Figure 6.8 (the equivalent profile by profile comparison between MORSE and the other instruments) shows that the biases found when using the linear retrieval are similar to those found when comparing the MORSE results, i.e. the linear retrieval agrees more closely with MORSE that other instruments.

To summarize the difference between the linear and MORSE retrieval results, Figure 7.17 shows a profile by profile comparison between the linear retrieval and MORSE for the same days as in Figure 7.16 divided in seasonal bins. The seasonal bins were constructed exactly as before (either Figure 7.16 or Chapter 6).

As in the zonal mean comparison for the 7th June 2007 (Figure 7.15), there seems to be an overestimation of the temperature by the linear retrieval in the three seasonal bins for pressures lower than around 0.1 hPa. This overestimation is around 3 K for the winter and equator and up to around 10 K for the equatorial and summer one. For greater pressures the bias found is less than 3 K.

7.4.1 Equatorial tide

To investigate the linear retrieval sensitivity at upper mesospheric pressures, Figure 7.18 shows the day−night difference of mean profiles between 5 S and 5 N for MORSE, MLS and the linear retrieval. As shown, the tide signatures derived from MORSE and the linear retrieval data are remarkably similar up to 0.5 hPa. Within this pressure levels, the MLS tide signature is also similar, the small differences are probably just a consequence of the different local solar times of the observations.

For smaller pressures while MLS shows the expected behaviour (a sinusoidal wave with an exponential increase), MORSE and the linear retrieval display odd values. MORSE seems to be losing sensitivity presumably due too using to much *apriori* information and the linear retrieval, although it seems to be retrieving the right structure the maxima around upper mesospheric heights seems to be to high presumably as a consequence of the regularization used.

7.5 VMR practical considerations

Once the pT conditions of the scene are known the gas concentrations may be retrieved since the only remaining unknown in the radiative transfer model equation is the VMR concentration. Hence, the gas of interest can be retrieved selecting an spectral region where it is the principal emitter or where the emissions of the other gases are already accurately known.

In order not to avoid running the radiative transfer model during the linear inversion scheme,

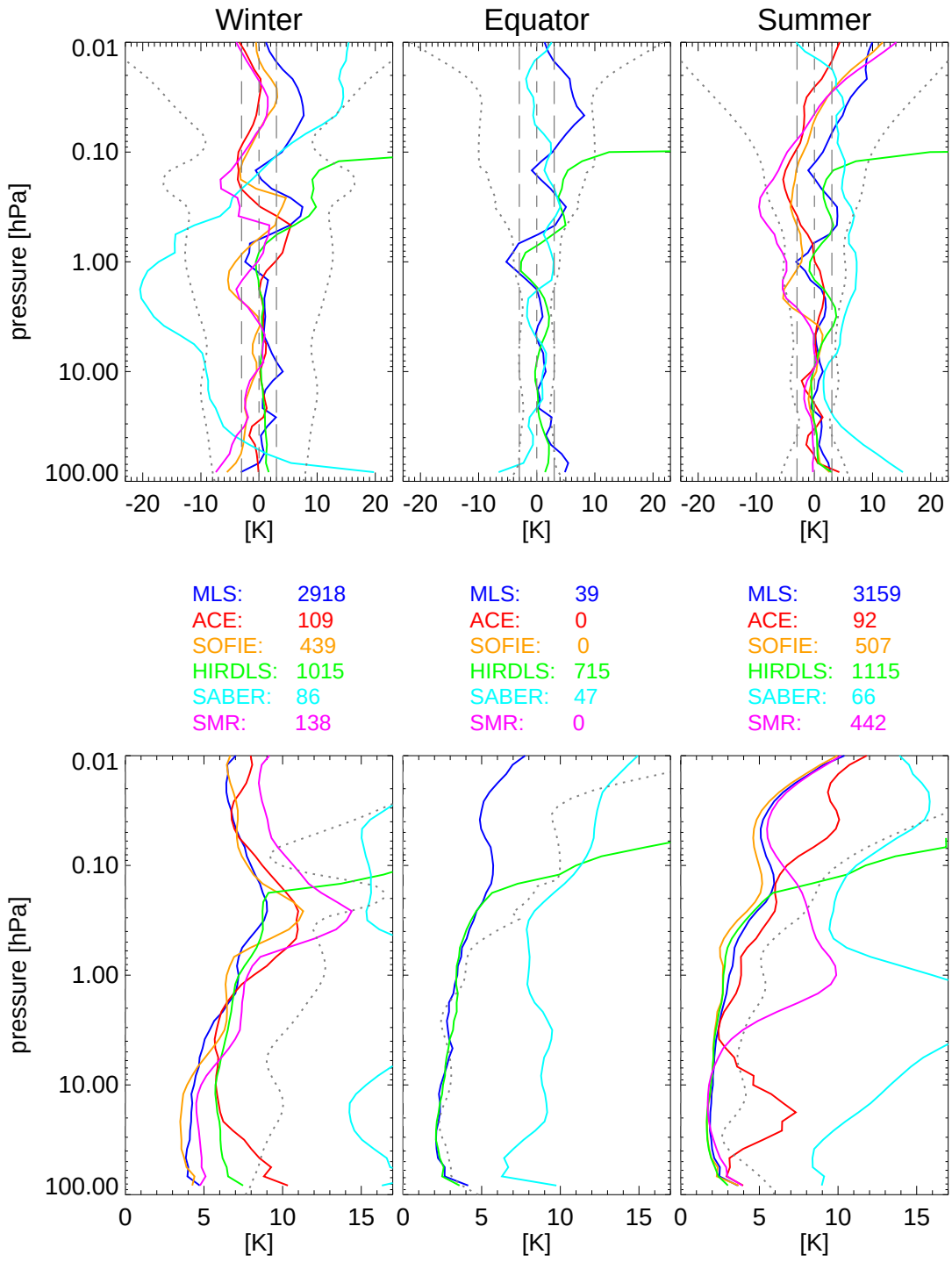

Figure 7.16: Seasonal temperature biases (top) and scatter (bottom) between linear retrieval six datasets (Linear−satellite). The gray dotted line (top) shows the expected temperature variability over the corresponding season while the gray dashed line shows a 3K difference. The Winter, Equator and Summer bins correspond to latitudes 90 S−50 S, 20 S−20 N and 50 N−90 N sorted according to the day analyzed.

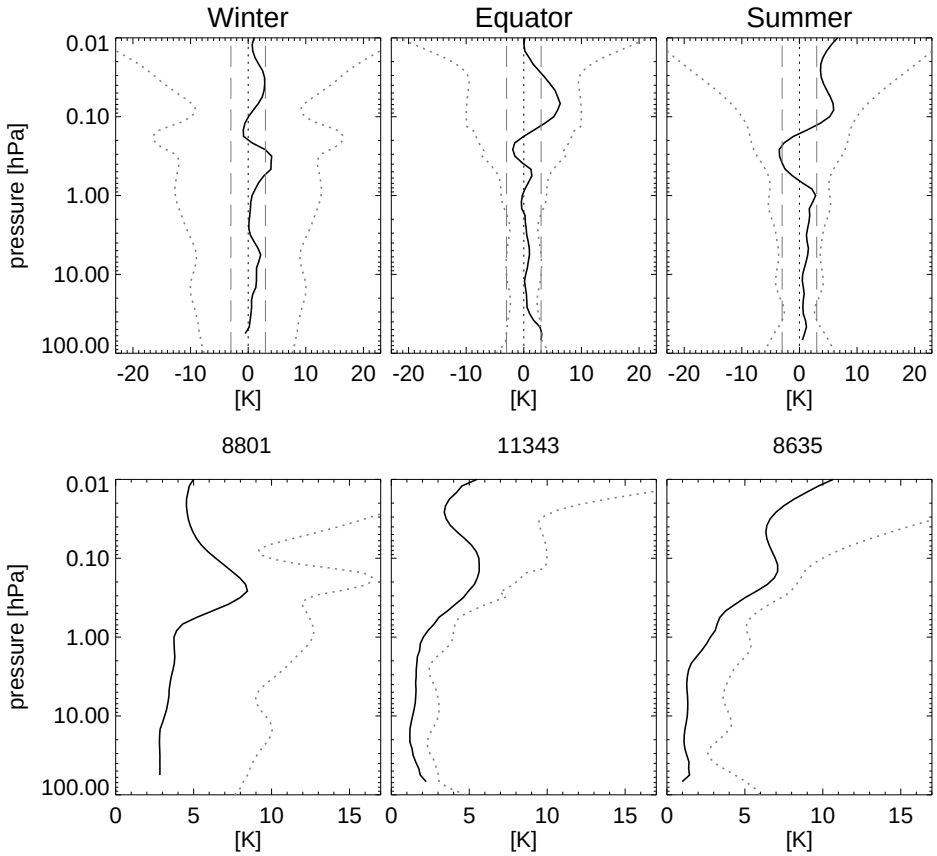

Figure 7.17: Seasonal temperature biases (top) and scatter (bottom) between linear retrieval and MORSE (LMR−MORSE). The gray dotted line (top) shows the expected temperature variability over the corresponding season while the gray dashed line shows a 3 K difference. The Winter, Equator and Summer bins correspond to latitudes 90 S−50 S, 20 S−20 N and 50 N−90 N sorted according to the day analyzed.

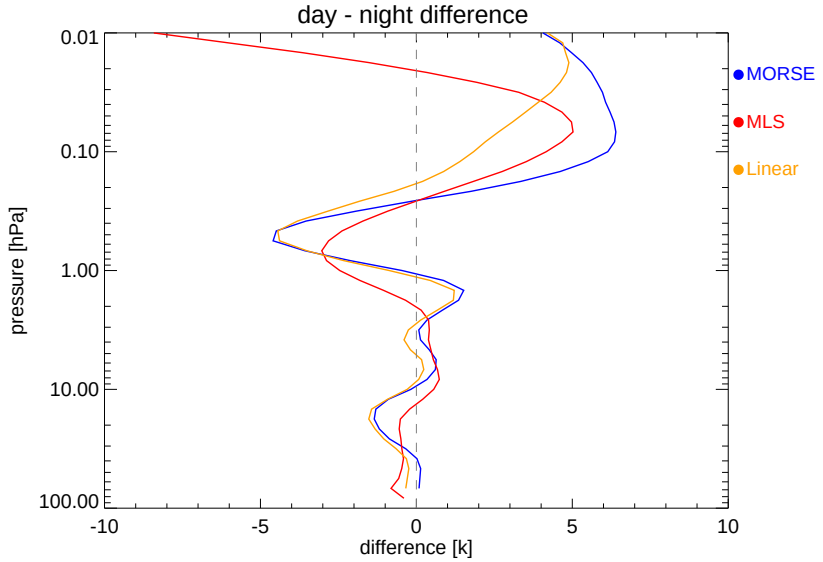

Figure 7.18: Day−night difference between 5 S and 5 N for MORSE, MLS and the linear retrieval revealing the equatorial solar tide as retrieved by each instrument.

the precomputed forward model simulations and Jacobians that were calculated for given pT IG conditions and have then to be adjusted to the pT conditions of the scene. These two adjustments (one for the forward model simulations and one for the Jacobians) are detailed in the following sections.

As for the pT retrievals, the VMR retrievals will be influenced by overlapping emissions of other gases and by nonLTE processes. The influence of the former can be reduced using spectral masks as described in section 7.2.1 while the influence of the nonLTE emissions could be reduced using spectral masks as described in section 7.2.2.

The measurement noise can be treated as described in section 7.2.4 and it will be the factor that determines the random error in the retrieved gases. Figure 7.19 shows the error estimate for several gases retrieved linearly using the noise present in MIPAS radiances (using an apodized correlated measurement error covariance matrix). As can be noted, most of these gases reach a 30% error near the upper stratosphere lower mesosphere region. These high error estimates are the upper limit of the linear retrieval. Above these altitudes, the retrieved values are dominated by noise. Although coaddition[2] could be used to retrieve gases concentrations at upper mesospheric altitudes, this approach is not pursued here.

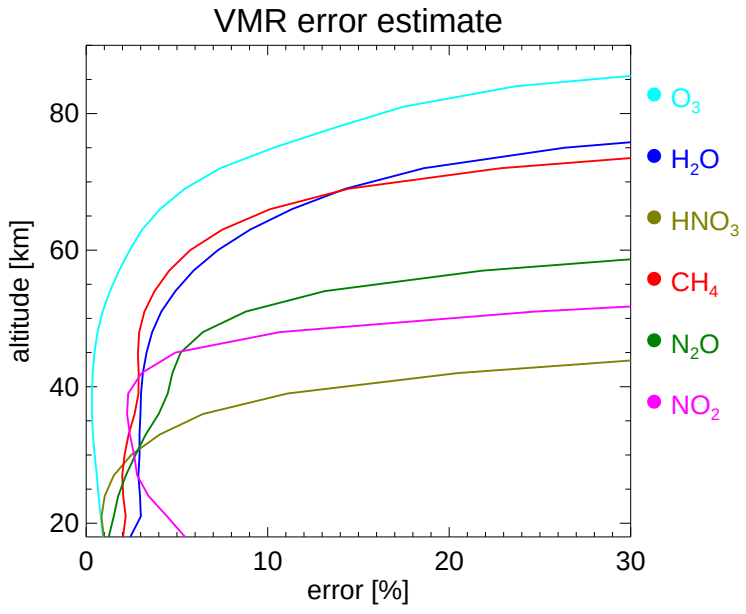

Figure 7.19: Random error estimates (assuming an apodized correlated measurement error covariance matrix) for different gases retrieved linearly when using midlatitude day-time conditions for the Jacobian calculations

[2]For instance, retrieving the products an averaging afterwards or averaging the radiances and then performing the retrievals.

7.5.1 VMR linearization points

As with temperature and pressure Figure 7.20 shows the CH_4 variation against a global, 60° and 30° latitude bin mean profiles for the MORSE MA mode days available in June, July and August for 2007, 2008 and 2009. As can be seen, even for a 30° climatology the variability may be up to 60%. Unfortunately, according to section 7.1.1, in order to achieved less than a 2% error margin due to the linearization of the forward model, the difference between the actual profile conditions and the initial guess needs to be less than 20%.

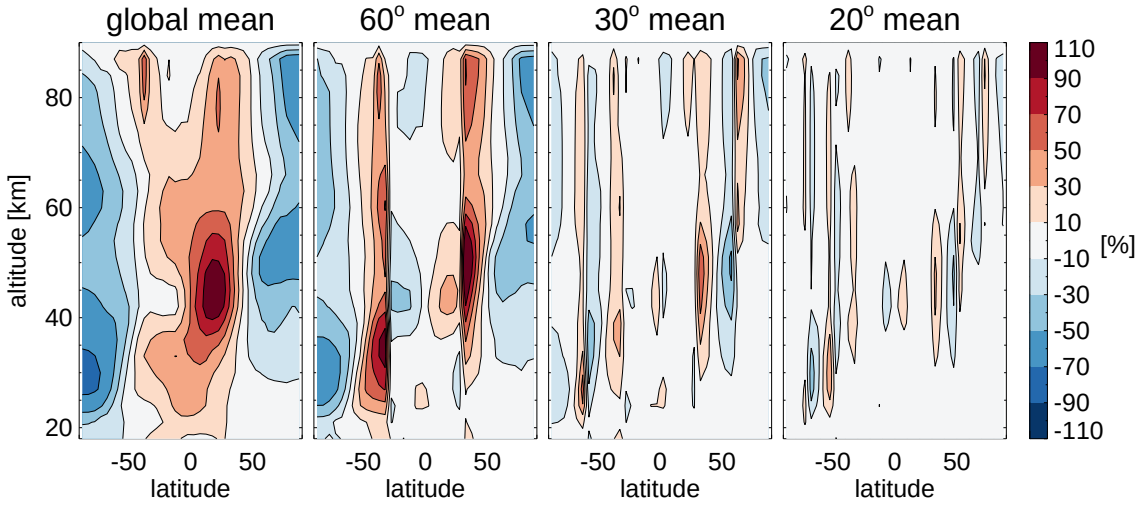

Figure 7.20: CH_4 variation about a Global, 60°, 30° and 20° latitude bin profiles for June, July and August for 2007, 2008 and 2009.

This Figure also shows the variation against a 20° latitude bin mean profile. As can be seen, a 20° climatology will be needed to ensure the required proximity.

7.5.2 VMR multiple linearization points

Currently, the VMR linear retrieval uses the same IG as selected as the best fit during the pT retrieval. However, if a climatology is built, retrievals for different CH_4 concentrations simulated for a given pT conditions (matching the ones used for the pT retrievals) can be performed selecting the best fit using equation 7.18 as criterion.

7.5.3 VMR forward model pT adjustment

The simulated spectra can simply be modified using the temperature and pressure Jacobian of the corresponding spectral range, i.e.,

$$\mathbf{F}^*(\mathbf{x}) = \mathbf{F}(\mathbf{x}_0) + \mathbf{K}_{\mathbf{T}_0}(\mathbf{T} - \mathbf{T}_0) + \mathbf{K}_{\mathbf{P}_0}(\mathbf{p} - \mathbf{p}_0) \tag{7.19}$$

where $\mathbf{F}^*(\mathbf{x})$ is the corrected spectrum for the actual pT scene conditions (**p**,**T**), $\mathbf{F}(\mathbf{x}_0)$ is the IG simulated spectrum and $\mathbf{K}_{\mathbf{T}_0}$ and $\mathbf{K}_{\mathbf{P}_0}$ are the IG temperature and pressure Jacobians respectively.

Figure 7.21 shows (left subplots) the linearity of the forward model for CH_4 spectral points due to changes in temperature (testing the '$\mathbf{K}_{\mathbf{T}_0}(\mathbf{T} - \mathbf{T}_0)$' term of equation 7.19). For these simulations CH_4 concentrations remain constant while temperature varies. As portrayed, for changes up to 10 K, the actual – estimated spectral difference is less than 10%.

This Figure also displays (right subplots) the CH_4 linear retrievals for such temperature increments. As shown in the actual – retrieved graph, for changes up to 10K, the difference are less than 20% practically at all heights. For a 20 K increment the retrieved values are nonrealistic, for this reason, the retrieved CH_4 corresponding to a 50 K increment is not shown.

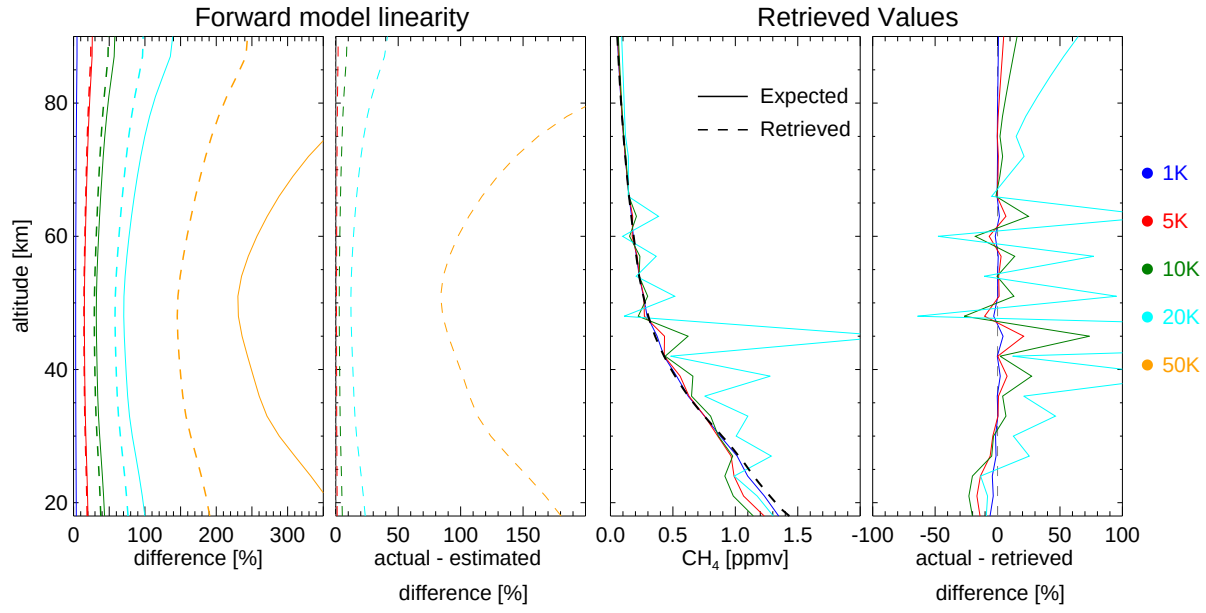

Figure 7.21: (left) forward model linearity with respect to changes in temperature when adjusting the CH_4 spectra (equivalent to Figure 7.2) (right) CH_4 concentrations linearly retrieved values after the adjustments (equivalent to Figure 7.3)

Figure 7.22 is the equivalent Figure for pressure increments (testing the '$\mathbf{K}_{\mathbf{P}_0}(\mathbf{p} - \mathbf{p}_0)$' term of equation 7.19). As can be seen (left subplots) in the actual – estimated spectral difference for changes up to 20% of the initial guess the spectral difference is less than 2%. This linearity can also be

appreciated in the corresponding retrieval subfigures (right plots). As shown in the actual – retrieved graph for changes up to 20%, the retrieval difference are for most of the heights less than 2%.

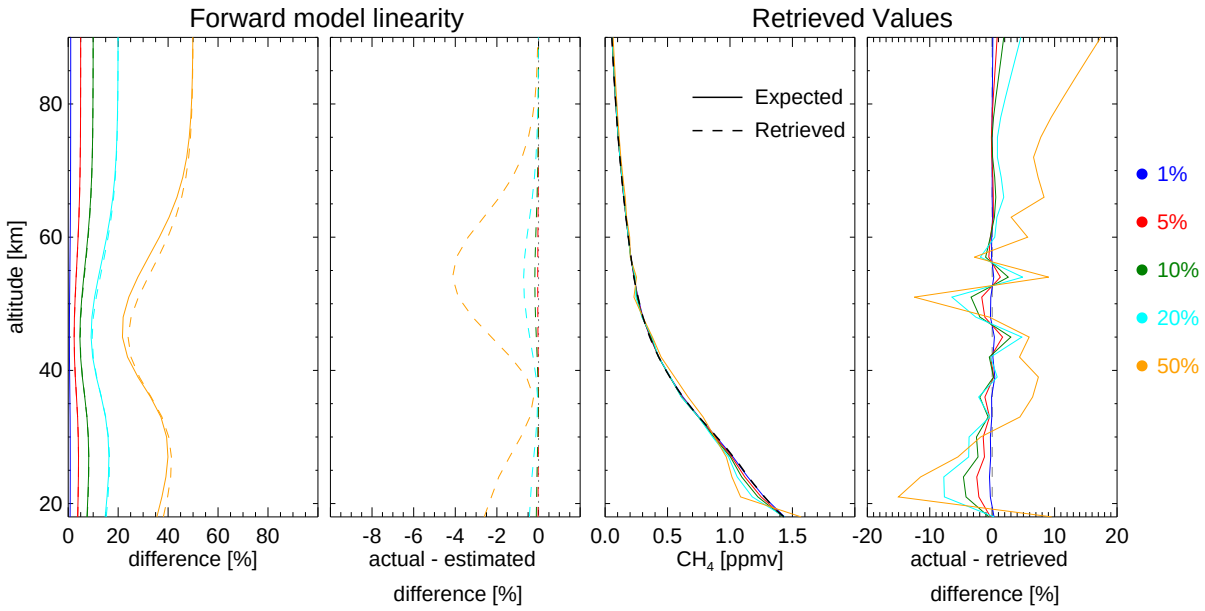

Figure 7.22: (left) forward model linearity with respect to changes in pressure when adjusting the CH_4 spectra (equivalent to Figure 7.2) (right) CH_4 concentrations linearly retrieved values after the adjustments (equivalent to Figure 7.3)

Figures 7.21 and 7.22 suggests that the VMR forward model simulations pT adjustment given by equation 7.19 may be valid as long as the temperature difference and pressure difference between the scan conditions and the IG are not greater than 10 K and 20% accordingly. Hence, as shown in section 7.3.2 a 30° bin climatology would be needed to ensure this proximity.

7.5.4 VMR Jacobians pT adjustment

As the forward model has been adjusted to the temperature and pressure of the scene, in a similar manner, the VMR Jacobians can be adjusted using,

$$\mathbf{K}_v^* = \mathbf{K}_{0v} + \mathbf{H}_T(\mathbf{T} - \mathbf{T}_0) + \mathbf{H}_p(\mathbf{p} - \mathbf{p}_0) \tag{7.20}$$

where $\mathbf{K}_v^*$ is the adjusted VMR Jacobian for the actual scene pT conditions (**p**,**T**), $\mathbf{K}_{0v}$ is the VMR Jacobian for the IG conditions ($\mathbf{p}_0$,$\mathbf{T}_0$) and where **H** corresponds to the changes of the VMR Jacobian with respect to either temperature or pressure, that is to say,

$$H_{Tijk} = \frac{\partial K_{v_{ij}}}{\partial T_k} = \frac{\partial}{\partial T_k}\left(\frac{\partial L_i}{\partial v_j}\right) = \frac{\partial^2 L_i}{\partial T_k \partial v_j} \tag{7.21}$$

$$H_{Pijk} = \frac{\partial K_{v_{ij}}}{\partial p_k} = \frac{\partial}{\partial p_k}\left(\frac{\partial L_i}{\partial v_j}\right) = \frac{\partial^2 L_i}{\partial p_k \partial v_j} \tag{7.22}$$

where i corresponds to the measurement tangent height while j and k correspond to perturbing heights. Theoretically, these matrices ranks are $m \times n \times n$ but it should be noted that (from equation 7.9),

$$\mathbf{K}_v = \frac{\partial L_i}{\partial v_j} \simeq B(T_j)\frac{p_j}{RT_j} l_j \sigma_j \tag{7.23}$$

and hence

$$\frac{\partial^2 L_i}{\partial T_k \partial v_j}, \frac{\partial^2 L_i}{\partial p_k \partial v_j} = 0 \quad \text{if} \quad k \neq j \tag{7.24}$$

$$\frac{\partial^2 L_i}{\partial T_k \partial v_j}, \frac{\partial^2 L_i}{\partial p_k \partial v_j} \neq 0 \quad \text{if} \quad k = j \tag{7.25}$$

which reduces the size of **H** to $m \times n$.

Although these matrices can be computed by perturbing height by height the temperature or pressure profiles and then subtracting the original VMR Jacobians as computed by the RFM, here a simpler technique was implemented. Noting that, while the VMR Jacobian at the scene conditions will be given by equation 7.23, the IG VMR Jacobian will be given by,

$$\mathbf{K}_{0v} = \frac{\partial L_{0i}}{\partial v_j} \simeq B(T_{0j})\frac{p_{0j}}{RT_{0j}} l_j \sigma_j \tag{7.26}$$

Hence, the IG VMR Jacobian can be modified to the pT scene conditions by,

$$\mathbf{K}_v^* = \mathbf{K}_{0v}\left[\frac{B(T_j)p_j}{B(T_{0j})p_{0j}}\frac{T_0}{T_j}\right] \tag{7.27}$$

The efficiency of this simple adjustment can be appreciated in Figure 7.23. This Figure (left) shows the actual−retrieved differences for different temperature increases when the VMR Jacobians used the pT IG conditions. Note that the only parameter that it is varying in these simulations is the temperature dependence of the VMR Jacobian to isolate its effects in the retrieval. As portrayed, the actual−retrieved difference for a 10 K change between the pT IG and scan conditions are up to 30% and for a 20 K change more than 40%.

This Figure also shows (right) the actual−retrieved differences when the VMR Jacobians (that used the pT IG conditions) were adjusted using equation 7.27. As can be seen the actual−retrieved differences are significantly reduced less than 10% for up to a change of 20 K and for 50 K change, less than 20%.

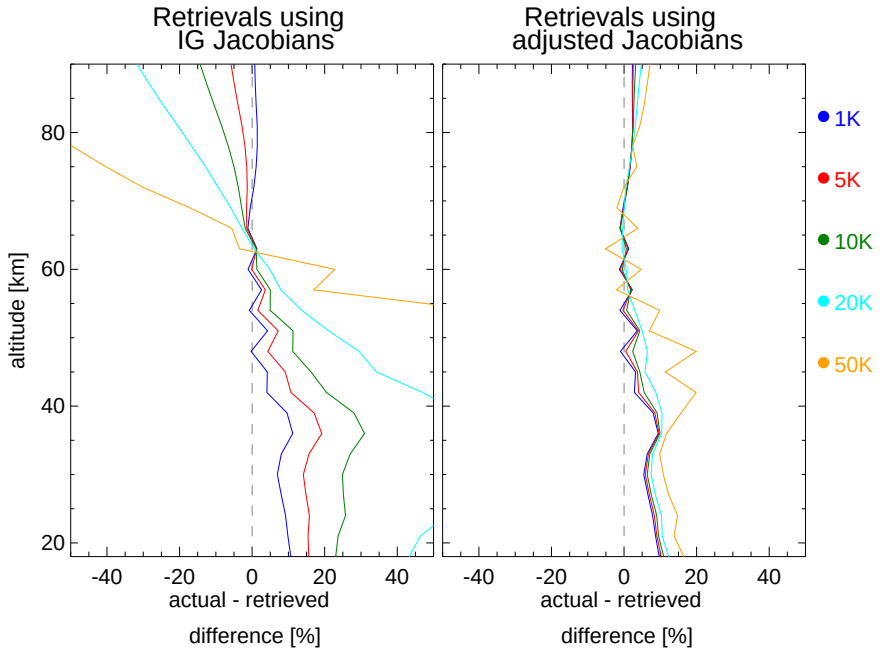

Figure 7.23: Difference between the actual and linearly retrieved CH_4 concentrations for different temperature increases when using the IG Jacobians (left) and when adjusting the IG Jacobians to the new temperature conditions (right).

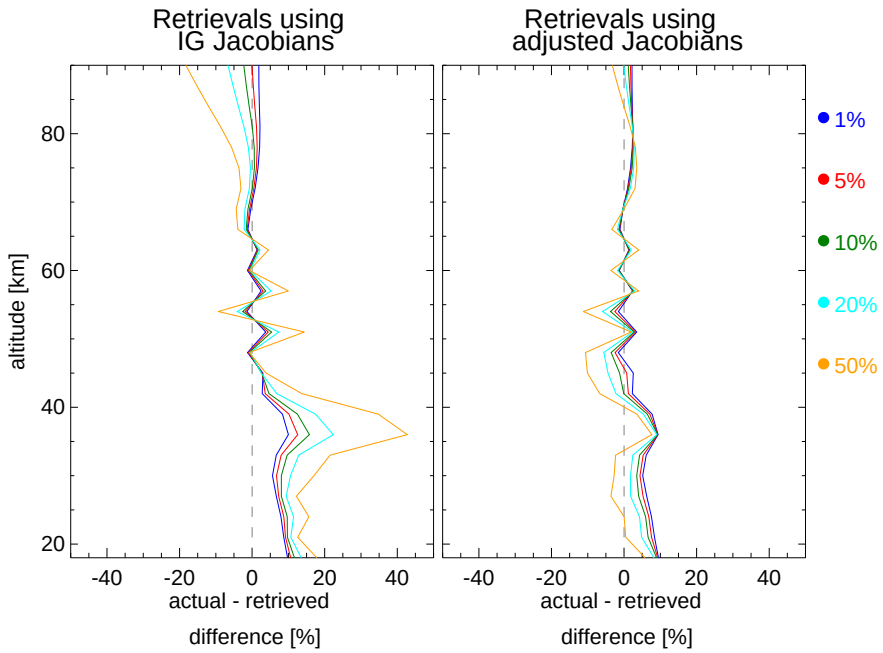

Figure 7.24: Difference between the actual and linearly retrieved CH_4 concentrations for several pressure increments when using the IG Jacobians (left) and when adjusting the IG Jacobians to the new pressure conditions (right)

Figure 7.24 is the equivalent Figure for pressure increments. As can be seen the actual–retrieved difference when the VMR Jacobians are adjusted to the pT conditions (right) of the scene are much smaller than when the VMR Jacobians are not adjusted (left).

7.6 VMR retrievals

As in section 7.3, the scan 14 of orbit 28800 were be linearly retrieved and compared against the MORSE CH_4 results. For CH_4 retrievals, the lower limit was set to the lowest level of the MIPAS MA mode (18 km) and the upper limit was set to 60 km where the error is around 10% (as shown in Figure 7.19).

To illustrate some of the VMR retrieval practical considerations discussed in section 7.5, Figure 7.25 shows the CH_4 linearly retrieved values for three different cases with the corresponding MORSE CH_4 results and the IG values (midlatitude conditions).

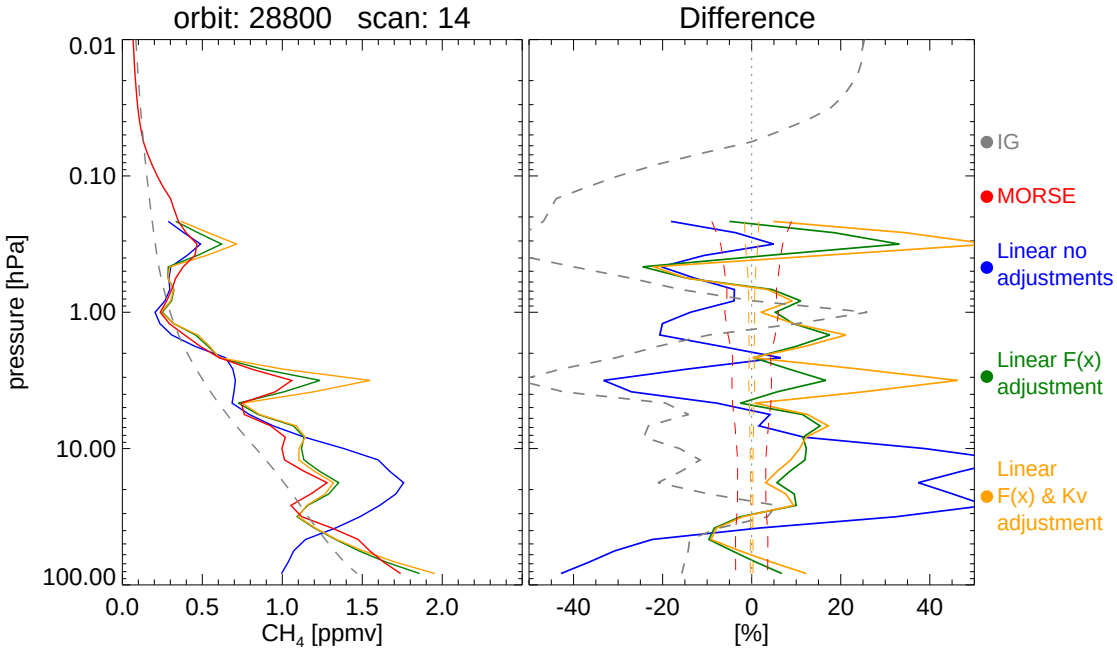

Figure 7.25: (left) CH_4 VMR retrieved linearly and (right) percentage difference (MORSE−other). The MORSE and 'Linear w F(x) and K_v adjustment' errors are also shown.

The first profile (Linear no adjustments) corresponds to a linear retrieval performed when neither the forward model simulations nor the VMR Jacobians has been adjusted to the pT scene conditions. The percentage difference between MORSE and this profile are up to 50%. The following profile shown (Linear F(x) adjustment) corresponds to a retrieval performed when the forward model simulations have been adjusted to the pT scene conditions using equation 7.19 but still using the VMR Jacobian for the IG conditions. This profile resembles well the structure shown in the MORSE profile and the percentage differences were reduced to less than 20% for most of the pressure levels.

The last profile shown (Linear F(x) and $\mathbf{K}_v$ adjustment) displays the CH_4 concentration retrieved when the forward model simulations have been adjusted using equation 7.19 and the VMR Jacobians

using equation 7.27. As can be noted for most pressure levels the result does not change much when implementing the VMR Jacobian pT adjustment and furthermore at some pressure levels the percentage difference has worsened. Note that theoretically the linear retrieval is more precise.

Although as shown in Figures 7.23 and 7.24 the Jacobian pT adjustment should theoretically improve the retrievals, it seems that the forward model adjustment is not correcting properly the pressure and temperature dependence of the simulations, making the Jacobian pT adjustment unnecessary under the current linear retrieval algorithm. Hence, the following section will discuss the linear CH_4 retrievals adjusting only the forward model to the pT scene conditions[3].

7.7 VMR evaluation

Figure 7.26 displays the zonal mean CH_4 comparison between the linear retrieval and MORSE for the 7th June 2007. It also displays the IG climatology for that period. The linear retrieval shows structure found in the climatology and in MORSE, however, as seen in the percentage difference subplot, the linear retrieval seems to overestimate the CH_4 concentration by around 20% for pressures between 10 and 1 hPa.

Figure 7.27 shows a profile by profile comparison between the linear results and ACE, SOFIE and HIRDLS as well as the standard deviation of such comparisons. As in Figure 7.16, two profiles were considered coincident within 500 km and 6 hours and the seasonal bins were defined by the same latitude and the date criteria.

For pressures lower than around 5 hPa, the biases displayed in the winter bin are within the expected variability. However, the biases encountered indicate up to 50% overestimation at certain pressure levels. For pressures greather than 5 hPa the ACE bias shows a 100% difference, the HIRDLS bias up to 50% while the SOFIE bias drops below -100%.

Unfortunately, in the equatorial seasonal bin, only comparisons against HIRDLS were available and hence no conclusions can be drawn from this comparisons. In general, this bias is within the expected variability and furthermore within a 20%.

In the summer seasonal bin comparison, most of the biases are within the expected variability and in general are within a 20% difference. This seasonal bin is the only one where the standard deviation of the comparisons is within the expected variability, in the other two the standard deviation is always higher denoting the high variability of the linear results (a smaller standard deviation was found in

[3]Note that this decision was not taken based only in this example.

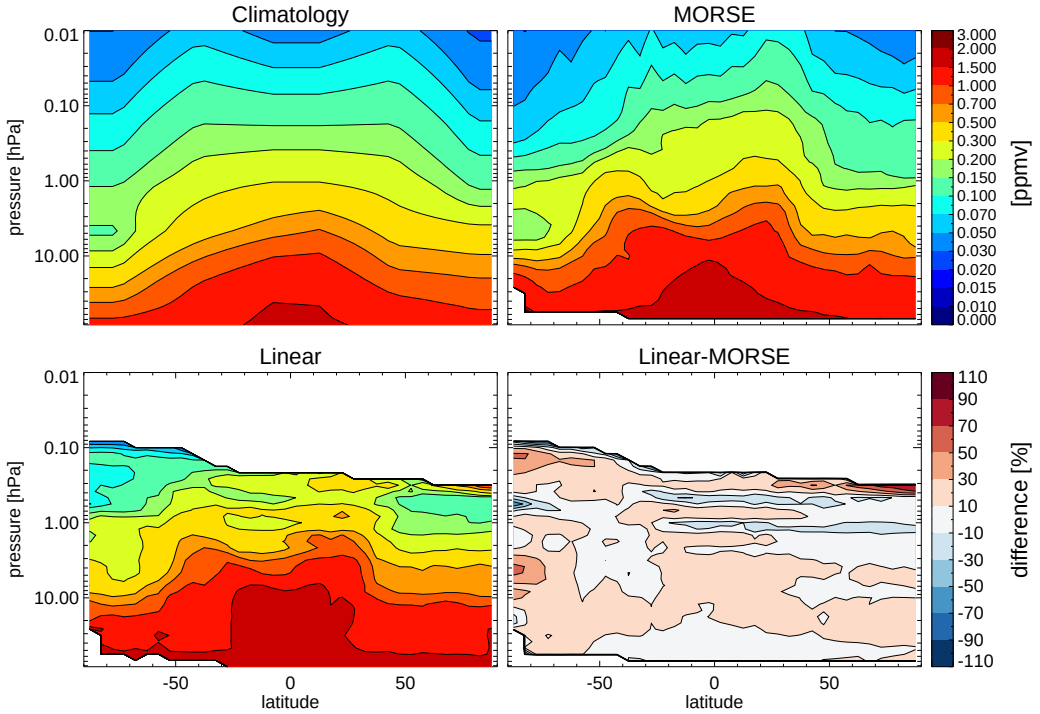

Figure 7.26: CH_4 zonal mean for the 7th June 2007 for climatology, MORSE and the linear retrieval. The top row displays climatology and MORSE while the bottom row displays the linear retrieval results as well as the absolute difference between the two retrievals (linear−MORSE).

the equivalent profile by profile comparison between MORSE and the other instruments.)

A comparison of Figure 7.27 against Figure 6.17 shows that the biases in the equatorial and summer seasonal bins are really similar to those found in the MORSE comparison. Unfortunately, it seems that the Linear retrieval is not retrieving well under polar winter conditions because the standard deviation in this seasonal bin is large and the three biases (without taking into account the SOFIE anomaly also present in the MORSE comparison) does not resemble the one found in the MORSE comparison.

To summarize the difference between the linear and MORSE retrieval results, Figure 7.28 shows a profile by profile comparison of these two approaches for the same days as before. As in Figure 7.27 the biases found in equatorial and summer seasonal bins are not only within the expected variability but also, in general, are less than 20%. The winter bias is also within the expected variability but its magnitude around 0.5 hPa is up to 50%. Note that the Linear retrieval is always overestimating the CH_4 concentrations. This overestimation may be due to not having a close enough linearization point.

Note that although the current linear VMR retrieval is probably not as good as MORSE, its results

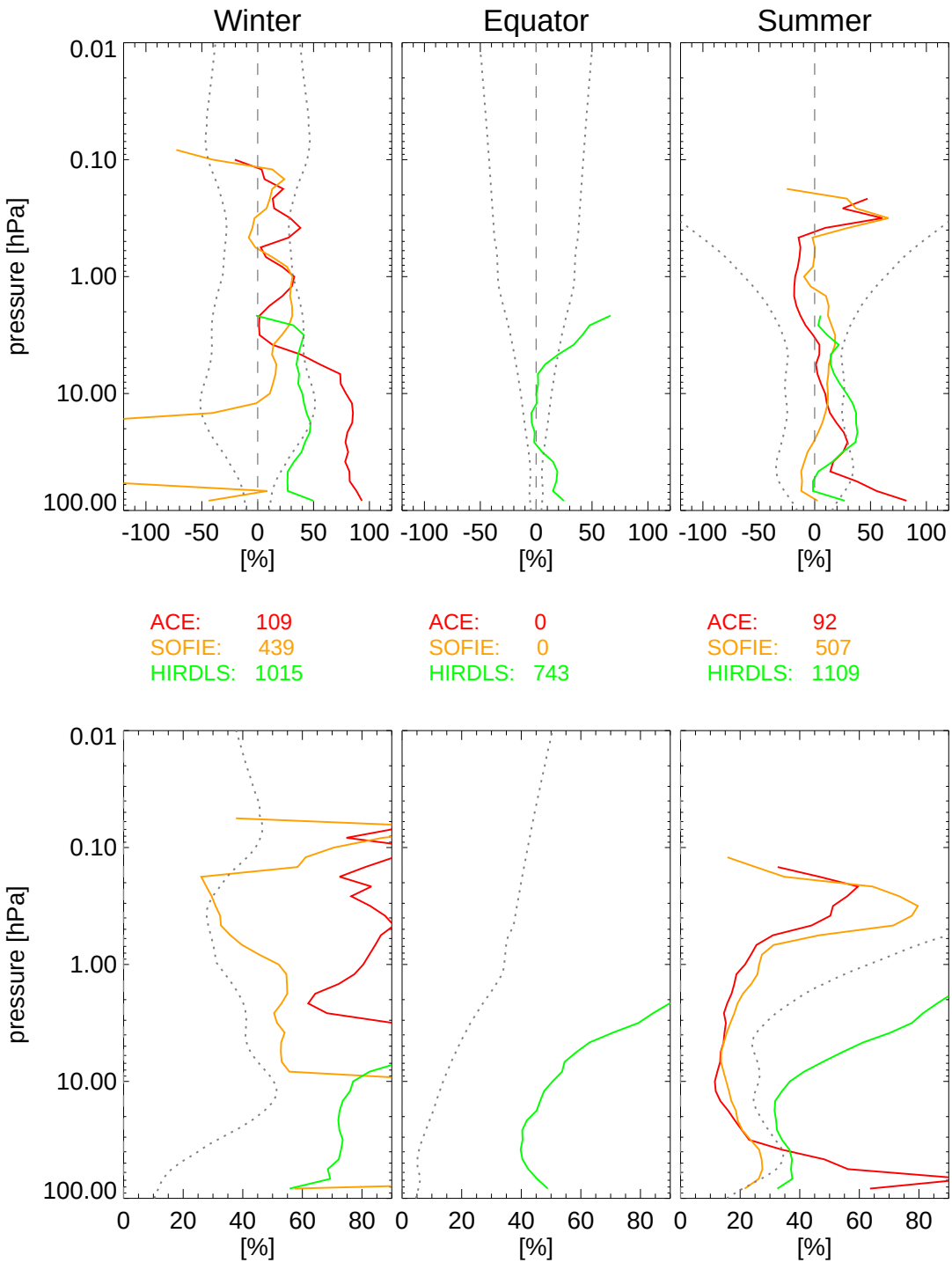

Figure 7.27: Seasonal CH_4 biases (top) and scatter (bottom) between linear retrieval and ACE, SOFIE and HIRDLS datasets (Linear−satellite). The gray dotted lines show the expected CH_4 climatological variability over the corresponding season. The Winter, Equator and Summer bins correspond to latitudes 90 S−50 S, 20 S−20 N and 50 N−90 N sorted according to the day analyzed. The number of profiles averaged is shown in the middle row.

are close enough to the MORSE solution that potentially, running the linear retrieval as a first iteration of MORSE (or any iterative scheme) should reduce the computing time considerably.

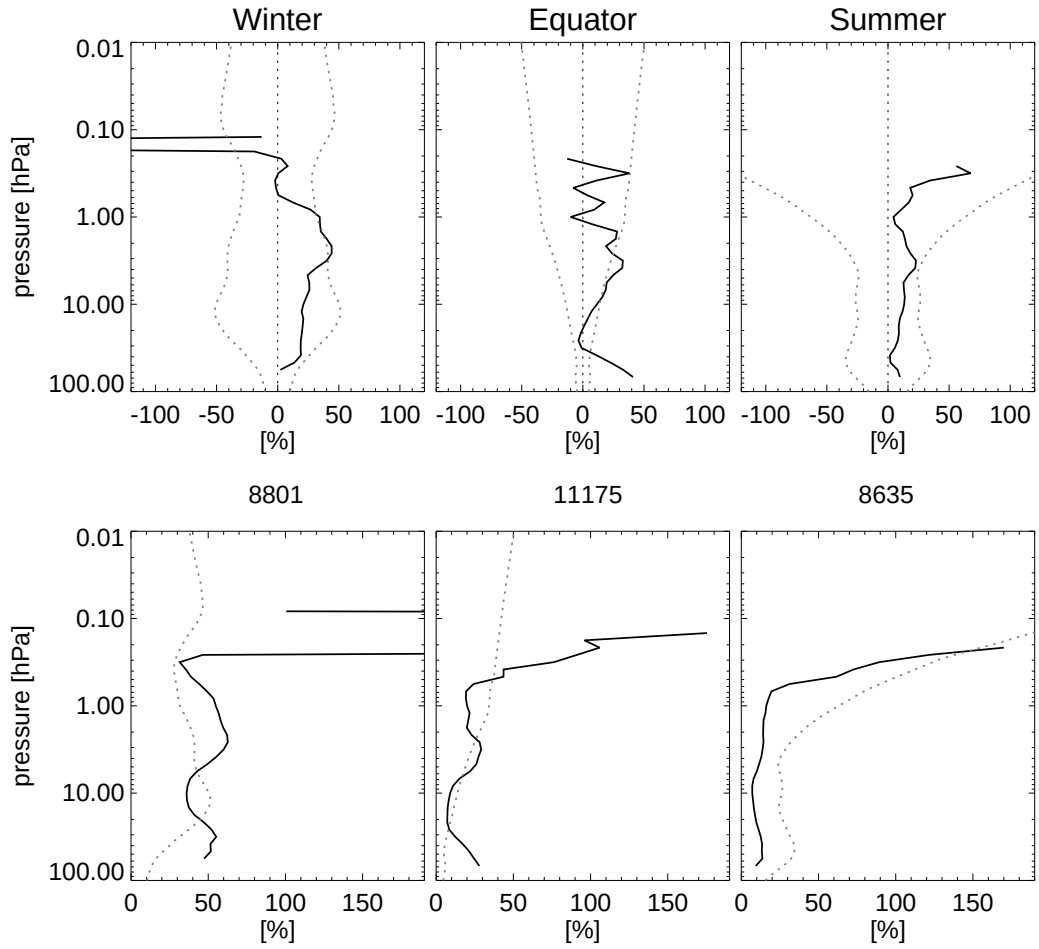

Figure 7.28: Seasonal CH_4 biases (top) and scatter (bottom) between linear retrieval and MORSE (Linear−MORSE). The gray dotted line (top) shows the expected CH_4 variability over the corresponding season. The Winter, Equator and Summer bins correspond to latitudes 90 S−50 S, 20 S−20 N and 50 N−90 N sorted according to the day analyzed. The number of profiles averaged is shown in the middle row.

7.7.1 Correlations

Correlations between the linear retrieval, MORSE and the IG has been performed (Figure 7.29) to investigate if the overestimation of CH_4 is due to the IG not being close enough to the solution.

As can be seen in the CH_4 correlation, most of the extremely high values (being either around the top of the retrieval ($\simeq 0.2$ hPa) or near the stratopause) of Linear−MORSE difference are outside the required proximity of the IG to the solution.

This figure also shows the correlation between the CH_4 linear retrieval performance against the proximity of the temperature IG to its solution. Again, most of the high values of the Linear−MORSE

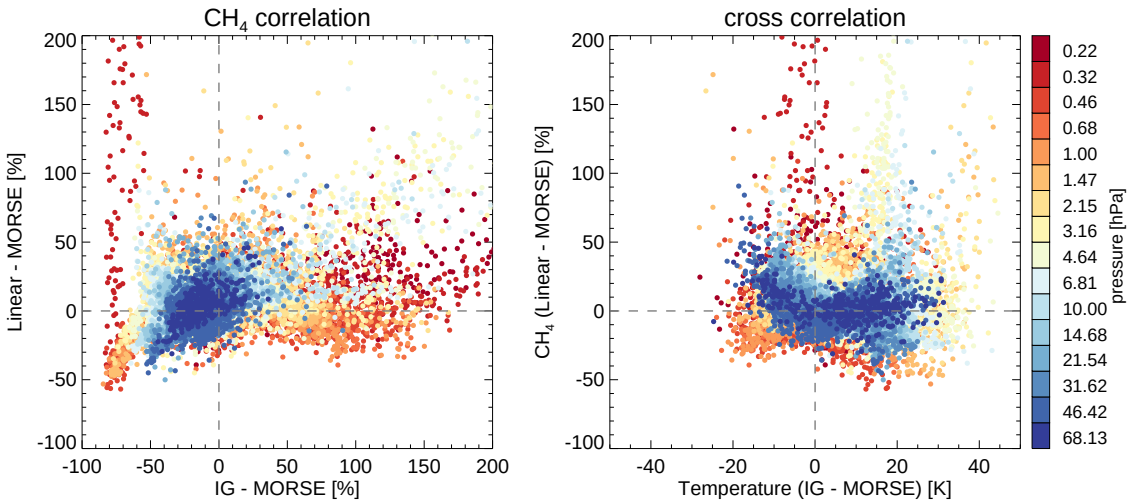

Figure 7.29: Correlations between the linear retrieval, MORSE and the IG for CH_4 and cross correlation for the 7th June 2007.

difference are outside the 10 K required proximity for the forward model pT adjustment (section 7.5.3)

These correlations suggest that when a IG climatology finer than 30° latitude is constructed, the performance of the linear retrieval should improve considerably.

7.8 Retrieval speed

An important feature of the linear retrieval is its speed. Since there is no need to run the radiative transfer model, once the error covariance matrices are inverted (only needed once a day), the main time consuming processes are ingesting the data into the retrieval and inverting the multiple pT linearization points (five in the current configuration of the scheme). Using the same computer to run MORSE and the Linear retrieval, it has been discovered that the linear retrieval is faster than MORSE at least by a factor of 20 (i.e. for a day of MA data reducing from weeks to a couple of hours) when retrieving pT and CH_4. It should be noted that speed of the linear retrieval can be improved by retrieving only some of the linearization points selecting them according to the time and latitude of the scene. Further speed may be gained by coding the linear retrieval in Fortran rather than in IDL.

7.9 Conclusions

An alternative algorithm to retrieve temperature, pressure and gas concentrations from limb viewing spectrometers has been introduced. This algorithm exploits the linear properties of an optically thin

path making it possible to perform the inversion without re-running the radiative transfer model as long as the initial guess is close enough to the scene conditions. This new algorithm uses the whole spectral band of the molecule rather than a small subset of it (the microwindows) and therefore, theoretically, leads to a higher precision.

It was shown that the retrievals of pressure, temperature and gas concentration (CH_4 in particular) can be treated linearly up to a difference between the IG and the scene conditions of 20% in CH_4 concentration for a 2% error margin due to the linearization of the problem, up to 20% pressure difference for a 3% error margin and up to 10K difference for a 3 K error margin near the stratopause and less than 1K elsewhere. In order to fulfill these restrictions it was found that a 30° latitude bin climatology was needed for pT and a climatology with finer resolution for CH_4. An alternative scheme was also presented using multiple IGs and selected the one that fits better the residuals.

This retrieval scheme was implemented using MIPAS radiances and compared to the results of several mesospheric instruments as well as the results of the iterative scheme MORSE. These comparisons revealed that the pT linear retrieval is within a 3 K range difference most of the time for pressures greater than 0.01 hPa. For lower pressures there seems to be an overestimation of the temperature by the Linear scheme varying from 3 up to 10 K depending on the season analyzed.

Unfortunately, the CH_4 linear retrieval comparison revealed an overestimation of around 20% at all pressure levels at any seasonal bin. This overestimation seems to be caused by difference between the IG and the scene conditions outside the required proximity. It should be noted that the current implementation of the linear retrieval only uses five IGs (equatorial, midlatitude day, midlatitude night, polar summer and polar winter conditions) and hence the linear retrieval performance should improve considerably once the required IG climatology is constructed.

Even if the linear retrievals are not as good as needed due to the artifacts induced by being far from of the IGs used, the results may be used as the first iteration of the iterative schemes, thereby reducing the processing time.

CHAPTER 8

NonLTE model validation

The inversion of temperature, pressure and gas concentrations from infrared measurements usually relies among other things on the assumption that the emitting species are in local thermodynamic equilibrium (LTE) [Gille and House, 1971; Rodgers, 1976, 2000]. This assumption implies that their populations are determined by the Boltzmann distribution at the local kinetic temperature and therefore the source function of the emission is given by the Planck function at this temperature.

In general, LTE conditions occur when collisions between molecules thermalize the energy level populations. Hence, at high pressures where collisions rates are high, LTE conditions tend to predominate. However, in the middle and upper atmosphere, where collisions decrease due to low pressures, several studies (for instance, Caledonia et al. [1985]; Solomon et al. [1986]; Kaye and Kumer [1987]; Kerridge and Remsberg [1989]; López-Puertas and Taylor [1989]) have shown that most of the infrared emission departs from LTE.

At low pressures, the energy level populations are controlled by radiating mechanisms and the source function is no longer given by the Planck Function but rather by the general source function (equation 2.3) and furthermore the absorption coefficient is also altered.

Following López-Puertas and Taylor [2001] the LTE calculations can be related to the nonLTE quantities by

$$J = Br_u \left(\frac{\overline{\sigma}}{\sigma}\right) \tag{8.1}$$

where J is the general source function, B is the Planck function r_u is the nonLTE to LTE population ratio of the upper level and $\overline{\sigma}/\sigma$ is the ratio of the LTE absorption coefficient to its nonLTE value. This factor is given by

$$\frac{\overline{\sigma}}{\sigma} = \frac{1}{r_l}\left[\frac{1-\Gamma}{1-\Gamma(r_u/r_l)}\right] \tag{8.2}$$

where r_l is the nonLTE to LTE population ratio of the lower level and Γ is the Boltzmann exponential factor given by $\Gamma = (g_l/g_u)\exp(-hv_0/kT)$[1].

Models have been developed to compute the nonLTE energy level populations needed to relate the radiative transfer calculations to its nonLTE forms using equations 8.1 and 8.2 and hence properly interpret the radiances affected by nonLTE emissions. These models solve the equations that describe the population balance between energy level due to collisions (the statistical equilibrium equation) and the radiative transfer equation for the transitions governed by them.

The statistical equilibrium equation accounts for the excitation and deexcitation processes such as thermal collisions or collisions with molecules already in nonLTE while the radiative transfer equation considers the incoming solar flux (as well as the reflected one), the transfer of photons between atmospheric layers and spontaneous emissions. A detailed discussion of the methods to solve these equations is outside the scope of this thesis but can be found in López-Puertas and Taylor [2001].

Normally, nonLTE models express the nonLTE populations in terms of a vibrational temperature

$$T_v = \frac{\Delta E}{k\log(n_l g_u/n_u g_l)} \tag{8.3}$$

where ΔE is the energy difference of the upper and lower level. These vibrational temperature are a convenient input for the radiative transfer models because the ratio of nonLTE to LTE populations for the level x is given by

$$r_{\mathrm{x}} = \exp\left(\frac{\Delta E}{k}\left(\frac{1}{T_v} - \frac{1}{T}\right)\right) \tag{8.4}$$

which can be computed if the vibrational and kinetic temperatures are known [Edwards et al., 1993]. This type of scheme has been implemented into the RFM. [Dudhia, 2002*c*].

In general, the vibrational temperatures used to estimate the nonLTE radiances in the MIPAS retrievals algorithms either for the microwindow selection (as in the case of MORSE) or for the selection of emission lines less affected by nonLTE processes (as in the Linear retrieval) are provided by the Generic RAdiative traNsfer AnD non-LTE population Algorithm (GRANADA) [Funke et al., 2002]. The purpose of this chapter is to use MIPAS middle atmosphere measurements to validate these vibrational temperatures (i.e. the modelling of the nonLTE distributions).

In the following sections a technique to validate the diurnal nonLTE effects rather that the absolute nonLTE emission is introduced. This technique relies on the ratio of the daytime to nighttime radiance

[1]Note that the r_l, r_u and $\overline{\sigma}/\sigma$ are unity under LTE conditions.

assuming small nighttime nonLTE effects. Even though the technique presented here can be applied to any molecule, for clarity it will be explained first for CO_2 and then it will be applied to other constituents.

8.1 Methodology

The MIPAS instrument measures the atmosphere around 10:30 local time on the descending and around 22:30 on the ascending part of its orbit. The difference between descending (day) and ascending (night) zonal mean spectra results from diurnal variations in gas concentrations, temperature and nonLTE effects. When observing the emission of a gas with no diurnal variation such as CO_2, the ratio between the day and the night radiances will depend on the small diurnal variation of kinetic temperature and on the nonLTE effects (e.g. the upper energy level of the vibrational transition is pumped by the solar radiation during day but not during night). This measured ratio can be compared against the ratio predicted by nonLTE models. Comparing the ratios rather than absolute differences allows any variation between the atmospheric and model kinetic temperature and volume mixing ratio to be eliminated hence leaving mainly the nonLTE effects.

The simulated data are created using the RFM for CO_2 for the same tangent heights measured by MIPAS for day and night midlatitude climatological profiles. These profiles include the vibrational temperatures calculated by the GRANADA nonLTE model for these two conditions and use the same kinetic temperature as well as CO_2 concentration for both scenarios.

The analysis starts by sorting the MIPAS middle atmosphere apodized spectra for midlatitudes north or south (ie. 30°N to 60°N or 60°S to 30°S). This latitude range is used because it avoids the equatorial region where there is a significant diurnal tide, and it avoids high latitude regions where the atmosphere is more variable and, furthermore, because only day and night vibrational temperatures for midlatitude conditions were available. These sorted apodized spectra are then separated into day time and night time data using the Solar Zenith Angle (SZA) information. Both data sets are then averaged height by height to produce representative day and night mean MIPAS radiances for midlatitude north and south conditions.

8.1.1 Spectral masks

As already mentioned, MIPAS wide spectral range enables the identification of the emission from a particular constituent in different parts of the spectra. As shown in Figure 8.1, CO_2 emissions are

significant in the spectral regions corresponding to the A, AB and D MIPAS bands. To demonstrate the nonLTE effects the simulated night nonLTE emission are overplotted on top of the simulated day nonLTE emissions.

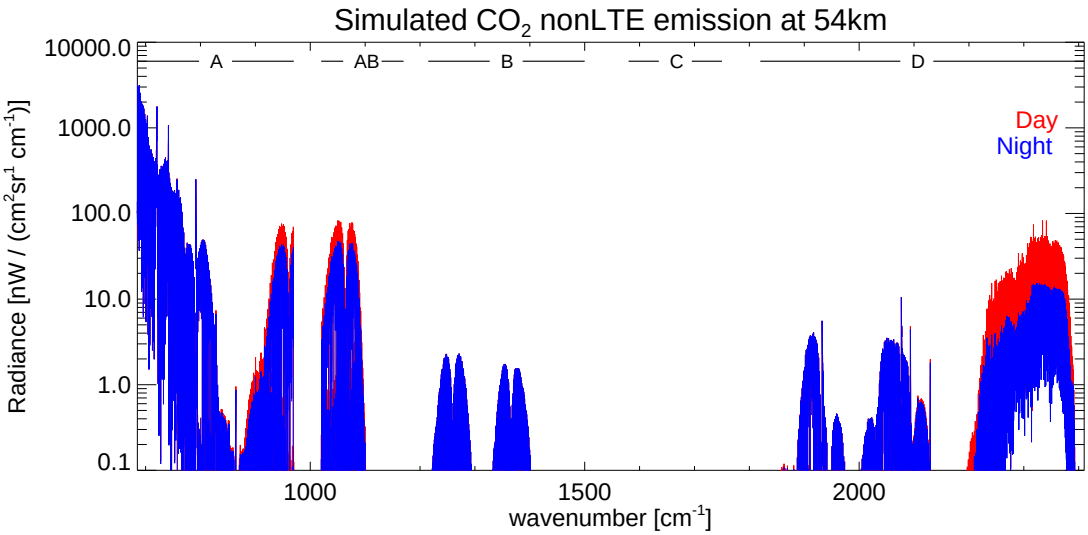

Figure 8.1: Simulated nonLTE CO_2 day and night emissions at 54 km for the day atmosphere

Spectral masks for each tangent height are used to isolated emissions from CO_2 in the corresponding bands. These spectral masks are created in a similar manner as for the linear retrieval (section 7.2.1). For this analysis, nonLTE emissions were not excluded.

8.1.2 Day/night ratio

These spectral masks were applied to the average midlatitude day and night spectra to discriminate the day and night CO_2 emission from the emission of the rest of the molecules observed by MIPAS and the ratio of these two "pure" CO_2 spectra was taken. This ratio is calculated using a weighted mean of the lines to minimises the influence of noise. The measurement ratio r_m is given by

$$r_\mathrm{m} = \frac{\sum_i m_{\mathrm{d}i} s_{\mathrm{n}i}}{\sum_i m_{\mathrm{n}i} s_{\mathrm{n}i}} \tag{8.5}$$

where $m_{\mathrm{d}i}$ and $m_{\mathrm{n}i}$ correspond to the measured radiance of the ith "pure" CO_2 day and night midlatitude MIPAS emission feature and $s_{\mathrm{n}i}$ correspond to the radiance of the ith CO_2 spectral line predicted by the nonLTE model using the night climatological profile.

This measurement ratio can be compared against the ratio predicted by the nonLTE model. This

simulated ratio r_{s} is given by

$$r_{\mathrm{s}} = \frac{\sum_i s_{\mathrm{d}i} s_{\mathrm{n}i}}{\sum_i s_{\mathrm{n}i}^2} \tag{8.6}$$

where $s_{\mathrm{d}i}$ corresponds to ith CO_2 spectral line predicted by the nonLTE model when using the day climatological profile.

8.2 CO_2 results

Figure 8.2 displays the result of the analysis for midlatitudes north and south for CO_2. When the day and night emission is in LTE or when the nonLTE emissions are not affected by solar illumination the expected result for the day/night ratio is one. Different days were analysed in order to allow for the effect of some SZA variation. Table 8.1 displays the mean SZA encountered in midlatitudes south and north for the day (d) and night (n) cases. In addition it also lists the day number relative to the summer solstice to the show the expected annual variation these days cover.

Table 8.1: Mean SZA variation

Date	Day no. relative to summer solstice	Midlatitude North	Midlatitude South
20070422	70	d:39.8 / n:118.0	d:64.8 / n:141.6
20070607	24	d:32.0 / n:107.7	d:72.8 / n:150.3
20070824	-54	d:42.5 / n:118.3	d:62.4 / n:141.6
20071013	-104	d:57.7 / n:137.1	d:43.8 / n:124.2
20080215	136	d:63.8 / n:118.3	d:44.5 / n:117.5

The first result that can be noted from Figure 8.2 is that the measured ratio does not change much between midlatitudes north and south. It also can be seen that the CO_2 emission from bands A and D, is in general, well modelled: the simulated ratio falls between the atmospheric variability encountered in the measured ratio. A small deviation from the simulated ratio is visible around 63 km for band A for all days at both midlatitudes. The AB simulated ratio differs significantly against the AB measured ratios.

8.3 Transitions

The analysis presented in the previous section can be extended to cope not only with the emission of CO_2 at different MIPAS bands, but also with the emission from different vibrational transitions for CO_2. This implies identifying inside the already CO_2 masked spectra the lines which correspond to

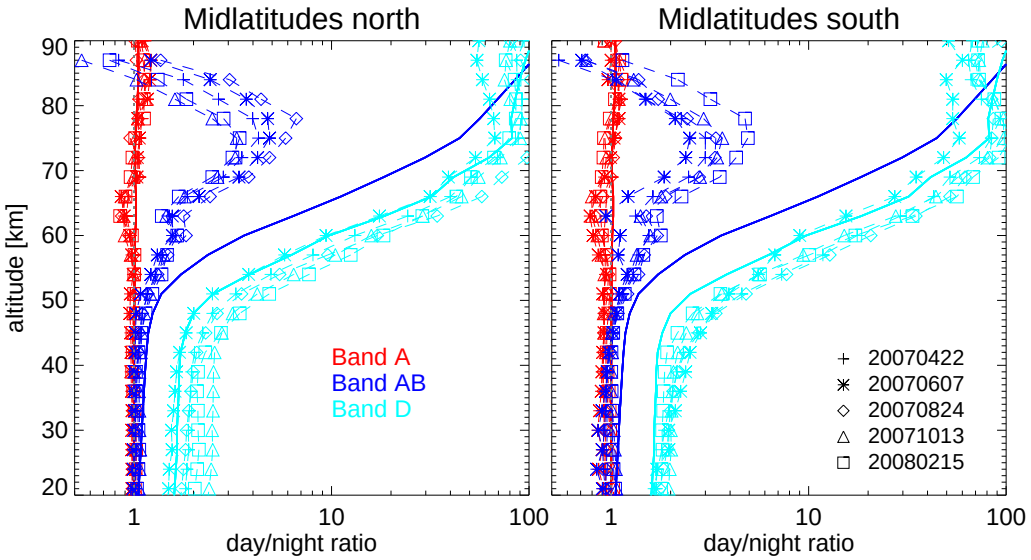

Figure 8.2: Simulated and measured day/night ratio for CO_2 for several days for midlatitude North and South scenarios. Dashed lines with different symbols represents the measured ratio for different days while the solid line corresponds to the simulated ratio. A gray dashed line represents the position at which the day/night ratio is equal to one.

different transitions.

Once the strongest transitions were identified, transition spectral masks were created using the same procedure as before in order to use them on top of the molecular spectral masks built previously.

Figure 8.3 displays the result of this extended analysis for midlatitudes south. The top panel shows the individual transitions identified for CO_2 in MIPAS band A, AB and D. The bottom panel shows the measured day/night ratio for the same days as in Figure 8.2.

Practically all the transitions in Figure 8.3 are in general well modelled. The exceptions are the transitions CO_2(5:9) in band A and the transition CO_2(3:9) in band AB. Both transitions have upper level "9" which suggests that discrepancy is a problem with the nonLTE model because the population of the upper level determines the emission from the transition. These transitions show a significant difference in magnitude below around 70 km and in both magnitude and trend above 70 km. The same results are found when analyzing the average midlatitudes north radiances.

Table 8.2 lists the standard HITRAN spectroscopic notation [Rothman et al., 1987] corresponding to these CO_2 HITRAN global quantum indices. This spectroscopic notation consists of quantum numbers (bands) denoted by 'v', 'ℓ' which represents the contribution of a given band to the angular rotation and 'r' which locates the level in the Fermi resonant group. A detailed discussion can be found in McClatchey et al. [1973].

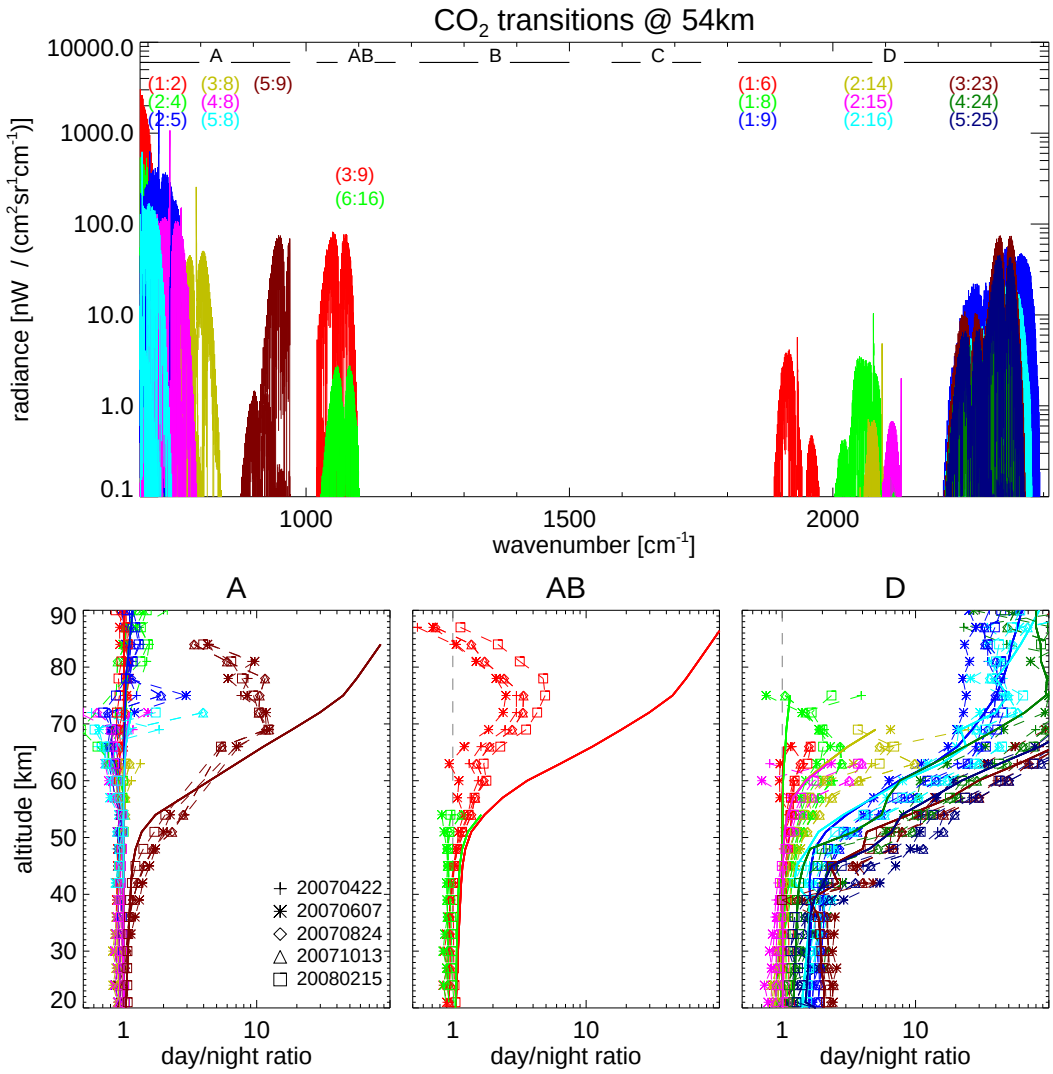

Figure 8.3: (top) Simulated CO_2 transitions and (bottom) simulated and measured day/night ratio for midlatitude south scenario. Dashed lines with different symbols represents the measured ratio for different days while the solid line corresponds to the simulated ratio. The numbers within brackets correspond to the HITRAN global quantum indices, for the HITRAN spectroscopic notation see table 8.2

8.4 Other molecules with no diurnal variation

Inside the MIPAS spectral range the molecules with little or no diurnal variation and which have a reasonable S/N ratio for at least some heights are: H_2O, HNO_3, CH_4, N_2O and CO. For these molecules, as in the case of CO_2, the only difference between the day and night simulated spectra are the vibrational temperatures given by the nonLTE model. In the following subsections, the analysis results correspond to the midlatitude south data but the same conclusions can be drawn from the midlatitude north data.

Table 8.2: CO_2

HITRAN global quantum indices	HITRAN spectroscopic notation [McClatchey et al., 1973]
	v_1 v_2 ℓ_2 v_3 r
1	00001
2	01101
3	10002
4	02201
5	10001
6	11102
8	11101
9	00011
14	12201
15	20001
23	10012
24	02211
25	10011

8.4.1 H_2O results

In the case of H_2O, its emission spreads over the complete MIPAS spectral range. However, strong "pure" lines required for this analysis appear mainly in the MIPAS bands B, C and D. H_2O emission in these spectral regions correspond mainly to the transition H_2O(1:2). Figure 8.4 shows that the behaviour of the MIPAS data is consistent from spectral region to spectral region. It can also be noted that the model predicts the observed ratio to within 10%. There is a discrepancy around 40 km where the model ratio is greater than one while the measured ratio is always lower than one.

Table 8.3 lists the standard HITRAN spectroscopic notation corresponding to these H_2O HITRAN global quantum indices. Note that these global quantum indices also apply for NO_2 and O_3.

Table 8.3: H_2O NO_2 O_3

HITRAN global quantum indices	HITRAN spectroscopic notation [McClatchey et al., 1973]
	v_1 v_2 v_3
1	000
2	010
3	020
4	100
5	001
7	110
8	011
13	101
14	002
18	111

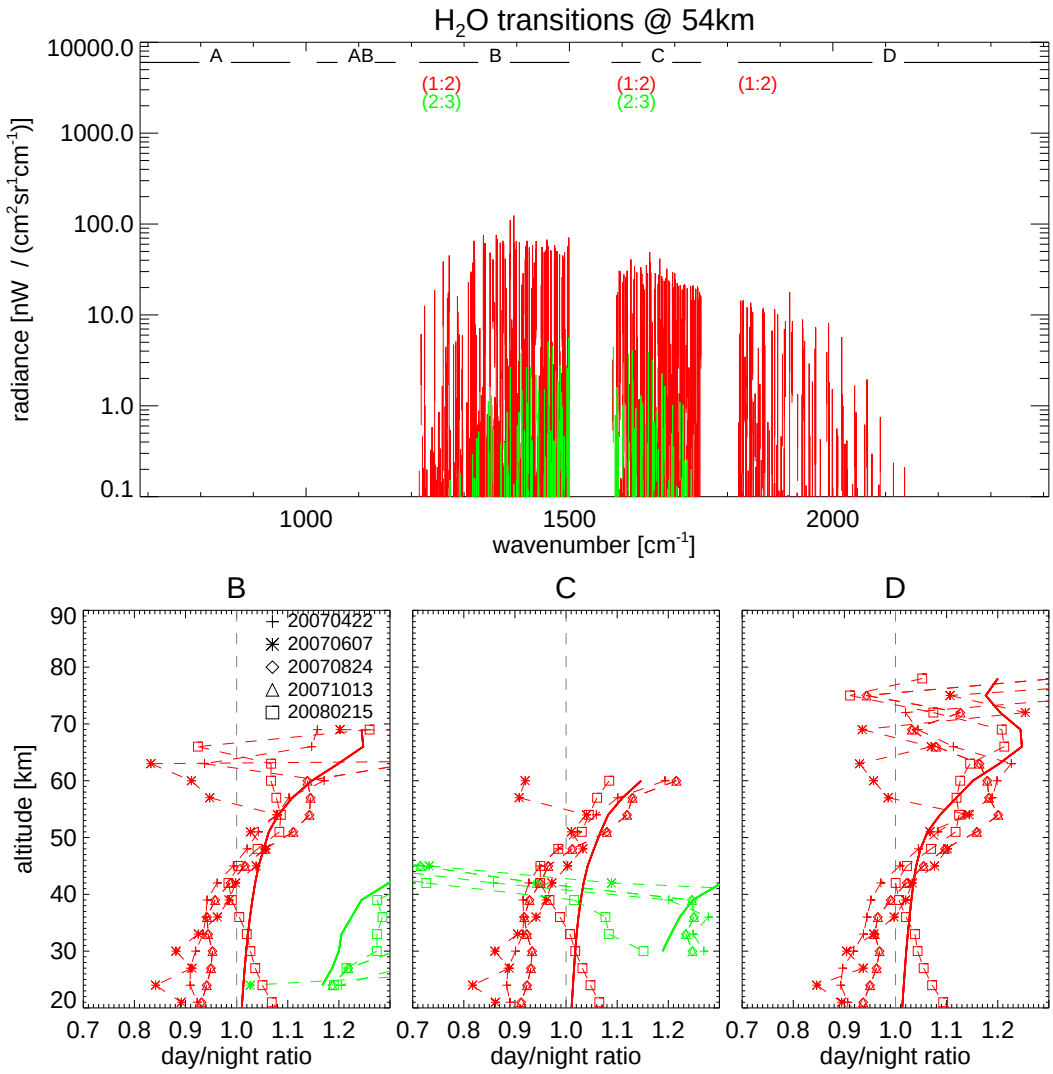

Figure 8.4: (top) Simulated H_2O transitions and (bottom) day/night ratios as found in the data (dashed lines) and in the simulations (solid line). The numbers within brackets correspond to the HITRAN global quantum indices, for the HITRAN spectroscopic notation see table 8.3

8.4.2 HNO_3 results

Figure 8.5 displays the transitions identified for HNO_3. These transitions are shown for a lower altitude than previously because there are no transitions of HNO_3 above 10% of the NESR expected for the MIPAS reduced resolution measurements above 50 km.

For this molecule strong "pure" lines required for this analysis appear only in MIPAS band A. The right panel shows the day/night ratio results. The analysis can only be extended up to about 40 km because at higher levels the S/N ratio is poor. At this low level, thermal collisions are assumed to be frequent enough to maintain the emission in LTE and therefore, the simulated ratio is equal to one. However, the measured ratio seems to be less than one at about 36 km and abruptly more than one

around 42 km. This behaviour is found in the transitions analyzed in practically all the days.

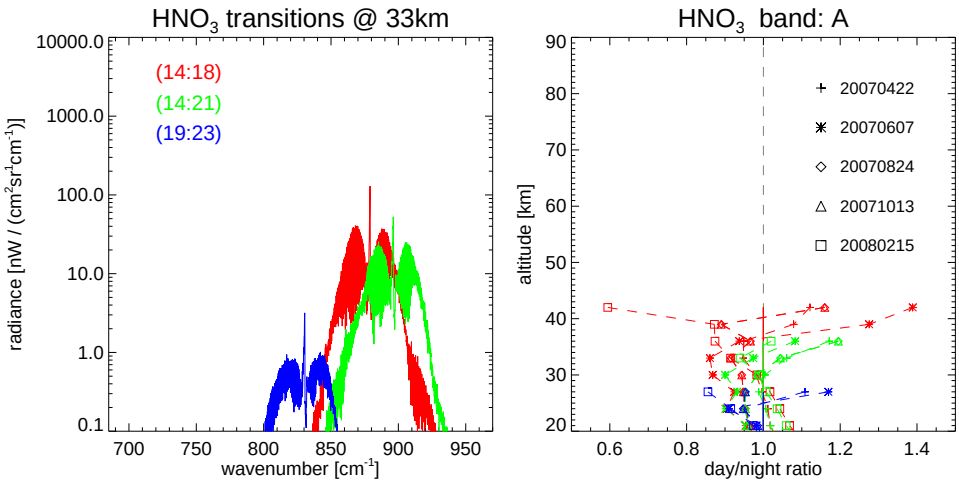

Figure 8.5: (left) Simulated HNO_3 transitions and (right) day/night ratios as found in the data (dashed lines) and in the simulations (solid line, in this case 1 everywhere). The numbers within brackets correspond to the HITRAN global quantum indices, for the HITRAN spectroscopic notation see table 8.4

Table 8.4 lists the standard HITRAN spectroscopic notation corresponding to these HNO_3 HITRAN global quantum indices. Note that since these vibrational quantum numbers cover whole bands they have been designated by indices to provide fast accessibility for applications such as nonLTE applications [Rothman et al., 1986].

Table 8.4: HNO_3

HITRAN global quantum indices	HITRAN spectroscopic notation [Rothman et al., 1987]
14	ground
18	V5
19	V9
21	2V9
23	3V9

8.4.3 CH_4 results

Figure 8.6 displays the results for CH_4. For this molecule strong "pure" lines required for this analysis appear only in MIPAS band B. The right panel shows the day/night ratio results. As in the H_2O day/night ratio there is an anomaly around 40 km where the model ratio is greater than one while the measured ratio is always lower than one. Above this altitude, the simulated ratio falls within the variability encountered in the measured ratio.

Table 8.5 lists the standard HITRAN spectroscopic notation corresponding to these CH_4 HITRAN global quantum indices.

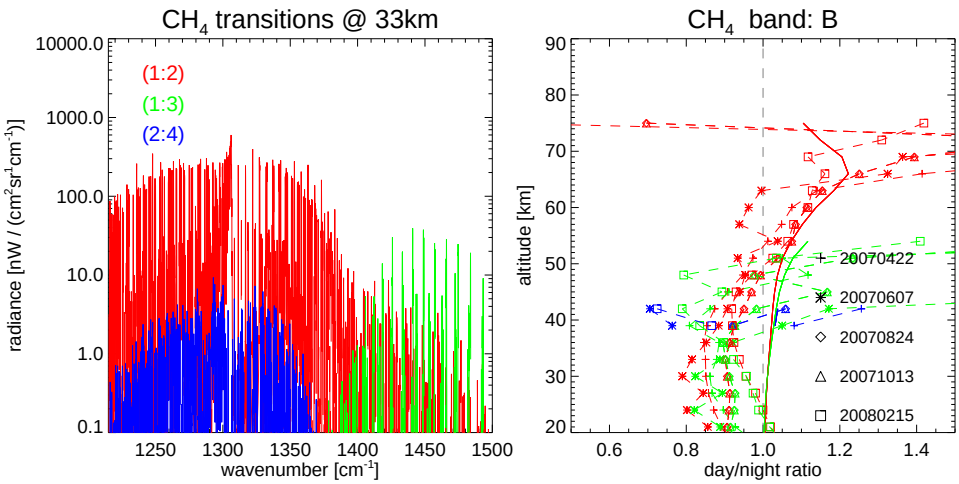

Figure 8.6: (left) Simulated CH_4 transitions and (right) day/night ratio as found in the data (dashed lines) and in the simulations (solid). The numbers within brackets correspond to the HITRAN global quantum indices, for the HITRAN spectroscopic notation see table 8.5

Table 8.5: CH_4

HITRAN global quantum indices	HITRAN spectroscopic notation [McClatchey et al., 1973] $v_1\ v_2\ \ell_2\ v_3\ \ell_3\ v_4\ \ell_4\ \ell$
1	00000000
2	00000111
3	01100001
4	00000202

8.4.4 CO results

Figure 8.7 displays the results for CO. Below 60 km, the simulated ratio falls inside the variability encountered inside the measured ratio, however, it seems to lie towards the high values. Above this altitude the simulated ratio always overestimates the measured ratio.

Table 8.6 lists the standard HITRAN spectroscopic notation corresponding to these CO HITRAN global quantum indices.

Table 8.6: CO

HITRAN global quantum indices	HITRAN spectroscopic notation [McClatchey et al., 1973] v_1
1	0
2	1

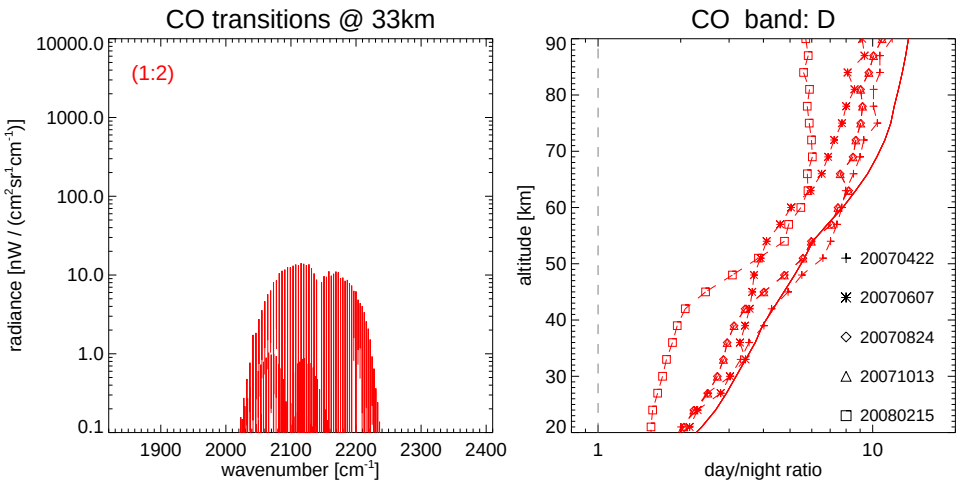

Figure 8.7: (left) Simulated CO transitions and (right) day/night ratios as found in the data (dashed lines) and in the simulations (solid line). The numbers within brackets correspond to the HITRAN global quantum indices, for the HITRAN spectroscopic notation see table 8.6

8.4.5 N_2O results

Figure 8.8 displays the N_2O results. In band B, the nonLTE model seems to assume LTE (simulated ratio equal one) while the measured ratio is negative up to 40 km and then abruptly becomes positive at around 50 km. In band D, the simulated ratio falls inside the huge variability shown in the measured ratio.

Table 8.7 lists the standard HITRAN spectroscopic notation corresponding to these N_2O HITRAN global quantum indices.

Table 8.7: N_2O

HITRAN global quantum indices	HITRAN spectroscopic notation [McClatchey et al., 1973] $v_1\ v_2\ \ell\ v_3$
1	0000
2	0110
4	0220
5	1000
8	1110
12	1220
14	0001
19	0111

8.5 Molecules with diurnal variation

The interpretation of the result of this analysis for gases that present a clear diurnal variation is not simple because the ratio will depend of the difference in the day–night concentration as well as in the

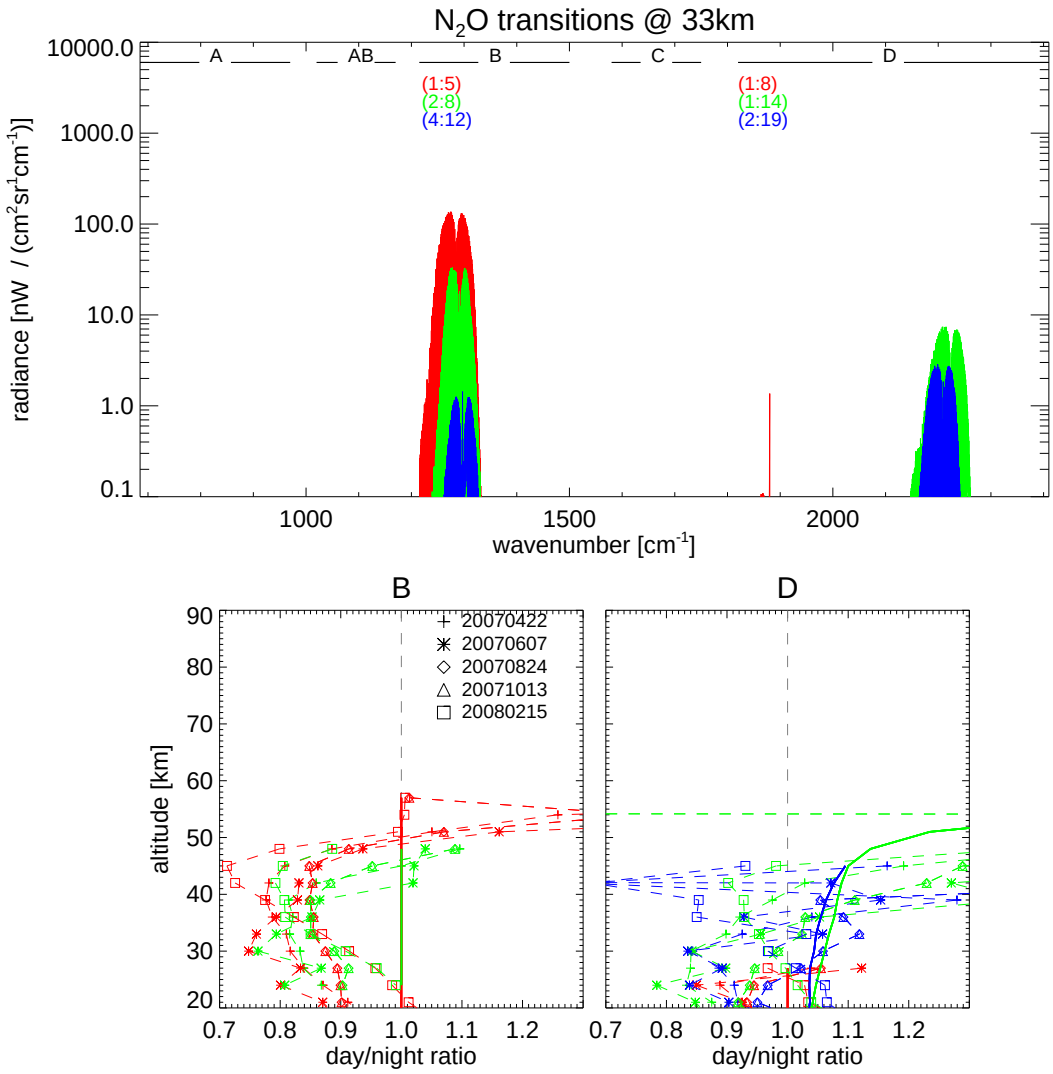

Figure 8.8: (top) Simulated N_2O transitions and (bottom) day/night ratios as found in the data (dashed lines) and in the simulations (solid line). The numbers within brackets correspond to the HITRAN global quantum indices, for the HITRAN spectroscopic notation see table 8.7

nonLTE effects. Nevertheless the analysis was applied to NO_2, NO and O_3,

In the case of NO_2 and NO, the day and night climatological profiles used to compute the simulated spectra include a diurnal variation and therefore the simulated ratio and the measured ratio should show relatively the same behaviour. In the case of O_3, the day and night climatological profiles used to computed the simulated spectra are identical, therefore, while the measurement ratio will reflect the nonLTE and day–night differences in concentration, the simulated ratio will only reflect the nonLTE day/night effects predicted by the model.

8.5.1 NO_2 results

Figure 8.9 displays on the results for NO_2 It can be seen that even though this molecule has a strong diurnal variation the simulated ratio shows the same trend as the variability encountered in the data. The worst case is around the lowest altitudes where the difference between the simulated ratio and the measured ratio is about 30%.

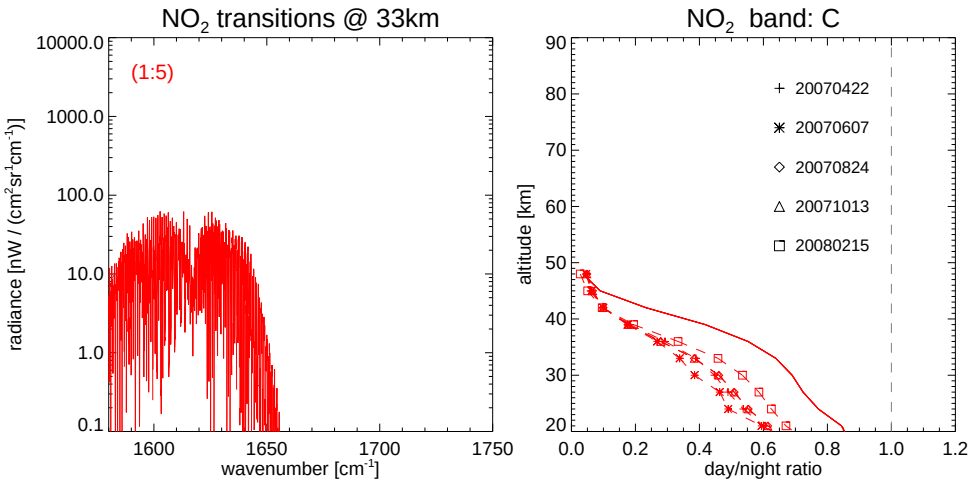

Figure 8.9: (left) Simulated NO_2 transitions and (right) day/night ratios as found in the data (dashed lines) and in the simulations (solid line). The numbers within brackets correspond to the HITRAN global quantum indices, for the HITRAN spectroscopic notation see table 8.3

The standard HITRAN spectroscopic notation corresponding to these NO_2 HITRAN global quantum indices are listed in Table 8.3.

8.5.2 NO results

Figure 8.10 displays the results for NO. Again, as for the NO_2 day/night ratio results, the simulated ratio shows the same trend as the measured ratio, however, for this molecule the offset encountered between the measured ratio and the simulated ratio is huge.

Table 8.8 lists the standard HITRAN spectroscopic notation corresponding to these NO HITRAN global quantum indices. Note that since these vibrational quantum numbers cover whole bands they have been designated by indices to provide fast accessibility for applications such as nonLTE applications [Rothman et al., 1986].

8.5.3 O_3 results

Figure 8.11 displays the results for O_3. As can be seen, the simulated transitional ratios predict no diurnal variation in the nonLTE effects. The measured ratio in band A and AB shows clear signatures

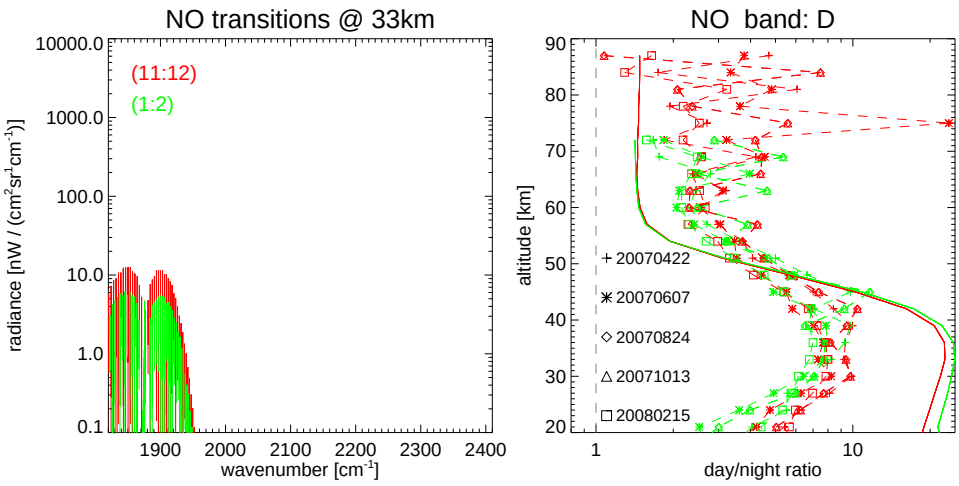

Figure 8.10: (left) Simulated NO transitions and (right) day/night ratios as found in the data (dashed lines) and in the simulations (solid line). The numbers within brackets correspond to the HITRAN global quantum indices, for the HITRAN spectroscopic notation see table 8.8

Table 8.8: NO

HITRAN global quantum indices	HITRAN spectroscopic notation [Rothman et al., 1987]
1	X3/2 0
2	X3/2 1
11	X1/2 0
12	X1/2 1

of the diurnal variation concentration with less ozone during daytime than during nighttime due to its destruction by UV solar radiation. However, the measured ratio in band D shows the opposite behaviour suggesting that some nonLTE effects are present. These nonLTE effects are not reflected in the simulated data and therefore assumed to be not modelled. Figure 8.11 also shows the ratio (black line) of the day nonLTE and the day LTE simulated radiance to show that there are some nonLTE effects predicted by the nonLTE model. This ratio is done with the entire signature of the molecule rather for a particular transition. The same ratio is found when analyzing the night nonLTE and LTE simulated radiances explaining why the simulated ratio is one.

The standard HITRAN spectroscopic notation corresponding to these NO HITRAN global quantum indices are listed in Table 8.3

8.6 Conclusions

A method to test the nonLTE model results is introduced. This method was used to analyze the main transitions of gases with no diurnal variation as CO_2, H_2O, HNO_3, CH_4, N_2O and CO, as well as

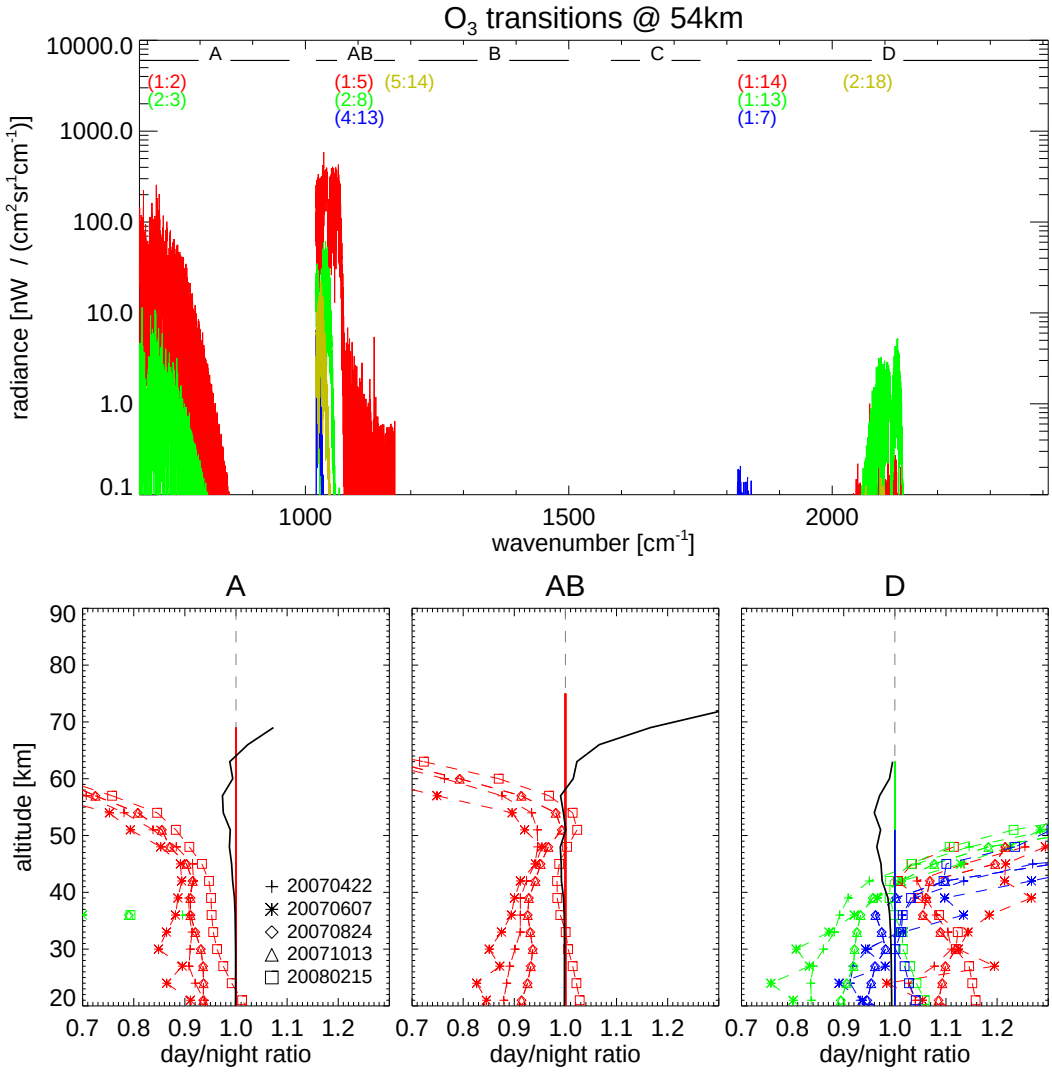

Figure 8.11: (top) Simulated O_3 transitions and (bottom) day/night ratios as found in the data (dashed lines) and in the simulations (solid line). The ratio between the day nonLTE and the day LTE is shown in black. The numbers within brackets correspond to the HITRAN global quantum indices, for the HITRAN spectroscopic notation see table 8.3

gases with diurnal variation such as NO_2, NO and O_3. In order to allow for the effect of some SZA variation, different days were analyzed.

The analysis of CO_2 transitions inside the MIPAS spectral range revealed a discrepancy in the modelling of the upper level "9" (00011) of the HITRAN global quantum indices, encountered in two different transitions, (5:9) in band A and (3:9) in band AB. This discrepancy suggests that there is a problem with the nonLTE model for this particular level because the population of the upper level determines the emission from the transition. The rest of the CO_2 transitions seem to fall inside the atmospheric variability encountered in the measured ratio.

The analysis of H_2O vibrational transition (1:2) revealed that the MIPAS data is consistent be-

tween spectral regions. It also displays a discrepancies around 40 km where the simulated ratio is always greater than one and the measured ratio is always lower than one. The same kind of discrepancy was found in the analysis of HNO_3, CH_4 and N_2O which suggests that this might be a temperature error rather than a nonLTE modelling discrepancy.

The results of NO_2 and NO prove that even though the ratio for these molecules is not only dependent on the nonLTE diurnal variation, the measured ratio and the simulated ratio shows relatively the same behaviour offseted by the diurnal variations and nonLTE differences between the simulated and the measured radiances.

The analysis of O_3 shows clear signatures of the diurnal variation in the measured ratio in band A and band AB while the measured ratio in band D suggest that some nonLTE effects are affecting the measured ratio but not modelled in the simulated ratio.

CHAPTER 9

Summary and conclusions

The mesosphere is gradually gaining attention in the climate change debate due to its predicted cooling as a result of greenhouse emissions. The purpose of this thesis was to investigate the feasibility of using satellite infrared remote sensing to retrieve temperature, pressure and composition at mesospheric heights; in particular, to assess the quality of the atmospheric data retrieved with the Michelson Interferometer for Passive Atmospheric Sounding (MIPAS) and the HIgh Resolution Dynamics Limb Sounder (HIRDLS).

To this end, the quality of the mesospheric measurements of both instruments was analyzed (chapter 4). In the case of HIRDLS, this was necessary because the HIRDLS radiances are subject to several correction algorithms to remove the radiation from a plastic film which is obstructing its field of view. It was discovered that, although the HIRDLS radiances show clear signatures of the secondary O_3 peak, they are not calibrated and hence not suitable for scientific studies for pressures lower than around 0.1 hPa.

In the case of MIPAS, this was necessary because the MIPAS middle atmosphere observations are not the nominal viewing mode and hence they have not been broadly used for scientific studies (i.e. not retrieved with the ESA operational processor). As part of this analysis, a technique to evaluate the calibration of MIPAS different viewing modes was introduced. Although in theory the different viewing modes should only differ in the tangent heights measured (i.e. all viewing modes should be equally well calibrated), this technique revealed anomalies in the MA viewing mode calibration presumably due to pointing problems.

Also, a technique to use the MIPAS mesospheric radiance to derive the radiometric offset and to validate the noise estimates was introduced. The radiometric offset derived between $800-860$ cm^{-1} was used to detect the PMCs emission despite their low emission due to the extremely cold

temperatures of the polar summer mesopause (chapter 5). Good agreement was found between an enhancement of the radiometric offset and PMCs detection by SCIAMACHY as well as ice supersaturation derived from MLS data.

Once established that the MIPAS radiances are suitable for mesospheric studies, an estimation of the quality of the MIPAS MORSE middle atmosphere retrievals as well as other mesospheric datasets was presented (chapter 6). In general, for pressure greater than 0.1 hPa the MORSE retrievals are within a 3 K or a 20% range difference. For lower pressures, this data may be used with caution depending on the molecule. Among the other instruments, the MLS, ACE and SOFIE datasets have the most potential to become an important source of mesospheric studies. For a complete summary of the results of these comparisons see table 6.3 and 6.4.

Next (chapter 7), an alternative algorithm to retrieve temperature, pressure and gas concentrations from limb viewing spectrometers was introduced. This algorithm exploits the linear properties of an optically thin path making it possible to perform the inversion without re-running the radiative transfer model as long as the initial guess is close enough to the scene conditions. The required proximity was established to be 20% for pressure and gas concentration (CH_4 in particular) and 10 K for temperature which may be achieved with a climatology of latitude resolution finer than 30°. An alternative scheme is also presented using multiple IGs and establishing which is the best.

This new retrieval scheme was implemented using MIPAS MA mode radiances. Currently the linear retrieval uses an ensemble of IGs corresponding to equatorial, day and night midlatitudes, polar summer and polar winter conditions. This new algorithm uses the whole spectral band of the molecule rather than small subset of it (the microwindows) and therefore, theoretically, leads to a higher precision.

Finally, a method for validating the modeled vibrational temperatures used in the MORSE and in the linear retrieval as part of the selection of spectral points used (chapter 8). This validation relies on the ratio of the daytime to nighttime radiances assuming that during nighttime the nonLTE processes are negligible. This validation was performed on the main transitions of CO_2, H_2O, HNO_3, CH_4, N_2O, CO, NO_2, NO and O_3 for midlatitudes. In general, most of the transitions analyzed fall inside the atmospheric variability encountered in the measurements, the main discrepancy being the CO_2 upper level 00011 of the HITRAN spectroscopic notation (the upper level of the laser band) which vibrational temperatures are now undergoing revision.

9.1 Suggestions for further work

- The MIPAS MORSE middle atmosphere retrievals need to be analyzed further for pressures lower than 0.1 hPa to determine whether the overestimation or underestimation at this pressure levels can be improved with better climatological values or if a better knowledge of the nonLTE processes affecting the corresponding radiances is needed.

- Once the MIPAS H_2O retrievals at upper mesospheric pressures is improved, maps of ice saturation derived from MIPAS data can be directly compared with maps of the $800-860\,\mathrm{cm}^{-1}$ radiometric enhancement to investigate how the PMCs evolve.

- The MIPAS MORSE middle atmosphere retrievals need to be revised in conjunction with the MIPAS nominal mode retrievals to improve consistency between the datasets.

- A better climatology needs to be constructed to fully analyze the potential of the linear retrieval.

- The linear retrieval of gas concentrations could be extended to incorporate more molecules.

- A radiometric offset needs to be fitted as part of the linear retrieval scheme to reduce its influence especially around mesospheric heights.

- A vibrational temperature climatology may be constructed using monthly averaged MIPAS radiances to retrieve them using monthly ACE, MLS and SOFIE data as kinetic temperatures and concentrations.

Bibliography

Aikin, A., Chanin, M., Nash, J. and Kendig, D. [1991], 'Temperature Trends in the lower mesosphere', *Geophysical Research Letters* **18**, 3, 416–419.

Andrews, D., Holton, J. and Leonvy, C. [1987], *Middle Atmosphere Dynamics*, Academic Press.

Backhouse, T. [1885], 'The luminous cirrus clouds of June and July', *Meteorological Magazine* **20**, 130.

Bailey, S., Merkel, A., Thomas, G. and Carstens, J. [2005], 'Observations of polar mesospheric clouds by the Student Nitric Oxide Explorer', *Journal of Geophysical Research* **110**, D13203.

Barnes, J., Kaplan, T., Vomel, H. and Read, W. [2008], 'NASA/Aura/Microwave Limb Sounder Water Vapor Validation at Mauna Loa Observatory by Raman Lidar', *Journal of Geophysical Research* **113**.

Barnett, J., Hepplewhite, C., Rokke, L. and Gille, J. [2005], 'Mapping the optical obscuration in the NASA Aura HIRDLS instrument', *Proceedings of SPIE* **5883**, 103 – 112.

Bates, D. and Nicolet, M. [1950], 'Atmospheric hydrogen', *Astronomical Society of the Pacific* **62**, 106–110.

Beer, R. [1992], *Remote Sensing by Fourier Transform Spectroscopy*, John Wiley and Sons.

Beig, G. [2002], 'Overview of the mesospheric temperature trend and factors of uncertainty', *Physics and Chemistry of the Earth* **27**, 509–519.

Bernath, P. F. [2006], 'Atmospheric chemistry experiment (ACE): Analytical chemistry from orbit', *Trends in Analytical Chemistry* **25-7**, 647–654.

Boone, C., McLeod, S. and Bernath, P. [2002], 'Apodization Effects in the Retrieval of Volume Mixing Ratio Profiles', *Applied Optics* **41**, 1029–1034.

Bourassa, A., Degenstein, D. and Llewellyn, E. [2008], 'SASKTRAN: A Spherical Geometry Radiative Transfer Code for Efficient Estimation of Limb Scattered Sunlight', *Journal Quantitative Spectroscopy and Raditive Transfer* **109**, 52–73.

Bovensmann, H., Burrows, J. P., Buchwitz, M., Frerick, J., Noel, S. and Rozanov, V. V. [1999], 'SCIAMACHY: Mission Objectives and Measurement Modes', *Journal of Atmospheric Sciences* **56 - 2**, 127–150.

Brasseur, G. and Solomon, S. [1986], *Aeronomy of the middle atmosphere*, D. Reidel 2nd Revision.

Caledonia, G. E., Green, B. D. and Nadile, R. M. [1985], 'The Analysis of SPIRE Measurements of Atmospheric Limb CO2(ν2) Fluorescence ', *Journal of Geophysical Research* **90**, A10 9783–9788.

Carlotti, M., Brizzi, G., Papandrea, E., Prevedelli, M., Ridolfi, M., Dinelli, B. and Magnani, L. [2006], 'GMTR: Two-dimensional geo-fit multitarget retrieval model for Michelson Interferometer for Passive Atmospheric Sounding / Environmental Satellite observations', *Applied Optics* **45**, 4.

CIRA [1988], 'CIRA 1986, Part I: Thermosphere Model', *Advance Space Research* **8**, 5–6.

Dials, M., Gille, J., Barnett, J. and J.Whitney [1998], 'Description of the High Resolution Dyanmics Limb Sounder (HIRDLS) instrument', *Proceedins of SPIE* **3437**, 84–91.

Dudhia, A. [2002*a*], 'MORSE: MIPAS optimal retrieval using sequential estimation'.
URL: *http://www.atm.ox.ac.uk/MORSE/*

Dudhia, A. [2002*b*], 'Oxford: MIPAS L2 products'.
URL: *http://www.atm.ox.ac.uk/group/mipas/L2OXF/index.html*

Dudhia, A. [2002*c*], 'Reference Forward Model software manual'.
URL: *http://www.atm.ox.ac.uk/RFM/*

Dudhia, A. [2007], 'Microwindow selection for the MIPAS reduce resolution mode', *Proceedings of the third workshop on the Atmospheric Chemistry Validation of Envisat (ACVE -3)* .

Dudhia, A., Jay, V. and Rodgers, C. [2002], 'Microwindow selection for high spectral resolution sounders', *Applied Optics* **41**, 3665–3673.

Edwards, D., Gille, J., , Bailey, P. and Barnett, J. [1995], 'Selection of the Sounding Channels for the High Resolution Dyanmics Limb Sounder (HIRDLS)', *Applied Optics* **34**, 30.

Edwards, D., Lopez-Puertas, M. and Lopez-Valverde, M. [1993], 'Non-Local Thermodynamic Equilibrium Studies of the 15-μm Bands of CO2 for Atmospheric Remote Sensing', *Journal of Geophysical Research* **98**, D8, 14,955–14,977.

Endemann, M. [1999], 'MIPAS instrument Concept and Performance', *ESA-ESTEC* .

Fischer, H., Blom, C., Oelhaf, H., Carli, B., Carlotti, M., Delbouille, L., Ehhalt, D., Flaud, J., Isaksen, I., Lopez-Puertas, M., McElroy, C. and Zander, R. [2000], 'ENVISAT-MIPAS, the Michelson Interferometer for Passive Atmospheric Sounding; An instrument for atmospheric chemistry and Climate Research ENVISAT Mipas An instrument for Atmospheric Chemistry and Climate Research'.

Francis, G., Edwards, D., Lambert, A., Halvorson, C., Lee-Taylor, J. and Gille, J. [2006], 'Forward modeling and radiative transfer for the NASA EOS-Aura High Resolution Dynamics Limb Sounder (HIRDLS) instrument', *Journal of Geophysical Research* **111**, D13301.

Frisk, U., and J. Ala-Laurinaho, M. H., Andersson, S., Berges, J., Chabaud, J., Dahlgren, M., Emrich, A., Floren, H., Florin, G., Fredrixon, M., Gaier, T., Haas, R., Hirvonen, T., Hjalmarsson, A., Jukkala, P., Kildal, P., Kollberg, E., Lassing, J., Lecacheux, A., Lehikoinen, P., Lehto, A., Jakobsson, B., Mallat, J., Marty, C., Michet, D., Narbonne, J., Nexon, M., Olberg, M., Olofsson, A., Olofsson, G., Origne, A., Petersson, M., Piironen, P., Pons, R., Pouliquen, D., Ristorcelli, I., Rosolen, C., Rouaix, G., Raisanen, A., Serra, G., Sjpberg, F., Stenmark, L., Torchinsky, S., Tuovinen, J., Ullberg, C., Vinterhav, E., Wadefalk, N., Zirath, H., Zimmermann, P. and Zimmermann, R. [2003], 'The Odin Satellite I. Radiometer design and test', *Astronomy and astrophysics* **402**.

Froidevaux, L., Jiang, Y., Lambert, A., Livesey, N., Read, W., Waters, J., Browell, E., Hair, J., Avery, M., McGee, T., Twigg, L., Sumnicht, G., Jucks, K., Margitan, J., Sen, B., Stachnik, R., Toon, G., Bernath, P., Boone, C., Walker, K., Filipiak, M., Harwood, R., Fuller, R., Manney, G., Schwartz, M., Daffer, W., Drouin, B., Cofield, R., Cuddy, D., Jarnot, R., Knosp, B., Perun, V., Snyder, W., Stek, P., Thurstans, R. and Wagner, P. [2008], 'Validation of Aura Microwave Limb Sounder stratospheric ozone measurements', *Journal of Geophysical Research* **113**(D15S20).

Funke, B., F.J. Martin-Torres, M. L.-P., Höpfner, M., López-Valverde, F. H. M. and Garcia-Comas, M. [2002], 'A generic non-LTE population model for MIPAS-ENVISAT data analysis', *Geophysical Research Abstract* **Abstract 4915**, 27.

Gille, J., Barnett, J., Arter, P., Barker, M., Bernath, P., Boone, C., Cavanaugh, C., Chow, J., Coffey, M., Craft, J., Craig, C., Dials, M., Dean, V., Eden, T., Edwards, D., Francis, G., Halvorson, C., Harvey, L., Hepplewhite, C., Khosravi, R., Kinnison, D., Krinsky, C., Lambert, A., Lee, H., Lyjak, L., Loh, J., Mankin, W., Massie, S., McInerney, J., Moorhous, J., Nardi, B., Packman, D., Randall, C., Reburn, J., Rudolf, W., Schwartz, M., Serafin, J., Stone, K., Torpy, B., Walker, K., Waterfall, A., Watkins, R., Whitney, J., Woodard, D. and Young, G. [2008], 'The High Resolution Dynamics Limb Sounder (HIRDLS): Experiment Overview, Recovery and Validation of Initial Temperature Data', *Journal of Geophysical Research* **27**.

Gille, J. and House, F. [1971], 'On the inversion of Limb Radiance Measurements I: Temperature and Thickness', *Journal of Atmospheric Sciences* **28**, 1427–1442.

Goody, R. [1964], *Atmospheric Radiation. I Theoretical basis*, Oxford University Press.

Gordley, L. L., Hervig, M. E., Fish, C., III, J. M. R., Bailey, S., Cook, J., Hansen, S., Shumway, A., Paxton, G., Deaver, L., Marshall, T., Burton, J., Magill, B., Brown, C., Thompson, E. and Kemp, J. [2009], 'The solar occultation for ice experiment', *Journal of Atmospheric and Solar-Terrestrial Physics* **71**, 300–315.

Grossmann, K., Gusev, O., Assou, M. and Witt, G. [2006], 'Spectral emission measurements of polar mesosperic clouds by CRISTA-2', *Atmospheric Chemistry and Physics* **68**, 1781–1790.

Haley, C., von Savigny, C., Brohede, S., Sioris, C., McDade, I., Llewellyn, E. and Murtagh, D. [2003], 'A comparison of methods for retrieving stratospheric ozone profiles from OSIRIS limb-scatter measurements', *Advances in Space Research* **34**, 769–774.

Hawkins, G., Hunneman, R., Barnett, J. and Whitney, J. [1998], 'Spectral design and verification of HIRDLS filters and antireflection coatings using an integrated system performance approach', *Proceedings of SPIE* **3437**, 102–112.

Hervig, M., Thompson, R., McHugh, M. and Gordley, L. [2001], 'First confirmation that water ice is the primary component of polar mesospheric clouds', *Geophysical Research Letters* **28**, 6, 971–974.

Hoffmann, L., Spang, R., Kaufmann, M. and Riese, M. [2005], 'Retrieval of CFC-11 and CFC-12 from Envisat MIPAS observations by means of rapid radiative transfer calculations ', *Advances in Space Research* **36**, 915–921.

Houghton, J. T. [1986], *The physiscs of atmospheres*, Cambridge University Press.

Jesse, O. [1887], 'Observations of Noctilucent Clouds', *Meteor* pp. Z. 4, 179–181.

Kaiser, J., von Savigny, C., Eichmann, K., Noël, S., Bovensmanns, H. and Burrows, J. [2004], 'Satellite-pointing retrieval from atmospheric limb-scattering of solar UV-B radiation', *Canadian Journal Physics* **82**, 1041–1052.

Kaplan, L. [1959], 'Inference of atmospheric structure from remote radiation measurements', *Journal of the Optical Society of America* **49**, 10.

Kaye, J. and Kumer, J. [1987], 'Nonlocal thermodynamic equilibrium effects in stratospheric NO and implications for infrared remote sensing', *Applied Optics* **26**, (22) 4747–4754.

Kerridge, B. and Remsberg, E. [1989], 'Evidence From the Limb Infrared Monitor of the Stratosphere for Nonlocal Thermodynamic Equilibrium in the v_2 Mode of Mesospheric Water Vapour and the v_3 Mode of Stratospheric Nitrogen Dioxide ', *Journal of Geophysical Research* **94**, D13, 16323–16342.

Kinnison, D., Gille, J., Barnett, J., Randall, C., Harvey, L., Lambert, A., Khosravi, R., Alexander, M., Bernath, P., Boone, C., Cavanaugh, C., Coffey, M., Craig, C., Dean, V., Eden, T., Ellis, T., Fahey, D., Francis, G., Halvorson, C., Hannigan, J., Hartsough, C., Hepplewhite, C., Krinsky, C., Lee, H., Mankin, B., Marcy, T., Massie, S., Nardi, B., Packman, D., Popp, P., Santee, M., Yudin, V. and Walker, K. [2008], 'Global Observations HNO3 from the High Resolution Dynamics Limb Sounder (HIRDLS) First Results', *Journal of Geophysical Research* **113**, D16S44.

Kleinert, A. [2007], 'MIPAS Level 1B algorithms overview: operational processing and characterisation', *Atmospheric Chemistry and Physics* **7**, 1395–1406.

Lambert, A., Bailey, P., Edwards, D. P., Gille, J., Johnson, B., Halvorson, C., Massie, S. and Stone, K. [1999], 'High-Resolution Dynamics Limb Sounder, Level-2 Algorithm Theoretical Basis Document', *Internal document* .

Leslie, R. [1885], 'Sky glows', *Nature* **33**, 245.

Livesey, N. [2007], 'EOS MLS version 2.2 level 2 data quality and description document', *Technical Report D-33509, Jet Propul. Laboratory California Institue of Technology* .

Livesey, N., Snyder, W., Read, W. and Wagner, P. [2006], 'Retrieval algorithms for the EOS Microwave Limb Sounder (MLS) instrument', *IEEE Transanctions Geosciences Remote Sensing 44* **5**, 1144–1155.

Llewellyn, E., Lloyd, N., Degenstein, D., Gattinger, R., Petelina, S., Bourassa, A., Wiensz, J., Ivanov, E., McDade, I., Solheim, B., McConnell, J., Haley, C., von Savigny, C., Sioris, C., McLinden, C., Griffioen, E., Kaminski, J., Evans, W., Puckrin, E., Strong, K., Wehrle, V., Hum, R., Kendall, D., Matsushita, J., Murtagh, D., Brohede, S., Stegman, J., Witt, G., Barnes, G., Payne, W., Pich, L., Smith, K., Warshaw, G., Deslauniers, D.-L., Marchand, P., Richardson, E., King, R., Wevers, I., McCreath, W., Kyrl, E., Oikarinen, L., Leppelmeier, G., Auvinen, H., Mgie, G., Hauchecorne, A., Lefvre, F., de La Ne, J., Ricaud, P., Frisk, U., Sjoberg, F., von Schele, F., and Nordh, L. [2004], 'The OSIRIS instrument on the Odin spacecraft', *Canadian Journal of Physics* **82**, 411–422.

López-Puertas, M., Funke, B., Bermejo-Pantaleón, D., Garcia-Comas, M., von Clarmann, T., Grabowski, U., Hopfner, M., Stiller, G., Kaufmann, M. and Koukouli, M. [2007], 'Measurements of the middle and upper atmosphere with MIPAS/ENVISAT', *Proceedings of the ENVISAT meeting 2007* .

López-Puertas, M. and Taylor, F. [1989], 'Carbon dioxide 4.3-μm emission in the earth's atmosphere: a comparison between NIMBUS 7 SAMS measurements and non-local thermodynamic equilibrium radiative transfer calculations', *Journal of Geophysical Research* **94**, (D10) 13045–13068.

López-Puertas, M. and Taylor, F. [2001], *non-LTE Radiative Transfer in the Atmosphere*, World Scientific.

Lubken, F. and von Zahn, U. [1991], 'Thermal structure of the Mesopause Region at Polar Latitudes', *Journal of Geophysical Research* **96**, D11, 20841–20857.

Marsh, D., Smith, A., Brasseur, G., Kaufmann, M. and Grossmann, K. [2001], 'The existence of a tertiary ozone maximum in the high-latitude middle mesosphere', *Geophysical Research Letters* **28**, 4531–4534.

Marti, J. and Mauersberger, K. [1993], 'A survey and new measurements of ice vapor pressures at temperature between 170K and 250K', *Geophysical Research Letters* **20-5**, 363–366.

Massie, S., Gille, J., Khosravi, R., Lee, H., Kinnison, D., Francis, G., Nardi, B., Eden, T., Craig, C., Halvorson, C., Coffey, M., Packman, D., Cavanaugh, C., Craft, J., Dean, V., Ellis, D., Barnett,

J., Hepplewhite, C., Lambert, A., Manney, G., Strawa, A. and Legg, M. [2007], 'High resolution Dynamics Limb Sounder observations of polar stratospheric clouds and subvisible cirrus', *Journal of Geophysical Research* **112**, D24S31.

Mauersberger, K. and Krankowsky, D. [2003], 'Vapor pressure above ice at temperature below 170K', *Geophysical Research Letters* **30-3**, 21 1–3.

McClatchey, R. A., Benedict, W. S., Clough, S. A., Burch, D. E., R. F. Calfee, K. F., Rothman, L. S. and Garing, J. S. [1973], 'AFCRL Atmospheric Absorption Line Parameters Compilation', *AFCRL-TR-0096 (AFCRL, Bedford, MA)* .

Mertens, C., Mlynczak, M., López-Puertas, M., Wintersteiner, P., Picard, R., Winick, J., Gordley, L. and III, J. R. [2001], 'Retrieval of mesospheric and lower thermospheric kinetic temperature from measurements of CO_2 15μm Earth limb emission under non-LTE conditions', *Geophysical Research Letters* **28**.

Milne, E. [1930], 'Thermodynamics of the stars', *Handbuch der Astrophysik (Reprinted in Selected Papers on the transfer radiation by Menzel, 1966)* **3**, 1.

Mlynczak, M. [1997], 'Energetics of the mesosphere and lower thermosphere and the SABER experiment', *Advance Space Research* **20**(6), 1177–1183.

Murgatroyd, R. J. and Singleton, F. [1961], 'Possible meridional circulations in the stratosphere and mesosphere', *Quarterly journal of the Royal Meteorological Society* **87 no.372**, 125–135.

Nardi, B., Gille, J., Barnett, J., Randall, C., Harvey, V., Waterfall, A., Reburn, W., Leblanc, T., McGee, T., Twigg, L., Thompson, A., Godin-Beekmann, S., Bernath, P., Bojkov, B., Boone, C., Cavanaugh, C., Coffey, M., Craft, J., Craig, C., Dean, V., Eden, T., Francis, G., Froidevaux, L., Halvorson, C., Hannigan, J., Hepplewhite, C., Kinnison, D., Khosravi, R., Krinsky, C., Lambert, A., Lee, H., Loh, J., Massie, S., McDermid, I. S., Packman, D., Torpy, B., Walverde-Canossa, J., Walker, K., Whiteman, D., Witte, J. and Young, G. [2008], 'Initial validation of ozone measurements from the High Resolution Dynamics Limb Sounder', *Journal of Geophysical Research* **113**, D16S36.

Norton, R. and Beer, R. [1976], 'New apodizing functions for Fourier spectrometry', *Journal of the Optical Society of America* **66 no. 3**.

ONSALA-webpage [2010].

URL: *http://www.chalmers.se/rss/oso-sv/popularvetenskap/forskningen/teleskop*

Petelina, S., Llewellyn, E., Degenestin, D. and Lloyd, N. [2006], 'Odin/OSIRIS limb observations of polar mesoshperic clouds in 2001-2003', *Journal of Atmospheric and Solar-Terrestrial Physics* **68**, 42–55.

Press, W., Flannery, B., Teukolsky, S. and Vetterling, W. [1986], *Numerical Recipes The art of scientific computing*, Cambridge University Press.

Pumphrey, H. C., Filipiak, M. J., Livesey, N. J., Schwartz, M. J., Boone, C., Walker, K. A., Bernath, P., Ricaud, P., Barret, B., Clerbaux, C., Jarnot, R. F., Manney, G. L., and Waters, J. W. [2007], 'Validation of middle-atmosphere carbon monoxide retrievals from the Microwave Limb Sounder on Aura', *Journal of Geophysical Research* **112**, D24S38.

Remedios, J., Leigh, R., Sembhi, H. and Waterfall, A. [2007], 'New IG2 seasonal climatologies for MIPAS', *Proceedings Envisat Symposium 2007* .

Remsberg, E., Lingenfelser, G., Harvey, V., W.Grose, III, J., Mlynczak, M., Gordley, L. and Marshall, B. [2003], 'On the verification of the quality of SABER temperature, geopotential height, and wind fields by comparison with Met Office assimilated analyses', *Journal of Geophysical Research* **108**(D20), ACL 4–1 ACL 4–10.

Ricaud, P., Alexandre, D., Barret, B., Flochmoen, E. L., Motte, E., Berthet, G., Lefevre, F. and Murtagh, D. [2007], 'Measurements of mid-stratospheric formaldehyde from the Odin/SMR instrument', *Journal of Quantitative Spectroscopy and Radiative Transfer* **107**, 91–104.

Ridolfi, M., Carli, B., Carlotti, M., von Clarmann, T., Dinelli, B., Dudhia, A., Flaud, J.-M., Hopfner, M., Morris, P., Raspollini, P., Stiller, G. and Wells, R. [2000], 'Optimised forward model and retrieval scheme for MIPAS near-real time and data processing', *Applied Optics* **39**, 8, 1323–1340.

Roble, R. and Dickinson, R. [1989], 'How will changes in carbon dioxide and methane modify the mean structure of the mesosphere and thermosphere?', *Geophysical Research Letters* **16**, 12, 1441–1444.

Rodgers, C. [1976], 'Retieval of Atmospheric Temperature Composition From Remote Measurements of Thermal Radiation', *Reviews of Geophysics and Space Physics* **14**, 4, 609–624.

Rodgers, C. D. [2000], *Inverse Methods for atmospheric sounding Theory and practice*, World Scientific.

Rothman, L. S., Gamache, R. R., Goldman, A., Brown, L. R., Toth, R. A., Pickett, H. M., Poynter, R. L., Flaud, J., Camy-Peyret, C., Barbe, A., Husson, N., Rinsland, C. P., and Smith, M. A. H. [1987], 'The HITRAN database: 1986 edition', *Applied Optics* **26**, 19.

Rothman, L. S., Gamache, R. R., Goldman, A., Brown, L. R., Toth, R. A., Pickett, H. M., Poynter, R. L., Flaud, J.-M., Camy-Peyret, C., Barbe, A., Husson, N., Rinsland, C. P. and Smith, M. A. H. [1986], 'The HITRAN database: 1986 edition', *Applied Optics* **26 (19)**, 4058–4097.

Russell, J. M., Bailey, S., Gordley, L. L., Rusch, D. W., Horanyi, M., Hervig, M. E., Thomas, G. E., Randall, C. E., Siskind, D. E., Stevens, M., Summers, M. E., Taylor, M., Englert, C., P, J. E. and Merkel, W. E. M. A. W. [2009], 'The Aeronomy of Ice in the Mesosphere (AIM) mission: Overview and early science results', *Journal of Atmospheric and Solar-Terrestrial Physics* **71**, 289–299.

SABER-webpage [2008].
URL: *http://saber.gats-inc.com/*

Santee, M., Lambert, A., Read, W., Livesey, N., Cofield, R., Cuddy, D., Daffer, W., Drouin, B., Froidevaux, L., Fuller, R., Jarnot, R., Knosp, B., Manney, G., Perun, V., Snyder, W., Stek, P., Thurstans, R., Wagner, P., Waters, J., Muscari, G., deZafra, R., Dibb, J., Fahey, D., Popp, P., Marcy, T., Jucks, K., Toon, G., Stachnik, R., Bernath, P., Boone, C., Walker, K., Urban, J. and Murtagh, D. [2007], 'Validation of Aura Microwave Limb Sounder HNO3 Measurements', *Journal of Geophysical Research* **112**.

Santee, M., Manney, G., Livesey, N. and Read, W. [2004], 'Three-dimensional structure and evolution of stratospheric HNO_3 based on UARS Microwave Limb Sounder measurements', *Journal of Geophysical Research* **109**, D15306.

Schwartz, M., Lambert, A., Manney, G., Read, W., Livesey, N., Froidevaux, L., Ao, C., Bernath, P., Boone, C., Cofield, R., Daffer, W., Drouin, B., Fetzer, E., Fuller, R., Jarnot, R., Jiang, J., Jiang, Y., Knosp, B., Kruger, K., Li, J.-L., Mlynczak, M., Pawson, S., III, J. R., Santee, M., Snyder, W., Stek, P., Thurstans, R., Tompkins, A., Wagner, P., Walker, K., Waters, J. and Wu, D. [2008], 'Validation of the Aura Microwave Limb Sounder Temperature and Geopotential Height Measurements', *Journal of Geophysical Research* **113**.

Solomon, S., J.Kiehl, Kerridge, B., Remsberg, E. E. and III, J. M. R. [1986], 'Evidence for Nonlocal

Thermodynamic Equilibrium in the $\nu 3$ Mode of Mesospheric Ozone', *Journal of Geophysical Research* **91**, (D9) 9865–9876.

Thomas, G. [1991], 'Mesospheric clouds and the physics of the mesopause region', *Reviews of Geophysics* **29**, 4 553–575.

Thomas, G. and Olivero, J. [1989], 'Climatology of Polar Mesospheric Clouds 2. Further Analysis of Solar Mesosphere Explorer Data', *Journal of Geophysical Research* **94**, D12, 14673–14681.

Thomas, G., Olivero, J., Jensen, E., Schroeder, W. and Toon, O. [1989], 'Relation between increasing methane and the presence of ice clouds at the mesopause', *Nature* **338**, 490–491.

von Clarmann, T., Glatthor, N., Grabowski, U., Höpfner, M., Kellmann, S., Kiefer, M., Linden, A., Mengistu Tsidu, G., Milz, M., Steck, T., Stiller, G. P., Wang, D. Y., Fischer, H., Funke, B., Gil-López, S. and López-Puertas, M. [2003], 'Retrieval of temperature and tangent altitude pointing from limb emission spectra recorded from space by the Michelson Interferometer for Passive Atmospheric Sounding (MIPAS)', *Journal of Geophysical Research* **108**(D23).

von Savigny, C., Haley, C. S., Sioris, C. E., McDade, I., Llewellyn, E., Degenstein, D., Evans, W., Gattinger, R. L., Griffioen, E., Kyrölä, E., Lloyd, N. D., McConnell, J., McLinden, C., Megie, G., Murtagh, D., Solheim, B. and Strong, K. [2003], 'Stratospheric ozone profiles retrieved from limb scattered sunlight radiance spectra measured by the OSIRIS instrument on the Odin satellite', *Geophysical Research Letters* **30 no.14**.

von Savigny, C., Kokhanovsky, A., Bovensmann, H., Eichmann, K.-U., Kaiser, J., Noel, S., Rozanov, A., J.Skupin and Burrows, J. [2004], 'NLC detection and particle size determination: first results from SCIAMACHY on ENVISAT', *Advances in Space Research* pp. 851–856.

Walker, J. [2008], *Retrieval of non-standard species from MIPAS-ENVISAT*, DPhil Thesis.

Walker, K., Butler, M. and Bernath, P. [2006], 'File format desciption for ACE-FTS level 2 data version 2.2 ASCII format', *Internal document* .

Waters, J., Froidevaux, L., Harwood, R., Jarnot, R., Pickett, H., Read, W., Siegel, P., Cofield, R., Filipiak, M., Flower, D., Holden, J., Lau, G., Livesey, N., Manney, G., Pumphrey, H., Santee, M., Wu, D., Cuddy, D., Lay, R., Loo, M., Perun, V., Schwartz, M., Stek, P., Thurstans, R., Boyles, M., Chandra, S., Chavez, M., Chen, G.-S., Chudasama, B., Dodge, R., Fuller, R., Girard, M., Jiang, J., Jiang, Y., Knosp, B., LaBelle, R., Lam, J., Lee, K., Miller, D., Oswald, J., Patel, N., Pukala,

D., Quintero, O., Scaff, D., Snyder, W., Tope, M., Wagner, P. and Walch, M. [2006], 'The Earth Observing System Microwave Limb Sounder (EOS MLS) on the Aura satellite', *IEEE Transactions Geosciences Remote Sensing 44* **5**.

Waters, J., Read, W., Froidevaux, L., Jarnot, R., Cofield, R., Flower, D., Lau, G., Pickett, H., Santee, M., Wu, D., Boyles, M., Burke, J., Lay, R., Loo, M., Livesey, N., Lungu, T., Manney, G., Nakamura, L., Perun, V., Ridenoure, B., Shippony, Z., Siegel, P., Thurstans, R., Harwood, R. and Filipiak, M. [1999], 'The UARS and EOS Microwave Limb Sounder Experiments', *Journal of Atmospheric Sciences* **56**, 194–218.

Waymark, C. [2009], *Joint validation of HIRDLS and TES*, DPhil Thesis.

Wintersteiner, P., Picard, R., Sharma, R. and Winick, J. [1992], 'Line-by-Line Radiative Excitation Model for the Non-Equilibrium Atmosphere: Application to CO_2 15-μm Emission', *Journal of Geophysical Research* **97**, D16, 18083–18117.